SOME NEW DIRECTIONS IN HOC METHODOLOGY: TACKLING CIRCULAR GEOMETRIES

by

Rajendra Kumar Ray

DEPARTMENT OF MATHEMATICS
INDIAN INSTITUTE OF TECHNOLOGY GUWAHATI,
GUWAHATI-781039, INDIA

February, 2009

SOME NEW DIRECTIONS IN HOC METHODOLOGY: TACKLING CIRCULAR GEOMETRIES

A Thesis Submitted

in Partial Fulfillment of the Requirements

for the Degree of

DOCTOR OF PHILOSOPHY

by

Rajendra Kumar Ray

(Roll Number: 04612303)

to the

DEPARTMENT OF MATHEMATICS

INDIAN INSTITUTE OF TECHNOLOGY GUWAHATI

4^{th} February, 2009

DECLARATION

It is certified that the work contained in the thesis titled **"Some new Directions in HOC Methodology: Tackling Circular Geometries"** has been done by me, a student in the department of Mathematics, Indian Institute of Technology Guwahati under the guidance of Dr. Jiten C. Kalita for the award of Doctor of Philosophy and that this work has not been submitted elsewhere for a degree.

4^{th} February, 2009

Rajendra Kumar Ray
Department of Mathematics
Indian Institute of Technology Guwahati

CERTIFICATE

It is certified that the work contained in the thesis titled **"Some new Directions in HOC Methodology: Tackling Circular Geometries"** by **Rajendra Kumar Ray**, a student in the department of Mathematics, Indian Institute of Technology Guwahati for the award of the degree of Doctor of Philosophy has been carried out under my supervision and this work has not been submitted elsewhere for a degree.

4^{th} February, 2009

Dr. Jiten C. Kalita
Associate Professor
Department of Mathematics
Indian Institute of Technology Guwahati

Dedicated
to
my Parents

Acknowledgement

This is the space in my dissertation to serve tribute to those individuals who stood behind me, encouraged me, believed in me, taught me and contributed in any way (direct or indirect) to overcome the hurdles of one of lifes most important challenges. The outcome of this tedious Ph.D work not only gives the academic excellence, but also provides the courage and confidence to carry on the journey on an uneven path of life.

I would like to express my deepest gratitude to my thesis supervisor **Dr. Jiten C. Kalita** for his confidence, kindness and patience with me for all these years. We have had a number of conversations about research, science, sports and many other topics that I value a lot. I consider myself lucky and most honored to be his research student.

I would like to thank Prof. D. C. Dalal, chairman of my doctoral committee and other members of the committee, Dr. S. Natesan and Dr. Manmohan Pandey for reviewing my research work regularly and for all their valuable suggestions for my doctoral research.

I specially acknowledge Prof. Anoop K. Dass of the department of Mechanical Engineering, IIT Guwahati for his valuable suggestions and constant encouragement through out this work. I am also conveying my gratitude to Prof. R. Alam, Dr. S. N. Bora, Dr. S. P. Chakrabarty, Dr. B. K. Sharma, Dr. N. Selvaraju and Dr. M. Prabhakar of the department of Mathematics, IIT Guwahati for their inspiration and support during the tenure of my research.

I am thankful to Prof. S. K. Samanta, Prof. S. Chakravarty and Dr. P. Chatterjee of my former institute, Visva-Bharati university, for their constant encouragement to do higher studies.

I express my sincere thanks to our lab. assistant Mr. Shantanu Majumder for technical support, the staff members of Mathematics department, Sridhar Samal and Manoj Boro for their help in official matters.

I am fortunate to have Safique da, Martha da, Swapan da, Tarakanta da, Bhupen da, Madhusmita di, Sasmita di as my Seniors. Their expertise has been a great help to me. I am also thankful to Rajesh, Kaushik, Akhilesh, Smruti, Jugal, Debajit, Raju,

Cosmika, Shubh and all the research scholars of Mathematics department, with whom I shared my wonderful time.

I express my sincere thanks to all my friends who helped me in whatever form during my stay at IIT Guwahati, particularly Patrada, Purnada, Santanuda, Biplabda, Manos, Bittoda, Laha, Avijit, Prabhanjan, Anto, Ballav, Sonit, Perumal, Ranjath, Anup, Anupam, Abhijit for all the (good and bad) moments we shared.

I am deeply indebted to my parents (Baba, Maa) and my brother (Bhai) for their moral support, constant encouragement, patience, inspiration, immense love through out my research period.

Finally, my sincere thanks are due to all those who have helped me in whatever manner during my Ph.D. work, some of whom I may have inadvertently forgotten to mention in this acknowledgement.

4^{th} February, 2009 **Rajendra Kumar Ray**

Abstract

The present work is mainly deals with the development of a class of higher-order compact (HOC) finite difference formulations to tackle the circular geometries both for the continuous and discontinuous cases. Depending upon this, the contains of the present work can be divided into two parts. The first part concerned with the development of HOC schemes for convection-diffusion equations in general and incompressible viscous flows in particular on nonuniform polar coordinate system. The basic difference between the proposed scheme and the earlier HOC schemes is that the proposed schemes are able to handle variable coefficients of the second order derivatives while the previous schemes could deal only with unit diffusion coefficients on cartesian or cylindrical polar coordinate on uniform grid. A fourth order accurate HOC scheme for the steady state convection-diffusion equations on non-uniform polar grid has been developed first. The scheme produces highly accurate results even in coarser grids for different fluid flow problems. An HOC treatment for the streamfunction-vorticity (ψ-ω) formulation of the two-dimensional unsteady, incompressible, viscous Navier-Stokes equations on polar grid has been developed next, specifically designed for the motion past circular cylinder problems. The scheme is second order accurate in time and at least third order accurate in space. The HOC treatment is also used to discretize the Neumann boundary conditions. The scheme is then used to solve the flow past an impulsively started circular cylinder problem for a wild range of Reynolds numbers (Re) and to solve the flow past rotating cylinder problems for wild range of both Re and rotation parameter (α). Present numerical results are then compared with the existing experimental and standard numerical results. In every case an excellent agreement has been found. In this process, some new properties have been found and some extended works have been carried out which have not been studied earlier.

The second part of the present work deals with the development of finite difference algorithms which are obtained by clubbing the existing HOC methodology with a special treatment to tackle the immersed interfaces for problems having discontinuities along the

circular interfaces. Firstly, a new methodology for numerically solving one-dimensional (1D) elliptic equations with discontinuous coefficients, fluxes and singular source terms and the corresponding unsteady parabolic equations on nonuniform space grids have been developed. Stability and convergence analysis of the newly developed scheme have been carried out next. Then, this 1D idea has been extended for the 2D elliptic problems with same type of discontinuities. For both the 1D and 2D cases, numerous numerical studies on a number of problems have been done and compared present results with those obtained by well known methods. In all cases, our formulation is found to produce better results on relatively coarser grids.

Contents

List of Figures

List of Tables

Chapter 1

Introduction

1.1 Background

When a fluid flows past a stationary body or, equivalently, when a body moves in a fluid at rest, a region of disturbed flow is always formed around the body. The extent of the disturbed flow region is largely dependent on the shape, orientation, and size of the body, the velocity and viscosity of the fluid, and may be influenced by a wide variety of small disturbances. This type of fluid flow problems frequently arise in the field of aerospace, civil, hydraulic, electric transmission lines, mechanical, nuclear, offshore, and wind engineering. Most of the bluff bodies having different shapes used in engineering applications have circular geometries. Due to the highly complex flow structures generated by them, this class of problems has attracted a great deal of research in all the three approaches in fluid dynamics: pure experimental, pure theoretical and computational.

The third approach, namely, Computational Fluid Dynamics (CFD) involves describing the fluid flow in terms of mathematical models that include convective and diffusive transport of some variables. These models consist of the governing equations in the form of ordinary or partial differential equations (ODEs or PDEs). As a great number of such model equations like the Navier-Stokes (N-S) equations do not possess analytical solutions, one has to resort to numerical methods. Amongst the popular methods that has been used quite frequently in CFD is the finite difference method. Here, the basic methodology involves discretizing the problem domain by setting up a grid (preferably structured) and then approximating the derivatives appearing in the governing equations by difference quotients at each grid point. Such approximation yields a system of algebraic equations which can then be solved by some matrix solution algorithm.

Over the years, the second order central difference schemes, because of their easy and straight-forwardness in application, have for quite some time been a popular choice for discrete approximation of partial differential equations. Such methods are known to yield quite good results on reasonable meshes if the solution is well behaved. But

for certain problems, such as the convection dominated flows, the solution may exhibit oscillatory behaviour if the mesh is not sufficiently refined. However, mesh refinement invariably brings in additional points into the system resulting in an increased system size and consequently more memory and CPU time are required to solve such problems on a computer. Again discretization on a non-compact stencil (generally associated with higher-order accurate methods) increases the band-width of the coefficient matrix arising out of the discretization process. Both mesh refinement and increased matrix band-width ultimately lead to increased arithmetic operations. Thus neither a lower-order accurate method on a fine mesh nor a higher-order accurate one on a non-compact stencil could be computationally cost-effective. Therefore, of late, the Higher Order Compact (HOC) finite difference schemes for the computation of incompressible viscous flows are gradually gaining popularity because of their high accuracy and advantages associated with compact difference stencils. A compact finite difference scheme is one which utilizes grid points located only directly adjacent to the node about which the differences are taken. In addition, if the scheme has an order of accuracy greater than two, it is termed a higher-order compact method.

There exists several mechanisms through which finite difference schemes can achieve higher-order compactness. To get higher order compactness Gupta *et al*. [51] apply series expansion to the differential equations. Dennis and Hudson [39] employ a transformation that involves expanding the exponential of a definite integral of the convective coefficient of the PDE. Gartland [49] uses discrete weighted mean approximation to get higher order compactness while Noye and Tan [87] apply weighted modified PDE method.

Another way of obtaining higher-order compactness is by using the original differential equation to substitute for the leading truncation error (TE) terms of the standard central difference approximation. This is the mechanism that has been adopted throughout the present work. Most of these schemes were developed for equations of the convection-diffusion type and were well equipped to simulate incompressible viscous flows governed by the Navier-Stokes equations as well. Lax and Wendroff [70] first use this idea to raise the temporal accuracy from one to two. They use this idea on transient hyperbolic PDEs and use the original PDE to approximate the second-order time derivative in a Taylor series expansion. Later on, Mackinnon and Carry [79] use the same idea to increase the spatial accuracy. Mackinnon and Johnson [80] develop an $O(h^4)$ HOC scheme (h is the grid spacing) for the two dimensional (2D) steady-state convection-diffusion problems using the same idea. At the same time, in a different way Abarbanel and Kumar [16] develop a higher order scheme for the Euler equations which is 4th order accurate in space and 2nd order accurate in time. These schemes are similar to those developed by Dukowicz [41] and Wong [117] though they were achieved in a different manner. The idea of Mackinnon and Johnson [80] is extended by Spotz and

Carey [106] to the steady-state stream-function vorticity (ψ-ω) formulation of the N-S equations and by Kalita *et al.* [61] to its unsteady counterpart. However majority of these HOC schemes developed so far are mostly on uniform grids [51, 61, 74, 106]. The very few attempts that have been made to develop HOC scheme on nonuniform grids for the convection-diffusion equations [91, 98, 107, 121] use the conventional transformation technique from the physical plane to the computational plane. Later on Kalita *et al.* [62, 64] extended this work for convection-diffusion equations as well as for the transient stream-function vorticity formulation of the Navier-Stokes equations on nonuniform grids in cartesian coordinate system. They showed that clustering the grids on the region where complexity is more, very accurate results can be achieved through HOC schemes with significantly small number of grid points.

It may be mentioned that all the above approaches result in formulations where the dependent variable is explicitly present in the formulation unlike the higher order schemes described by Lele [72] and others [17, 55, 101, 103, 112] on compact stencils. These schemes [17, 55, 72, 101, 103, 112] are based on Padé [6] approximation, which is an implicit relation between the derivatives and functions at adjacent nodal points. They include information not only from the adjacent points to the node about which the differences are taken, but also includes information from nodal points located at distance two or three steps away from that node.

1.2 Motivation

A careful study of the works discussed so far reveals a plethora of issues concerning HOC schemes and their applicability to convection-diffusion problems in general and incompressible viscous flows in particular. The differential equation based HOC schemes discussed earlier do not cover problems on irregular geometries described in curvilinear coordinate system involving variable diffusion coefficients of the second order derivatives. Very few attempts have been made to handle these variable coefficients on nonuniform grids, that too in transformed planes only. In particular, no HOC scheme has been developed to solve the complex flow problem like flow past circular cylinders. This type of flow problems frequently arise in various engineering fields which offer tough challenges particularly at high Reynolds numbers. Also the idea of using this type of HOC schemes has not been explored for problems having various kinds of discontinuities present in the governing differential equation and problems involving domains having circular interfaces. Thus, work in the development and application of HOC algorithms for these problems is a challenging one and is replete with many interesting possibilities. These are the major motivating factors behind this work.

1.3 Objectives

The objective of the present work is to develop some new HOC finite difference algorithms for the 2D linear and nonlinear convection-diffusion equations in curvilinear coordinate system without transforming the original physical domain, more specifically for the Navier-Stokes equations in circular geometries. In the process, we aim to validate these algorithms by applying them to complex flow problems like the flow past circular cylinders. Also intended is to explore the possibility of extending some existing HOC algorithms to tackle problems having discontinuities around circular interfaces.

1.4 The Work

The present work is mainly divided into two parts. The first part deals with the development of HOC finite difference algorithms for the two-dimensional (2D) linear and nonlinear convection-diffusion equations, more specifically for the N-S equations in curvilinear coordinate system and the second part deals with the development of finite difference algorithms for problems having discontinuities along circular interfaces which are obtained by clubbing some existing HOC methodologies with special interface treatments.

In the first part, we develop a class of HOC schemes on non-uniform cylindrical polar coordinate system. The basic difference between the proposed scheme and the earlier HOC schemes is that the proposed schemes are able to handle variable coefficients of the second order derivatives while the previous schemes could deal only with unit diffusion coefficients. This perhaps is the reason that majority of the earlier endeavors to develop HOC schemes on cylindrical polar coordinates were confined to the Poisson equation on uniform grids [52, 59, 60, 68, 69, 123]. Here, firstly we develop a fourth order accurate HOC scheme for the steady state convection-diffusion equations on non-uniform polar grids and show the way for its extension to curvilinear coordinate systems. We then employ the proposed scheme on three different problems. The first of these problems has an exact solution and we compare our numerical results with the exact ones; in the process, we also demonstrate the fourth order accuracy of our scheme. Next we compute the steady flow past a circular cylinder which is governed by the N-S equations. We compare our computed solutions with existing experimental and numerical results and in each case our results agree very well with the benchmark results. Finally, we numerically solve the driven polar cavity flow. Here also, we obtain excellent agreements with the existing experimental and numerical results.

Next, we develop an HOC scheme for the ψ-ω formulation of the unsteady N-S equations in polar grids, specifically designed for the motion past a circular cylinder problem. The scheme is second order accurate in time and at least third order accurate

in space. Its extension to the curvilinear coordinate system is also straightforward.

To validate the proposed scheme, we apply it to the famous problem of unsteady flow past an impulsively started circular cylinder for a wide range of Reynolds numbers (Re) ranging from 10 to 9500. In the process, we have also developed transient HOC approximation for the Neumann boundary condition for vorticity. For moderate and low Re, we compute the flow until steady state or till the flow becomes periodic. For the higher range of Re, we compute the solution in the initial stages of the flow. For all the Reynolds numbers, detailed discussions on the flow structure and comparison with experimental and numerical [2, 10, 12, 14, 18, 26, 34, 35, 44, 46, 47, 77, 78, 86, 100, 111, 116] results are provided. In each case, our solution agrees very well, both qualitatively and quantitatively with established numerical and experimental results, confirming the efficiency of the proposed scheme. The robustness of the scheme however is better realized when it captures the periodic nature of the flow for $Re = 60$ and 200 characterized by vortex shedding represented by the von Kármán street and also by the fact that it very accurately captures the so called α and β-phenomena for higher Re.

We then extend the applicability of the newly developed transient HOC scheme to capture the more complex phenomena of unsteady flow past a rotating and translating cylinder for Reynolds numbers 200, 500 and 1000 for the range of rotational parameters $0.5 \leq \alpha \leq 3.25$. We not only compute the flow for the early stages of the flow, but also for long enough time to investigate the vortex shedding phenomenon as well. We provide quantitative comparison between our numerical results with the existing theoretical and experimental [19, 20, 21, 29, 30, 31, 36, 57, 58, 66, 82, 84, 98] results in terms of the lift and drag coefficients, vorticity profile on the solid cylinder, the path of the first and second vortex centers, the radial and tangential velocities for certain combinations of Re and α values. We also compare the simulations of the flow patterns computed by us with the experimental flow visualizations and numerical results that are available in the literature. In all the cases, our numerical results are in excellent agreement with the existing results. It is worth mentioning that for both the impulsively started and rotating cylinder problems, the flow simulations from our computations are much closer to the experimental visualization than any other existing numerical simulation available in the literature.

The second part of the PhD work is concerned with the development of HOC algorithms for problems having discontinuities along circular interfaces in Cartesian coordinates. Here, we firstly develop a new methodology for numerically solving one-dimensional (1D) elliptic equations with discontinuous coefficients, fluxes and singular source terms and the corresponding unsteady parabolic equations on nonuniform space grids. This higher order compact formulation is at least third order accurate for the points far from the points of discontinuities (termed regular points) and exactly third

order accurate at points just next to the discontinuity (termed irregular points). We perform stability and convergence analysis, and conduct numerous numerical studies on a number of problems [23]. We then extend our 1D methodology to the 2D elliptic equations on uniform space grids where the equation has discontinuous coefficients and singular source terms along circular interfaces. This higher order compact formulation is fourth order accurate at regular grid points and second order accurate at irregular points. For both the 1D and 2D cases, we conduct numerous numerical studies on a number of problems and compare our results with those obtained with immersed interface [73] and other well known methods. In all cases our formulation is found to produce better results on relatively coarser grids.

1.5 Organization of the work

This thesis work is organized in eight chapters. In Chapter 2, we develop an HOC scheme for 2D steady-state convection diffusion equations that can be easily applied to the 2D steady-state N-S equations. Chapter 3 describes the extension of this scheme to unsteady N-S equations. In Chapter 4, we make a comprehensive study of the motion past an impulsively started circular cylinder with the help of the scheme developed in Chapter 3. Chapter 5 studies the rotating counterpart of this problem. In Chapter 6, we develop a new methodology for numerically solving one-dimensional elliptic equations with discontinuous coefficients, fluxes and singular source terms and the corresponding unsteady parabolic equations on nonuniform space grids. Chapter 7 discusses the extension of this 1D methodology to 2D interface problems on uniform Cartesian grids. Finally, Chapter 8 summarizes the whole work and throw some light on the scope for future work.

Chapter 2

A transformation-free HOC scheme for steady incompressible viscous flows on nonuniform polar grids

2.1 Introduction

The steady two-dimensional (2D) convection-diffusion equation in cartesian coordinate system (x, y) for a transport variable ϕ in some continuous domain with suitable boundary conditions can be written as

$$-\nabla^2\phi + c_1(x,y)\frac{\partial\phi}{\partial x} + c_2(x,y)\frac{\partial\phi}{\partial y} = f(x,y), \tag{2.1}$$

where c_1 and c_2 are the convection coefficients, and f is a forcing function. In equation (2.1), the magnitude of the convection coefficients determines the ratio of convection to diffusion and is sometimes referred to as the Reynolds number (Re). The equation becomes convection dominated for large Re and diffusion dominated for small Re. Most of the steady 2D flows are expressed in this form. It represents the convection-diffusion of many fluid variables such as mass, heat, energy, vorticity etc. With proper choice of c_1, c_2 and f, it can also be used to represent the complete Navier-Stokes (N-S) equations.

In polar coordinate system (r, θ), equation (2.1) takes the form

$$-\nabla^2\phi + c_1(r,\theta)\frac{\partial\phi}{\partial r} + c_2(r,\theta)\frac{\partial\phi}{\partial \theta} = f(r,\theta). \tag{2.2}$$

The direct implementation of the existing HOC approaches ([51, 53, 61, 62, 74, 106, 107, 108]) on polar coordinates are not possible because of the fact that the second order partial derivatives of the transport variable representing the phenomenon of diffusion invariably come with variable coefficients. All these schemes were equipped to deal with variable convection coefficients only. This is where the need of develop a new HOC approach to solve the equation of type (2.2) arises. Though equations (2.1) and (2.2) are identical, the Laplacians appearing in the two equations are different in terms

of coefficients of the second order partial derivatives with respect to the independent variables. Assorting derivatives of different orders, (2.2) may be written as

$$-\frac{\partial^2\phi}{\partial r^2} - \frac{1}{r^2}\frac{\partial^2\phi}{\partial\theta^2} + \left(c_1(r,\theta) - \frac{1}{r}\right)\frac{\partial\phi}{\partial r} + c_2(r,\theta)\frac{\partial\phi}{\partial\theta} = f(r,\theta). \tag{2.3}$$

In this chapter, we extend the philosophy outlined in reference [62] to develop a transformation-free HOC scheme for 2D convection-diffusion equations on nonuniform cylindrical polar grids [1]. This is accomplished by considering the coefficients of all the partial derivatives appearing in equation (2.3) as variables, thus making way for a straightforward extension of the proposed formulation to orthogonal curvilinear coordinate system as well. It may be mentioned that majority of the earlier endeavors to develop HOC schemes on cylindrical polar coordinates were confined to the Poisson equation on uniform grids [25, 52, 59, 60, 69, 83, 123]. Even the very few attempts that have been made to develop HOC scheme on nonuniform grids for the convection-diffusion equations [90, 91, 97, 107, 121] use the conventional transformation technique from the physical plane to the computational plane. The solution is then computed on a rectangular uniform grid on the computational plane and eventually transformed back to the physical plane. This inevitably brings in the complications of having to deal with some new cross-derivative terms in the transformed partial differential equations (PDE) in addition to the increase in terms of arithmetic operations.

To validate the proposed scheme, we first apply it to a problem of pure diffusion in polar coordinates with known analytical solution and also carry out error analysis. In the process, we also establish the theoretical rate of convergence of the scheme. The robustness of the scheme however is better realized when it is applied to the problems of flow past an impulsively started circular cylinder and the driven polar cavity. Both these flows are governed by the steady-state incompressible N-S equations. We have used the streamfunction-vorticity formulation of the N-S equations for computing the flows. For the pure diffusion problem, our numerical results are extremely close to the analytical results, whereas for the cylinder and cavity problems, our solution agree very well, both qualitatively and quantitatively with established numerical and experimental results. The scheme is also seen to handle both Dirichlet (in the first problem) and Neumann boundary conditions with ease (in the other two).

The chapter has been arranged in four sections. Section 2.2 deals with the mathematical formulation and discretization, Section 2.3 with the solution of the algebraic system of equations, section 2.4 with the numerical test cases and finally, Section 2.5 summarizes the whole work.

[1] Part of this work has been published in *International Journal for Numerical Methods in Fluids* [95].

2.2 Mathematical Formulations and Discretization Procedures

A more generalized form of equation (2.3) in an annular region $[r_1, r_2] \times [\theta_1, \theta_2]$ may be written as

$$a(r,\theta)\frac{\partial^2\phi}{\partial r^2} + b(r,\theta)\frac{\partial^2\phi}{\partial\theta^2} + c(r,\theta)\frac{\partial\phi}{\partial r} + d(r,\theta)\frac{\partial\phi}{\partial\theta} = f(r,\theta). \tag{2.4}$$

Constructing on it, a nonuniform polar mesh (see a typical stencil in figure 2.1), the higher order compact approximations for the first and second derivatives appearing in (2.4) at the $(i,j)^{\text{th}}$ node [62] can be obtained as follows:

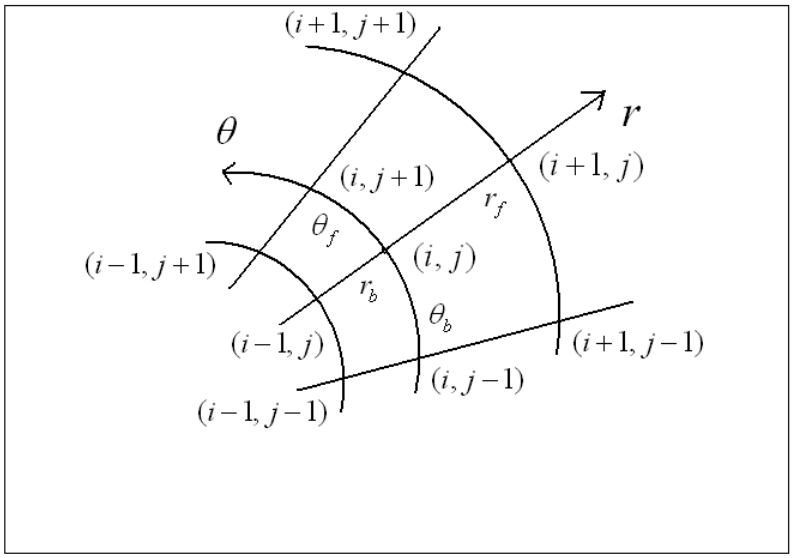

Figure 2.1: *The non-uniform HOC stencil on polar coordinates.*

$$\left.\frac{\partial\phi}{\partial r}\right|_{i,j} = \delta_r\phi_{i,j} - \frac{1}{2}(r_f - r_b)\delta_r^2\phi_{i,j} - \frac{r_f r_b}{6}\left.\frac{\partial^3\phi}{\partial r^3}\right|_{i,j} - \frac{1}{24}r_f r_b(r_f - r_b)\left.\frac{\partial^4\phi}{\partial r^4}\right|_{i,j} + O\left(\frac{r_f^5 + r_b^5}{r_f + r_b}\right), \tag{2.5}$$

$$\begin{aligned}\left.\frac{\partial^2\phi}{\partial r^2}\right|_{i,j} &= \delta_r^2\phi_{i,j} - \frac{1}{3}(r_f - r_b)\left.\frac{\partial^3\phi}{\partial r^3}\right|_{i,j} - \frac{1}{12}(r_f^2 + r_b^2 - r_f r_b)\left.\frac{\partial^4\phi}{\partial r^4}\right|_{i,j} \\ &- \frac{1}{60}(r_f - r_b)(r_f^2 + r_b^2)\left.\frac{\partial^5\phi}{\partial r^5}\right|_{i,j} + O\left(\frac{r_f^5 + r_b^5}{r_f + r_b}\right).\end{aligned} \tag{2.6}$$

The derivatives with respect to θ can be obtained in a similar way; here, $r_f = (r_{i+1} - r_i)$, $r_b = (r_i - r_{i-1})$ and $\theta_f = (\theta_{j+1} - \theta_j)$, $\theta_b = (\theta_j - \theta_{j-1})$. The details of the non-uniform central difference operators δ_r, δ_r^2, δ_θ, and δ_θ^2 can be found in Appendix-A. In view of

the above equations, equation (2.4) may be approximated at the point (i, j) as

$$\left[a\delta_r^2 + b\delta_\theta^2 + c\{\delta_r - 0.5(r_f - r_b)\delta_r^2\} + d\{\delta_\theta - 0.5(\theta_f - \theta_b)\delta_\theta^2\}\right]\phi_{i,j} + \tau_{i,j} = f_{i,j}, \quad (2.7)$$

where $\tau_{i,j}$ is the truncation error given by

$$\begin{aligned}\tau_{i,j} = -H_1\frac{\partial^3\phi}{\partial r^3} - K_1\frac{\partial^3\phi}{\partial\theta^3} - H_2\frac{\partial^4\phi}{\partial r^4} - K_2\frac{\partial^4\phi}{\partial\theta^4} + (r_f - r_b)(r_f^2 + r_b^2)\phi_1 \\ +(\theta_f - \theta_b)(\theta_f^2 + \theta_b^2)\phi_2 + O\left(\frac{r_f^5 + r_b^5}{r_f + r_b}, \frac{\theta_f^5 + \theta_b^5}{\theta_f + \theta_b}\right), \quad (2.8)\end{aligned}$$

with ϕ_1, ϕ_2 being the leading truncation error terms and

$$H_1 = \frac{1}{6}\{2a(r_f - r_b) + cr_fr_b\}, \quad H_2 = \frac{1}{24}\{2a(r_f^2 + r_b^2 - r_fr_b) + cr_fr_b(r_f - r_b)\},$$

$$K_1 = \frac{1}{6}\{2b(\theta_f - \theta_b) + d\theta_f\theta_b\}, \quad K_2 = \frac{1}{24}\{2b(\theta_f^2 + \theta_b^2 - \theta_f\theta_b) + d\theta_f\theta_b(\theta_f - \theta_b)\}.$$

Successive differentiation of (2.4) with respect to r and rearranging terms yield

$$\frac{\partial^3\phi}{\partial r^3} = -\frac{1}{a}\left\{(a_r + c)\,\delta_r^2\phi + c_r\delta_r\phi + d\delta_r\delta_\theta\phi + b\delta_r\delta_\theta^2\phi + d_r\delta_\theta\phi + b_r\delta_\theta^2\phi - f_r\right\}, \quad (2.9)$$

$$\begin{aligned}\frac{\partial^4\phi}{\partial r^4} &= L_1\delta_r^2\phi + L_2\delta_r\phi + L_3\delta_r\delta_\theta\phi + L_4\delta_r\delta_\theta^2\phi - \frac{d}{a}\delta_r^2\delta_\theta\phi - \frac{b}{a}\delta_r^2\delta_\theta^2\phi + L_5\delta_\theta\phi + L_6\delta_\theta^2\phi \\ &- \frac{1}{a^2}(2a_r + c)f_r + \frac{1}{a}f_{rr}, \quad (2.10)\end{aligned}$$

with

$$\begin{aligned}L_1 &= \frac{1}{a^2}(2a_r^2 + 3ca_r + c^2) - \frac{1}{a}(a_{rr} + 2c_r), \\ L_2 &= \frac{c_r}{a^2}(2a_r + c) - \frac{c_{rr}}{a}, \\ L_3 &= \frac{d}{a^2}(2a_r + c) - \frac{2d_r}{a}, \\ L_4 &= \frac{b}{a^2}(2a_r + c) - \frac{2b_r}{a}, \\ L_5 &= \frac{d_r}{a^2}(2a_r + c) - \frac{d_{rr}}{a}, \\ L_6 &= \frac{b_r}{a^2}(2a_r + c) - \frac{b_{rr}}{a}.\end{aligned}$$

Likewise,

$$\frac{\partial^3\phi}{\partial\theta^3} = -\frac{1}{b}\left\{(b_\theta + d)\,\delta_\theta^2\phi + d_\theta\delta_\theta\phi + c\delta_r\delta_\theta\phi + a\delta_r^2\delta_\theta\phi + c_\theta\delta_r\phi + a_\theta\delta_r^2\phi - f_\theta\right\}, \quad (2.11)$$

$$\begin{aligned}\frac{\partial^4\phi}{\partial\theta^4} &= \left\{\frac{1}{b^2}\left(2b_\theta^2+3db_\theta+d^2\right)-\frac{1}{b}\left(b_{\theta\theta}+2d_\theta\right)\right\}\delta_\theta^2\phi+\left\{\frac{d_\theta}{b^2}(2b_\theta+d)-\frac{c_{\theta\theta}}{b}\right\}\delta_\theta\phi \\ &+ \left\{\frac{c}{b^2}(2b_\theta+d)-\frac{2c_\theta}{b}\right\}\delta_r\delta_\theta\phi+\left\{\frac{a}{b^2}(2b_\theta+d)-\frac{2a_\theta}{b}\right\}\delta_r^2\delta_\theta\phi-\frac{a}{b}\delta_r^2\delta_\theta^2\phi-\frac{c}{b}\delta_r\delta_\theta^2\phi \\ &+ \left\{\frac{c_\theta}{b^2}(2b_\theta+d)-\frac{c_{\theta\theta}}{b}\right\}\delta_r\phi+\left\{\frac{a_\theta}{b^2}(2b_\theta+d)-\frac{a_{\theta\theta}}{b}\right\}\delta_r^2\phi \\ &- \frac{1}{b^2}(2b_\theta+d)f_\theta+\frac{1}{b}f_{\theta\theta}. \end{aligned} \tag{2.12}$$

Using (2.9) to (2.12), equation (2.8) can be written as

$$\begin{aligned}\tau_{i,j} = \big[&E1_{i,j}\delta_r^2+E2_{i,j}\delta_\theta^2+E3_{i,j}\delta_r+E4_{i,j}\delta_\theta+E5_{i,j}\delta_r\delta_\theta+E6_{i,j}\delta_r\delta_\theta^2 \\ &+E7_{i,j}\delta_r^2\delta_\theta+E8_{i,j}\delta_r^2\delta_\theta^2\big]\phi_{i,j}-F1_{i,j}\end{aligned} \tag{2.13}$$

where,

$$E1_{i,j}=\frac{(a_r+c)}{a}\{H_1-\frac{H_2}{a}(2a_r+c)\}+\frac{H_2}{a}(a_{rr}+2c_r)+\frac{a_\theta}{b}\{K_1-\frac{K_2}{b}(2b_\theta+d)\}+\frac{K_2a_{\theta\theta}}{b},$$

$$E2_{i,j}=\frac{b_r}{a}\{H_1-\frac{H_2}{a}(2a_r+c)\}+\frac{H_2b_{rr}}{a}+\frac{(b_\theta+d)}{b}\{K_1-\frac{K_2}{b}(2b_\theta+d)\}+\frac{K_2}{b}(b_{\theta\theta}+2d_\theta),$$

$$E3_{i,j}=\frac{c_r}{a}\{H_1-\frac{H_2}{a}(2a_r+c)\}+\frac{H_2c_{rr}}{a}+\frac{c_\theta}{b}\{K_1-\frac{K_2}{b}(2b_\theta+d)\}+\frac{K_2c_{\theta\theta}}{b},$$

$$E4_{i,j}=\frac{d_r}{a}\{H_1-\frac{H_2}{a}(2a_r+c)\}+\frac{H_2d_{rr}}{a}+\frac{d_\theta}{b}\{K_1-\frac{K_2}{b}(2b_\theta+d)\}+\frac{K_2c_{\theta\theta}}{b},$$

$$E5_{i,j}=\frac{d}{a}\{H_1-\frac{H_2}{a}(2a_r+c)\}+\frac{2H_2d_r}{a}+\frac{c}{b}\{K_1-\frac{K_2}{b}(2b_\theta+d)\}+\frac{2K_2c_\theta}{b},$$

$$E6_{i,j}=\frac{b}{a}\{H_1-\frac{H_2}{a}(2a_r+c)\}+\frac{2H_2b_r}{a}+\frac{K_2c}{b},$$

$$E7_{i,j}=\frac{H_2d}{a}+\frac{a}{b}\{K_1-\frac{K_2}{b}(2b_\theta+d)\}+\frac{2K_2a_\theta}{b},$$

$$E8_{i,j}=\frac{bH_2}{a}+\frac{aK_2}{b},$$

and

$$F1_{i,j}=\left[\frac{1}{a}\{H_1-\frac{H_2}{a}(2a_r+c)\}\delta_r+\frac{H_2}{a}\delta_r^2+\frac{1}{b}\{K_1-\frac{K_2}{b}(2b_\theta+d)\}\delta_\theta+\frac{K_2}{b}\delta_\theta^2\right]f_{i,j}.$$

Substituting (2.13) in (2.7), the HOC approximation of equation (2.4) on nonuniform polar grids can be written as

$$\big[A_{i,j}\delta_r^2+B_{i,j}\delta_\theta^2+C_{i,j}\delta_r+D_{i,j}\delta_\theta+G_{i,j}\delta_r\delta_\theta+H_{i,j}\delta_r\delta_\theta^2+K_{i,j}\delta_r^2\delta_\theta+L_{i,j}\delta_r^2\delta_\theta^2\big]\phi_{i,j}=F_{i,j} \tag{2.14}$$

which is at least third order accurate in space. Note that the order of accuracy is exactly four on uniform grid. Here the coefficients are given by

$$A_{i,j}=a_{i,j}+E1_{i,j}-0.5(r_f-r_b)c_{i,j}$$

$$B_{i,j} = b_{i,j} + E2_{i,j} - 0.5(\theta_f - \theta_b)d_{i,j}$$

$$C_{i,j} = c_{i,j} + E3_{i,j}, \quad D_{i,j} = d_{i,j} + E4_{i,j}, \quad G_{i,j} = E5_{i,j}$$

$$H_{i,j} = E6_{i,j}, \quad K_{i,j} = E7_{i,j}, \quad L_{i,j} = E8_{i,j}, \quad F_{i,j} = f_{i,j} + F1_{i,j}.$$

Letting (r, θ) replaced by (u_1, u_2), where u_1 and u_2 are the coordinate curves of an orthogonal curvilinear coordinate system, (2.14) also represents the HOC scheme on nonuniform grids for equation (2.4) in curvilinear coordinate system (u_1, u_2). Thus the extension of the current scheme from polar coordinates to general orthogonal curvilinear coordinate system in 2D is a mere formality.

It is important to note that while simulating flows on curvilinear geometries by solving equations of the form (2.4), one may come across terms of the form 0/0. In such cases, one may resolve the 0/0 form by using the L'Hospital rule whenever possible or employ a local Cartesian mesh at the point of singularity [9]. Other strategies for handling such singularities can be found in references [33, 83, 123].

2.3 Solution of algebraic systems

We now discuss the solution of algebraic systems associated with the newly proposed finite difference approximations. The system of equations (2.14) can be written as

$$\sum_{k_1=-1}^{1}\sum_{k_2=-1}^{1} \eta_{i+k_1,j+k_2}\ \phi_{i+k_1,j+k_2} = \sum_{k_1=-1}^{1}\sum_{k_2=-1}^{1} \xi_{i+k_1,j+k_2}\ f_{i+k_1,j+k_2}, \tag{2.15}$$

where η, ξ's are functions of the coefficients a, b, c and d appearing in equation (2.4), their derivatives and the step lengths r_f, r_b, θ_f and θ_b. In matrix form, the system of algebraic equations given by (2.15) can now be written as

$$A\Phi = F \tag{2.16}$$

where the coefficient matrix A is an asymmetric sparse matrix with each row containing at most nine non-zero entries. For a grid of size $m \times n$, A is of size $mn \times mn$, and Φ and F are mn-component vectors.

The next step now is to solve equation (2.16); as the coefficient matrix A is not generally diagonally dominant, conventional solvers such as Gauss-Seidel cannot be used. On uniform grids in cartesian coordinates, some of the associated matrices are symmetric and positive definite, which allows algorithms like conjugate-gradient (CG) [5, 105] to be used. As nonuniform grid and variable coefficients a, b, c and d of equation (2.4) invariably leads to non-symmetric matrices, in order to solve these systems, we use the hybrid biconjugate gradient stabilized method BiCGStab(2) [5, 105] without preconditioning.

It may be noted that for the coupled nonlinear PDEs (such as the ψ-ω form of the N-S equations), an iterative solution procedure must be adopted. These iterations may be termed as outer iterations. We use a decoupled algorithm where vorticity and stream functions are solved iteratively and sequentially through hybrid BiCGStab(2) and lagging the appropriate terms. The latter iterations may be termed inner iterations which must be carried out at every outer iteration with updated data. We utilize a relaxation parameter γ for the inner iteration cycles for both ω and ψ. In general, for larger values of Reynolds number, we needed smaller values of γ.

All of our computations were carried out on a Pentium 4 based PC with 512 MB RAM. For the inner iterations, the computations were stopped when the norm of the residual vector $\bar{\mathbf{r}} = F - A\Phi$ arising out of equation (2.16) fell below 0.5×10^{-6}. For the steady-state solution of the problems governed by the N-S equations, steady-state was assumed to reach when the maximum ω-error between two successive outer iteration steps was smaller than 1.0×10^{-9}.

2.4 Numerical experiments

In order to study the validity and effectiveness of the proposed scheme, it is applied to three problems. These are (i) a problem of pure diffusion, (ii) the flow past an impulsively started circular cylinder and (iii) the driven polar cavity flow problem. As the first problem has analytical solution, Dirichlet boundary conditions are used, while for the next two, both Dirichlet (for ψ) and Neumann (for ω) boundary conditions are applied.

2.4.1 Test problem 1: a problem of pure diffusion

We consider the equation

$$\frac{\partial^2 \phi}{\partial r^2} + \frac{1}{r}\frac{\partial \phi}{\partial r} + \frac{1}{r^2}\frac{\partial^2 \phi}{\partial \theta^2} = 0 \tag{2.17}$$

in the region $[\alpha, \beta] \times [0, \frac{\pi}{2}]$, with the boundary conditions

$$\phi(\alpha, \theta) = \theta\left(\frac{\pi}{2} - \theta\right) \quad \text{and} \quad \phi(\beta, \theta) = 0 \quad \text{for } 0 \le \theta \le \pi/2$$

$$\phi(r, 0) = \phi\left(r, \frac{\pi}{2}\right) = 0 \quad \text{for } \alpha \le r \le \beta$$

The analytical solution of (2.17) is given by

$$\phi(r, \theta) = \sum_{n=1}^{\infty} \frac{2}{\pi} \frac{1}{(2n-1)^3} \left(\frac{\alpha}{r}\right)^{(4n-2)} \sin(4n-2)\theta \left(\frac{r^{(8n-4)} - \beta^{(8n-4)}}{\alpha^{(8n-4)} - \beta^{(8n-4)}}\right) \tag{2.18}$$

We present our results computed on grid sizes ranging from 21×21 to 161×161 for $\alpha = 1$ and $\beta = 10$ in Figures 2.2 and 2.3 and Table 2.1. Figure 2.2 displays the analytical

Table 2.1: *Problem 1: Rate of convergence at selected grid points*

Grid Size	Location	Computed solution	Analytical solution.	Abs. error	Convergence Rate
[21 × 21]		1.973200e-1		5.252619e-5	
					4.0070
[41 × 41]	(1.781165,0.863938)	1.973692e-1	1.973725e-1	3.267036e-6	
					4.0017
[81 × 81]		1.973723e-1		2.039531e-7	
					3.9993
[161 × 161]		1.973725e-1		1.275361e-8	
[21 × 21]		2.270335e-1		4.072842e-5	
					4.0085
[41 × 41]	(1.413912,0.392699)	2.270717e-1	2.270742e-1	2.530637e-6	
					4.0021
[81 × 81]		2.270741e-1		1.579332e-7	
					4.0000
[161 × 161]		2.270742e-1		9.871125e-9	
[21 × 21]		6.007732e-3		5.516783e-6	
					4.0046
[41 × 41]	(7.989783,0.785398)	6.012905e-3	6.013249e-3	3.437078e-7	
					3.9966
[81 × 81]		6.013227e-3		2.153169e-8	
					3.8526
[161 × 161]		6.013247e-3		1.490525e-9	
[21 × 21]		6.257496e-2		3.414488e-5	
					4.0069
[41 × 41]	(3.172549,0.785398)	6.260698e-2	6.260911e-2	2.123918e-6	
					4.0014
[81 × 81]		6.260898e-2		1.326146e-7	
					3.9947
[161 × 161]		6.260910e-2		8.319174e-9	

and numerical contours of the solution. It is heartening to note that on a grid of size 21×21 only, one can hardly distinguish the numerical solutions from the exact ones. This fact is also confirmed by Figure 2.3, where the surface plots of the errors are shown on two different grid sizes 21×21 and 41×41 for which the maximum absolute errors are extremely small, namely 5.29×10^{-5} and 1.03×10^{-5} only.

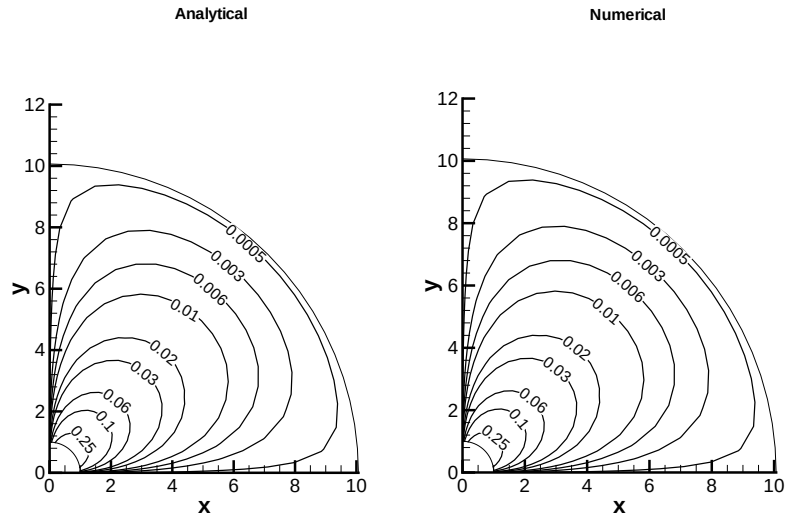

Figure 2.2: *Contours of the analytical and numerical solutions on a* 21×21 *grid for Problem 1.*

In Table 2.1, we exhibit the analytical and computed solutions at four representative

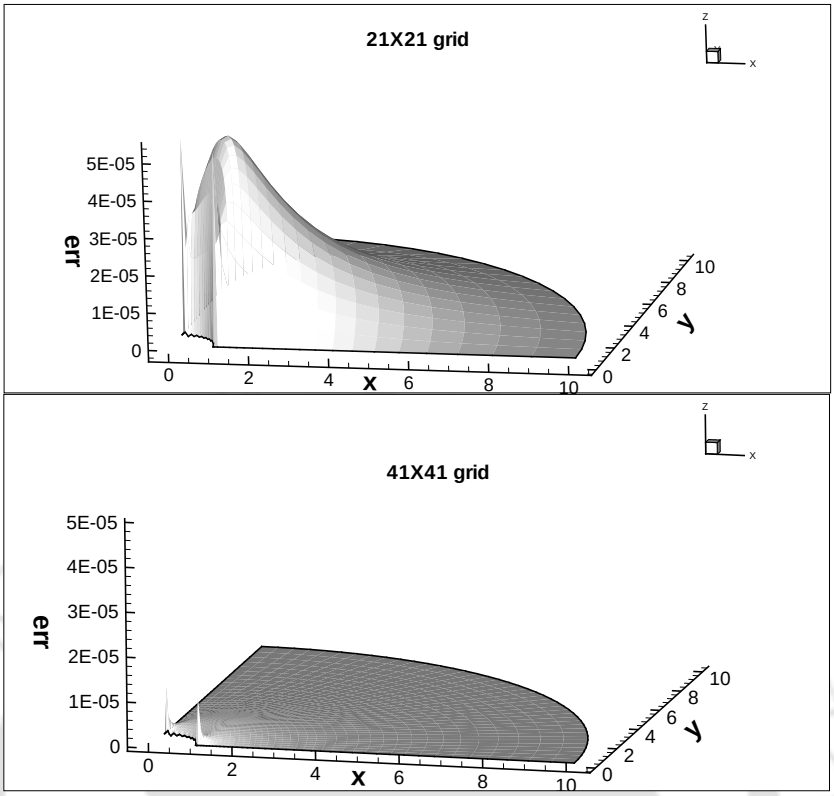

Figure 2.3: *Surface plots of errors on* 21×21 *(top) and* 41×41 *(bottom) grids for Problem 1.*

points on the solution domain along with the absolute errors on four different grid sizes. It is seen from the table that with grid refinement, the point-wise error decays with $O(h^4)$, as expected. Here the rate of convergence is calculated as

$$M = \frac{\log(\frac{e_1}{e_2})}{\log(\frac{N_2}{N_1})},$$

where e_1, e_2 are the absolute errors estimated at a particular point for two different grids with N_1+1 and N_2+1 points in the either direction. It may be noted that the maximum errors for different grids occur at different points and are not directly comparable.

2.4.2 Test problem 2: Flow past an impulsively started circular cylinder:

Next we consider the steady, incompressible, viscous flow over an infinitely long cylinder of circular cross-section. The flow is governed by the incompressible N-S equations. We use the ψ-ω formulation of the N-S equations in cylindrical polar coordinates (r, θ). In non-dimensional form, they are given by

$$\frac{\partial^2\omega}{\partial r^2} + \frac{1}{r}\frac{\partial\omega}{\partial r} + \frac{1}{r^2}\frac{\partial^2\omega}{\partial\theta^2} = Re\big(u\frac{\partial\omega}{\partial r} + \frac{v}{r}\frac{\partial\omega}{\partial\theta}\big), \tag{2.19}$$

$$\frac{\partial^2\psi}{\partial r^2} + \frac{1}{r}\frac{\partial\psi}{\partial r} + \frac{1}{r^2}\frac{\partial^2\psi}{\partial\theta^2} = -\omega. \tag{2.20}$$

Here ψ is the streamfunction, ω the vorticity, u, v repectively are the radial and tangential velocity components and $Re = \dfrac{UD}{\nu}$ is the Reynolds number with U being the characteristic velocity, D the diameter of the cylinder and ν the kinematic viscosity. The velocities u and v in terms of ψ are given by

$$u = \frac{1}{r}\frac{\partial\psi}{\partial\theta} \quad \text{and} \quad v = -\frac{\partial\psi}{\partial r}, \tag{2.21}$$

and the vorticity ω is given by

$$\omega = \frac{1}{r}\left[\frac{\partial}{\partial r}(vr) - \frac{\partial u}{\partial\theta}\right]. \tag{2.22}$$

We assume the cylinder to be of unit radius placed in an infinite domain. At the

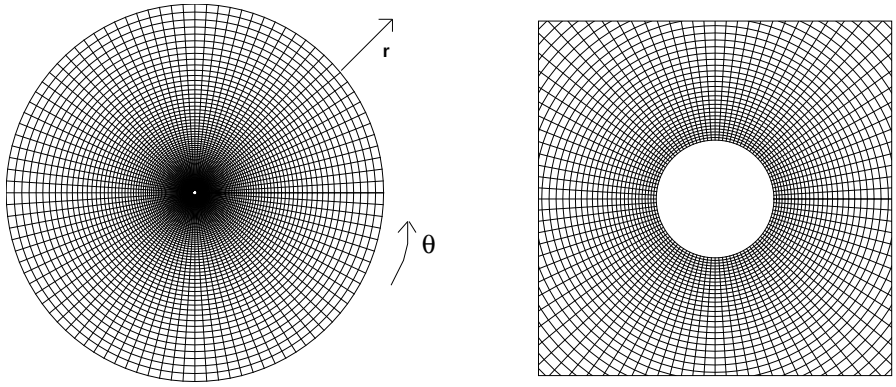

Figure 2.4: *A typical* 101×101 *mesh for the flow past a circular cylinder problem.*

far-field, a potential flow is assumed with uniform free-stream velocity $\mathbf{U}_\infty = (1, 0)$. A typical computational grid of size 101×101 is shown in Figure 2.4. We employ a uniform grid spacing along the θ- direction and nonuniform grid spacing in the r-direction with clustering around the surface of the cylinder using the following functions:

$$\theta_j = \frac{2\pi}{j_{\max}} \quad \text{and} \quad r_i = \exp\left(\frac{\lambda\pi i}{i_{\max}}\right).$$

Here the parameter λ determines the outer radius of the computational domain. The continuity conditions at $\theta = 0$ and $\theta = 2\pi$ are taken as the boundary conditions along those two lines.

We now derive the boundary conditions for stream function and vorticity. On the solid surface $r = R_0$, $u = v = \psi = 0$. In the far stream $r = R_\infty$, velocity becomes uniform and equal to U_∞ as $r \to \infty$. In terms of stream function, this condition is expressed as $\psi \to U_0 r sin\theta$ as $r \to \infty$.

For vorticity, the far-stream condition is given by $\omega = 0$ at $r = R_\infty$. On the solid surface $r = R_0$, however, vorticity is not zero. Making use of the fact that $\psi = 0$, $\dfrac{\partial \psi}{\partial r} = 0$ on $r = R_0$, we arrive at $\omega = -\dfrac{\partial^2 \psi}{\partial r^2}$ thereat. We proceed to obtain a compact approximation of the vorticity on the solid boundary as follows:

$$\begin{aligned} -v_{0,j} &= \left(\frac{\partial \psi}{\partial r}\right)_{0,j} \\ &= \delta^+ \psi_{0,j} - \frac{r_f}{2}\left(\frac{\partial^2 \psi}{\partial r^2}\right)_{0,j} - \frac{r_f^2}{6}\left(\frac{\partial^3 \psi}{\partial r^3}\right)_{0,j} + O\left(r_f^3\right) \end{aligned}$$

so that we get the finite difference approximation as

$$\begin{aligned} 0 &= \frac{\psi_{1,j}}{r_f} - \frac{r_f}{2}\left(-\omega_{0,j}\right) - \frac{r_f^2}{6}\left(-\left(\frac{\partial \omega}{\partial r}\right)_{0,j}\right), \\ 0 &= \frac{\psi_{1,j}}{r_f} + \frac{r_f}{2}\omega_{0,j} + \frac{r_f^2}{6}\left(\frac{\omega_{1,j} - \omega_{0,j}}{r_f}\right), \end{aligned}$$

$$\text{yielding} \quad 2\omega_{0,j} + \omega_{1,j} = -\frac{6}{r_f^2}\psi_{1,j} \tag{2.23}$$

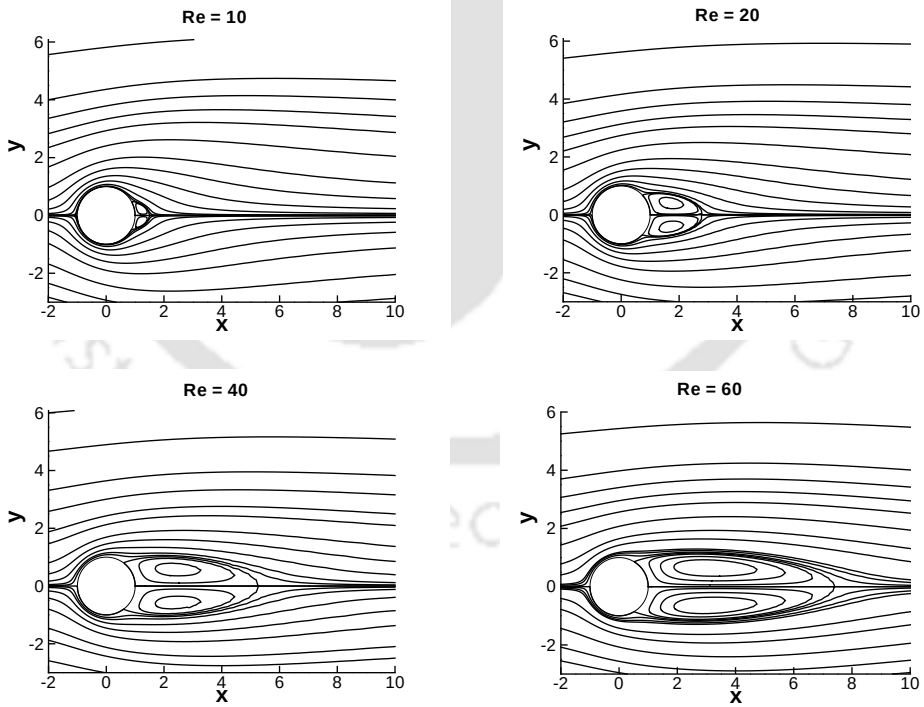

Figure 2.5: *Steady-state stream-lines for* $Re = 10$, 20, 40 *and* 60 *for the motion past a circular cylinder problem.*

We present steady-state results for this flow for Reynolds numbers $Re = 10, 20, 40$ and 60 in Figures 2.5 to 2.8 and Tables 2.2 to 2.4. Simulation for higher Reynolds

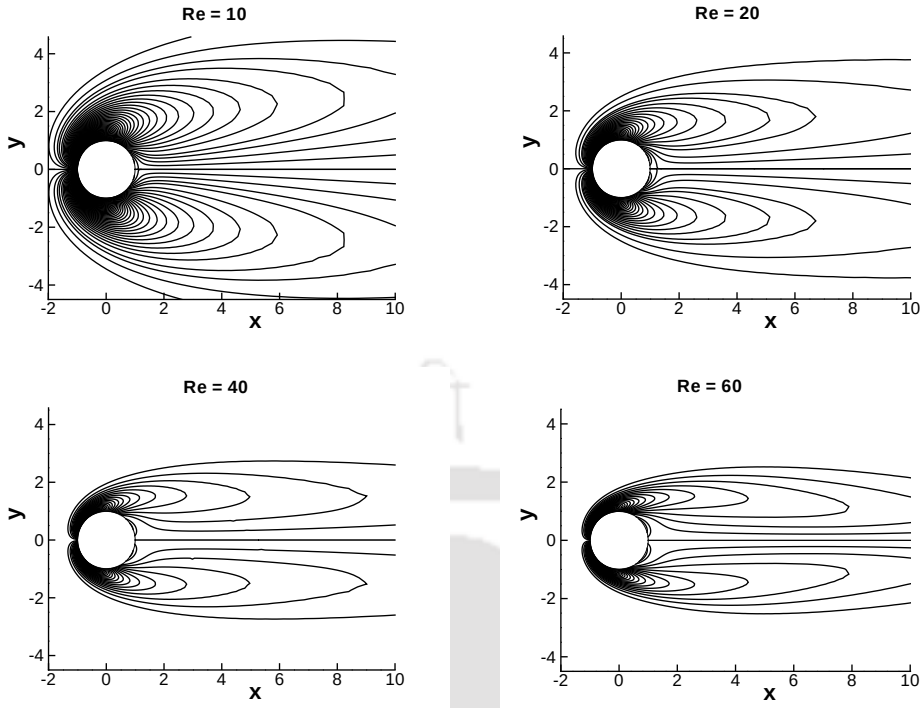

Figure 2.6: *Steady-state vorticity contours for Re = 10, 20, 40 and 60 for the motion past a circular cylinder problem.*

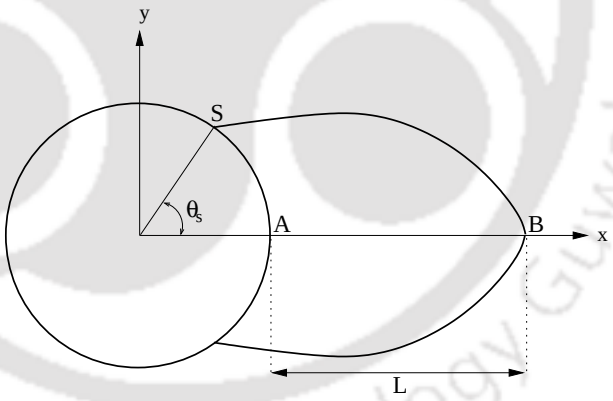

Figure 2.7: *Geometrical parameters of the closed wake for the motion past a circular cylinder problem.*

Table 2.2: *Problem 2: Effect of grid size on wake lengths and separation angles.*

	$Re = 20$			$Re = 40$		
Grid	75	101	151	75	101	151
θ_s	43.2022	43.2805	43.3118	51.4521	51.5374	51.5411
L	1.8315	1.8294	1.8212	4.4061	4.3962	4.3906

Table 2.3: *Problem 2: Effect of far field boundary on the wake lengths and separation angles.*

	$Re = 20$			$Re = 40$		
R_∞	35.03	60.14	75.17	35.03	60.14	75.17
θ_s	43.4232	43.3155	43.2022	51.8811	51.6929	51.4521
L	1.8217	1.8288	1.8315	4.3957	4.4007	4.4061

Table 2.4: *Comparison of the wake lengths and separation angles for different Reynolds numbers.*

	Re	Ref. [38]	Ref. [111]	Ref. [77]	Ref. [44]	Ref. [54]	Ref. [97]	Present
L	20	1.88	-	1.87	1.82	1.842	1.77	1.8315
	40	4.69	-	4.27	4.48	4.49	4.21	4.4061
θ_s	20	43.7	-	-	42.9	42.96	41.3277	43.2022
	40	53.8	-	-	51.5	52.84	51.0249	51.4521
C_D	20	2.045	2.05	-	2.001	2.152	2.0597	2.0108
	40	1.522	1.55	-	1.498	1.499	1.5308	1.5119

number was not considered because earlier numerical studies [38, 44] indicated that the flow no longer remains steady for Res beyond 60. Therefore, we present flow profiles for Reynolds numbers up to 60 only, more so for $Re = 20$ and $Re = 40$, for which experimental and numerical results [38, 44, 54, 67, 77, 85, 97, 109] exists in plenty.

In Figure 2.5, we exhibit the streamlines from $Re = 10$ to 60. In all the cases, two symmetrical, stationary circulating eddy develops behind the cylinder. With increase in Re values, one can see the increase in the sizes of the vortices. The corresponding vorticity contours for the same range of Reynolds numbers are shown in figure 2.6.

It is worth mentioning that though several studies [38, 44, 45] have presented the so called steady-state results for this flow at $Re = 60$, many experimental and numerical results have shown conclusively that eventually asymmetry sets in and the flow becomes unsteady for this Reynolds number [2, 8, 10, 12, 14, 81, 111, 116]. This will be discussed in details in our next chapter. Therefore, the results presented in this chapter for $Re = 60$

may be termed as the simulated converged solution of the N-S equations governing the flow.

We also compute the wake length L: the distance between the rear most point A of the cylinder to the end B of the wake (figure 2.7), and the angle of separation θ_s, which is the angle between the x-axis and the line joining the center of the cylinder and the point of separation S on the cylinder (figure 2.7). These parameters are then compared in table 2.2 in order to verify the grid-independence; the grid sizes range from 75×75 to 151×151. Table 2.3 shows the variation of the same parameters to check the dependence of the computed solution on the assumed far-field where R_∞s range from 35.03 to 75.17. Here the grid size has been fixed at 75×75. From these tables, it is clear that a grid

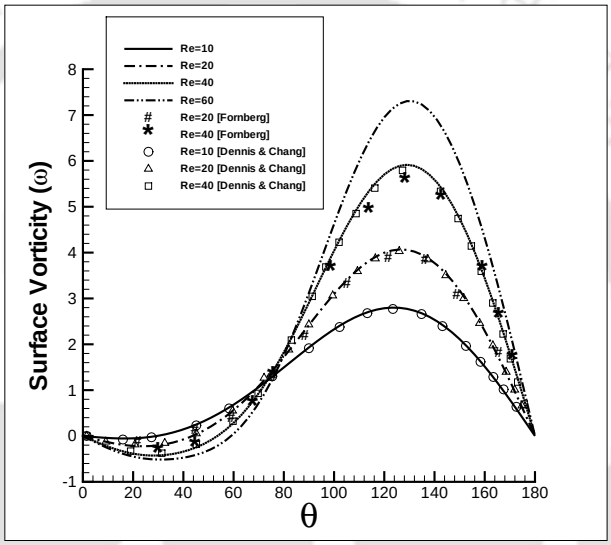

Figure 2.8: *Comparison of vorticities on the cylinder surface for different Re with the results of references [38] and [44] for the motion past a circular cylinder problem.*

of size 101×101 and a far-field given by $R_\infty = 75$ are enough for accurate resolution of the flow. In table 2.4, we present our computed L, θ_s and the drag coefficient C_D with those obtained by [38, 44, 54, 77, 97, 111]. We also compare the vorticities along the surface of the cylinder for the range of Reynolds number considered here with those of references [38, 44] in Figure 2.8. In all the cases, excellent comparison with the established numerical results are obtained, both qualitatively and quantitatively.

2.4.3 Test problem 3: Driven Polar Cavity flow

Lastly, to validate our proposed HOC scheme, we apply it to solve the driven polar cavity problem. Here also, the flow is governed by the N-S equations (2.19)-(2.21). This problem was first studied both experimentally as well as numerically by Fuchs and Tillmark [48]. A schematic diagram of the problem is shown in Figure 2.9. Here the

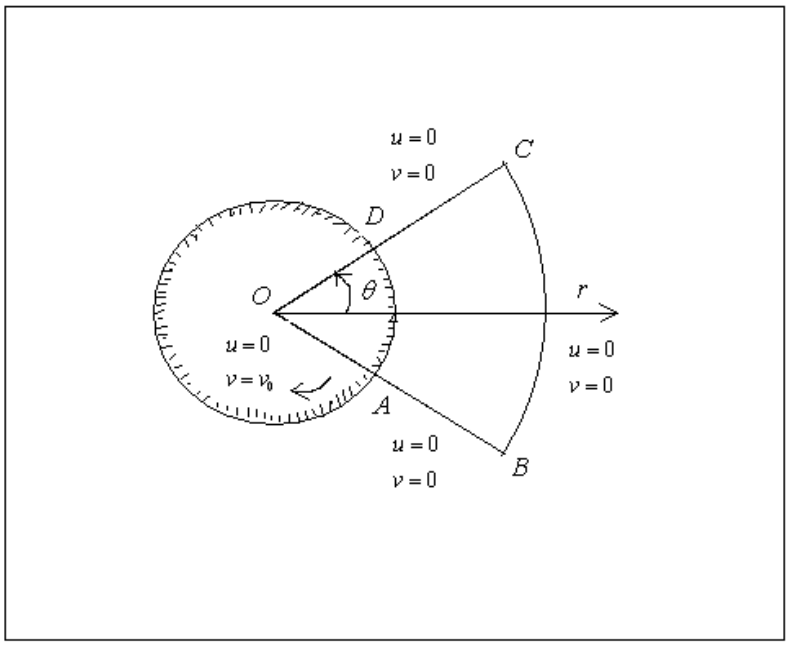

Figure 2.9: *Schematic diagram of driven polar cavity problem.*

region $ABCD$ is the domain of the problem. The inner circle DA is moving with an angular clock-wise velocity $v = v_0 = 1$ which drives the flow. All the other boundary walls are fixed. Here, u and v are the radial and tangential velocities respectively; the Reynolds number, Re, is given by $\frac{v_0 R_0}{\nu}$, where $OD = OA = R_0$ is the radius of the inner circle, v_0 is the surface velocity of the rotating cylinder and ν is the kinematic viscosity of the fluid. No slip boundary conditions are applied on the solid walls. Thus boundary conditions for u and v are given by: $u = 0$, $v = 1$ on $\widehat{DA}$ and $u = v = 0$ on the other three walls. Using the normal velocity boundary conditions ([48]) we can get $\psi = 0$ on all the boundary walls. Making use of the fact that

$$\frac{\partial^2 \psi}{\partial r^2} + \frac{1}{r}\frac{\partial \psi}{\partial r} = -\omega, \quad \psi = 0 \text{ and } \quad v = -\frac{\partial \psi}{\partial r} = 1$$

along the boundary $\widehat{DA}$, we obtain a third order accurate approximation of ω as:

$$\Rightarrow \omega_{0,j} + \frac{\omega_{1,j}}{2} = -\frac{3}{h_0}\left(1 + \frac{\psi_{1,j}}{h_0} - \frac{h_0}{2r_0} + \frac{h_0^2}{6r_0^2}\right) \tag{2.24}$$

as in problem 2, where $h_0 = (r_1 - r_0)$. In a similar way, one can approximate the vorticities along the other three boundaries as:
along $\widehat{AB}$

$$\omega_{i,0} + \frac{\omega_{i,1}}{2} = \frac{3}{r_i^2 \Delta\theta_0^2}\psi_{i,1} \tag{2.25}$$

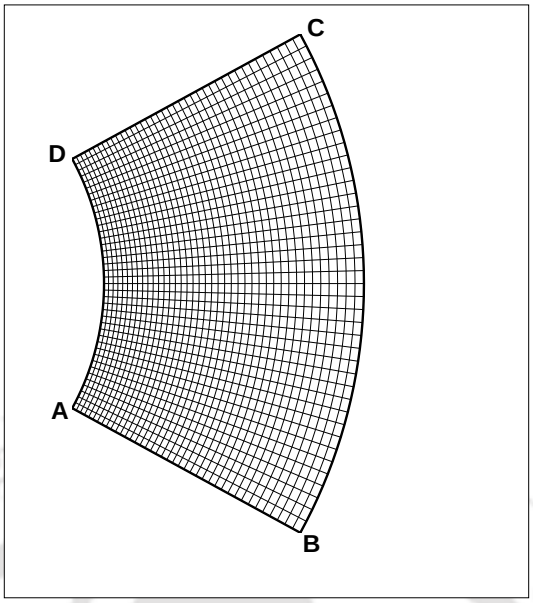

Figure 2.10: *A typical* 41×41 *non-uniform grid for the driven polar cavity problem.*

along $\widehat{BC}$:

$$\omega_{n-1,j} + \frac{\omega_{n-2,j}}{2} = \frac{3}{h_{n-2}^2}\psi_{n-2,j} \tag{2.26}$$

along $\widehat{CD}$:

$$\omega_{i,m-1} + \frac{\omega_{i,m-2}}{2} = -\frac{3}{r_i^2 \Delta\theta_{m-2}^2}\psi_{i,m-2} \tag{2.27}$$

where $h_{n-2} = r_{n-1} - r_{n-2}$, $\Delta\theta_0 = \theta_1 - \theta_0$, $\Delta\theta_{n-2} = \theta_{m-1} - \theta_{m-2}$ with $n-1$ and $m-1$ denoting the maximum index along r and θ-directions respectively. In their work, Lee and Tsuei ([71]) observed that large solution errors propagate near the rotating boundary. Therefore we cluster the region in the vicinity of the rotating boundary using the same stretching functions used in problem 2; Figure 2.10 shows a typical 41×41 non-uniform mesh used for this problem.

We present our computed solutions in Figures 2.11 to 2.21 and Table 2.5. In Figure 2.11, we present streamlines obtained from our numerical simulation on a 81×81 grid side by side with the one obtained from the experimental results of [48] for $Re = 55$. The corresponding comparison for $Re = 350$ on a same grid size is shown in Figure 2.12.

In Figure 2.13 and 2.14 we respectively present the u and v velocity profiles along $\theta = 0$ on four different grid sizes 41×41, 61×61, 81×81 and 101×101 for Res 55 and 350 respectively. From these figures, it is clear that a 61×61 grid is enough to achieve grid-independence for $Re = 55$ while we needed an 81×81 grid for $Re = 350$.

Figure 2.15 shows the vorticity contours for $Re = 55$ and $Re = 350$. In figure 2.16, we show the streamlines and vorticity contours for $Re = 1000$; our streamline patterns

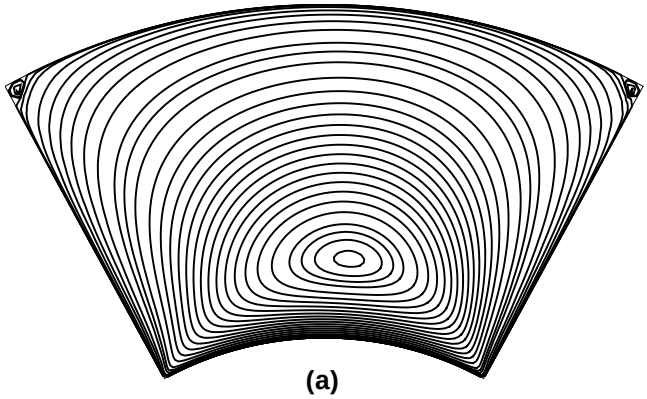

(a)

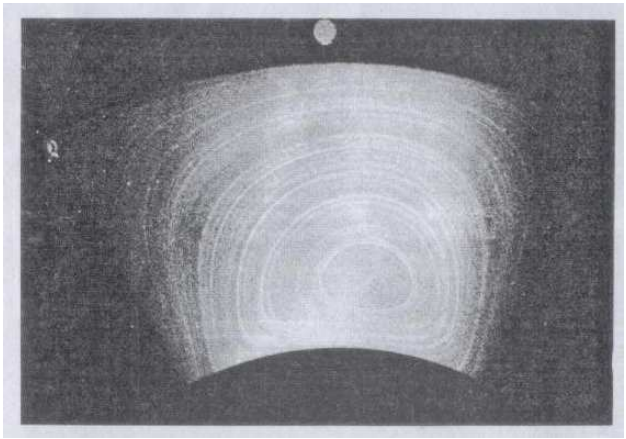

(b)

Figure 2.11: *Steady-state streamlines for the driven polar cavity problem for* $Re = 55$*: (a) numerical and (b) experimental ([48]).*

are very similar to those in reference [48]. In Figures 2.17(a) and 2.17(b), we exhibit the variation of the vorticity along the rotating wall $\widehat{DA}$ and the radial line $\theta = 0$ respectively.

In figure 2.18(a), we present the u and v-velocities along the radial line $\theta = 0$ obtained through our computation on a 81×81 grid for $Re = 55$ along with the experimental results of [48]. Similar comparison for $Re = 350$ is presented in Figure 2.18(b). In both the cases we achieve an excellent agreement between the numerical and experimental results. It may be mentioned that in [48], although the numerical results were close to the experimental ones for lower Res, their high Re results, even on the finest grids were not adequate enough to match the experimental results. The reason for this could be the use of lower order (first or at most second order) approximation of the derivative terms. The corresponding computed u and v-velocities along the radial line $\theta = 0$ for $Re = 1000$ are shown in figure 2.19. In table 2.5, we present the optimal successive under-relaxation

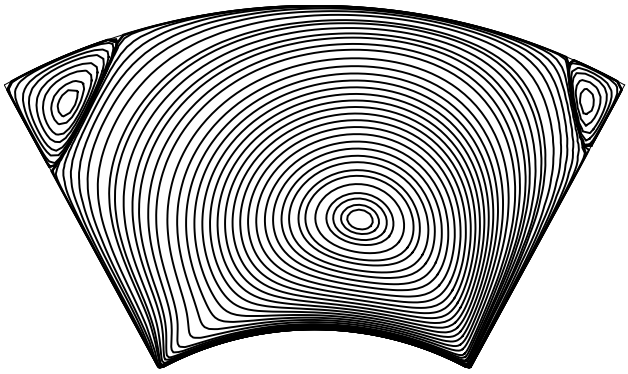

(a)

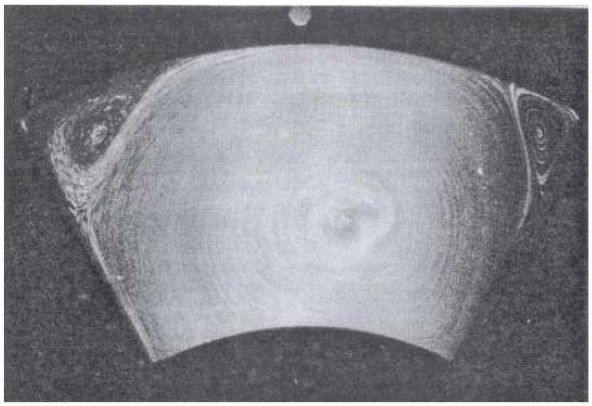

(b)

Figure 2.12: *Steady-state streamlines for the driven polar cavity problem for* $Re = 350$*: (a) numerical and (b) experimental ([48]).*

parameter γ for the inner BiCGStab(2) iterations used in our computations for $Re = 55$ and 350 on three different grids along with the CPU times. For the outer iterations, the γ value was fixed at 0.650 for both ψ and ω after a series of experiments. It is heartening to note that on a relatively finer 81×81 grid, for $Re = 350$, steady-state solution is obtained in less than 1.5 minutes.

We also exhibit the convergence history in figures 2.20 and 2.21 which provides a clear picture of the fall of the inner BiCGStab(2) iteration number and the infinity norm against the outer iteration number till steady-state. In figure 2.20, we present the convergence history of the inner BiCGStab(2) iteration against the outer iterations for ω and ψ for $Re = 55$ and 350; likewise in figure 2.21, we present the fall of the infinity norm for the same flow variables and Reynolds numbers. These figures clearly indicate that the convergence pattern is smooth in all the cases.

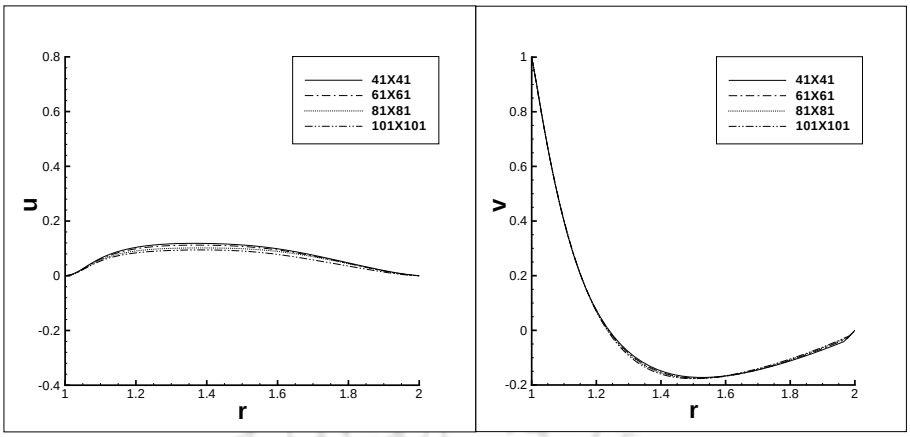

Figure 2.13: *The u- and v-velocity profiles on different grid sizes for the driven polar cavity flow problem along $\theta = 0$ for $Re = 55$.*

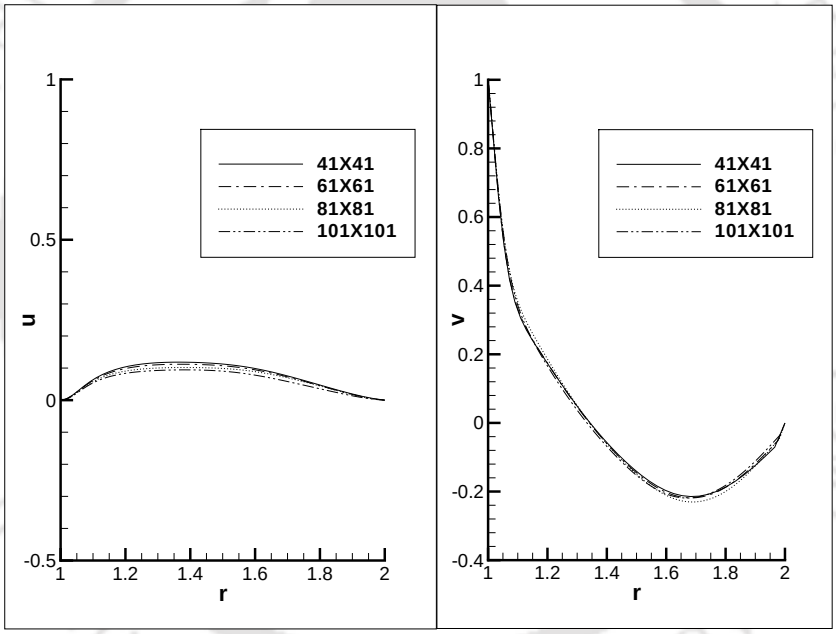

Figure 2.14: *The u- and v-velocity profiles on different grid sizes for the driven polar cavity flow problem along $\theta = 0$ for $Re = 350$.*

2.5 Conclusion

In this chapter, we extend a recently developed HOC scheme for the steady-state convection diffusion equations on nonuniform Cartesian grids to cylindrical polar grids; further extension of the scheme to general curvilinear coordinate system is straightforward. To bring out different aspects of the scheme, we first apply this new approach to a diffusion equation having analytical solution, then to the motion past a circular cylinder and finally to the driven polar cavity problem. In the process, we also demonstrate the

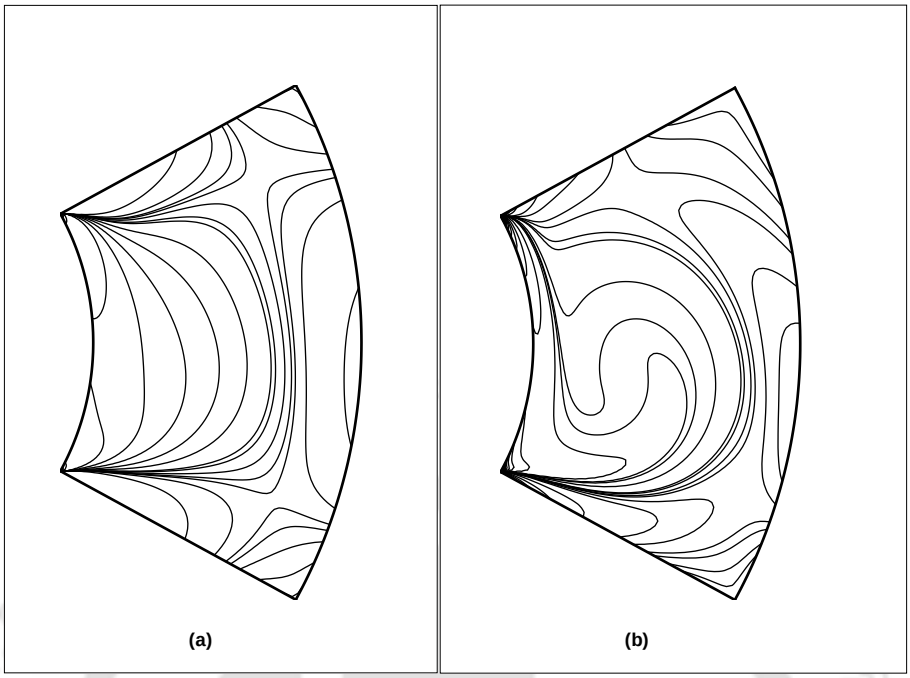

Figure 2.15: *Vorticity contours for (a) $Re = 55$ and (b) 350 for the driven polar cavity problem.*

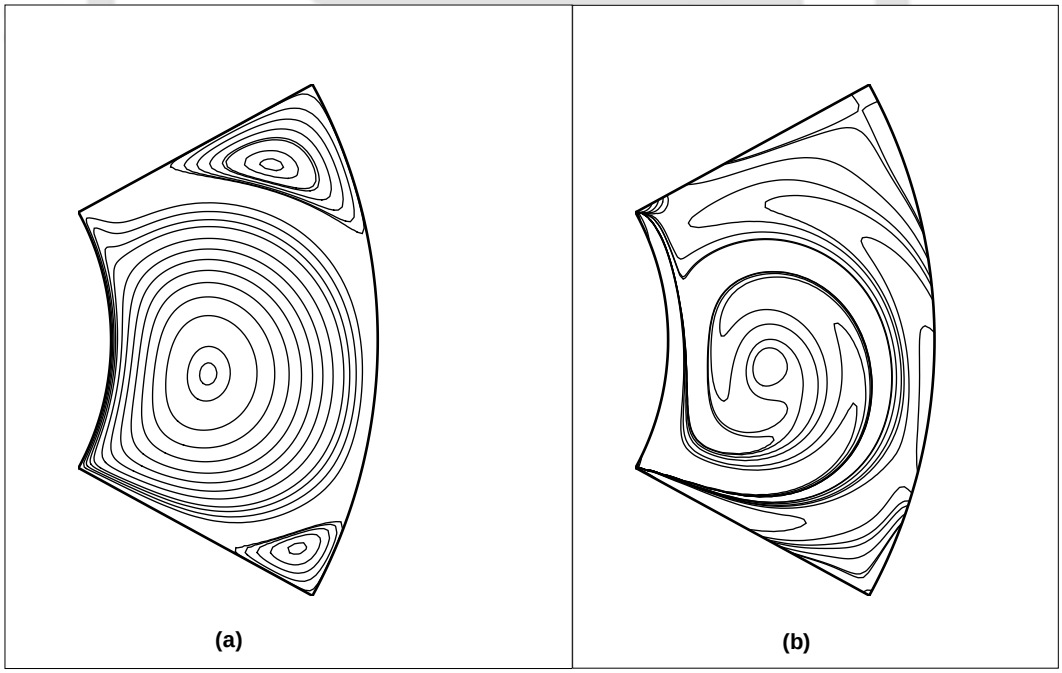

Figure 2.16: *The (a) streamlines and (b) vorticity contours for $Re = 1000$ for the driven polar cavity problem.*

fourth order spatial accuracy of our scheme. In the first problem, Dirichlet boundary conditions are used and for the other two, compact higher order approximations have

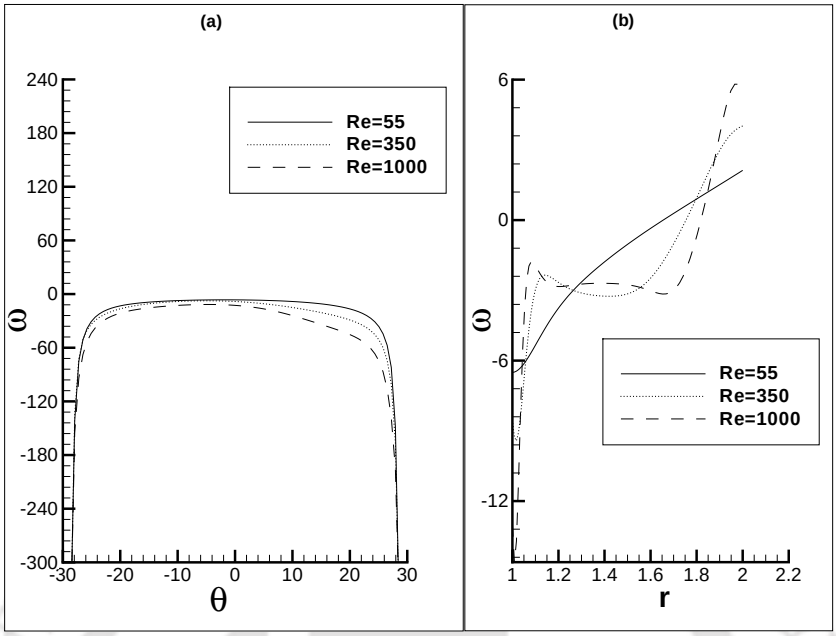

Figure 2.17: *Vorticity (a) along the rotating wall, and (b) along the radial line $\theta = 0$ for the driven polar cavity problem.*

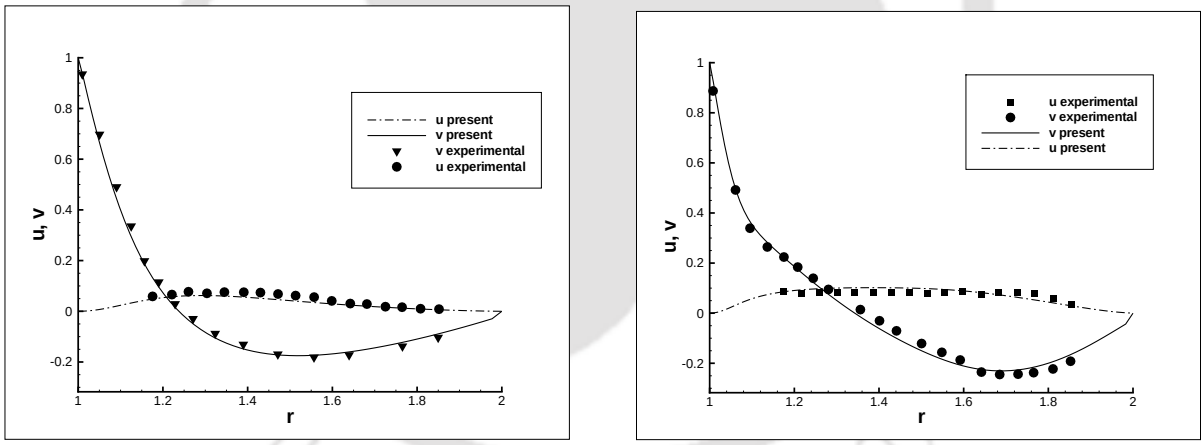

(a) (b)

Figure 2.18: *Comparison between experimental and present numerical u- and v-velocity profiles for (a) $Re = 55$ and (b) $Re = 350$ along the radial line $\theta = 0$.*

been developed and successfully implemented for the Neumann boundary conditions. The robustness of the scheme is illustrated by its applicability to the last two fluid flow problems of varying physical complexities and their accurate computations. Also, the use of the hybrid biconjugate gradient stabilized algorithm for solving the algebraic systems arising at every outer iteration step makes the solution procedure computationally efficient in capturing the steady-state solutions. The results obtained in all the test cases on relatively coarser grids are in excellent agreement with analytical, experimental

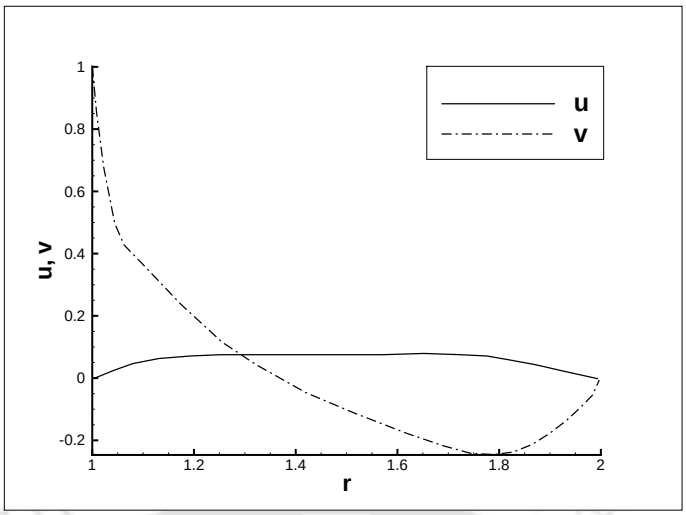

Figure 2.19: *u- and v-velocity profiles for* $Re = 1000$ *along the radial line* $\theta = 0$.

Table 2.5: *Problem 3: Comparison of CPU times and under-relaxation parameter* γ *for the BiCGStab inner ieratios on different grids for* $Re = 55$ *and* 350.

Re	Grid Size	γ for ω	γ for ψ	CPU time (in seconds)
55	$[21 \times 21]$	0.305	0.650	0.408
	$[41 \times 41]$	0.205	0.500	4.368
	$[81 \times 81]$	0.150	0.350	40.011
350	$[21 \times 21]$	0.325	0.600	0.944
	$[41 \times 41]$	0.225	0.500	7.516
	$[81 \times 81]$	0.175	0.375	81.237

and established numerical results, underlying the high accuracy of the scheme. As our scheme has the added advantage of being applicable to general orthogonal curvilinear coordinate system, it has tremendous potential for efficient computation of more complex problems of incompressible viscous flows. In the next chapter, we will develop an extension of this formulation to transient flows.

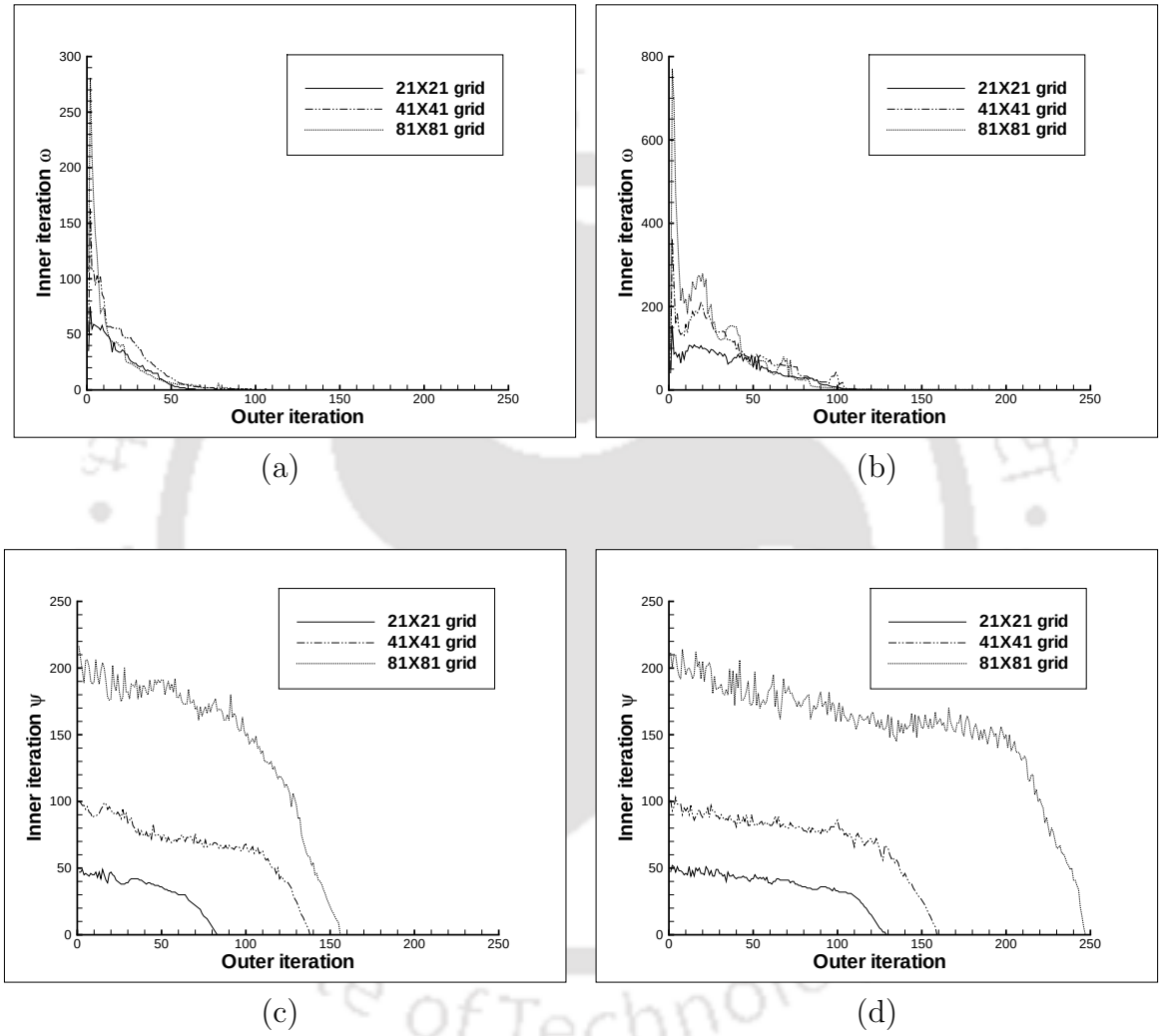

Figure 2.20: *Convergence history: Outer iteration versus inner iteration of (a) ω for $Re = 55$, (b) ω for $Re = 350$,(c) ψ for $Re = 55$ and (d) ψ for $Re = 350$.*

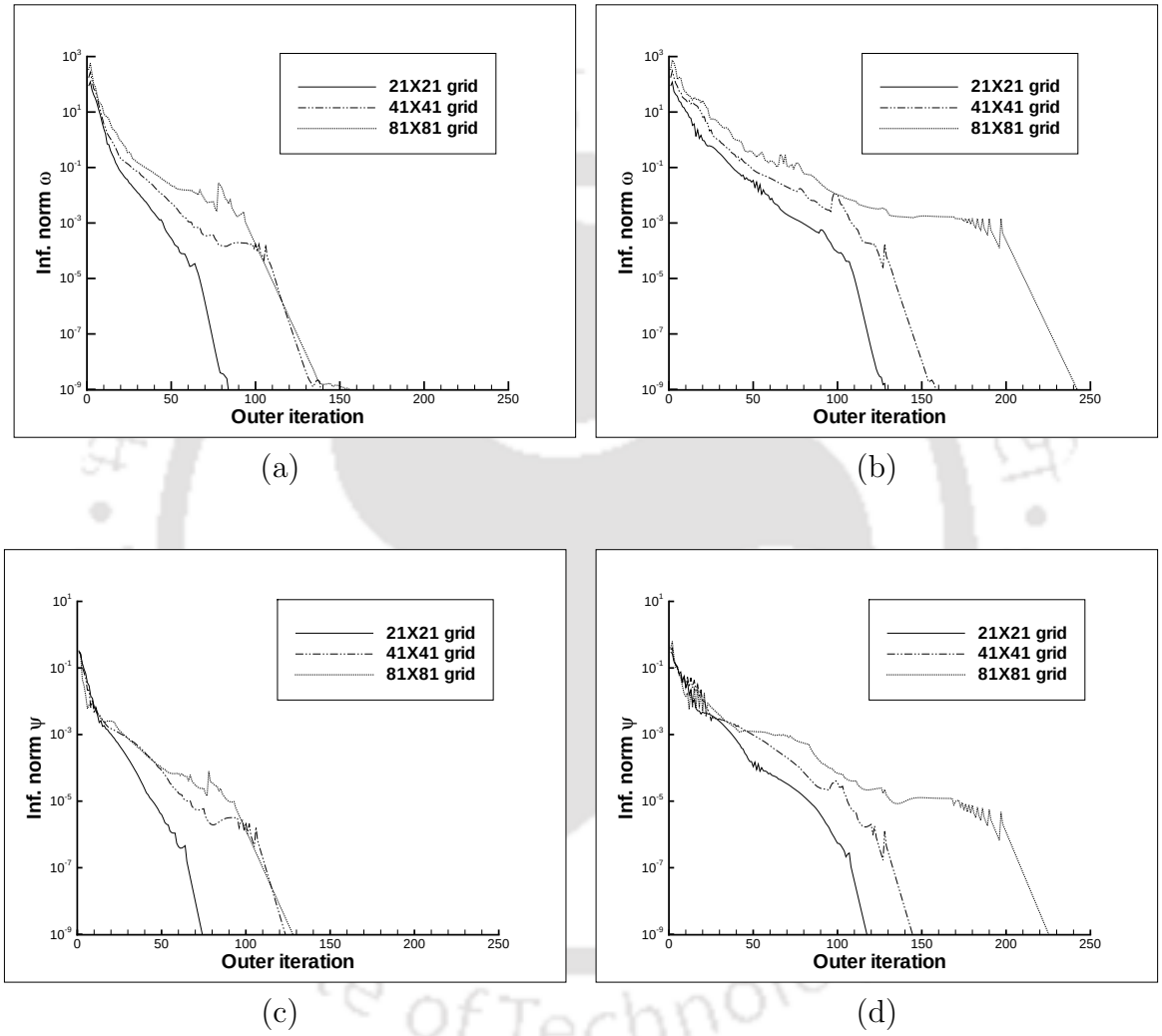

Figure 2.21: *Convergence history: Outer iteration versus infinity norm of (a) ω for $Re = 55$, (b) ω for $Re = 350$,(c) ψ for $Re = 55$ and (d) ψ for $Re = 350$.*

Chapter 3

A transformation-free HOC scheme for unsteady incompressible viscous flows on nonuniform polar grids

3.1 Introduction

In this chapter, we extend the steady-state formulation of incompressible Navier-Stokes equations discussed in Chapter 2 to unsteady flows. This chapter has been arranged in four sections. Section 3.2 deals with the governing equations, Section 3.3 with the mathematical formulation and discretization procedure, and Section 3.4 the conclusion.

3.2 The governing equations

In non-dimensional form, the streamfunction-vorticity formulation of the two-dimensional unsteady, viscous, incompressible Navier-Stokes equations in cylindrical polar coordinates (r, θ) are given by,

$$\frac{\partial^2\omega}{\partial r^2} + \frac{1}{r}\frac{\partial\omega}{\partial r} + \frac{1}{r^2}\frac{\partial^2\omega}{\partial\theta^2} = Re\big(u\frac{\partial\omega}{\partial r} + \frac{v}{r}\frac{\partial\omega}{\partial\theta} + \frac{\partial\omega}{\partial t}\big) \tag{3.1}$$

$$\frac{\partial^2\psi}{\partial r^2} + \frac{1}{r}\frac{\partial\psi}{\partial r} + \frac{1}{r^2}\frac{\partial^2\psi}{\partial\theta^2} = -\omega \tag{3.2}$$

Here ψ is the streamfunction, ω the vorticity, u, v repectively are the radial and tangential velocity components, t is the time and $Re = \dfrac{UD}{\nu}$ is the Reynolds number with U being the characteristic velocity, D a characteristic length (like the diameter of a cylinder) and ν the kinematic viscosity. The velocities u and v in terms of ψ are given by

$$u = \frac{1}{r}\frac{\partial\psi}{\partial\theta} \quad \text{and} \quad v = -\frac{\partial\psi}{\partial r}, \tag{3.3}$$

and the vorticity ω is given by

$$\omega = \frac{1}{r}\left[\frac{\partial}{\partial r}(vr) - \frac{\partial u}{\partial\theta}\right]. \tag{3.4}$$

3.3 Mathematical Formulation and Discretization Procedure

From the governing equations (3.1)-(3.4), it can be seen that, only equation (3.1) contains a term involving time. So, the HOC discretization of the equations other than equation (3.1) will be same as the steady state case discussed in Chapter 2. Here we will primarily discuss about the HOC discretization procedure of equation (3.1). We construct a nonuniform polar mesh (see a typical stencil at the n or $(n+1)^{\text{th}}$ time level in figure 3.1) on the annular region $\Omega = [R_0, R_\infty] \times [0, 2\pi]$ by the points (r_i, θ_j) which are not necessarily equally spaced. At a typical $(i, j)^{\text{th}}$ node, the forward and backward step lengths in the r-direction are given by $r_f = (r_{i+1} - r_i)$, $r_b = (r_i - r_{i-1})$ respectively. Similarly in the θ-direction, $\theta_f = (\theta_{j+1} - \theta_j)$, $\theta_b = (\theta_j - \theta_{j-1})$.

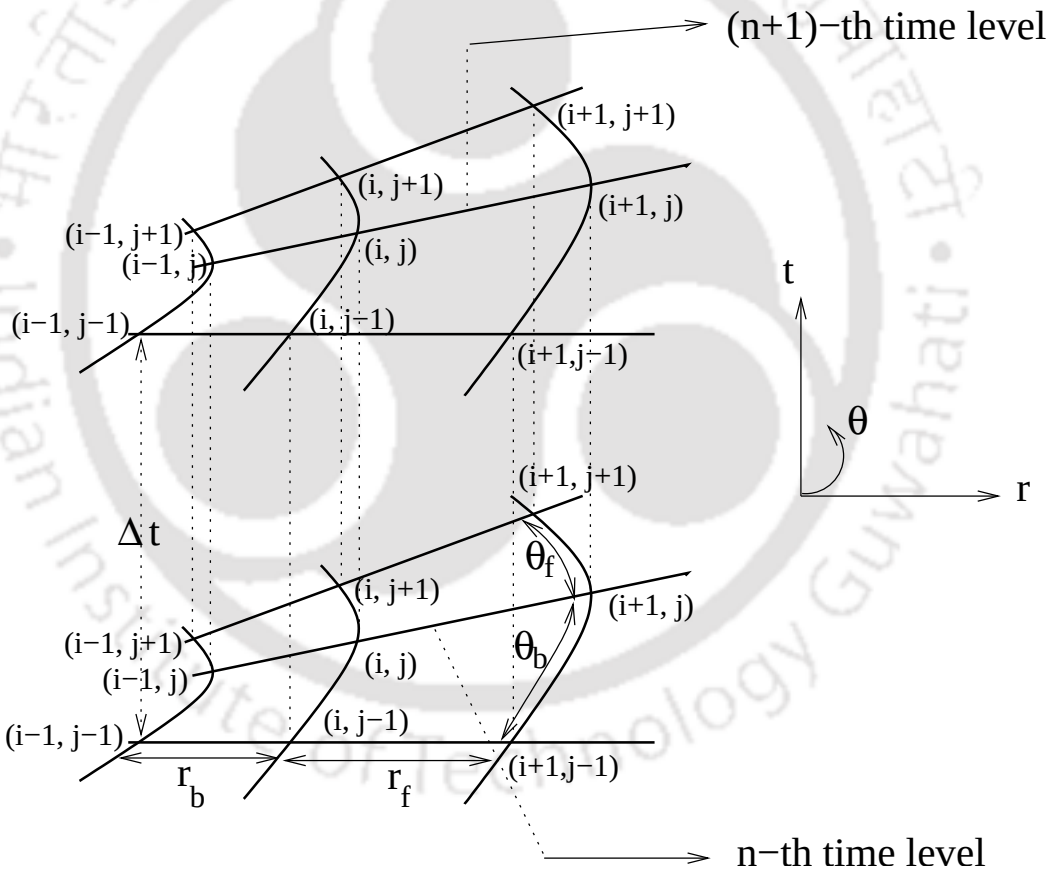

Figure 3.1: *The unsteady HOC stencil on nonuniform polar grid.*

Now, using the higher order compact finite difference approximations of the first and second order partial derivatives given in equations (2.5) and (2.6), equation (3.1) can be approximated at the $(i, j)^{\text{th}}$ point as

$$\big[\delta_r^2 + \frac{1}{r_i^2}\delta_\theta^2 + c_1\{\delta_r - 0.5(r_f - r_b)\delta_r^2\} - d_1\{\delta_\theta - 0.5(\theta_f - \theta_b)\delta_\theta^2\}\big]\omega_{i,j} - (\tau_1)_{i,j} = Re\big(\frac{\partial \omega}{\partial t}\big)_{i,j} \quad (3.5)$$

where,

$$c_1 = \frac{1}{r_i} - Re\ u_{i,j}, \quad d_1 = \frac{Re\ v_{i,j}}{r_i},$$

$$(\tau_1)_{i,j} = H_{11}\frac{\partial^3\omega}{\partial r^3} + K_{11}\frac{\partial^3\omega}{\partial\theta^3} + H_{12}\frac{\partial^4\omega}{\partial r^4} + K_{12}\frac{\partial^4\omega}{\partial\theta^4} + (r_f - r_b)(r_f^2 + r_b^2)\phi_{11} + (\theta_f - \theta_b)(\theta_f^2 + \theta_b^2)\phi_{12} + O\left(\frac{r_f^5 + r_b^5}{r_f + r_b}, \frac{\theta_f^5 + \theta_b^5}{\theta_f + \theta_b}\right), \tag{3.6}$$

with ϕ_{11}, ϕ_{12} being the leading truncation error terms and

$$H_{11} = \frac{1}{6}\{2(r_f - r_b) + cr_fr_b\}, \quad H_{12} = \frac{1}{24}\big\{2(r_f^2 + r_b^2 - r_fr_b) + cr_fr_b(r_f - r_b)\big\},$$

$$K_{11} = \frac{1}{6}\{\frac{2}{r_i^2}(\theta_f - \theta_b) - d\theta_f\theta_b\}, \quad K_{12} = \frac{1}{24}\big\{\frac{2}{r_i^2}(\theta_f^2 + \theta_b^2 - \theta_f\theta_b) - d\theta_f\theta_b(\theta_f - \theta_b)\big\}.$$

To obtain a higher order spatial compact finite difference approximation (at least up to third order spatial accuracy on nonuniform grids) for (3.1), the third and fourth order derivatives appearing in τ_1 are compactly approximated ([64]) to at least second order spatial accuracy. In order to accomplish this, the original equation (3.1) is treated as auxiliary relation that can be differentiated to obtain higher order derivatives. Successive differentiation of (3.1) with respect to r and θ and rearranging terms yield

$$\begin{aligned}\frac{\partial^3\omega}{\partial r^3} &= (Re\ u - \frac{1}{r})\frac{\partial^2\omega}{\partial r^2} + (Re\ u_r + \frac{1}{r^2})\frac{\partial\omega}{\partial r} + \frac{Re\ v}{r}\frac{\partial^2\omega}{\partial r\partial\theta} - \frac{1}{r^2}\frac{\partial^3\omega}{\partial r\partial\theta^2} \\ &+ \Big(\frac{Re\ v_r\ r - Re\ v}{r^2}\Big)\frac{\partial\omega}{\partial\theta} + \frac{2}{r^3}\frac{\partial^2\omega}{\partial\theta^2} + Re\frac{\partial}{\partial r}\left(\frac{\partial\omega}{\partial t}\right)\end{aligned} \tag{3.7}$$

$$\begin{aligned}\frac{\partial^4\omega}{\partial r^4} &= T_1\frac{\partial^2\omega}{\partial r^2} + T_2\frac{\partial\omega}{\partial r} + T_3\frac{\partial^2\omega}{\partial r\partial\theta} + T_4\frac{\partial^3\omega}{\partial r\partial\theta^2} + \frac{Re\ v}{r}\frac{\partial^3\omega}{\partial r^2\partial\theta} - \frac{1}{r^2}\frac{\partial^4\omega}{\partial r^2\partial\theta^2} \\ &+ T_5\frac{\partial\omega}{\partial\theta} + T_6\frac{\partial^2\omega}{\partial\theta^2} + (Re\ u - \frac{1}{r})Re\frac{\partial}{\partial r}\left(\frac{\partial\omega}{\partial t}\right) + Re\frac{\partial^2}{\partial r^2}\left(\frac{\partial\omega}{\partial t}\right)\end{aligned} \tag{3.8}$$

where,

$$T_1 = \big(Re\ u - \frac{1}{r}\big)^2 + 2\big(Re\ u_r + \frac{1}{r^2}\big), \qquad T_2 = \big(Re\ u - \frac{1}{r}\big)\big(Re\ u_r + \frac{1}{r^2}\big) + \big(Re\ u_{rr} - \frac{2}{r^3}\big),$$

$$T_3 = \big(Re\ u - \frac{1}{r}\big)\frac{Re\ v}{r} + 2\big(\frac{Re\ v_r\ r - Re\ v}{r^2}\big), \qquad T_4 = \frac{4}{r^3} - \big(Re\ u - \frac{1}{r}\big)\frac{1}{r^2}$$

$$T_5 = \big(Re\ u - \frac{1}{r}\big)\big(\frac{Re\ v_r\ r - Re\ v}{r^2}\big) + \big(\frac{Re\ v_{rr}\ r^2 - 2Re\ v_r\ r + 2Re\ v}{r^3}\big),$$

$$T_6 = \big(Re\ u - \frac{1}{r}\big)\frac{2}{r^3} - \frac{6}{r^4}.$$

and

$$\frac{\partial^3\omega}{\partial\theta^3} = Re\ v\ r\frac{\partial^2\omega}{\partial\theta^2} + Re\ v_\theta\ r\frac{\partial\omega}{\partial\theta} + (Re\ u\ r^2 - r)\frac{\partial^2\omega}{\partial r\partial\theta} - r^2\frac{\partial^3\omega}{\partial r^2\partial\theta} + Re\ u_\theta r^2\frac{\partial\omega}{\partial r} + Re\ r^2\frac{\partial}{\partial\theta}\left(\frac{\partial\omega}{\partial t}\right)$$

$$\begin{aligned}\frac{\partial^4\omega}{\partial\theta^4} &= \{(Re\ v\ r)^2 + 2Re\ v_\theta r\}\frac{\partial^2\omega}{\partial\theta^2} + (Re^2\ v_\theta v\ r^2 + Re\ v_{\theta\theta}r)\frac{\partial\omega}{\partial\theta} \\ &+ \{Re\ v\ r(Re\ u\ r^2 - r) + 2Re\ u_\theta r^2\}\frac{\partial^2\omega}{\partial r\partial\theta} - Re\ vr^3\frac{\partial^3\omega}{\partial r^2\partial\theta} \\ &- r^2\frac{\partial^4\omega}{\partial r^2\partial\theta^2} + (Re\ u\ r^2 - r)\frac{\partial^3\omega}{\partial r\partial\theta^2} + (Re^2 u_\theta v\ r^3 + Re\ u_{\theta\theta}\ r^2)\frac{\partial\omega}{\partial r} \\ &+ Re^2\ v\ r^3\frac{\partial}{\partial\theta}\left(\frac{\partial\omega}{\partial t}\right) + Re\ r^2\frac{\partial^2}{\partial\theta^2}\left(\frac{\partial\omega}{\partial t}\right)\end{aligned}$$

The approximations for the mixed derivatives such as $\frac{\partial^3\omega}{\partial r^2\partial\theta}$, $\frac{\partial^3\omega}{\partial r\partial\theta^2}$ and $\frac{\partial^4\omega}{\partial r^2\partial\theta^2}$ can be found out by the successive applications of the approximations for the first and second derivatives given in equations (2.5) and (2.6). Note that all the derivatives appearing in τ_1 being approximated are of the form $\frac{\partial^{p+q}\omega}{\partial r^p\partial\theta^q}$ where $p, q \leq 2$. Therefore the central difference approximations of these derivatives do not extend beyond one mesh length away from the point about which the finite differences are taken. As a result of this, the HOC computational stencil is always restricted to a maximum of nine points as shown in figure 3.1. Once all the approximations are substituted for the derivatives, the spatially HOC approximation of equation (3.1) can be written as

$$\Big[A1_{i,j}\delta_r^2 + A2_{i,j}\delta_\theta^2 + A3_{i,j}\delta_r + A4_{i,j}\delta_\theta + A5_{i,j}\delta_r\delta_\theta + A6_{i,j}\delta_r\delta_\theta^2 + A7_{i,j}\delta_r^2\delta_\theta + A8_{i,j}\delta_r^2\delta_\theta^2\Big]\omega_{i,j} = G_{i,j} \tag{3.9}$$

where the coefficients are given by

$$A1_{i,j} = 1 - 0.5c_1(r_f - r_b) - (H_{12}c_1^2 - c_1H_{11}) - 2H_{12}\big(Re(u_r)_{i,j} + \frac{1}{r_i^2}\big),$$

$$A2_{i,j} = \frac{1}{r_i^2} + 0.5d_1(\theta_f - \theta_b) - \frac{2}{r_i^3}(H_{11} - H_{12}c_1) + \frac{6H_{12}}{r_i^4} - Re\ v_{i,j}r_i(K_{11} + Re\ v_{i,j}r_iK_{12}) - 2K_{12}Re(v_\theta)_{i,j}r_i,$$

$$\begin{aligned}A3_{i,j} &= c_1 - (H_{11} - c_1H_{12})\big(Re(u_r)_{i,j} + \frac{1}{r_i^2}\big) - H_{12}\big(Re(u_{rr})_{i,j} - \frac{2}{r_i^3}\big) \\ &- Re(u_\theta)_{i,j}r_i^2(K_{11} + Re\ v_{i,j}r_iK_{12}) - K_{12}Re(v_{\theta\theta})_{i,j}r_i^2,\end{aligned}$$

$$A4_{i,j} = -d_1 \;-\; (H_{11} - c_1 H_{12})\big((v_r)_{i,j} r_i - v_{i,j}\big)\frac{Re}{r_i^2} - H_{12}\big((v_{rr})_{i,j} r_i^2 - 2(v_r)_{i,j} r_i + 2v_{i,j}\big)\frac{Re}{r_i^3} - Re(v_\theta)_{i,j} r_i\big(K_{11} + Re\; v_{i,j} r_i K_{12}\big) - K_{12} Re(v_{\theta\theta})_{i,j} r_i,$$

$$A5_{i,j} = -d_1(H_{11} - c_1 H_{12}) - 2H_{12}\big((v_r)_{i,j} r_i - v_{i,j}\big)\frac{Re}{r_i^2} + c_1 r_i^2 (K_{11} + Re\; v_{i,j} r_i K_{12}) - 2K_{12} Re(v_\theta)_{i,j} r_i^2,$$

$$A6_{i,j} = (H_{11} - c_1 H_{12})\frac{1}{r_i^2} - \frac{4H_{12}}{r_i^3} + c_1 K_{12} r_i^2,$$

$$A7_{i,j} = -d_1 H_{12} + r_i^2 (K_{11} + Re\; v_{i,j} r_i K_{12}),$$

$$A8_{i,j} = \frac{H_{12}}{r_i^2} + K_{12} r_i^2$$

$$G_{i,j} = \Big[Re + Re(H_{11} - c_1 H_{12})\delta_r + H_{12} Re \delta_r^2 + Re\; r_i^2 (K_{11} + Re\; v_{i,j} r_i K_{12})\delta_\theta + K_{12} Re r_i^2 \delta_\theta^2\Big]\frac{\partial \omega}{\partial t},$$

The details of all the spatial finite difference operators appearing in equations (3.9) can be found in Appendix-A.

Note that the expression $G_{i,j}$ in equation (3.9) has a temporal derivative term $\frac{\partial \omega}{\partial t}$. We use forward difference to discretize this term and then a weighted average parameter value of $\frac{1}{2}$ for this derivative ([61, 64, 91]) to arrive at a Crank-Nicolson type of approximation for equation (3.9)

$$\Big[A11_{i,j}\delta_r^2 + A12_{i,j}\delta_\theta^2 + A13_{i,j}\delta_r + A14_{i,j}\delta_\theta + A15_{i,j}\delta_r\delta_\theta + A16_{i,j}\delta_r\delta_\theta^2 + A17_{i,j}\delta_r^2\delta_\theta + A18_{i,j}\delta_r^2\delta_\theta^2\Big]\omega_{i,j}^{n+1} = \Big[A21_{i,j}\delta_r^2 + A22_{i,j}\delta_\theta^2 + A23_{i,j}\delta_r + A24_{i,j}\delta_\theta + A25_{i,j}\delta_r\delta_\theta + A26_{i,j}\delta_r\delta_\theta^2 + A27_{i,j}\delta_r^2\delta_\theta + A28_{i,j}\delta_r^2\delta_\theta^2\Big]\omega_{i,j}^{n} \qquad (3.10)$$

where,

$$A11_{i,j} = (H_{12}Re - 0.5\Delta t A1_{i,j}), \quad A21_{i,j} = (H_{12}Re + 0.5\Delta t A1_{i,j}),$$

$$A12_{i,j} = (r_i^2 K_{12} Re - 0.5\Delta t A2_{i,j}), \quad A22_{i,j} = (r_i^2 K_{12} Re + 0.5\Delta t A2_{i,j}),$$

$$A13_{i,j} = \big(Re(H_{11} - c_1 H_{12}) - 0.5\Delta t A3_{i,j}\big), \quad A23_{i,j} = \big(Re(H_{11} - c_1 H_{12}) + 0.5\Delta t A3_{i,j}\big),$$

$$A14_{i,j} = \big(r_i^2 Re(K_{11} + r_i Re\; v_{i,j} K_{12}) - 0.5\Delta t A4_{i,j}\big),$$

$$A24_{i,j} = \big(r_i^2 Re(K_{11} + r_i Re\; v_{i,j} K_{12}) + 0.5\Delta t A4_{i,j}\big)),$$

$$A15_{i,j} = -0.5\Delta t\; A5_{i,j}, \qquad A25_{i,j} = 0.5\Delta t A5_{i,j},$$

$$A16_{i,j} = -0.5\Delta t\ A6_{i,j}, \qquad A26_{i,j} = 0.5\Delta t A6_{i,j},$$
$$A17_{i,j} = -0.5\Delta t\ A7_{i,j}, \qquad A27_{i,j} = 0.5\Delta t A7_{i,j},$$
$$A18_{i,j} = -0.5\Delta t\ A8_{i,j}, \qquad A28_{i,j} = 0.5\Delta t A8_{i,j}.$$

Thus (3.10) is the HOC approximation of the vorticity equation (3.1) which is at least third order accurate in space and second order accurate in time. It may be noted that on a uniform grid, the spatial accuracy of (3.9) is exactly four.

3.4 Conclusion

In this chapter, we have developed a transformation free HOC scheme for the unsteady, viscous, incompressible N-S equations on nonuniform polar grids. The scheme is second order accurate in time and at least third order accurate in space. In the next two chapters, we will discuss about the implementation of the scheme to the complex flows past (a) impulsively started and (b) rotating cylinders respectively.

Chapter 4

A comprehensive study of the unsteady incompressible viscous flow past an impulsively started circular cylinder

4.1 Introduction

The classical problem of the evolution of incompressible viscous flow induced by an impulsively started circular cylinder is one of the most widely studied problems in computational fluid dynamics. It has continued to generate tremendous interest amongst researchers over the last century mainly because of the fact that it displays almost all the fluid mechanical phenomena for incompressible viscous flows in the simplest of geometric settings. However, the flow structure is very complex, especially for large Reynolds numbers, thus making the computation of the flow even more challenging and intriguing. Because of its popularity, a plethora of experimental, theoretical and numerical results are readily available for this problem in the literature.

The theoretical studies related to this problem can be dated back to the work of Blasius [24] in 1908 which was generally based on the boundary layer theory. This was further persisted by Goldstein *et al.* (1936) [50], Schuh (1953) [99], Wundt (1955) [118] and Watson (1955) [114] all of whom considered the limiting case of infinite Reynolds number. Later on, Wang (1967) [113] and Collins and Dennis (1973) [32] extended this work for finite but higher Reynolds numbers. In all the cases, results could be found only for short span of time in the early stage of the flow after the start.

Besides these theoretical works, for a better understanding of the phenomena of the unsteady wake formation, several experimentalists [26, 34, 35, 47, 86, 111, 116] performed a series of tests based on the visualization the flow for various Reynolds numbers. These experimental works have been of immense help to the computational fluid dynamics community; new computational methods are being developed and conse-

quently improved upon to solve this complex flow problem [18, 22, 38, 40, 44, 45, 46, 54, 67, 75, 77, 78, 94, 97, 100, 104, 119]. We now have enough experimental data that can be compared with the outcome of the numerical results, paving the way for computing complicated and extended flow phenomena for Reynolds numbers hitherto unexplored by experimentalists.

In this Chapter, we apply the newly developed HOC scheme in Chapter 3 to this well known problem for a wide range of Re ranging from 10 to 9500 [1]. In the process, we have also developed transient HOC approximation for the Neumann boundary condition for vorticity. For low and moderate Re, we compute the flow until steady state or till the flow becomes periodic. For the higher range of Re, we compute the solution in the initial stages of the flow. For all the Reynolds numbers, detailed discussion on the flow structure and comparison with experimental and numerical results are provided. In each case, our solution agrees very well, both qualitatively and quantitatively with established numerical and experimental results, confirming the efficiency of the proposed scheme. The robustness of the scheme however is better realized when it captures the periodic nature of the flow for $Re = 60$ and 200 characterized by vortex shedding represented by the von Kármán street and also by the fact that it very accurately captures the so called secondary phenomena for moderate Re, and α and β-phenomena for higher Re.

The chapter has been arranged in eight sections. Section 4.2 deals with the problem and the governing equations, section 4.3 with the approximation of the boundary conditions. In section 4.4 and Section 4.5 we discuss about the calculation of drag and lift coefficients, and the grid used. Section 4.6 deals with the solution of the algebraic system of equations, section 4.7 deals with the numerical results and discussion and finally, Section 4.8 summarizes the whole work.

4.2 The problem and the governing equations

We consider the unsteady, incompressible flow over an infinitely long cylinder of circular cross-section of radius R_0 (see the schematic diagram in figure 4.1). The flow is governed by the incompressible N-S equations. In non-dimensional form, the ψ-ω formulation of the N-S equations in cylindrical polar coordinates (r, θ) are given by,

$$\frac{\partial^2\omega}{\partial r^2} + \frac{1}{r}\frac{\partial\omega}{\partial r} + \frac{1}{r^2}\frac{\partial^2\omega}{\partial\theta^2} = Re\big(u\frac{\partial\omega}{\partial r} + \frac{v}{r}\frac{\partial\omega}{\partial\theta} + \frac{\partial\omega}{\partial t}\big) \tag{4.1}$$

$$\frac{\partial^2\psi}{\partial r^2} + \frac{1}{r}\frac{\partial\psi}{\partial r} + \frac{1}{r^2}\frac{\partial^2\psi}{\partial\theta^2} = -\omega \tag{4.2}$$

Here ψ is the streamfunction, ω the vorticity, u, v respectively are the radial and tangential velocity components, t is the time and $Re = \dfrac{UD}{\nu}$ is the Reynolds number with

[1] Part of this work has been published in *Journal of Computational Physics* [65].

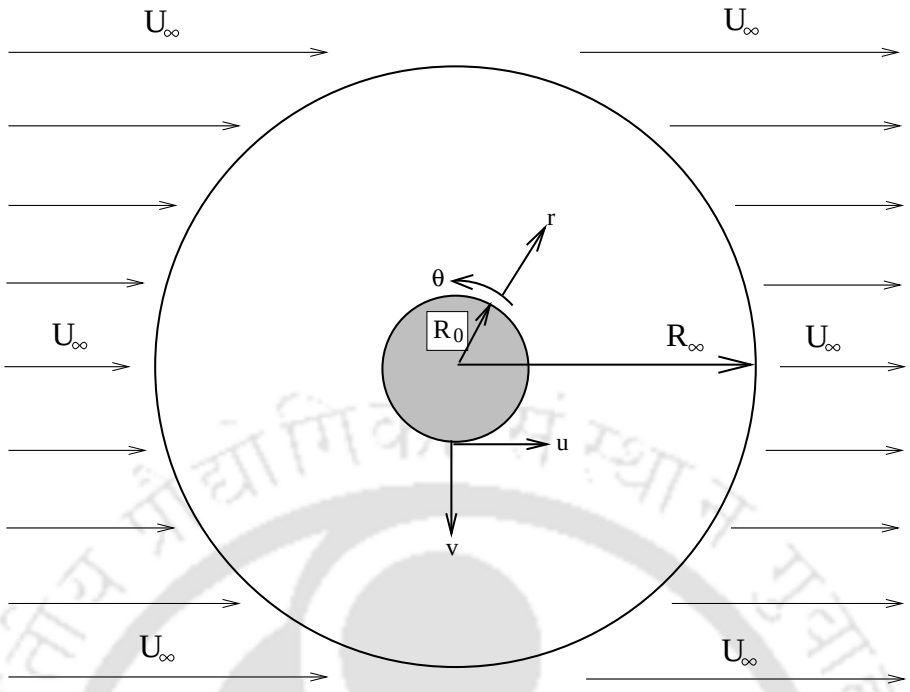

Figure 4.1: *Schematic diagram of the flow around a circular cylinder.*

U being the characteristic velocity, D the diameter of the cylinder and ν the kinematic viscosity. The velocities u and v in terms of ψ are given by

$$u = \frac{1}{r}\frac{\partial \psi}{\partial \theta} \quad \text{and} \quad v = -\frac{\partial \psi}{\partial r}, \tag{4.3}$$

and the vorticity ω is given by

$$\omega = \frac{1}{r}\left[\frac{\partial}{\partial r}(vr) - \frac{\partial u}{\partial \theta}\right]. \tag{4.4}$$

We assume the cylinder to be of unit radius placed in an infinite domain. At the far-field, a potential flow is assumed ([18]) with uniform free-stream velocity $U_\infty = 1$. Thus

$$(u_\infty(r,\theta), v_\infty(r,\theta)) = \left(U_\infty\left(1 - \frac{R_0^2}{r^2}\right)\cos\theta, -U_\infty\left(1 + \frac{R_0^2}{r^2}\right)\sin\theta\right). \tag{4.5}$$

The initial and the boundary conditions are as follows:

$$\omega(r,\theta,0) = 0 \qquad R_0 \le r \le \infty, \;\; 0 \le \theta \le 2\pi, \tag{4.6}$$

$$(u(r,\theta,t), v(r,\theta,t)) = (u_\infty(r,\theta), -v_\infty(r,\theta)) \;\; r \to \infty, \;\; 0 \le \theta \le 2\pi, \tag{4.7}$$

On the surface of the cylinder $r = R_0$, $0 \le \theta \le 2\pi$

$$(u(r,\theta,t), v(r,\theta,t)) = (0,0) \tag{4.8}$$

The boundary conditions for ψ on the surface of the cylinder can be derived from those of the velocities in (4.8) as

$$\psi(r,\theta) = 0, \quad \frac{\partial \psi}{\partial r}(r,\theta) = 0 \quad 0 \le \theta \le 2\pi, \tag{4.9}$$

At the far field where $r \to \infty$,

$$\psi(r,\theta) = \left(r - \frac{R_0^2}{r}\right)\sin\theta, \quad \frac{\partial \psi}{\partial r}(r,\theta) = \left(1 + \frac{R_0^2}{r^2}\right)\sin\theta \;\; 0 \le \theta \le 2\pi, \tag{4.10}$$

4.3 Approximation of the Boundary Conditions

The numerical implementation of the boundary conditions for u, v and ψ are straightforward. The vorticity ω at the far field is zero. At the solid boundary, making use of equation (4.2) and (4.9), for all θ at $r = R_0$, we have

$$\omega = -\frac{\partial^2 \psi}{\partial r^2} \tag{4.11}$$

thereat. We proceed to obtain a compact approximation of the vorticity on the solid boundary as follows:

Employing a Taylor series expansion, we get

$$0 = -\left.\frac{\partial \psi}{\partial r}\right|_{0,j} = -\delta_r \psi_{0,j} + \frac{r_f}{2}\left.\frac{\partial^2 \psi}{\partial r^2}\right|_{0,j} + \left.\frac{r_f^2}{6}\frac{\partial^3 \psi}{\partial r^3}\right|_{0,j} + + \left.\frac{r_f^3}{24}\frac{\partial^4 \psi}{\partial r^4}\right|_{0,j} + O(r_f^4) \tag{4.12}$$

Using (4.11) in (4.12), we get the fourth order accurate expression

$$0 = -\delta_r \psi_{0,j} - \left.\left(\frac{r_f\ \omega_{0,j}}{2} + \frac{r_f^2}{6}\frac{\partial \omega}{\partial r} + \frac{r_f^3}{24}\frac{\partial^2 \omega}{\partial r^2}\right)\right|_{0,j} + O(r_f^4) \tag{4.13}$$

Making use of the fact that on the solid wall $u = 0$, $v = 0$, equation (4.1) yields,

$$\frac{\partial^2 \omega}{\partial r^2} = Re\frac{\partial \omega}{\partial t} - \frac{1}{r_0}\frac{\partial \omega}{\partial r} - \frac{1}{r_0^2}\frac{\partial^2 \omega}{\partial \theta^2} \tag{4.14}$$

Using (4.14) in (4.13) and after some simplifications we get,

$$0 = -\delta_r \psi_{0,j} - \frac{r_f}{2}\omega_{0,j} + \left(\frac{r_f^3}{24 r_0} - \frac{r_f^2}{6}\right)\left.\frac{\partial \omega}{\partial r}\right|_{0,j} - \left.\frac{r_f^3 Re}{24}\frac{\partial \omega}{\partial t}\right|_{0,j} + \left.\frac{r_f^3}{24 r^2}\frac{\partial^2 \omega}{\partial \theta^2}\right|_{0,j} \tag{4.15}$$

Using forward difference for the temporal derivative and second order one-sided difference for the derivatives along r-direction, we finally get

$$\begin{aligned}
\omega_{0,j}^{n+1} &= \frac{24\Delta t}{r_f^3\ Re}\left[\left\{\frac{r_f^3\ Re}{24\Delta t} - \frac{r_f}{2} - \left(\frac{r_f^3}{24 r_0} - \frac{r_f^2}{6}\right)\left(\frac{(r_2 - r_0)^2 - r_f^2}{r_f(r_2 - r_0)(r_2 - r_1)}\right)\right.\right. \\
&- \left.\left.\frac{r_f^3}{24 r_0^2 \Delta\theta}\left(\frac{1}{\theta_f} + \frac{1}{\theta_f}\right)\right\}\omega_{0,j}^n + \frac{r_f^3}{24 r_0^2 \theta_b \Delta\theta}\omega_{0,j-1}^n + \frac{r_f^3}{24 r_0^2 \theta_f \Delta\theta}\omega_{0,j+1}^n \right. \\
&+ \left.\left(\frac{r_f^3}{24 r_0} - \frac{r_f^2}{6}\right)\left(\frac{(r_2 - r_0)^2 \omega_{1,j}^n - r_f^2 \omega_{2,j}^n}{r_f(r_2 - r_0)(r_2 - r_1)}\right)\right]
\end{aligned} \tag{4.16}$$

4.4 Calculation of Drag and Lift coefficients

In the case of viscous flows for bluff bodies immersed in fluids, the forces that are being exerted on the body come from surface pressure distribution and surface friction. The surface pressure distribution can be calculated from the tangential momentum equation at the surface of the body. To calculate the lift (C_L) and drag coefficients (C_D), we use the following formulas [67, 104] respectively,

$$C_L = \frac{1}{Re}\int_0^{2\pi}\left[\left(\frac{\partial\omega}{\partial r}\right)_{R_0} - \omega_{R_0}\right] cos\theta \; d\theta \tag{4.17}$$

$$C_D = \frac{1}{Re}\int_0^{2\pi}\left[\left(\frac{\partial\omega}{\partial r}\right)_{R_0} - \omega_{R_0}\right] sin\theta \; d\theta \tag{4.18}$$

The integral over θ along the cylinder is numerically computed using Trapezoidal rule.

4.5 The Grid used

As in Chapter 2, employ a uniform grid spacing along the θ- direction and nonuniform grid spacing in the r-direction with clustering around the surface of the cylinder using the following functions:

$$\theta_j = \frac{2\pi}{j_{\max}} \;\text{ and }\; r_i = \exp\left(\frac{\lambda\pi i}{i_{\max}}\right),$$

with the parameter λ determining the outer radius of the computational domain. Again, the continuity conditions at $\theta = 0$ and $\theta = 2\pi$ are taken as the boundary conditions along those two lines. A typical computational grid for this flow has already been shown in Figure 2.4.

4.6 Solution of algebraic systems

We now discuss the solution of algebraic systems associated with the newly proposed finite difference approximations. The system of equations arising out of (2.14) and (3.10) can be written as

$$\sum_{k_1=-1}^{1}\sum_{k_2=-1}^{1} \eta 1_{i+k_1,j+k_2}\; \psi_{i+k_1,j+k_2} = \sum_{k_1=-1}^{1}\sum_{k_2=-1}^{1} \xi 1_{i+k_1,j+k_2}\; g_{i+k_1,j+k_2}, \tag{4.19}$$

and

$$\sum_{k_1=-1}^{1}\sum_{k_2=-1}^{1} \eta 2_{i+k_1,j+k_2}\; \omega^{n+1}_{i+k_1,j+k_2} = \sum_{k_1=-1}^{1}\sum_{k_2=-1}^{1} \xi 2_{i+k_1,j+k_2}\; \omega^{n}_{i+k_1,j+k_2}, \tag{4.20}$$

where $\eta 1$, $\xi 1$ and $\eta 2$, $\xi 2$'s are functions of the coefficients appearing in the corresponding equations (4.2) and (4.1), their derivatives and the step lengths r_f, r_b, θ_f, θ_b and Δt. In matrix form, the system of algebraic equations given by (4.19) or (4.20) can now be written as

$$A\Phi = B \tag{4.21}$$

where the coefficient matrix A is an asymmetric sparse matrix with each row containing at most nine non-zero entries. ϕ is the unknown vector ψ or ω and B is the known (source) term. For a grid of size $m \times n$, A is of size $mn \times mn$, and Φ and B are mn-component vectors.

The next step now is to solve equation (4.21); as the coefficient matrix A which has the same structure as the one appearing in equation (2.16) of Chapter 2. However, in order to solve these systems, we use the hybrid biconjugate gradient stabilized method BiCGStab(2) [5, 105] without preconditioning, which is known to be more robust [105] than the BiCGStab solver that had been used for the steady-state case.

It may be noted that for the coupled nonlinear PDEs (such as the ψ-ω form of the N-S equations), an iterative solution procedure must be adopted to solve the matrix equation of the type (4.21) at each time step. Both the vorticity (4.20) and stream function (4.19) equations are solved using hybrid BiCGStab(2) which may be termed inner iterations. We utilize a relaxation parameter γ for the inner iteration cycles for both ω and ψ. For larger values of Reynolds number, we needed smaller values of γ.

All of our computations were carried out on a Pentium 4 based PC with 512 MB RAM. For the inner iterations, the computations were stopped when the norm of the residual vector $\bar{\mathbf{r}} = B - A\Phi$ (ϕ being either ω or ψ) arising out of equation (4.21) fell below 0.5×10^{-6}. For the cases where steady-state solution is obtained with a time marching strategy, the steady-state is assumed to reach when the maximum ω-error between two successive time steps is smaller than 0.5×10^{-7}.

4.7 Results and Discussion

We have used the proposed HOC scheme to visualize and analyze the flow patterns for Reynolds numbers ranging from 10 to 9500. Different grid sizes and outflow boundaries are used to capture the gradually increasing complex flow patterns. The flow regime has been divided into four parts depending upon the almost identical flow characteristics observed within each range. In the first part we discuss about the flow structures for $10 \leq Re \leq 40$; available experimental and the numerical results [26, 34, 35, 38, 44, 78, 97] show that steady-state is possible for this range. In the second part we discuss about the flow structures for $Re = 60$ and 200; here the wake behind the cylinder becomes unstable. Oscillations in the wake grow in amplitude and finally forms a trail of vortices known as

von Kármán vortex street. For the next higher Reynolds numbers being discussed here, we consider only the early stage of the flow in the laminar regime. The first of these are $Re = 300$ and 550; for these Re, the flow properties are unsteady; secondary vortices develop at the initial stages, but do not split up further. The flow is characterized by the secondary phenomena: (i) bulge phenomenon and (ii) isolated secondary eddy. In the last part, we discuss the range $1000 \leq Re \leq 9500$ having the most complicated flow properties associated with the so called α- and β-phenomena ([26, 78, 97]).

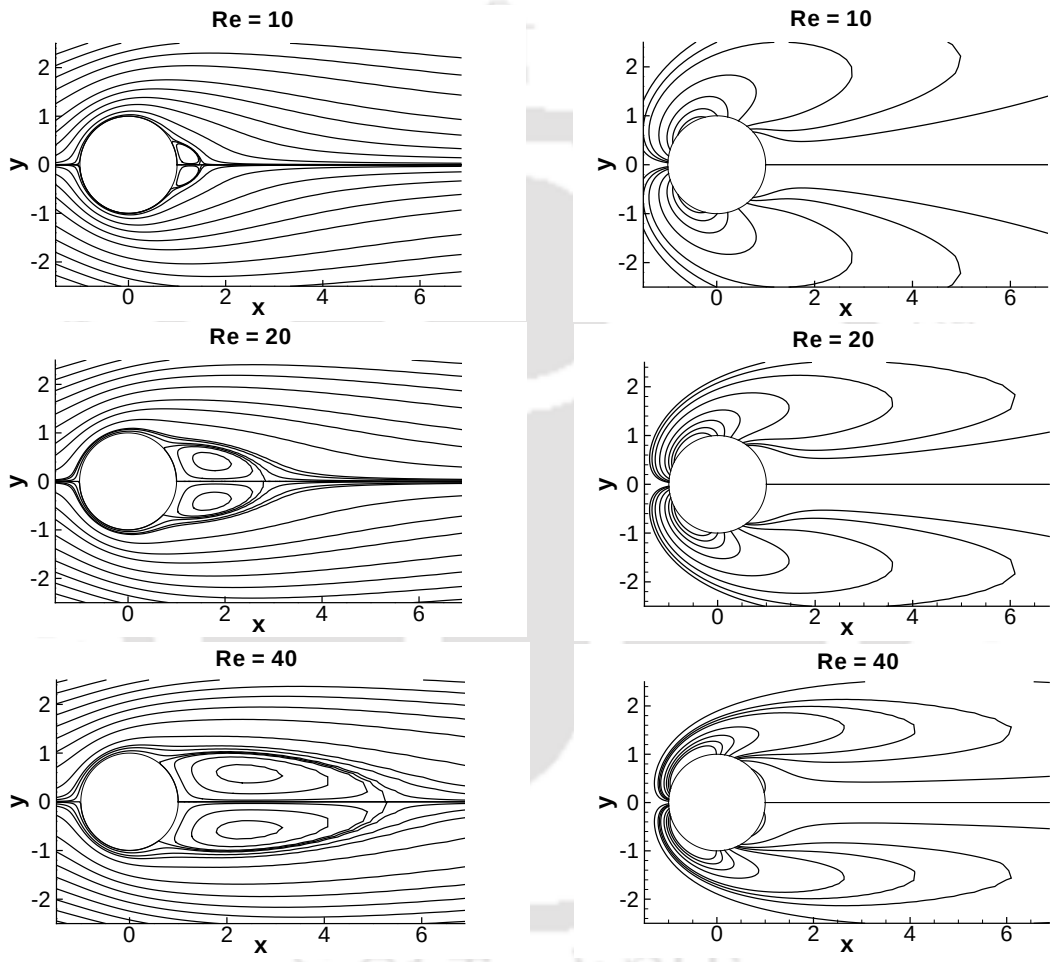

Figure 4.2: *Steady-state stream-lines (left) and vorticity contours (right) for* $Re = 10$, 20 *and* 40 *for the motion past a circular cylinder problem.*

4.7.1 Flows for $10 \leq Re \leq 40$

As stated earlier, for the flow past an impulsively started circular cylinder, steady-state is possible up to $Re = 40$. So, in this section, we compare our time-marching steady-state results with existing numerical and experimental results [35, 38, 44, 45, 54, 67, 77, 97, 111] for Reynolds numbers $Re = 10,\ 20,$ and 40 in Figures 4.2-4.4 and Tables 4.1-4.3.

In Figure 4.2, we exhibit the streamlines and vorticity contours from $Re = 10$ to 40. In all the cases, two symmetrical, stationary circulating eddy develops behind the cylinder. With increase in Re values, one can see the increase in the sizes of the vortices. We also compute the wake length L and the angle of separation θ_s(refer to figure 2.7).

Table 4.1: *Effect of grid size on wake lengths and separation angles.*

	$Re = 20$			$Re = 40$		
Grid	75	101	151	75	101	151
θ_s	42.9248	43.2756	43.4224	51.3012	51.5342	51.7018
L	1.8331	1.8276	1.8226	4.4135	4.3988	4.3921

Table 4.2: *Effect of far field boundary on the wake lengths and separation angles.*

	$Re = 20$			$Re = 40$		
R_∞	35.03	60.14	75.17	35.03	60.14	75.17
θ_s	43.6248	43.2156	42.9248	51.9612	51.6342	51.3012
L	1.8177	1.8253	1.8331	4.4044	4.4101	4.4135

These parameters are then compared in table 4.1 in order to verify the grid-independence;

Table 4.3: *Comparison of the wake lengths and separation angles for different Reynolds numbers.*

	Re	Ref. [38]	Ref. [111]	Ref. [77]	Ref. [44]	Ref. [54]	Ref. [97]	Present
L	20	1.88	-	1.87	1.82	1.842	1.77	1.8331
	40	4.69	-	4.27	4.48	4.49	4.21	4.4135
θ_s	20	43.7	-	-	42.9	42.96	41.3277	42.9248
	40	53.8	-	-	51.5	52.84	51.0249	51.3012
C_D	20	2.045	2.05	-	2.001	2.152	2.0597	2.0193
	40	1.522	1.57	-	1.498	1.499	1.5308	1.5145

the grid sizes range from 75×75 to 151×151. Table 4.2 shows the variation of the same parameters to check the dependence of the computed solution on the assumed far-field where R_∞s range from 35.03 to 75.17. Here the grid size has been fixed at 75×75. From these tables, it is clear that a grid of size 101×101 and a far-field given by $R_\infty = 75$ are enough for accurate resolution of the flow. In table 4.3, we present our computed L, θ_s and the drag coefficient C_D along with those obtained by [38, 44, 54, 77, 97, 111].

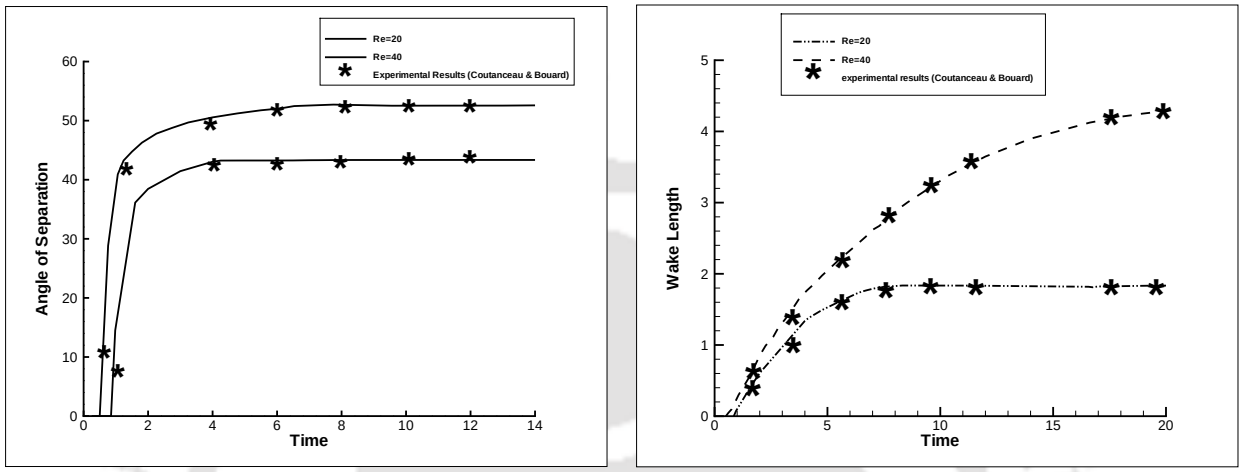

(a) (b)

Figure 4.3: *Comparison of (a) angle of separation and (b) wake length, for low Re values with the results of references [35] for the motion past a circular cylinder problem.*

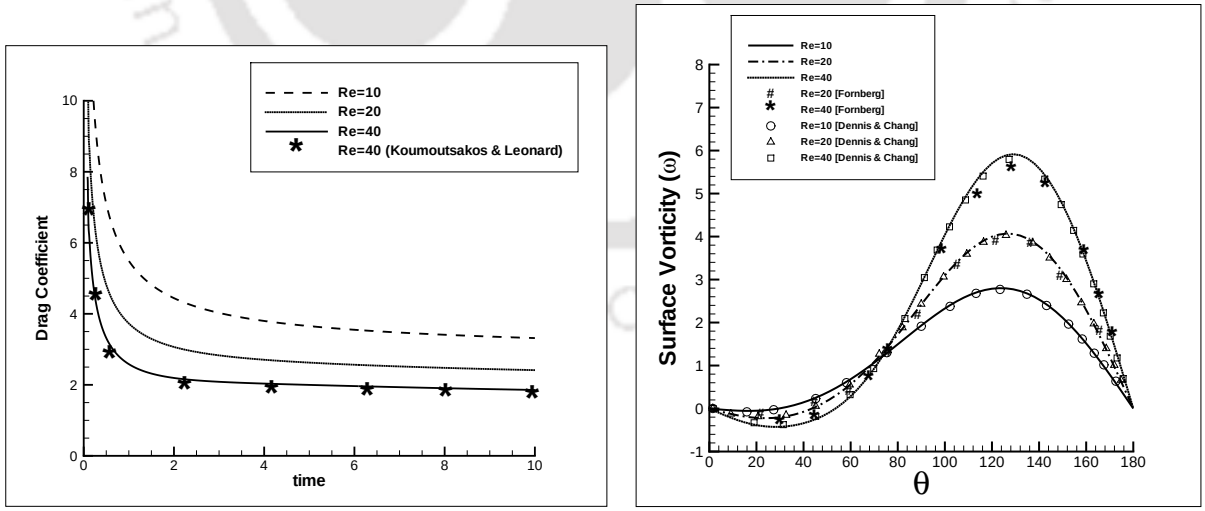

(a) (b)

Figure 4.4: *Comparison between present results and (a) reference [67] for drag coefficients and (b) references [38] and [44] for vorticities on the cylinder surface for low Re values for the motion past a circular cylinder problem.*

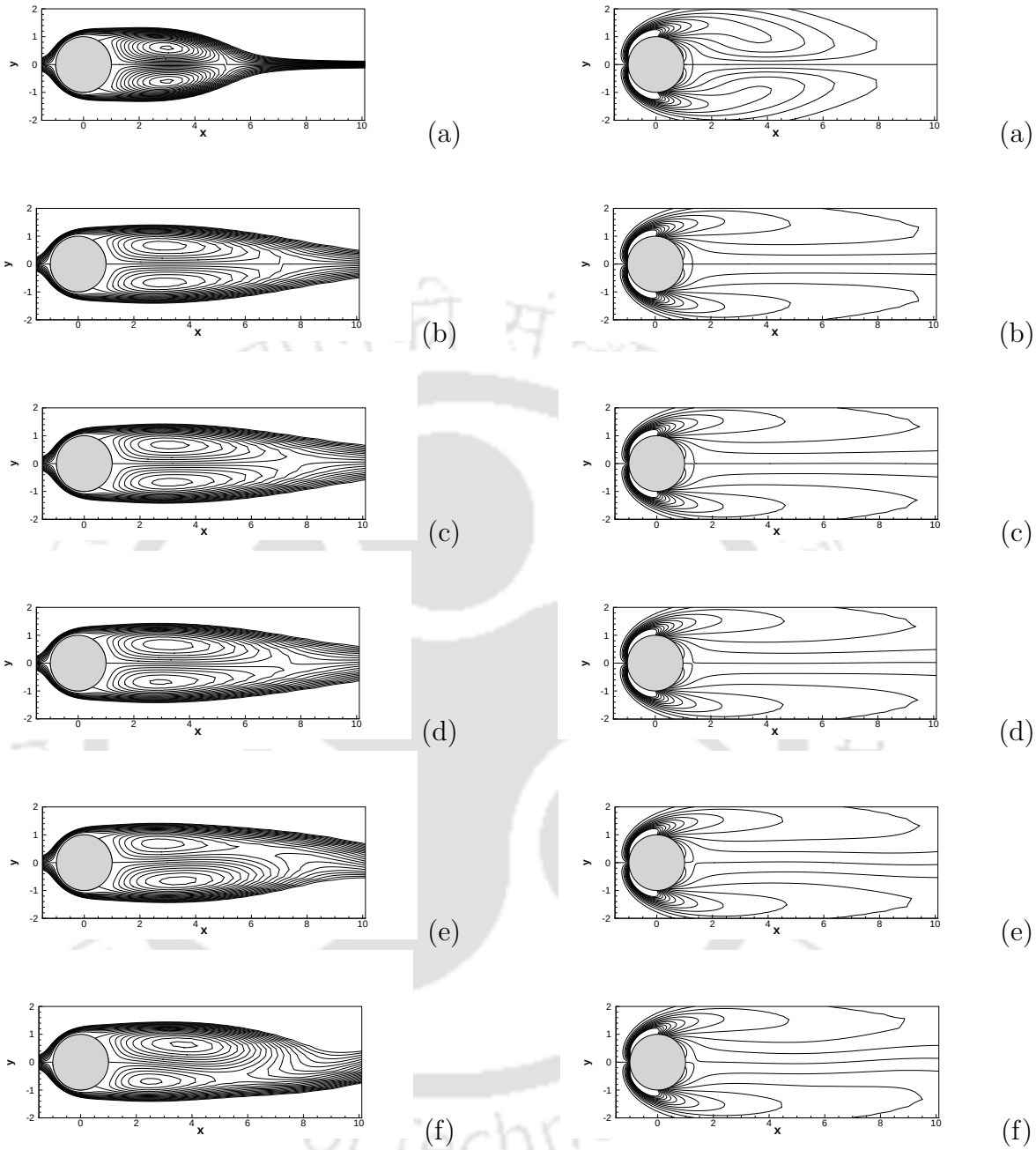

Figure 4.5: *Streamlines (left) and vorticity contours (right) at* $Re = 60$ *for flow past a circular cylinder at : (a)* $t = 20$*, (b)* 70*, (c)* 329*, (d)* 363*, (e)* 428 *and (f)* 468.

In figures 4.3(a) and 4.3(b), we compare the evolution of the angles of separation and wake lengths at the earlier stages of the flow for $10 \leq Re \leq 40$ with the results of [35]; figure 4.4(a) shows the time evolution of the computed drag coefficients in the range $10 \leq Re \leq 40$ along with those of [67]. We also compare the vorticity values

along the surface of the cylinder for the range of Reynolds numbers considered here with those of references [38, 44] in Figure 4.4(b). In all the cases, we obtain excellent comparisons with the established numerical and experimental results, both qualitatively and quantitatively.

4.7.2 Flows for $Re = 60$ and 200:

The flow around a impulsively started circular cylinder for $Re = 60$ and 200 eventually becomes periodic and is known to develop vortex shedding represented by the von Kármán vortex street [10, 14]. The basic difference between the flow patterns of this Re range with the previous one is that, the velocities increase with time more rapidly in the recirculating zone and the secondary vortices develop in this region. In these Re values, flow becomes unsteady. Careful flow visualization reveals that the flow in the early stage of development in the laminar wake region is still two-dimensional and symmetric about the axis $\theta = 0$. Therefore, quite a few number of studies [18, 38, 44, 45, 78] have used only the upper half circular annular region to compute the flow. However use of the complete annular region for computational purpose enabled us to capture the unsteady periodic nature of the flow for $Re = 60$ and 200 as well. For these two Reynolds numbers, we have used a 181×181 grid and R_∞ is taken as around 35 times of the cylinder radius.

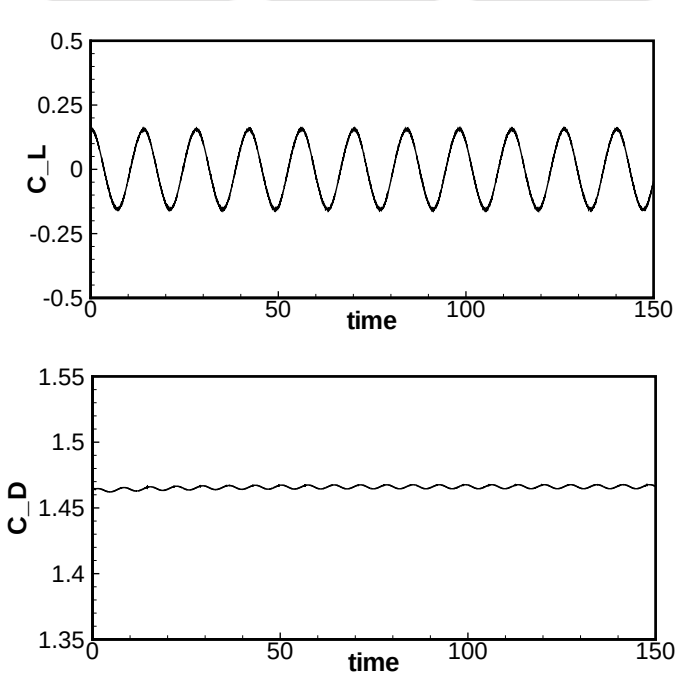

Figure 4.6: *For $Re = 60$, (a) time history of the lift and drag coefficients for the temporally periodic solution.*

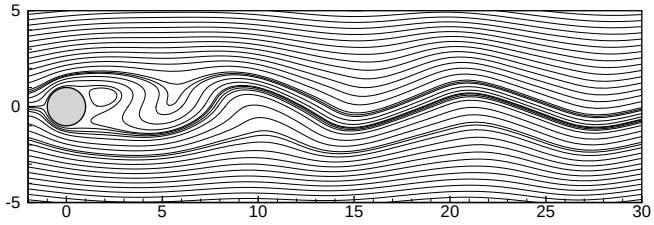

(a)

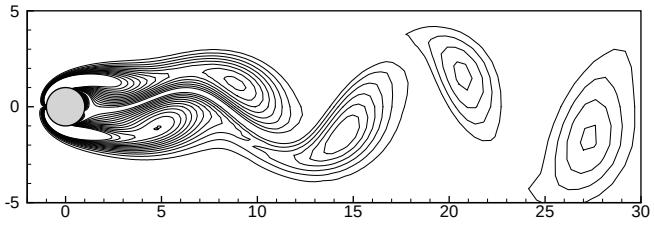

(b)

Figure 4.7: *For $Re = 60$, (a) streamline and (b) vorticity contours (corresponding to the peak value of the lift coefficient) for the temporally periodic solution.*

In figure 4.5, we show the evolution of streamlines and vorticity contours for $Re = 60$ from $t = 20$ having a symmetric pattern and leading to the onset of asymmetry in the streamlines at a later time around $t = 329$. The asymmetry in vorticity becomes apparent only when t reaches a value around 428. In figure 4.6, we show the time histories of the lift and drag coefficients for $Re = 60$, and in figures 4.7(a) and 4.7(b), we show the streamfunction and vorticity fields for the temporally periodic solution corresponding to the peak value of the lift coefficient. Our observations are consistent with ones found in [81]. More details are presented for the next Reynolds number 200, where we exhibit our numerical results for $Re = 200$ from an early to a periodic stage in figures 4.8 to 4.10. In Figure 4.8, solution profiles are presented for various values of t till the onset of periodicity. As seen from the figure, a symmetric flow was observed at the beginning (figure 4.8(a)-(c)), but the flow became unstable later on, and finally the flow lost its symmetry (figures 4.8(d) onwards). Eventually, the flow settled into a periodic nature (figure 4.8(n)). We present the temporal evolution of streamlines and vorticity over one complete vortex shedding cycle of duration T in figures 4.9 and 4.10 respectively. The evolution of an impressive von Kármán vortex street, which is a regular feature for the Reynolds numbers considered here, is clearly seen in these figures.

From Figure 4.9, one can see the formation of eddies just behind the cylinder; these eddies are then washed away into the wake region. Two eddies are shed just behind the cylinder within each period (see also Figures 4.8(n) and 4.9(a)). Figures 4.9(a) and 4.9(b) are half a vortex-shedding cycle apart, and middle figure 4.9(b) is a mirror image

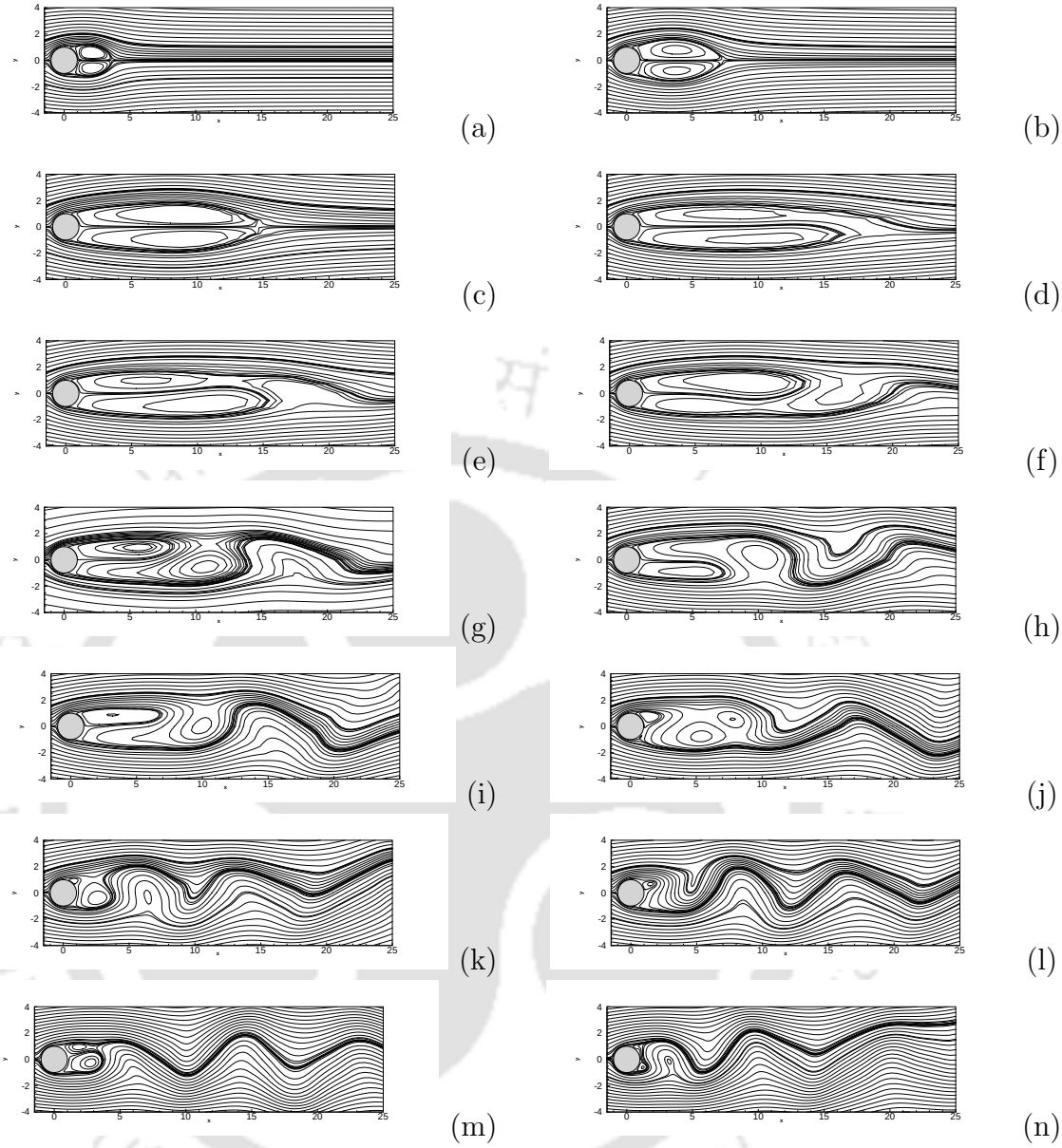

Figure 4.8: *Streamlines at* $Re = 200$ *for flow past a circular cylinder at : (a)* $t = 12$, *(b)* 34, *(c)* 100, *(d)* 229, *(e)* 280 *(f)* 300, *(g)* 305, *(h)* 316, *(i)* 324, *(j)* 350, *(k)* 360, *(l)* 364, *(m)* 372 *and (n)* 400.

of Figures 4.9(a) and 4.9(c).

The corresponding vorticity contours are depicted in figures 4.10(a)-(c). The staggered nature of the Kármán shedding is clear from these plots. The crests and troughs of the sinuous waves in the streamlines reflect the alternatively positive and negative vorticities of the eddies. Apart from figures 4.9 and 4.10, the periodic nature of the flow is apparent from figure 4.11 where we have depicted the time evolution of the drag

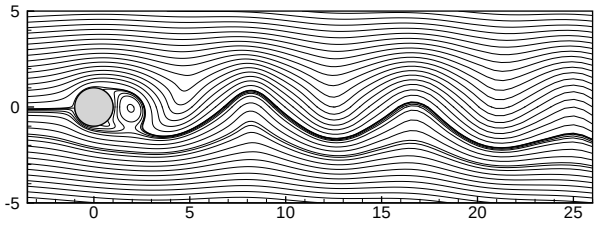

(a)

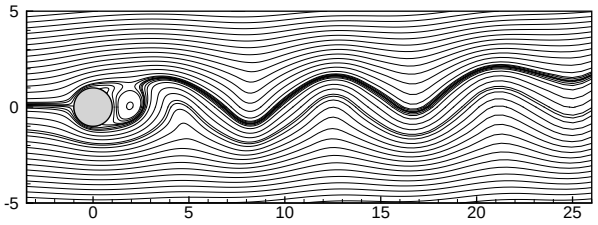

(b)

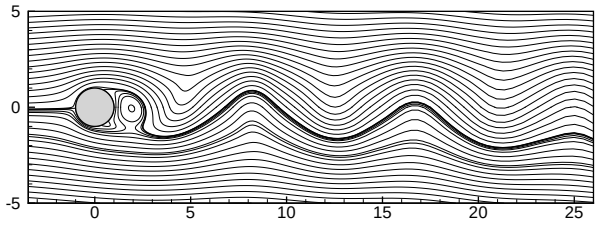

(c)

Figure 4.9: *The streamfunction contours depicting the wake behind three successive instants of time over one vortex shedding period for* $Re = 200$. *(a)* $t = t_0$, *(b)* $t = t_0 + \frac{T}{2}$ *and (c)* $t = t_0 + T$

and lift coefficients for this Reynolds number. In figure 4.12(a), we compare the radial velocity values obtained by our computations at earlier stages along the axis of flow with those of the experimental results of Bouard and Coutanceau ([26]). Note that $u^* = \dfrac{u}{U_\infty}$ and $x^* = \dfrac{x}{D}$ here. Our results match excellently with the experimental ones. In figure 4.13(b), vorticity distribution along the solid surface are shown for the same interval of time. We also calculate the Strouhal St number for $Re = 60$ and 200, which characterizes the vortex shedding process and is estimated from the periodic variation of the lift coefficient. It is defined as $St = \dfrac{nD}{U_\infty}$ [111], where n is the dominant frequency of the lift variations, which we compute by a spectral analysis of a time sample of the lift coefficients. The power density spectra of this analysis is shown in figure 4.13(a). Figure 4.13(b) displays the phase-plane of u-v velocity at the monitoring point $(1.260, -0.067)$ for the same time sample; it clearly establishes the periodic nature of the flow for these two Reynolds numbers. In table 4.4, we compare our computed Strouhal numbers, drag

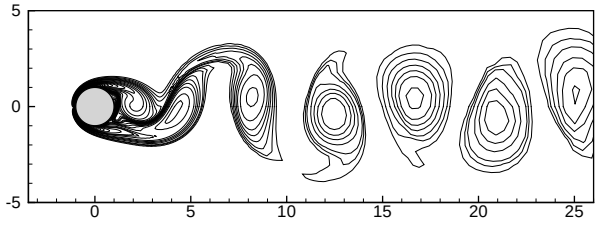

(a)

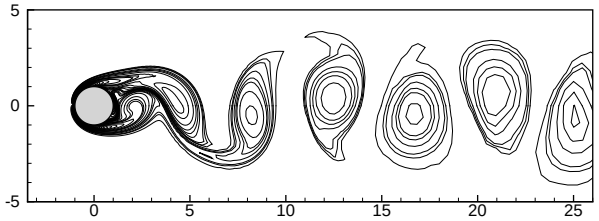

(b)

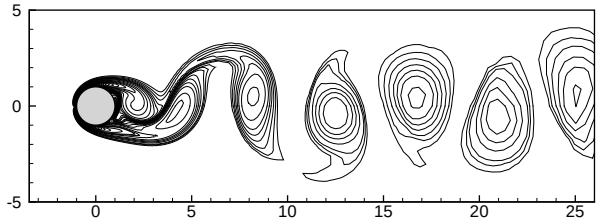

(c)

Figure 4.10: *The vorticity contours depicting the wake behind three successive instants of time over one vortex shedding period for* $Re = 200$. *(a)* $t = t_0$, *(b)* $t = t_0 + \frac{T}{2}$ *and (c)* $t = t_0 + T$

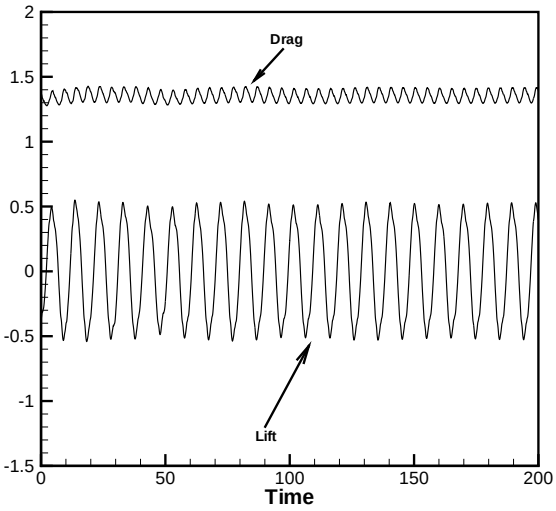

Figure 4.11: *Evolution of drag and lift coefficients for the motion past a circular cylinder for* $Re = 200$.

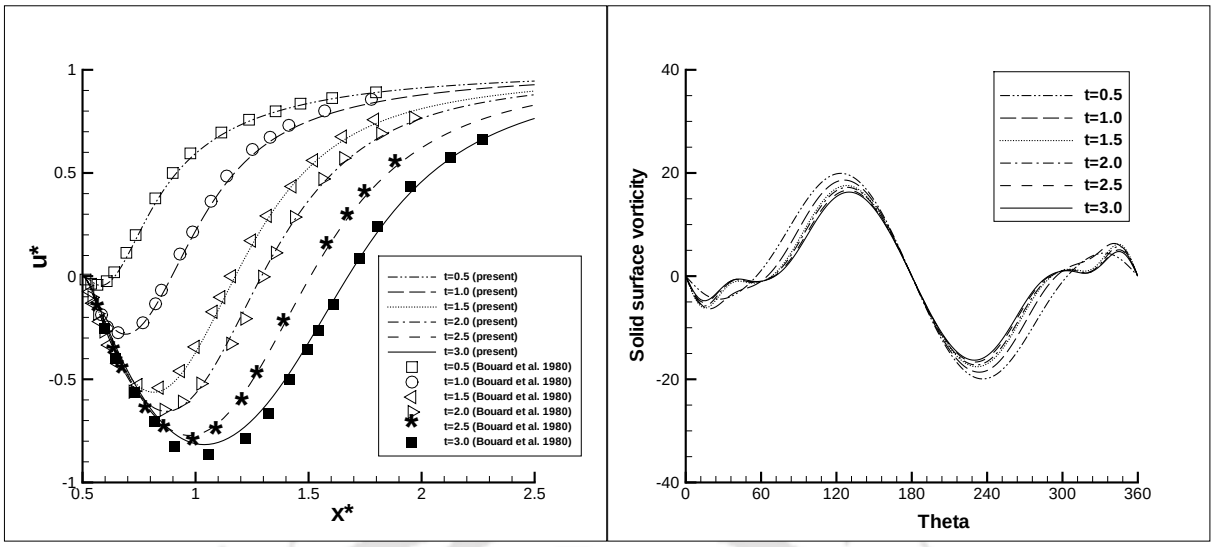

(a) (b)

Figure 4.12: *(a) Radial velocity along the axis of flow and (b) Vorticity along the solid surface, for the motion past a circular cylinder for* $Re = 200$ *at the earlier stages of the flow.*

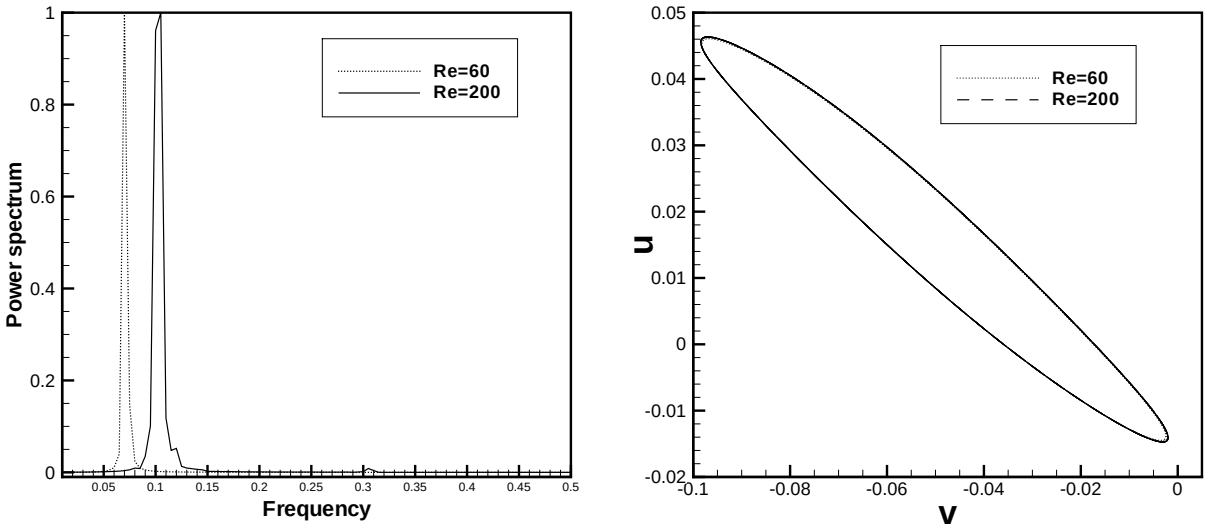

(a) (b)

Figure 4.13: *Periodic flow for* $Re = 60$ *and* 200*: (a) Power spectra of the time series of the lift coefficient, (b) Phase plane trajectories of* u*-*v *velocities.*

and lift coefficients for these two Re with established experimental and numerical results; for both Re, we obtain very close comparisons.

Table 4.4: *Comparison of Strauhal numbers, drag and lift coefficients of the periodic flow for $Re = 60$ and 200.*

Re	Reference	St	C_D	C_L
$Re = 60$	Williamson (exp.)[116]	0.135		
	Tritton [111]	0.137	1.387	
	Norberg (exp.) [86]	0.140		
	Friehe [47]	0.135		
	Mittal and Raghuvanshi[81]	0.142	1.489±0.002	±0.144
	Present Study	0.140	1.464±0.003	±0.151
$Re = 200$	Williamson (exp.) [116]	0.197		
	Le *et al.* [75]	0.187	1.34±0.030	±0.43
	Linnick and Fasel [75]	0.197	1.34±0.044	±0.69
	Frank *et al.* [46]	0.194	1.31	±0.65
	Berthelsen and Faltinsen [22]	0.200	1.37±0.046	±0.70
	Present Study	0.210	1.35±0.053	±0.53

4.7.3 Flows for 300 and 550:

For these two Reynolds numbers, the flow eventually becomes three-dimensional. For computational purpose, we have used a 181×181 grid for both Re and R_∞ is taken as around 35 times of the cylinder radius for $Re = 300$, and 20 times for $Re = 550$. We present the flow patterns for $Re = 300$ and $Re = 550$ at different instances of the early stages of the development of the wake in figures 4.14 and 4.15 repectively. Both these figures show the gradual increase in the length and width of the wake as time progresses. However, no development of secondary vortex is seen for $Re = 300$ at this initial stage which is visible for $Re = 550$ at $t = 2.0$. The equivorticity contours in these figures are also in close agreement with the ones available in literature [22]. The length of the wake for $Re = 300$ is larger than that of $Re = 550$ for the same instants of time; also for $Re = 550$, for $t > 1.5$, the width of the wake is larger than the cylinder. All these observations are consistent with the experimental studies of [35].

In figures 4.16(a) we compare our numerical results with the experimental results ([26]) for $Re = 300$ and in 4.16(b), the same for $Re = 550$ at $t = 2.5$. These figures clearly depict the extreme closeness of our numerical results with the experimental ones, thus demonstrating the efficiency of our scheme. They also represent the secondary phenomena ([26]): (i) the bulge phenomenon and (ii) isolated secondary eddy. In figure 4.16(a) (top), the streamlines near the cylinder wall which are almost halfway between the stagnation and separation points show some distortion. The fluid particles passing through this region deviate from the cylinder which cause a bulge in the streamline pattern. This is known as the bulge phenomenon. On the other hand, for greater values of Re ($500 \leq Re \leq 800$), this bulge gives rise to closed streamlines which form a small

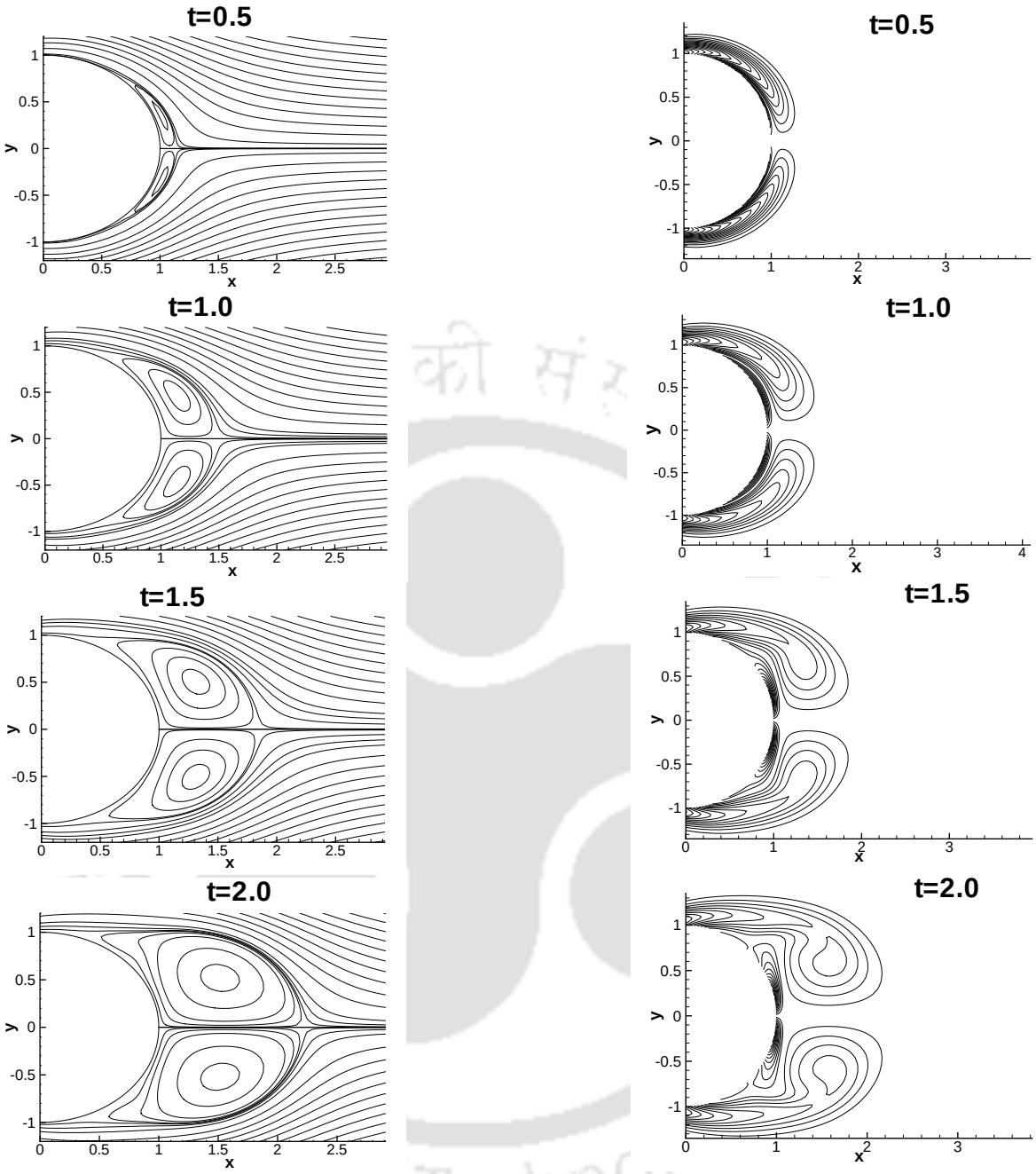

Figure 4.14: *Stream lines and vortcity contours for* $Re = 300$ *at different instants of time.*

secondary eddy (see figure 4.16(b) (top)).

4.7.4 Flows for $Re = 1000$, 3000, 5000 and 9500:

Flow around a cylinder at these Reynolds numbers eventually becomes three-dimensional and turbulent, and we do not intend to cover that regime. We only want to focus on the early stage of the flow development in which the two-dimensional laminar assumption

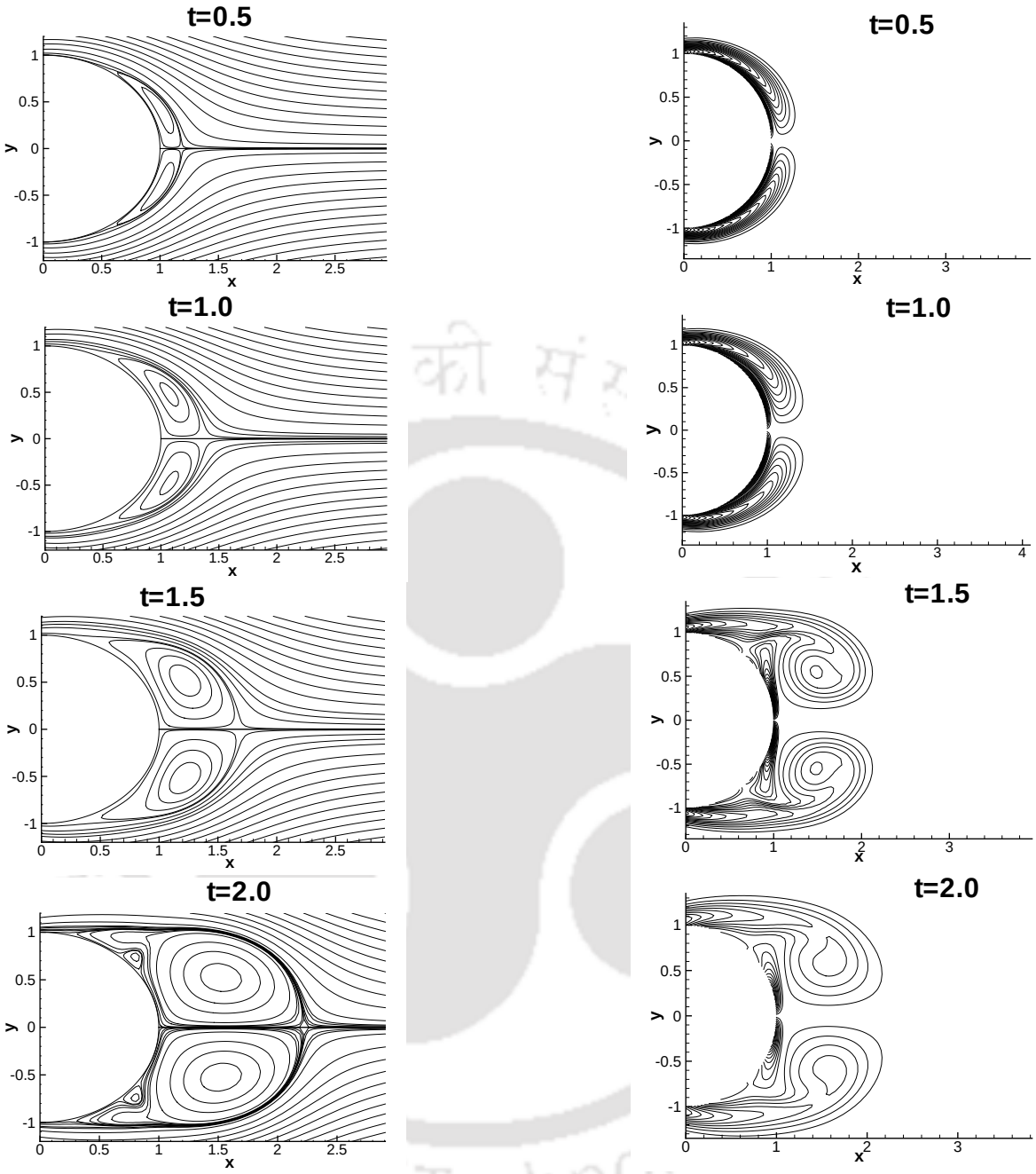

Figure 4.15: *Stream lines and vortcity contours for* $Re = 550$ *at different instants of time.*

has been justified by experiments. Another important feature of this flow range is that, the flow exhibits the so called α- and β-phenomena ([26]).

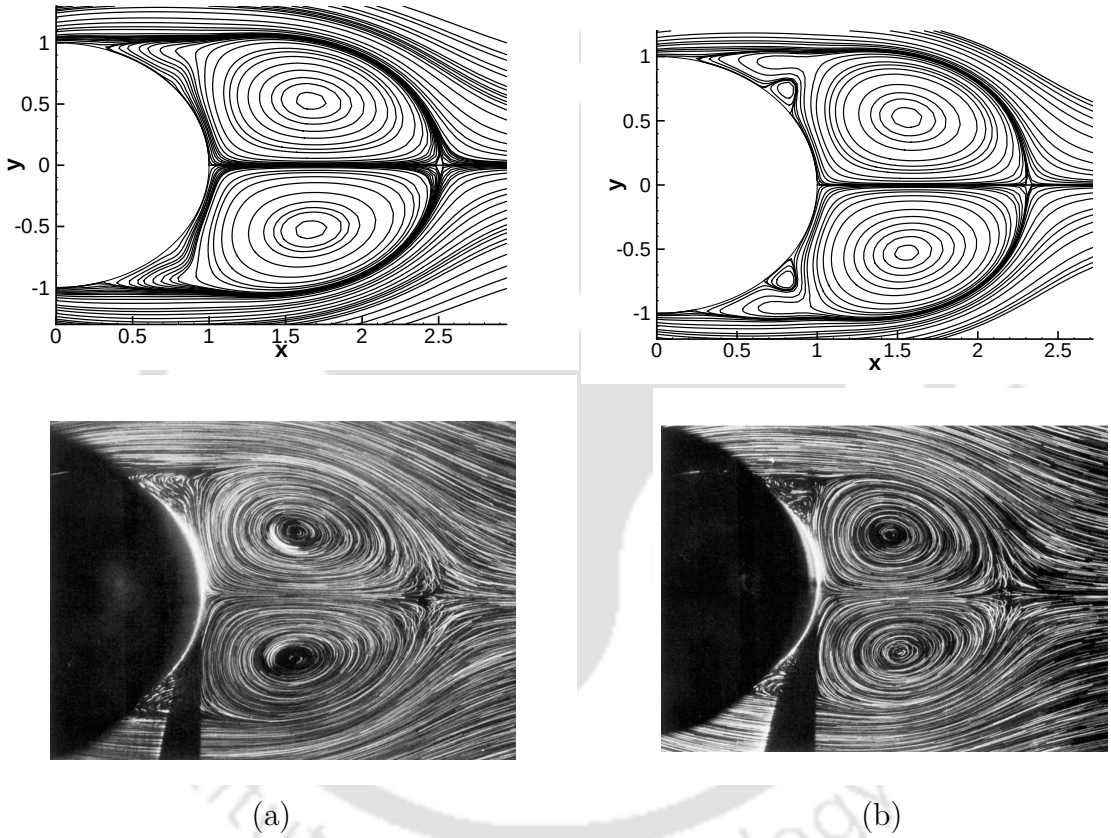

Figure 4.16: *Comparison of streamlines for (a) $Re = 300$ and (b) $Re = 550$, at time $t = 2.5$: (top) numerical; (bottom) Experimental ([26]).*

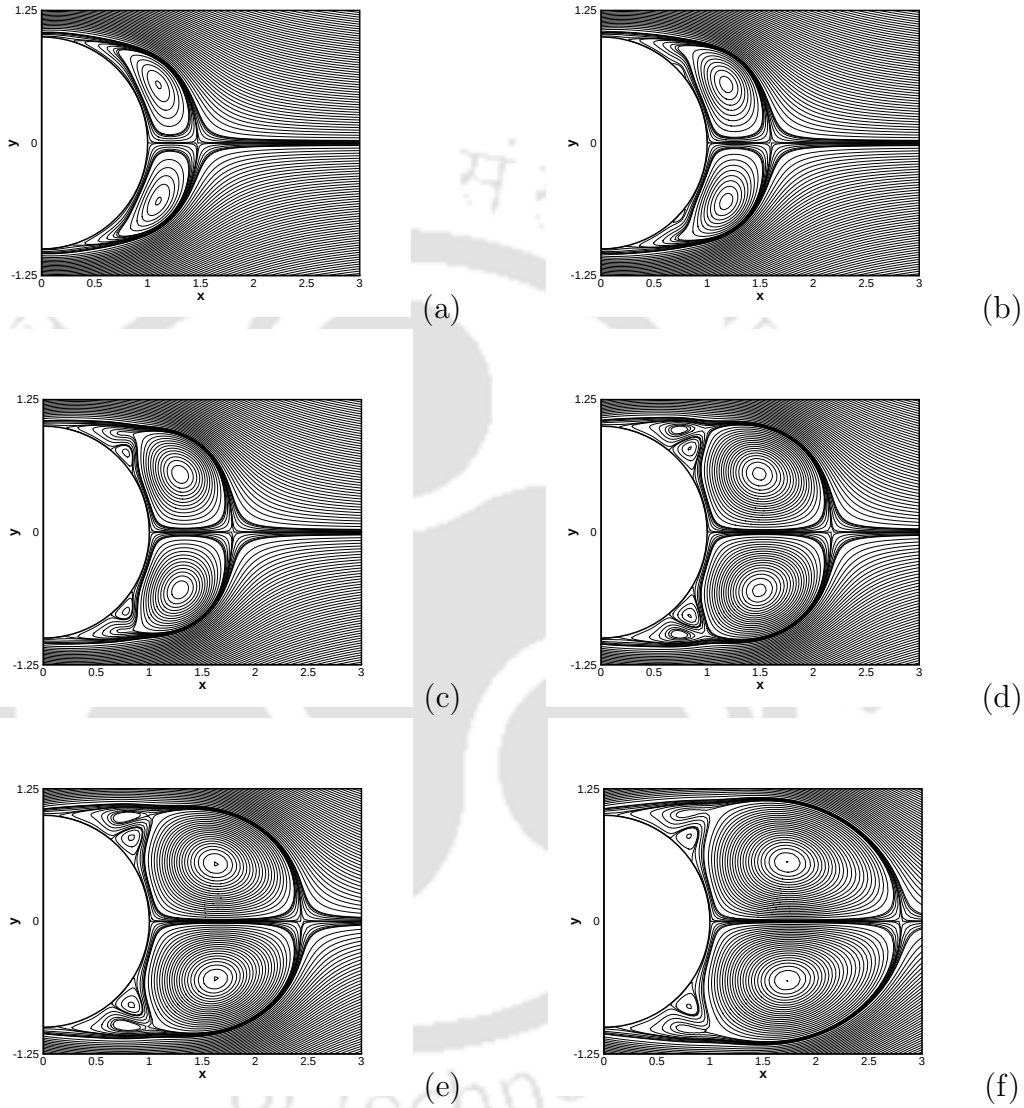

Figure 4.17: *Streamlines for Re=1000 at (a)* $t = 1.25$*, (b)* $t = 1.75$*, (c)* $t = 2.50$*, (d)* $t = 3.50$*, (e)* $t = 4.50$ *and (f)* $t = 6.00$.

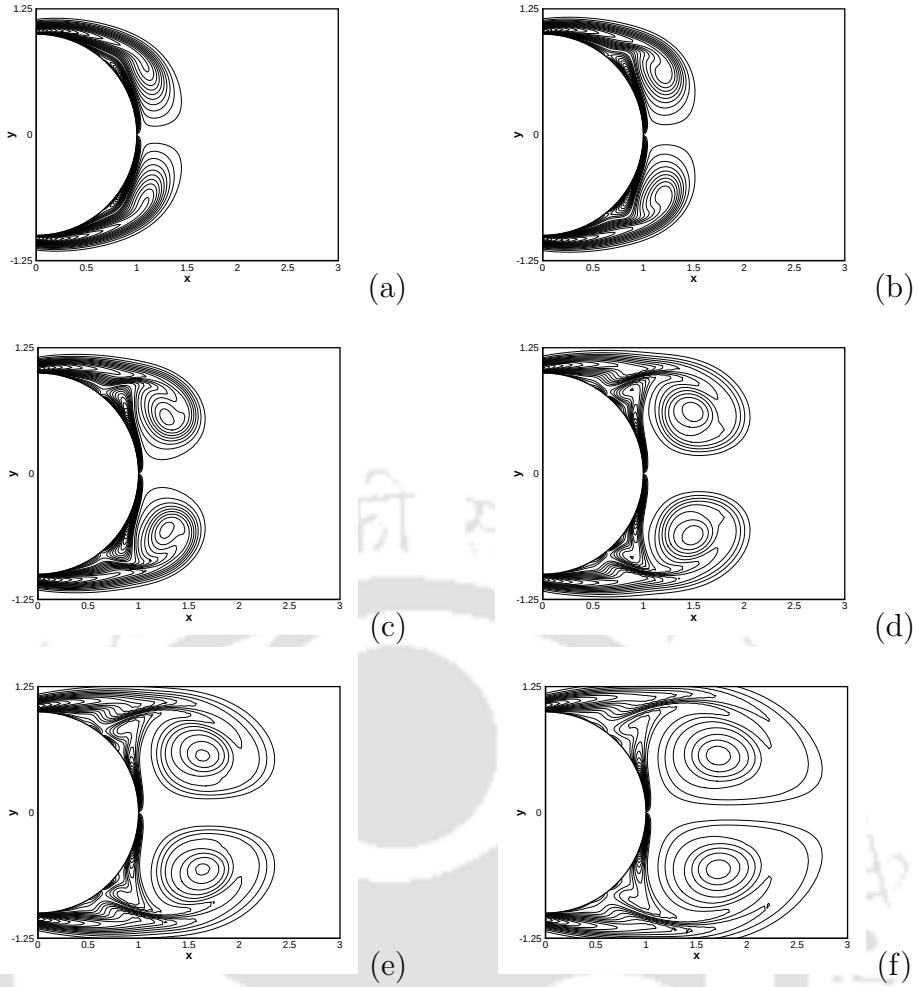

Figure 4.18: *Vorticity contours for Re=1000 at (a) $t = 1.25$, (b) $t = 1.75$, (c) $t = 2.50$, (d) $t = 3.50$, (e) $t = 4.50$ and (f) $t = 6.00$.*

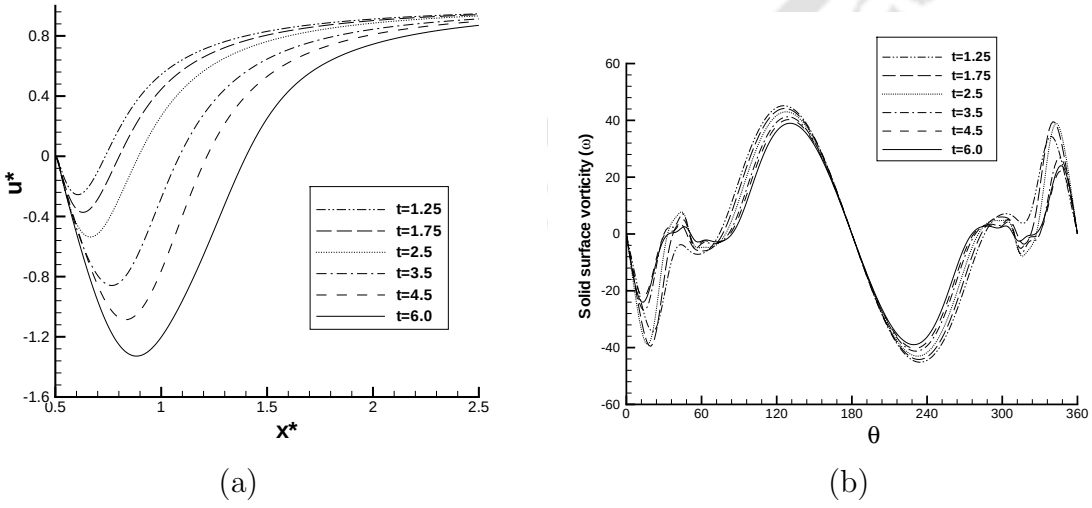

Figure 4.19: *(a) Radial velocity along the axis of flow and (b) Vorticity along the solid surface, for the motion past a circular cylinder for $Re = 1000$ at the earlier stages of the flow.*

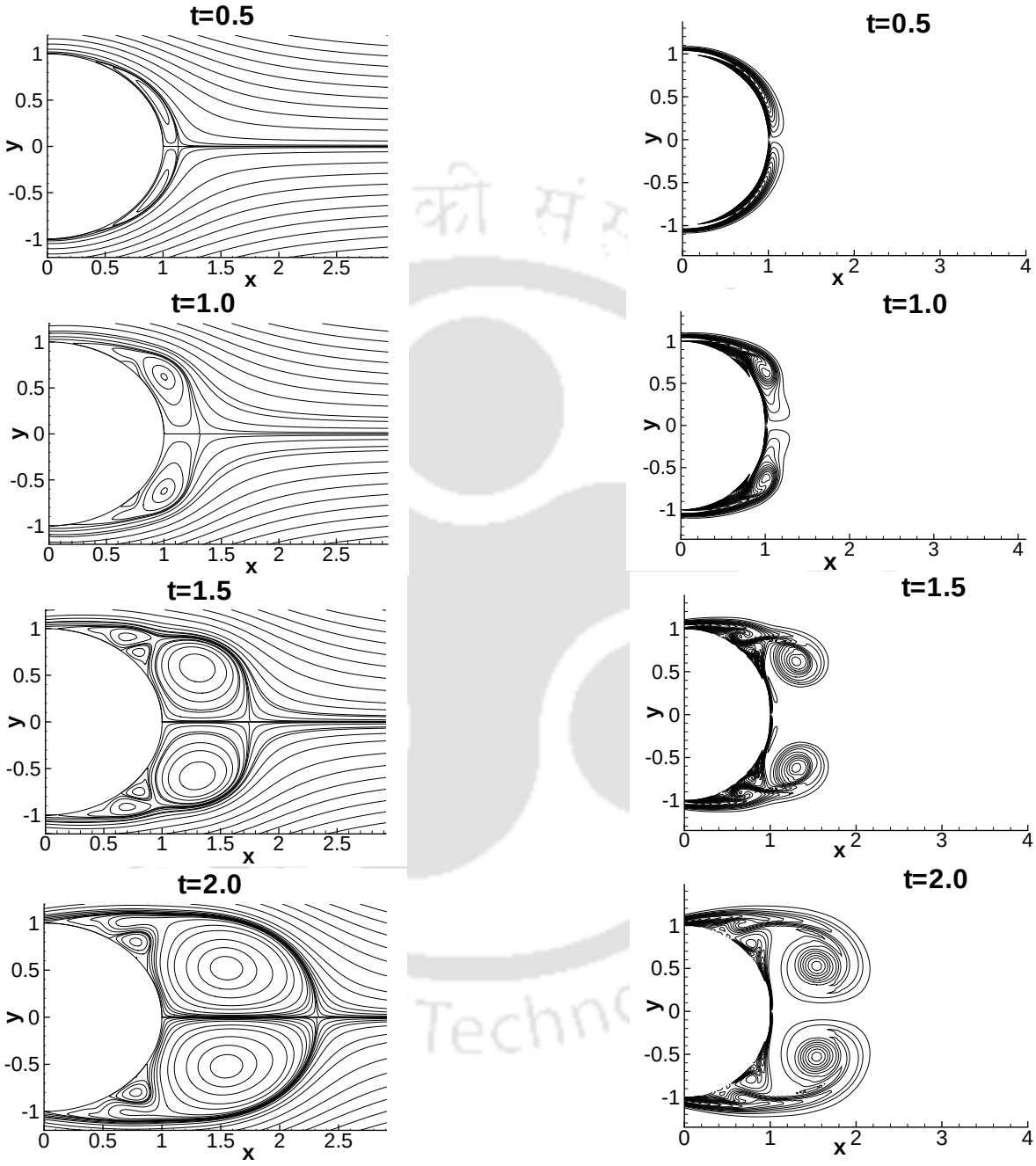

Figure 4.20: *Streamlines (left) and vortcity contours (right) for* $Re = 3000$ *at different instants of time.*

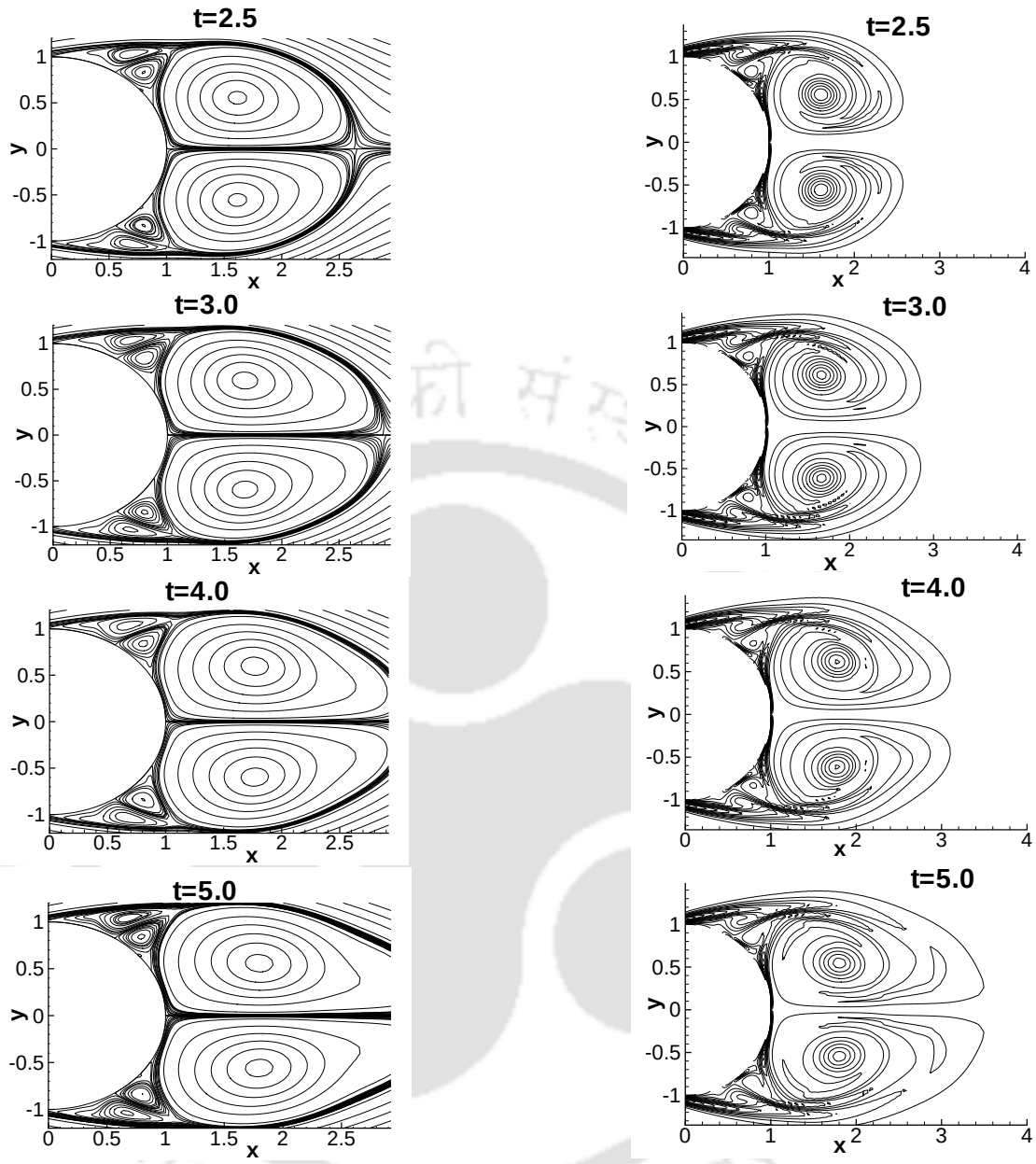

Figure 4.21: *Streamlines (left) and vortcity contours (right) for* $Re = 3000$ *at different instants of time.*

Experimental results [26] suggest that the α-phenomenon is distinctly visible in the range of Reynolds numbers $800 < Re < 5000$. As such, we start with $Re = 1000$ to depict this phenomenon through our numerical results. Figure 4.17(a) shows that at $t = 1.25$, the secondary vortex is yet to appear. Its appearance can be seen at $t = 1.75$ (figure 4.17(b)). When the primary vortex is still stable, the secondary vortex grows enough in size for its exterior boundary to touch the boundary of the main recirculating zone (figures 4.17(c) and (d)). Thus the main eddy is split into two parts and the region in the wake next to the separation point gets isolated and another secondary eddy is

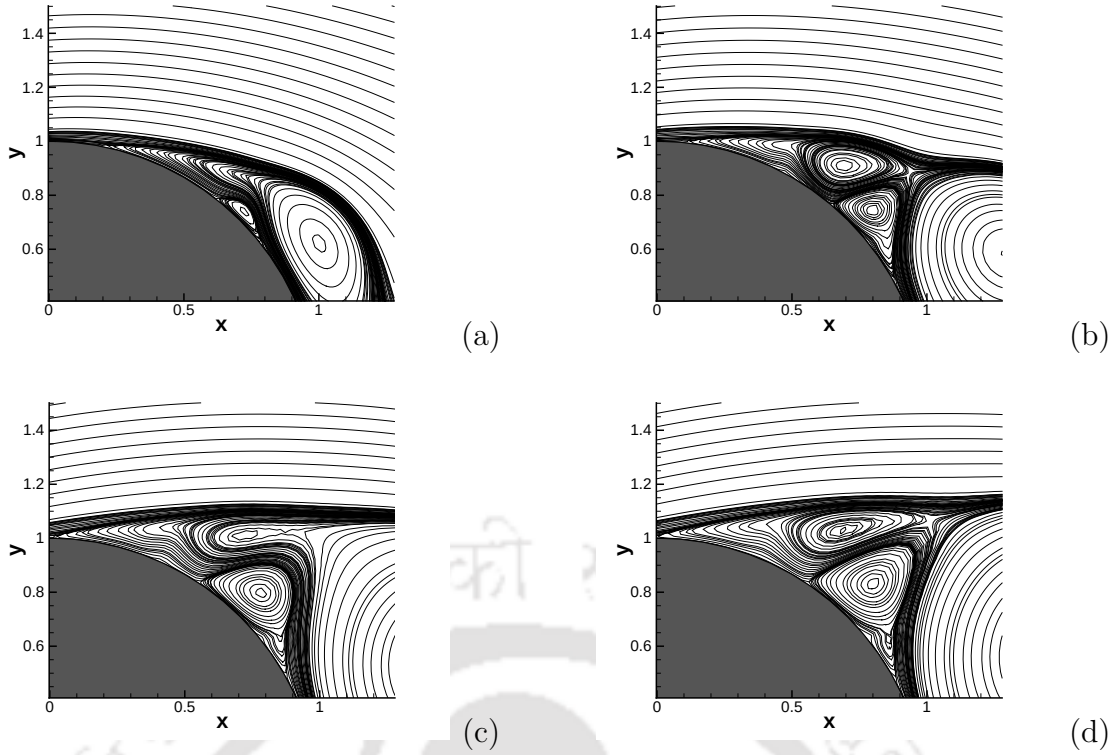

Figure 4.22: *Development of secondary vortices behind the cylinder for Re=3000 at (a)* $t = 1.0$, *(b)* $t = 1.5$, *(c)* $t = 2.0$, *(d)* $t = 2.50$.

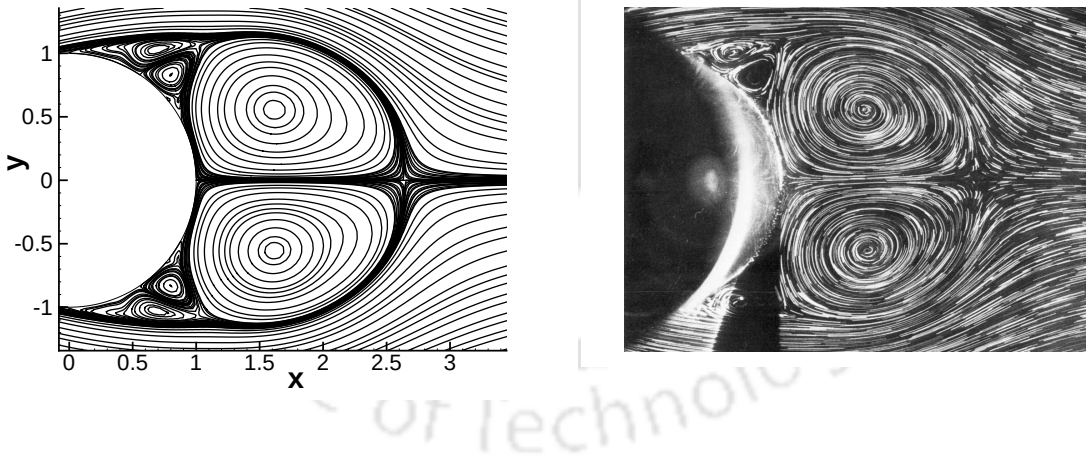

Figure 4.23: *Comparison of streamlines for* $Re = 3000$ *at time* $t = 2.5$*: (a) numerical and (b) Experimental ([26]).*

formed. These two secondary eddies thus formed are equivalent in strength and size and constitute a pair of secondary eddies (figures 4.17(e) and (f)). This is what is known as the α-phenomenon. The corresponding vorticity patterns for this time period are shown in figures 4.18(a) to (f) which are very close to the ones presented in [18, 67, 94, 104]. In figure 4.19(a), we show the distribution of our computed radial velocity values at the initial stages of the flow and in figure 4.19(b), vorticity distribution along the solid

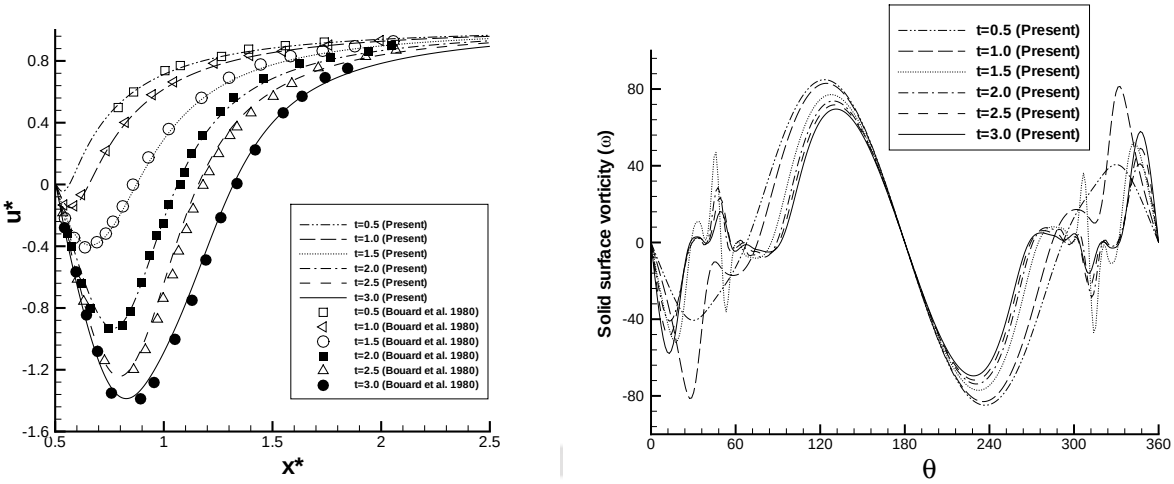

(a) (b)

Figure 4.24: *(a) Radial velocity along the axis of flow and (b) Vorticity along the solid surface, for the motion past a circular cylinder for* $Re = 3000$ *at the earlier stages of the flow.*

surface for the same interval of time for $Re = 1000$. In figures 4.20 and 4.21, we show the temporal evolution of the stream-function and vorticity values side by side for the initial stages of flow for $Re = 3000$ from $t = 0.5$ to $t = 5.0$. This evolution of streamlines along with the close-up of the secondary vortices in the upper part of the cylinder shown in figure 4.22 clearly exhibit the development of α-phenomenon for $Re = 3000$. The comparison of the streamlines captured by our scheme at $t = 2.5$ with the experimental result of reference [26] is shown in figure 4.23. Again the experimental and numerical results are extremely close, thus demonstrating the robustness of our scheme.

The accuracy of our results can also be seen from figure 4.24(a), where we compare the radial velocity values for $Re = 3000$ obtained by our computations at earlier stages of the flow with those of [26]; like the previous comparisons, the graphs demonstrate excellent agreements between the experimental and our numerical results. In figure 4.24(b), we show the corresponding vorticity distribution along the solid surface for the same Reynolds number.

In table 4.5, we present comprehensive data of the parameter values used for the Reynolds numbers considered for computation in the early stages of the flow. Here γ represents the under-relaxation parameter and N_{in} is the upper limit of the number of inner iterations required for the residual to fall below the tolerance limit as described in section 4.6. As can be seen from the table, computational complexity increases with higher Reynolds numbers.

In table 4.6, the effect of the grid size and the far field boundary conditions are

presented for $Re = 9500$ at time $t = 1$. Figure 4.25 compares the streamlines for $R_\infty = 5$ and $R_\infty = 10$ at the same instant on a grid of size 241×401. The table and the figures suggest that the influence of grid size and the domain of computation on the flow structure induces a slight variation. The percentage change in both L and θ_s were 0.8 as R_∞ was increased to 10 from 5.

Figures 4.26 and 4.27 show the comparison of the experimental ([26]) and our computed results for the streamline patterns at time $t = 0.75$ and $t = 1.00$ respectively. In both the cases the match is very close. These two figures represent the so called β-phenomenon: at a very early stage of the flow (at around $t = 0.5$ [26]), a very thin recirculating wake (fitting exactly the cylinder shape) is formed; but soon afterwards at $t = 0.75$ (figure 4.26), the core of this recirculating zone rotates in one piece, much faster compared to the other part of the separated zone, forming a vortex which increases in size and strength with time.

Table 4.5: *Parameter values used for different Reynolds numbers at the initial stage of the computation.*

Re	Δt	R_∞	Grid size	λ		Iterations	
				ω	ψ	ω	ψ
200	0.001	$35 \times R_0$	181×181	0.6	1.0	100	800
	0.005	$60 \times R_0$	281×281	0.4	0.6	150	1000
300	0.001	$35 \times R_0$	181×181	0.6	0.8	350	800
550	0.001	$20 \times R_0$	181×181	0.6	0.8	500	1000
1000	0.005	$20 \times R_0$	241×241	0.6	0.8	1000	1200
3000	0.005	$10 \times R_0$	251×251	0.4	0.6	1500	1700
5000	0.005	$10 \times R_0$	301×301	0.4	0.6	2000	1800
9500	0.01	$5 \times R_0$	401×241	0.18	0.4	3000	2500
	0.01	$10 \times R_0$	401×241	0.1	0.4	3000	2500

Table 4.6: *Effect of far field and grid size on the wake lengths and separation angles for* $Re = 9500$ *at* $t = 1.0$.

Grid Size	R_∞	L	θ_s
201×201	5		
301×301	10	0.1809	75.601
241×401	5	0.1841	72.45
241×401	10	0.1851	73.04

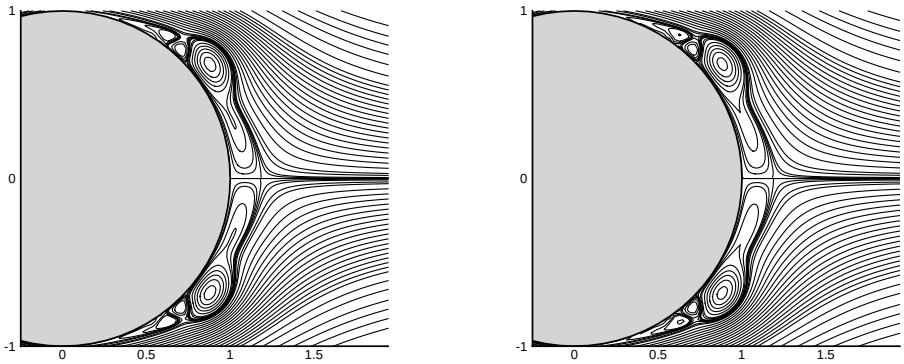

(a) (b)

Figure 4.25: *Far field effect for the motion past a circular cylinder, streamlines for* $Re = 9500$ *at time* $t = 1.00$*: (a)* $R_\infty = 5$*, (b)* $R_\infty = 10$*.*

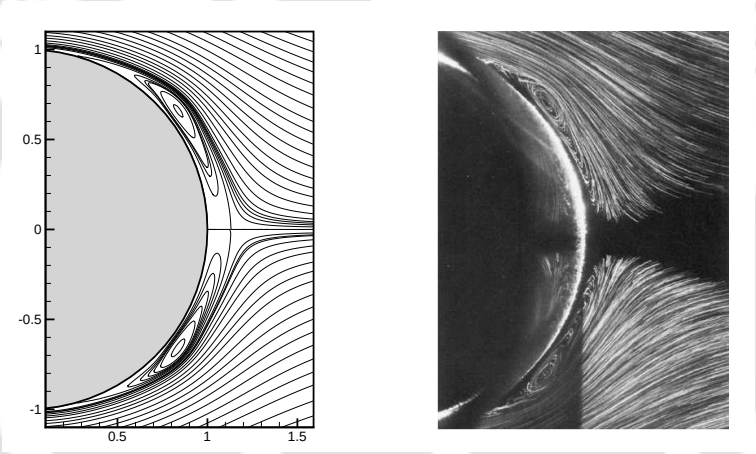

Figure 4.26: *The motion past a circular cylinder, streamlines for* $Re = 9500$ *at time* $t = 0.75$*: (left) Numerical, (right) Experimental ([26]).*

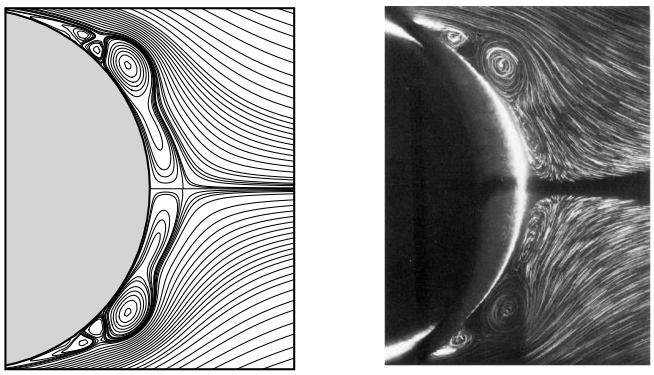

Figure 4.27: *The motion past a circular cylinder, streamlines for* $Re = 9500$ *at time* $t = 1.00$*: (left) Numerical, (right) Experimental ([26]).*

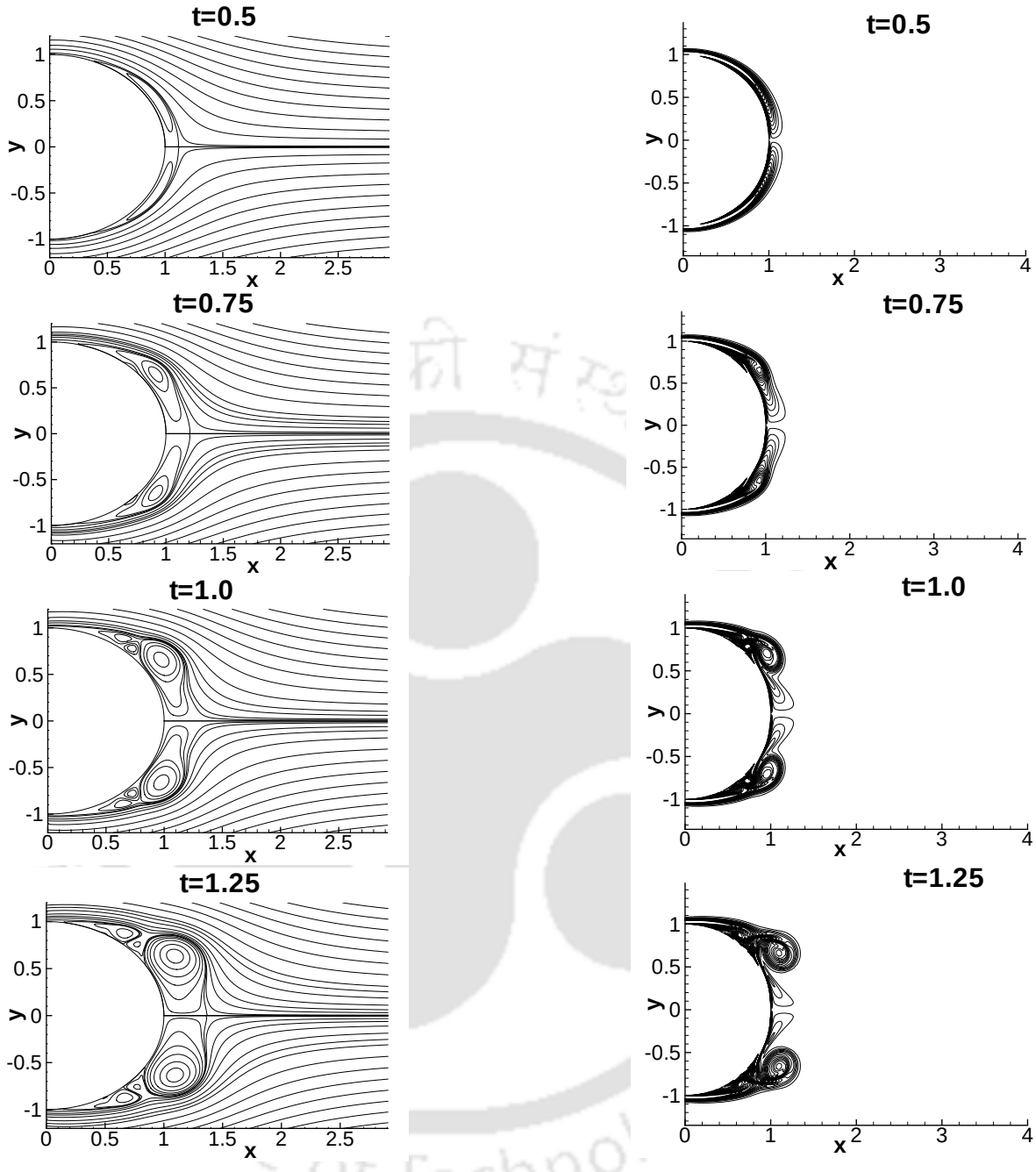

Figure 4.28: *Streamlines (left) and vortcity contours (right) for* $Re = 5000$ *at different instants of time.*

At time $t = 1.00$ (figure 4.27), this vortex separates the initial wake into two parts. The one situated near the point of separation S (as had been detailed in figure 2.7) is occupied by a pair of secondary vortices whose nature is similar to those that had been described for $Re = 1000$ and 3000, but differing in details. Interestingly, while only the β-phenomenon is observed for $Re = 9500$ at the very initial stage of the flow, for $Re = 5000$, both α and β phenomena are observed one after another ([26, 77, 78]). One

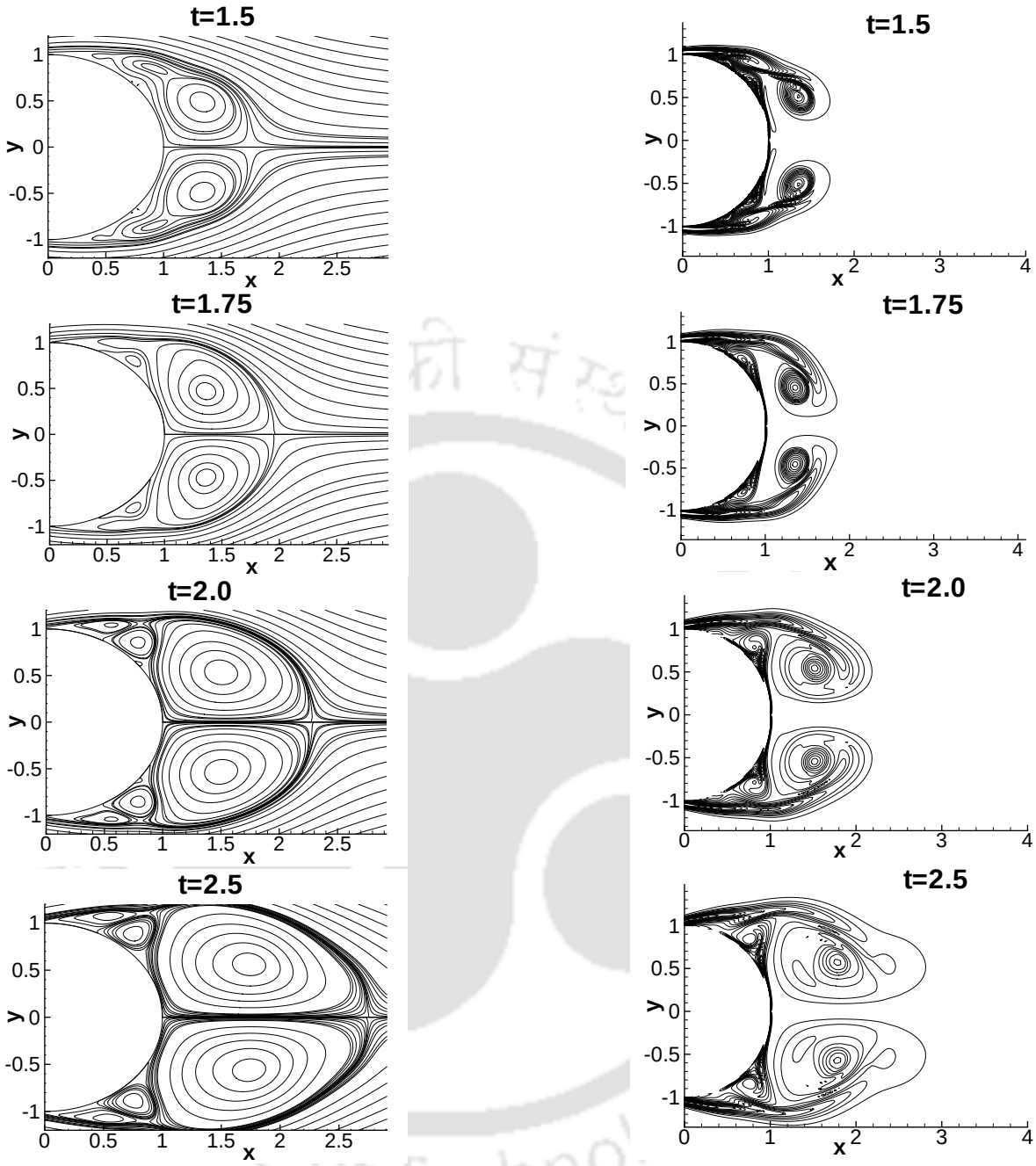

Figure 4.29: *Streamlines (left) and vortcity contours (right) for* $Re = 5000$ *at different instants of time.*

can visualize the evolution of stream-function and vorticity contours for early stages of flow at $Re = 5000$ from our simulations in figures 4.28 and 4.29. From figure 4.28 and the close-up view of the streamlines in figure 4.30, one can observe the β-phenomenon up to $t = 1.25$; after some time, the vortices behind the cylinder starts to change its shape and at around $t = 1.5$ (figures 4.29 and 4.30), the streamlines begin to exhibit the so-called α-phenomenon; we show this phenomenon till $t = 2.5$. Next, we compare side by side,

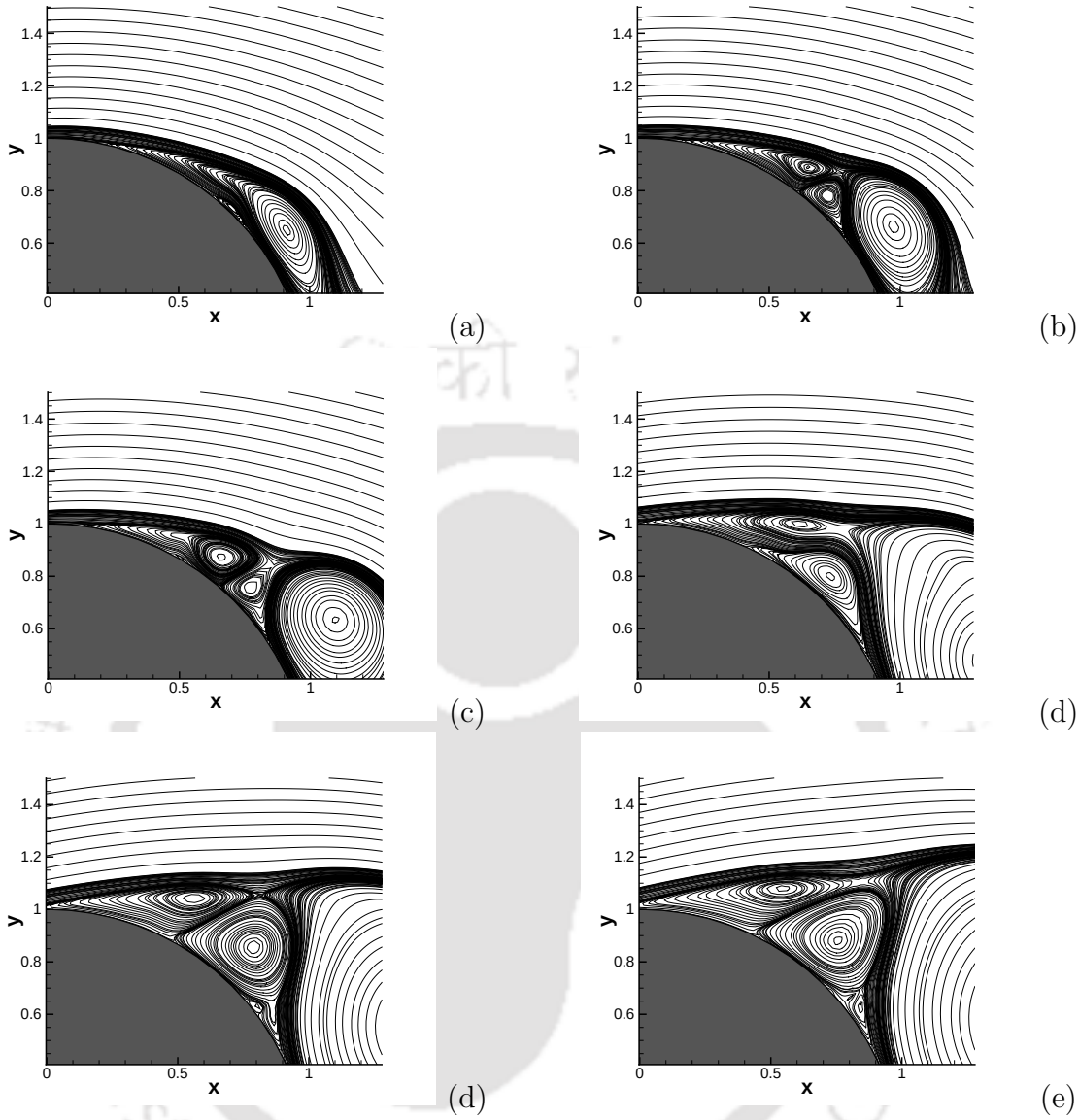

Figure 4.30: *Development of secondary vortices behind the cylinder for Re=5000 at (a)* $t = 0.75$, *(b)* $t = 1.0$, *(c)* $t = 1.25$, *(d)* $t = 1.75$, *(b)* $t = 2.0$, *(c)* $t = 2.5$.

our simulation of this flow at $t = 1.0$ and 1.5 with the experimental results of Bouard and Coutanceau [26] in figure 4.31. In the figures that follow, namely 4.32 and 4.33, we not only compare our numerical simulations at $t = 2.0$ and 2.5 with the experimental results of Bouard and Coutanceau [26], but also with the numerical simulations of [100] and [97] for this Reynolds number. These comparisons clearly show that our numerical results for this Reynolds number are closest to the experimental ones compared to the other two studies cited here.

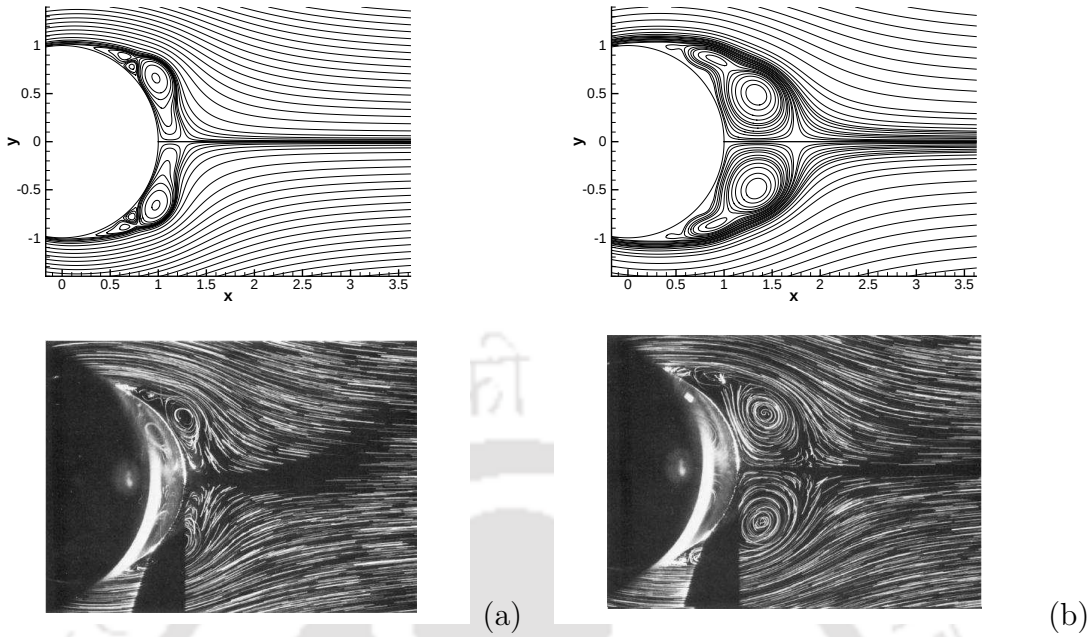

Figure 4.31: *The motion past a circular cylinder, streamlines for* $Re = 5000$ *at time (a)* $t = 1.00$ *and (b)* $t = 1.50$*: (top) Numerical, (bottom) Experimental ([26]).*

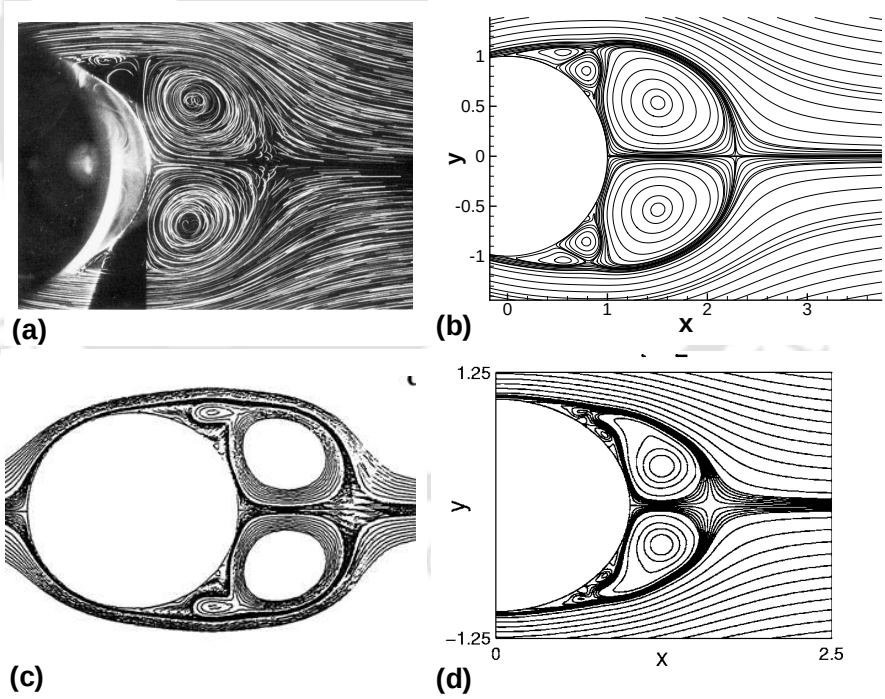

Figure 4.32: *Streamlines comparisons for* $Re = 5000$ *at time* $t = 2.0$*: (a) Experimental ([26]), (b) present, (c) Sengupta and Sengupta ([100]), (d) Sanyasiraju and Manjula ([97]).*

4.8 Conclusion

In this chapter, the scheme developed in Chapter 3 is applied to simulate flows in the classical problem of unsteady incompressible viscous flow past an impulsively started

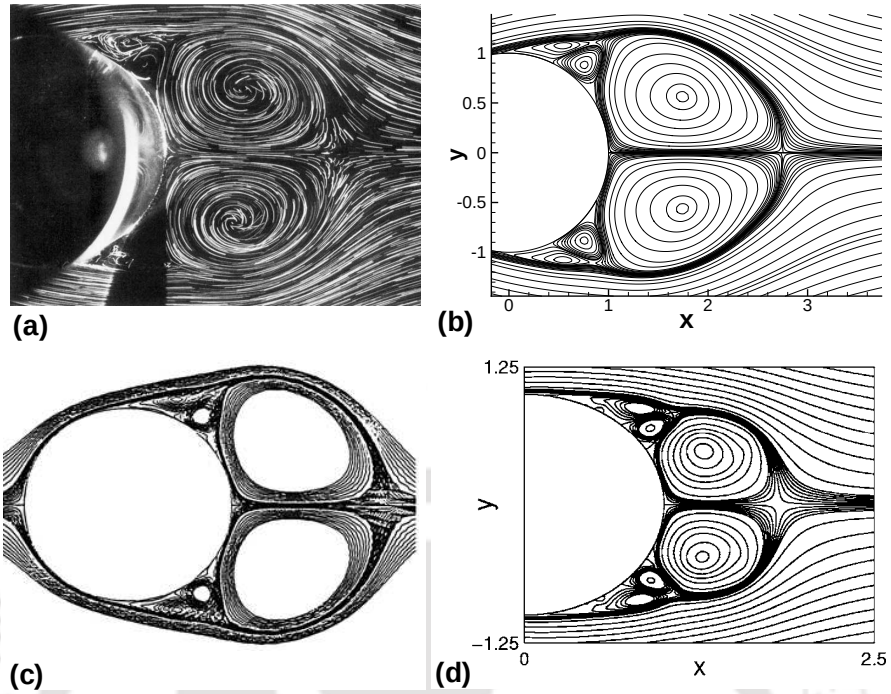

Figure 4.33: *Streamlines comparisons for $Re = 5000$ at time $t = 2.5$: (a) Experimental ([26]), (b) present, (c) Sengupta and Sengupta ([100]), (d) Sanyasiraju and Manjula ([97]).*

cylinder. In the process, we have also developed compact higher order approximations for the Dirchlet boundary conditions for vorticity. We computed the flow for a wide range of Reynolds numbers ranging from 10 to 9500. The flow features which are typical of certain sub-ranges of the Re considered are discussed in details. We compare our results with established experimental and numerical results, and excellent comparison is obtained in all the cases, both qualitatively and quantitatively. The robustness of the scheme is highlighted when it captures the periodic nature of the flow for $Re = 60$ and 200 which is characterized by vortex shedding represented by the von Kármán street and also by the fact that it very accurately captures the so called secondary phenomena for moderate and α and β-phenomena for higher Re. The scheme also very efficiently and accurately captures the flow past a rotating cylinder, which will be discussed in the next chapter. The strength of our scheme is exemplified by the fact that flow simulations from our computations are much closer to the experimental visualization than other existing numerical simulations ([97], [100]) available in the literature, particularly for the higher Reynolds numbers.

भारतीय प्रौद्योगिकी संस्थान गुवाहाटी
Indian Institute of Technology Guwahati

Chapter 5

Simulation of unsteady incompressible viscous flow past a rotating circular cylinder

5.1 Introduction

Flow past a rotating cylinder is a prototypical problem in the study of unsteady flow separation. It is also of considerable practical importance in boundary-layer control on airfoils and related structures. Unlike the flow past a translating circular cylinder where the flow becomes asymmetric only at higher Reynolds numbers and larger time, in the rotating cylinder case, the flow is asymmetric even for small Reynolds numbers as well as for times just after the start due to the impulsive rotation of the body. This asymmetry introduces different complex behaviors in the fluid flow. Because of these reasons, this problem is gradually gaining popularity amongst the computational fluid dynamics community in the last few decades. This is reflected in recent growth in the experimental, theoretical and numerical investigations done on this problem [21, 29, 30, 31, 66, 82, 84, 89, 98].

The study of the flow past a rotating cylinder was first initiated by Prandtl and Tietjens [2, 11, 93] in the middle of the first half of the past century. With the development and growth of computers, the problem gradually became popular amongst the researchers in the second half of the century; experimental works also continued side by side. In 1975, Loc [76] investigated the steady flow past a rotating cylinder for small Reynolds numbers at lower values of the rotational rate α; Ingham in 1983 [57] studied this problem for $Re = 5$, 20 and $0 \leq \alpha \leq 0.5$. Coutanceau and Menard, in 1985 [36], investigated the unsteady flow past a rotating cylinder experimentally for $Re = 200$ and $0.5 \leq \alpha \leq 3.25$. In the same year, Badr and Dennis [19] provided numerical comparisons of the experimental results given by Coutanceau and Menard for $Re = 200$ and $\alpha = 0.5$ and 1.0. In the same paper, they also numerically investigated the flow patterns

for $Re = 500$ with the same α values. In 1989, Badr *et al.* [20] threw some lights on the steady-state limit for this flow. In 1990, Ingham and Tang [58] studied the steady two-dimensional flow past a rotating cylinder for $Re = 5$, 20 and $0 \leq \alpha \leq 3$. In the very next year, they investigated the same for $Re = 60$ and 100 and $0 \leq \alpha \leq 1$. In 1990, Badr *et al.* [21] investigated the unsteady flow past a circular cylinder for $Re = 10^3$ and 10^4, which starts translating and rotating impulsively from rest in a viscous fluid; this study was both theoretical and experimental in the range of α between 0.5 and 3. They found good agreements between numerical and experimental results except for the highest rotational velocity where they observed three-dimensional and turbulence effects.

There are two basic parameters in the problem. Apart from the Reynolds number, another important parameter is the ratio of the peripheral to translation speed which is known as rotational parameter, denoted by $\alpha = \dfrac{\omega_0 R_0}{U_\infty}$, where ω_0 is the angular speed of the cylinder. When $\alpha = 0$, the motion is symmetrical about the direction of translation. When α is non-zero, many important effects which are otherwise absent appear.

The basic interest in this problem is to determine the value of α for a particular Re, beyond which the process of vortex shedding disappears. In other words, the main issue is to investigate whether cylinder rotation can suppress vortex shedding. The vortex shedding and wake development of a two-dimensional viscous incompressible flow generated by a circular cylinder starting its rotation and translation impulsively in a stationary fluid was investigated by Chew *et al.* in 1995 [30] for $Re = 1000$ and $0 \leq \alpha \leq 6$. This was followed by several investigators for various combinations of Re and α, both numerically and experimentally. Some of the most recent numerical and experimental work that may be cited are by Nair *et al.* [84], *Kang et al.* [66], Chou [31], Mittal *et al.* [82], and Padrino and Joseph [89], Sanaysiraju and Manjula [98].

In this chapter, we explore the possibility of extension of the scheme discussed in Chapter 3 to even more complex flows by applying it to capture this unsteady flow past a rotating and translating cylinder for Reynolds numbers $Re = 200,\ 500$ and 1000 for the range of rotational ratios $0.5 \leq \alpha \leq 3.25$ [1]. We not only compute the flow for the early stage of the flow, but also for long enough duration of time to investigate the vortex shedding phenomenon as well. We provide qualitative comparison between our numerical results with the existing theoretical and experimental results in terms of the drag coefficients, vorticity profile on the solid cylinder, the path of the first and second vortex centers, and the radial and tangential velocities for certain combinations of Re and α values. We also compare the simulations of the flow patterns computed by us with the experimental flow visualizations and numerical results that are available in the

[1] Review of parts of this work are in progress in (i) *Journal of Scientific Computing and (ii) Computers and Fluids.*

literature. In all the cases, our numerical results are in excellent agreement with the existing results.

The chapter is arranged in the following way. In section 5.2, we discuss about the governing equations. Section 5.3 deals with the approximation of Boundary Conditions. In section 5.4, we provide detailed discussions on our numerical results and comparisons with existing experimental and numerical results. In the last section we summarize our observations in the conclusions.

5.2 The Governing Equations

The governing equations and boundary conditions for the rotating counterpart of the flow past an impulsively started circular cylinder are the same (equations (4.1)-(4.4)) except on the surface of the cylinder where $r = R_0$, $0 \leq \theta \leq 2\pi$ and the velocities are given by

$$(u(r, \theta, t), v(r, \theta, t)) = (0, \alpha). \tag{5.1}$$

The boundary conditions for ψ on the surface of the cylinder can be derived from those of the velocities in (4.7) and (5.1) as

$$\psi(r, \theta) = 0, \quad \frac{\partial \psi}{\partial r}(r, \theta) = -\alpha. \tag{5.2}$$

The initial conditions and boundary conditions at the far field are same as in the impulsive cylinder case (equations (4.5)-(4.7) and (4.10)).

5.3 Approximation of Boundary Conditions

The numerical implementation of the boundary conditions for u, v and ψ are straightforward. The vorticity ω at the far field is zero. At the solid boundary, making use of equation (4.2) and (5.2), for all θ at $r = R_0$, we have

$$\omega = \frac{\alpha}{R_0} - \frac{\partial^2 \psi}{\partial r^2} \tag{5.3}$$

thereat. In what follows, we obtain a compact approximation of the vorticity on the solid boundary.

Employing a Taylor series expansion about a point on the solid surface and assuming that r_i is the radial distance of the i^{th} point from the surface, we get

$$\alpha = -\left.\frac{\partial \psi}{\partial r}\right|_{0,j} = -\delta_r \psi_{0,j} + \left.\frac{r_1}{2}\frac{\partial^2 \psi}{\partial r^2}\right|_{0,j} + \left.\frac{r_1^2}{6}\frac{\partial^3 \psi}{\partial r^3}\right|_{0,j} + \left.\frac{r_1^3}{24}\frac{\partial^4 \psi}{\partial r^4}\right|_{0,j} + O(r_1^4) \tag{5.4}$$

Using (5.3) in (5.4), we get the fourth order accurate expression

$$\alpha = -\delta_r\psi_{0,j} + \frac{\alpha\ r_1}{2R_0} - \frac{\alpha\ r_1^2}{6R_0^2} + \frac{\alpha\ r_1^3}{12R_0^3} - \left(\frac{r_1\ \omega}{2} + \frac{r_1^2}{6}\frac{\partial\omega}{\partial r} + \frac{r_1^3}{24}\frac{\partial^2\omega}{\partial r^2}\right)\Bigg|_{0,j} + O(r_1^4) \tag{5.5}$$

Making use of the fact that on the solid wall $u = 0,\ \ v = \alpha$, equation (4.1) yields,

$$\frac{\partial^2\omega}{\partial r^2} = Re\frac{\partial\omega}{\partial t} - \frac{1}{R_0}\frac{\partial\omega}{\partial r} - \frac{1}{R_0^2}\frac{\partial^2\omega}{\partial\theta^2} + \frac{\alpha\ Re}{R_0}\frac{\partial\omega}{\partial\theta} \tag{5.6}$$

Using (5.6) in (5.5) and after some simplifications we get,

$$\begin{aligned}\alpha &= -\delta_r\psi_{0,j} - \frac{r_1}{2}\omega_{0,j} + \left(\frac{r_1^3}{24R_0} - \frac{r_1^2}{6}\right)\frac{\partial\omega}{\partial r}\Bigg|_{0,j} - \frac{r_1^3 Re}{24}\frac{\partial\omega}{\partial t}\Bigg|_{0,j} \\ &+ \frac{r_1^3}{24r^2}\frac{\partial^2\omega}{\partial\theta^2}\Bigg|_{0,j} - \frac{r_1^3\ Re\ \alpha}{24R_0}\frac{\partial\omega}{\partial\theta}\Bigg|_{0,j} + \frac{r_1\alpha}{2R_0} - \frac{r_1^2\alpha}{6R_0^2} + \frac{r_1^3\alpha}{12R_0^3}\end{aligned} \tag{5.7}$$

Using forward difference for the temporal derivative and second order one-sided difference for the derivatives along r-direction, we finally get

$$\begin{aligned}\omega_{0,j}^{n+1} &= \frac{24\Delta t}{r_1^3\ Re}\left[\left\{\frac{r_1^3\ Re}{24\Delta t} - \frac{r_1}{2} - \left(\frac{r_1^3}{24R_0} - \frac{r_1^2}{6}\right)\left(\frac{(r_2-R_0)^2 - r_1^2}{r_1(r_2-R_0)(r_2-r_1)}\right)\right.\right. \\ &- \left.\left.\frac{r_1^3}{12R_0^2(\Delta\theta)^2}\right\}\omega_{0,j}^n + \left(\frac{r_1^3\ Re\ \alpha}{48R_0\Delta\theta} + \frac{r_1^3}{24R_0^2(\Delta\theta)^2}\right)\omega_{0,j-1}^n \right. \\ &+ \left(\frac{r_1^3}{24R_0^2\theta_1\Delta\theta} - \frac{r_1^3\ Re\ \alpha}{48R_0\Delta\theta}\right)\omega_{0,j+1}^n + \left(\frac{r_1^3}{24R_0} - \frac{r_1^2}{6}\right)\left(\frac{(r_2-R_0)^2\omega_{1,j}^n - r_1^2\omega_{2,j}^n}{r_1(r_2-R_0)(r_2-r_1)}\right) \\ &+ \left.\left(\frac{r_1}{2R_0} - 1\right)\alpha - \frac{r_1^2\alpha}{6R_0^2} + \frac{r_1^3\alpha}{12R_0^3}\right].\end{aligned} \tag{5.8}$$

Here Δt is the uniform temporal step length and $\Delta\theta$ is the uniform spatial step length along the θ-direction.

NOTE: Three parameters used in the computation are of utmost importance for obtaining accurate numerical solution of this flow. The first one is the Reynolds number Re, the second parameter is the non dimensional angular rectilinear speed α and most importantly, the non-dimensional time scale $t = U_\infty t^*/R_0$, with t^* being the actual time. From the computational point of view, this third parameter plays a vital role in the exact time matching of the numerical results with the existing experimental ones. The convergence criteria used to solve the matrix equation resulting from the discretization of the governing equations and the successive under-relaxation parameter used for the inner iterations are different for different numerical schemes. This invariably leads to a constant time-lagging between the numerical and the experimental solutions ([104]). Therefore, one must re-scale the numerical time, particularly for higher Reynolds numbers. In this chapter, we adopt the same time scale that was used by Badr and Dennis (1985) [19]; our dimensionless time is two times the ones used by Coutanceau and Menard (1985) [36].

5.4 Results and Discussion

We employ the HOC scheme developed in Chapter 3 to simulate the flow past a rotating and translating circular cylinders for Reynolds number 200, 500 and 1000, and for rotational parameter α ranging from 0.5 to 3.25. The combinations of Re and α values are chosen in such a way that enough experimental and numerical results exist in the available literature for comparing our results. We present detailed comparison of our results, both qualitatively and quantitatively with the existing experimental and numerical results and excellent comparison is obtained in all the cases. For $Re = 200$, a 181×181 grid is used and far field is fixed at a distance 35 times the radius of the cylinder; the time increment Δt is fixed as 0.001. For $Re = 500$ and 1000, the grid size, Δt and R_∞ are fixed as 181×181, 0.001, 20 and 256×256, 0.005, 20 respectively. The procedure for solving the system of algebraic equations arising out of discretization of the governing equations are the same as that of the impulsively started circular cylinder (section 4.6) except for the fact that we use 1.0×10^{-5} as a tolerance limit for the inner BiCGSTab(2) iterations.

5.4.1 Flow at $Re = 200$

In this section we will make observations and detailed discussions on the effect of increasing rotational parameter α on the flow for $Re = 200$ so that insightful comments can be made on the flow for subsequent higher Reynolds numbers, namely 500 and 1000.

5.4.1.1 $Re = 200$ and $\alpha = 0.5$

We start with the case $\alpha = 0.5$; soon after the impulsive start of the motion, at time $t = 1$ (figure 5.1(a)), the first vortex starts to grow behind the cylinder above axis of flow (the positive x-axis). After a while, a second vortex forms (at around $t = 2$, shown in figure 5.1(b)) below the x-axis. During the next few instants of time, the second vortex slowly moves up and grows in size while the first vortex begins to detach from the cylinder surface and moves downstream (figures 5.1(c) and 5.1(e)). Figure 5.1(c) is our computed result at $t = 4$, which agrees very well with the corresponding experimental result (figure 5.1(d)) of Coutanceau and Menard ([36]). At around $t = 7$, the first vortex totally opens up and sheds into the downstream and the second vortex begins to detach from the cylinder surface (figure 5.1(f)). At the same time, a pair of tertiary vortices start to form above and below the axis of flow. As time progresses, these tertiary vortices grow in size and the secondary vortex slowly opens up and sheds into the downstream (figures 5.2(g) and 5.2(i)). After some times, the tertiary vortex below the x-axis moves toward the other tertiary vortex; they come closer and closer and coalesce with each other at around $t = 12$ (figure 5.2(k)). Identical flow patterns

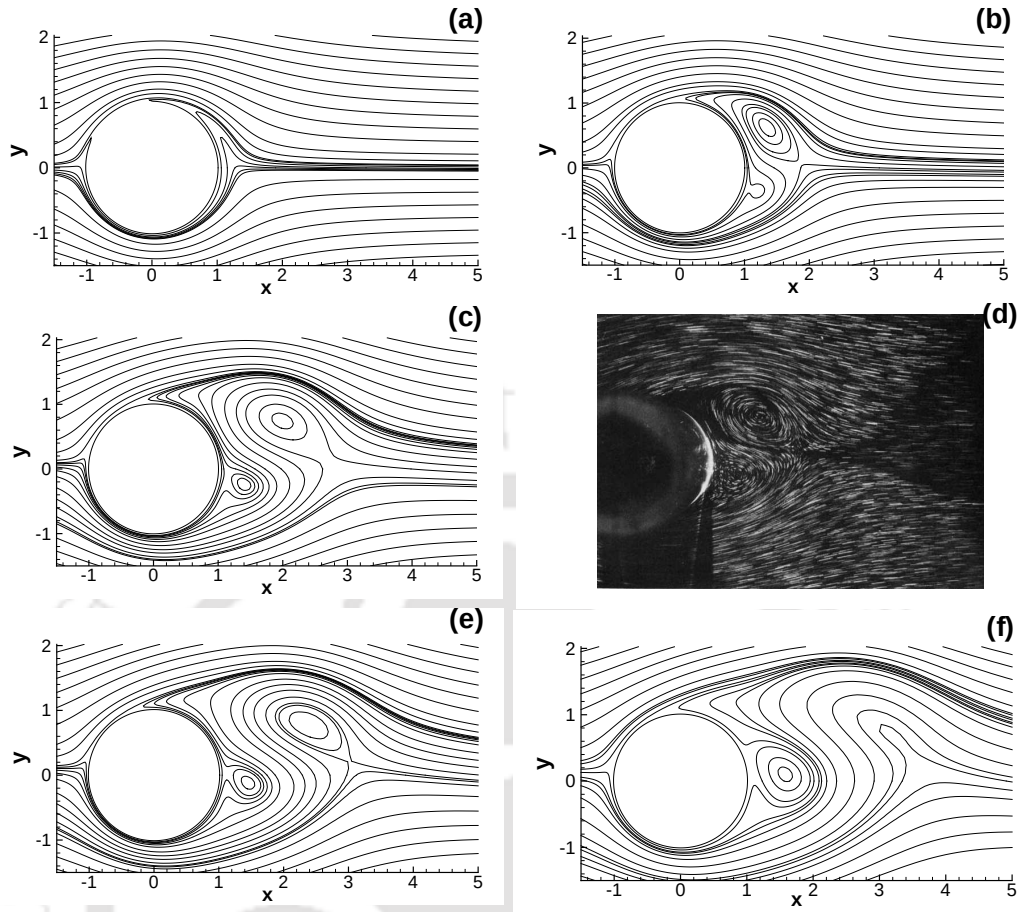

Figure 5.1: *Instantaneous streamlines for* $Re = 200$, $\alpha = 0.5$ *at various times. (a) t=1.0, (b) t=2.0, (c) t=4.0, (d) t=4.0 ([36]), (e) t=5.0, (f) t=7.0.*

can be seen from the experimental visualizations (figures 5.2(h), 5.2(j), and 5.2(l)) of Coutanceau and Menard ([36]). This common vortex then starts to grow with time and starts to move into the downstream (figure 5.3(m)). Around this time, a new vortex forms on the cylinder wall below the axis of flow. It starts to move upwards increasing in size and slowly gets detached from the cylinder wall as time progress (figures 5.3(m) and 5.3(n)). At around $t = 18$, another pair of vortices begin to form above and below the x-axis (figure 5.3(n)) like the ones observed at time $t = 7$. The same flow pattern between $t = 7$ and $t = 12$ gets repeated for a while and the two vortices club into a single vortex and grows bigger and bigger and shed into the downstream with time (figures 5.3(o) to 5.3(r)). Our computations in the time interval $0 \leq t \leq 24$ are in excellent agreement with the experimental works of Coutanceau and Menard [36] for $1 \leq t \leq 13$ and the computed results of Badr and Dennis [19] for $1 \leq t \leq 12$, Chen *et. al.* [29] for $0 \leq t \leq 24$ and Sanyasiraju and Manjula [98] for $0 \leq t \leq 23$.

Figure 5.4 shows the evolution of vorticity contours (the dotted and solid lines respectively depict negative and positive vorticity contours) for the same Re-α combination.

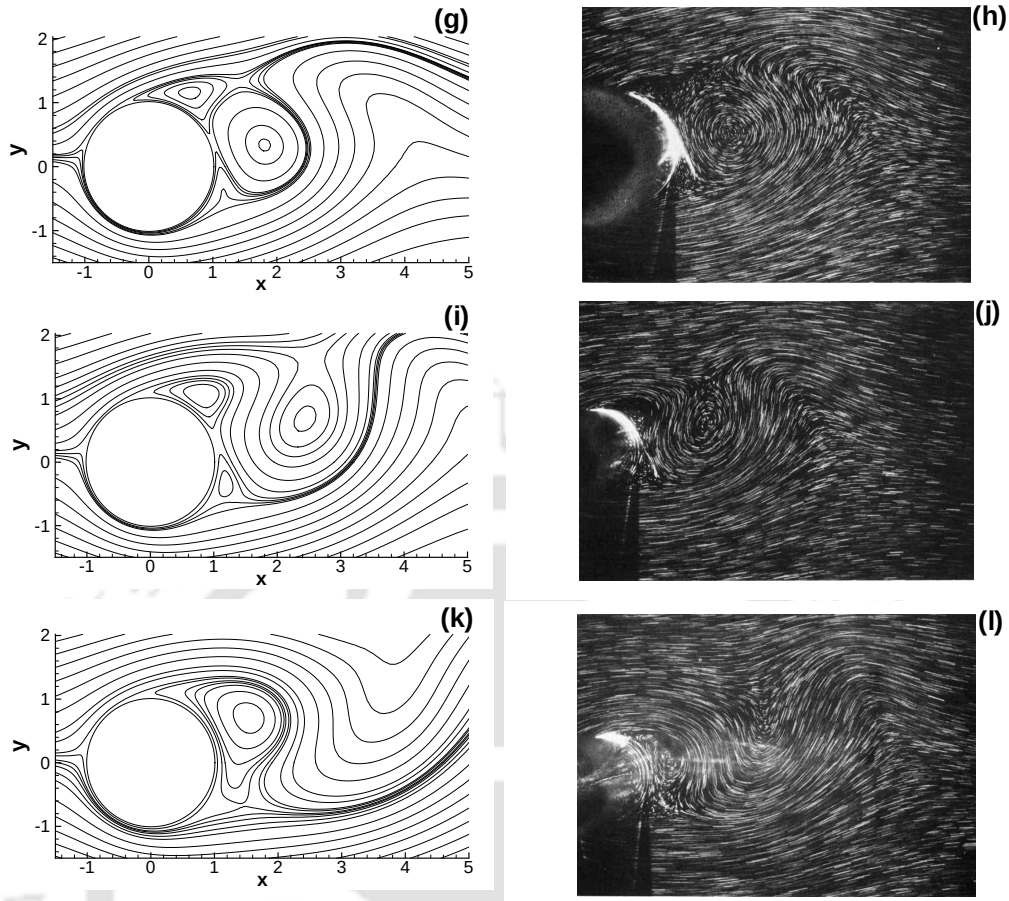

Figure 5.2: *Instantaneous streamlines for* $Re = 200$, $\alpha = 0.5$ *at various times. (g) t=8.0, (h) t=8.0 ([36]), (i) t=10.0, (j) t=10.0 ([36]), (k) t=12.0, (l) t=12.0 ([36]).*

Here one can see the difference between the flow patterns for the rotating and non-rotating ($\alpha = 0.0$) cases. As rotation of the cylinder divides the cylinder surface into upstream ($0 < \theta < \pi$) and downstream ($\pi < \theta < 2\pi$) moving parts, the symmetry associated with a T-periodic flow given by

$$\omega(r, \theta, t) = -\omega(r, -\theta, t - t_0)$$

(where $0 < t_0 < T$ is a phase difference) is lost ([29]). For this lower value of α, the shedding of vortices of opposite rotational direction is connected with the contraction and detachment of the stretched out vorticity contours emanating from opposite sides of the cylinder. This is similar to the purely non-rotational case of $\alpha = 0.0$. As is observed for $\alpha = 0.0$, vortices of different orientation lie on the opposite sides of the so called von Kármán street; however the midline of the street, instead of being parallel to the axis of translation, is now shifted upwards due to rotation.

We also make further quantitative comparisons for the velocity profiles in several locations. Figures 5.5(a) and 5.5(b) show the time development of the u and v ve-

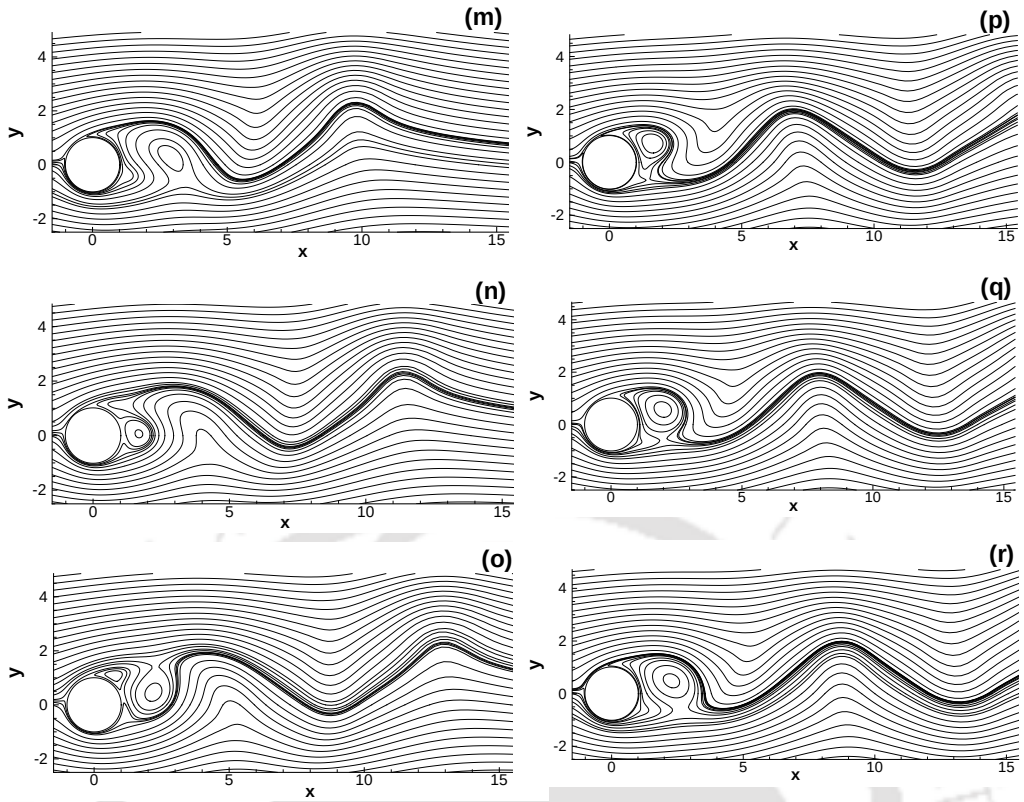

Figure 5.3: *Instantaneous streamlines for* $Re = 200$, $\alpha = 0.5$ *at various times. (m) t=15.0, (n) t=18.0, (o) t=20.0, (p) t=22.0, (q) t=23.0, (r) t=24.0.*

locity profiles along $\theta = 0$ line and their comparisons with the experimental results of Coutanceau and Menard ([36]). In figure 5.6(a), we show the time development of the u velocity profile on the line $\theta = 90^0$ and its comparison with the corresponding experimental results of [36]. Here u^*, v^*, x^*, y^* are the same dimensionless variables defined in [36]. In all the cases we get excellent agreements between our computed and the experimental results. In figure 5.6(b), we show the vorticity values on the cylinder surface at different time levels. It is obvious from the figure that the variation in the separated region where the cylinder is moving upstream ($0 < \theta < 40^o$) is different from the variation in the downstream direction ($320^o < \theta < 360^o$).

5.4.1.2 $Re = 200$ and $\alpha = 1.0$

To observe the effect of the increment in the rotation parameter on the flow structure, we then compute the flow for $\alpha = 1$. There is a noticeable change in the vortex formation below the x-axis. While the second vortex (below the positive x-axis) for $\alpha = 0.5$ was observed at around $t = 2$, here it makes its appearance (much above the positive x-axis) only at around $t = 6$ (figure 5.7(f)). Before that, the first vortex starts to form much above the x-axis (figure 5.7(a)) and continues to grow in size and simultaneously moves

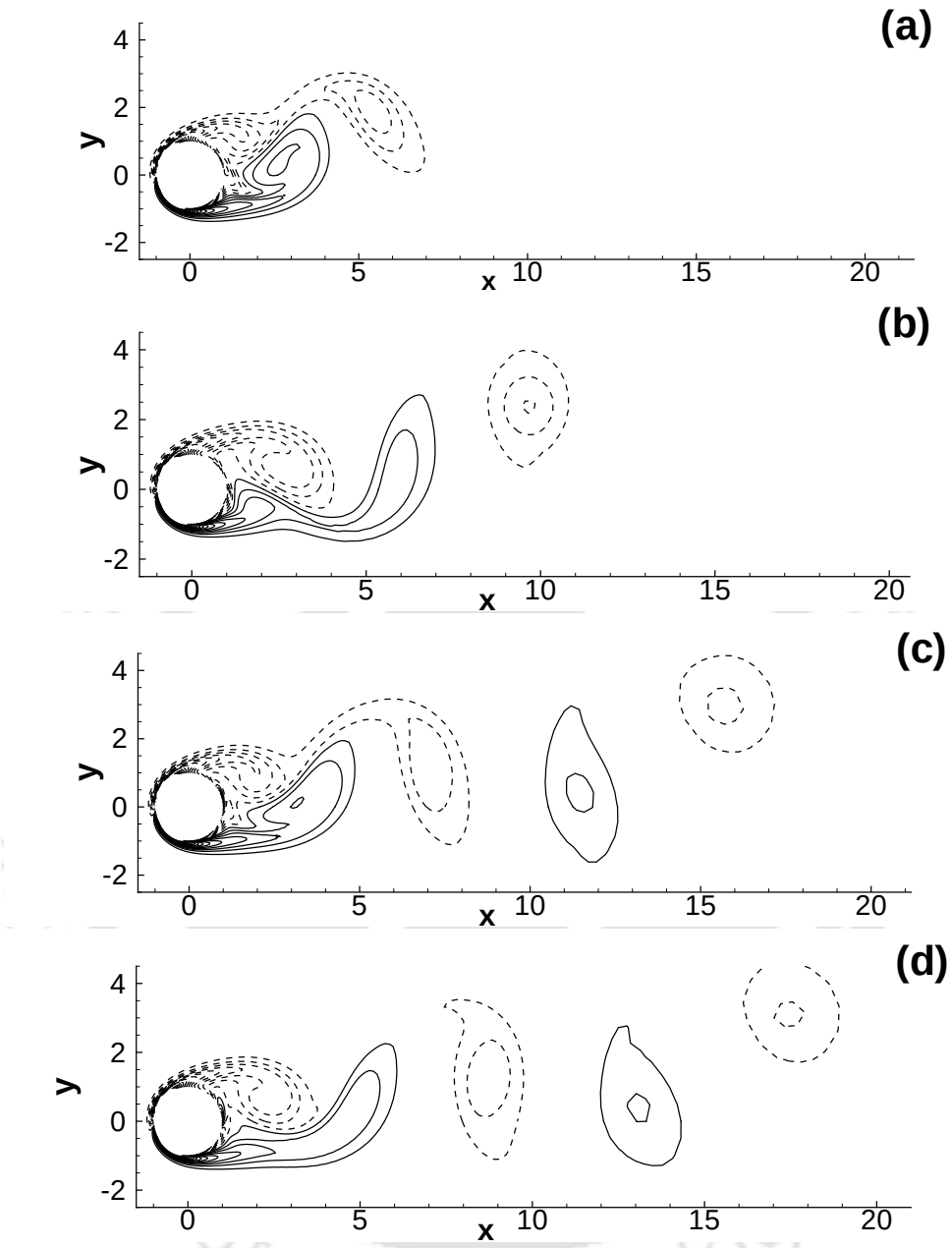

Figure 5.4: *Vorticity contours for* $Re = 200$ *and* $\alpha = 0.5$ *at (a) t=12.0, (b) t=15.0, (c) t=22.0, (d) t=24.0.*

towards the downstream till $t = 5$ (figures 5.7(b), 5.7(c) and 5.7(e)). Figure 5.7(c) is our computed result at $t = 4$, which again agrees very well with the experimental result (figures 5.7(d)) of Coutanceau and Menard ([36]). At around $t = 6$, a small secondary vortex starts forming at angle 70 degrees from the positive x-axis. Immediately after that, at time t=6.5 another vortex forms just below the secondary vortex, but much above the positive x-axis ([98]). After a while, this third vortex having detached from the cylinder, starts opening up and moves towards the downstream. During this time, the

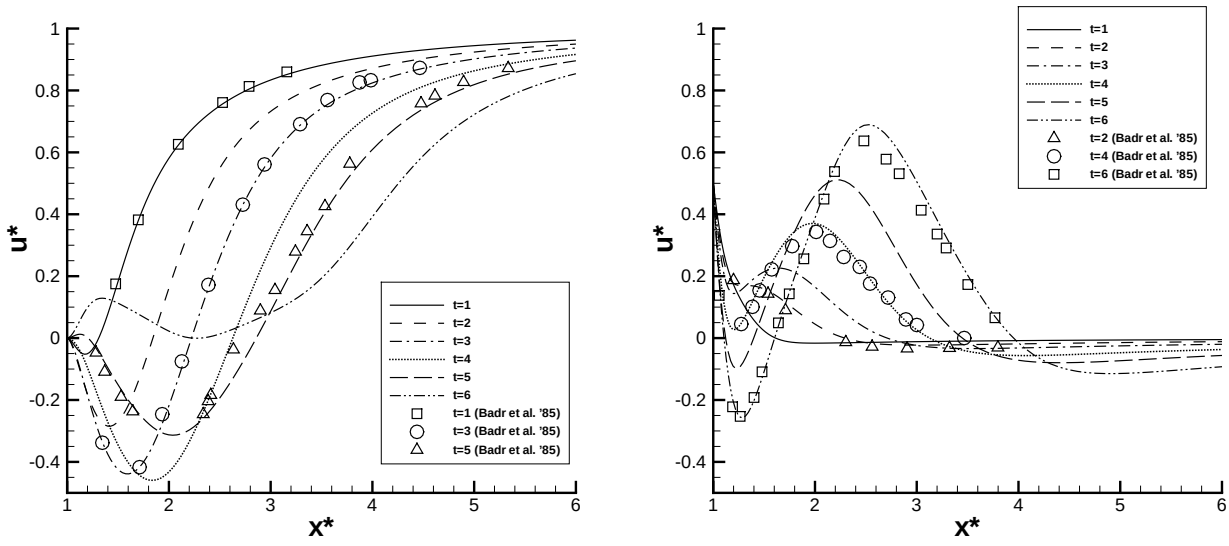

(a) (b)

Figure 5.5: *Time development of velocity profiles and comparison with the experimental results of [36] for* $Re = 200$, $\alpha = 0.5$. *(a) u-velocity on* $\theta = 0$, *(b) v-velocity on* $\theta = 0$.

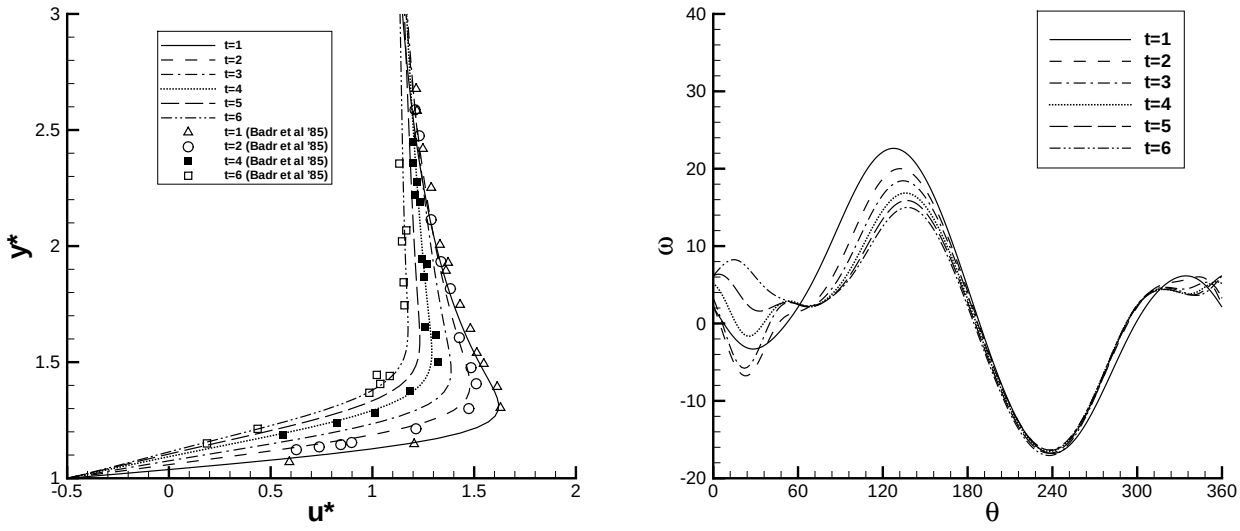

(a) (b)

Figure 5.6: *(a)The time development of the u-velocity and with the experimental results of [36] on* $\theta = 90^0$ *and (b) computed results for solid surface vorticity for the same time levels, for* $Re = 200$, $\alpha = 0.5$.

second vortex grows in size without changing its position (figures 5.8(g), 5.8(i), 5.8(k)). We present the corresponding experimental results at the same instants of time side by

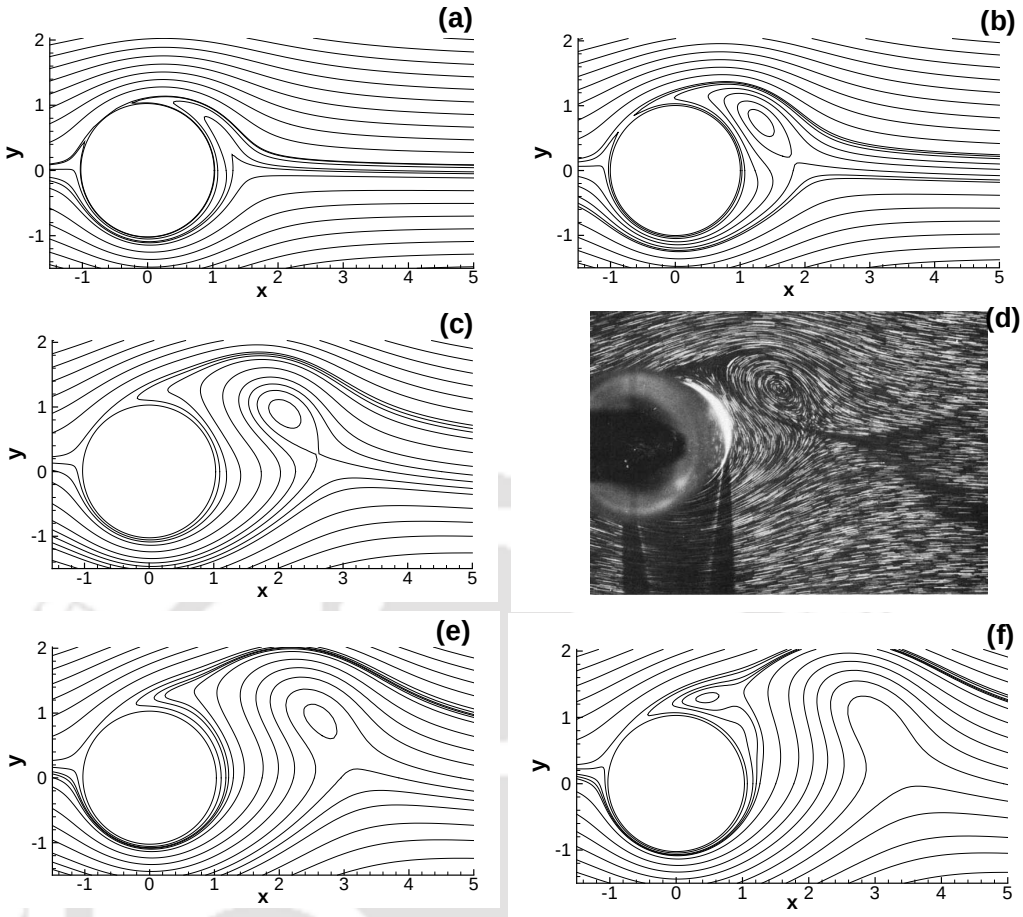

Figure 5.7: *Instantaneous streamlines for* $Re = 200$, $\alpha = 1.0$ *at various times. (a) t=1.0, (b) t=2.0, (c) t=4.0, (d) t=4.0 ([36]), (e) t=5.0, (f) t=6.0.*

side these figures (figures 5.8(h), 5.8(j), 5.8(l)) and excellent match is obtained here as well. At around $t = 11$, the second vortex also starts to detach from the cylinder surface and gradually opens up and moves towards the downstream (figure 5.9 (m), 5.9(n), 5.9(o)). Meanwhile, at around $t = 13$, the fourth vortex stars to form just below the positive x-axis (figures 5.9(n)). As time progresses, this new vortex gradually increase in size and moves upward (figures 5.9(o)). At around $t = 17$, a pair of vortex appear on the cylinder surface just above and below the fourth vortex (figure 5.9(p)). During the next few instants, these pair of vortices increase in size, come closer and closer and coalesce with each other to form a single vortex (figures 5.9(q) and 5.9(r)) while the fourth vortex opens up and sheds into the downstream. The present computations performed for the time interval $0 \leq t \leq 24$ again show excellent agreements with the experimental works of [36] for $1 \leq t \leq 13$ and the computed results of [19] for $1 \leq t \leq 12$, [29] for $0 \leq t \leq 24$ and [98] for $0 \leq t \leq 23$.

In figure 5.10, we show the time evolution of vorticity contours depicting a periodic nature as in the case of $\alpha = 0.5$. However, the midline of the vortex street moves further

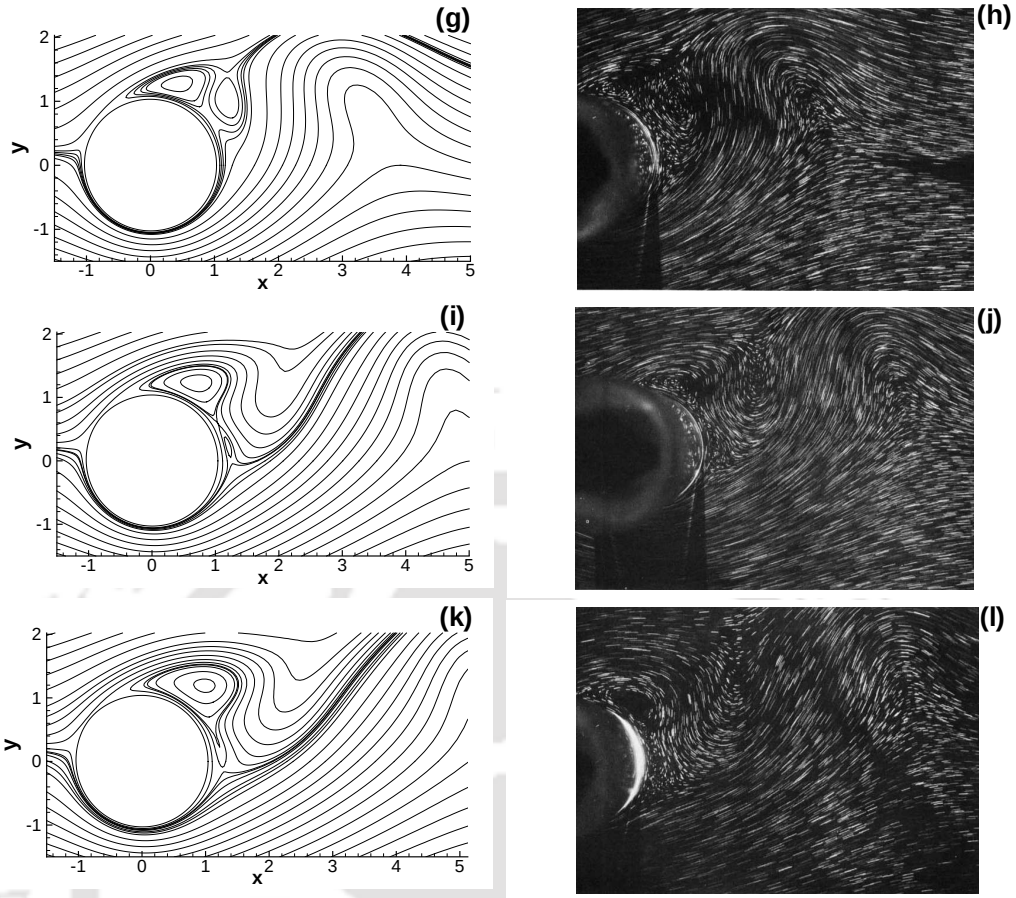

Figure 5.8: *Instantaneous streamlines for* $Re = 200$, $\alpha = 1.0$ *at various times. (g) t=6.5, (h) t=6.5 ([36]), (i) t=8.0, (j) t=8.0 ([36]), (k) t=9.0, (l) t=9.0 ([36]).*

above the x-axis. Our observations are similar to those in [29]. In figures 5.11(a) and 5.11(b), we compare the time development of u and v velocity profiles along $\theta = 0$ line with the experimental results of Coutanceau and Menard [36]. In both the cases, we obtain very good agreements. Figure 5.12(a) depicts the time development of the u velocity profile along the line $\theta = 90^0$; our results are very similar to the ones obtained by Badr and Dennis ([19]). In figure 5.12(b), we show the vorticity values on the cylinder surface at different time levels. As in the case of $\alpha = 0.5$, the variation in the separated region where the cylinder is moving upstream ($0 < \theta < 40^o$) is different from the variation in the downstream direction ($320^o < \theta < 360^o$).

5.4.1.3 $Re = 200$ and $\alpha = 2.07$

With further increase in the value of α, substantial changes are observed in the flow patterns; the flow structure becomes more complex. Badr and Dennis [19] pointed out that as the value of α increases, the vorticity layer generated at the upstream-moving side of the cylinder intensifies, resulting in even larger radial derivatives. As a result of

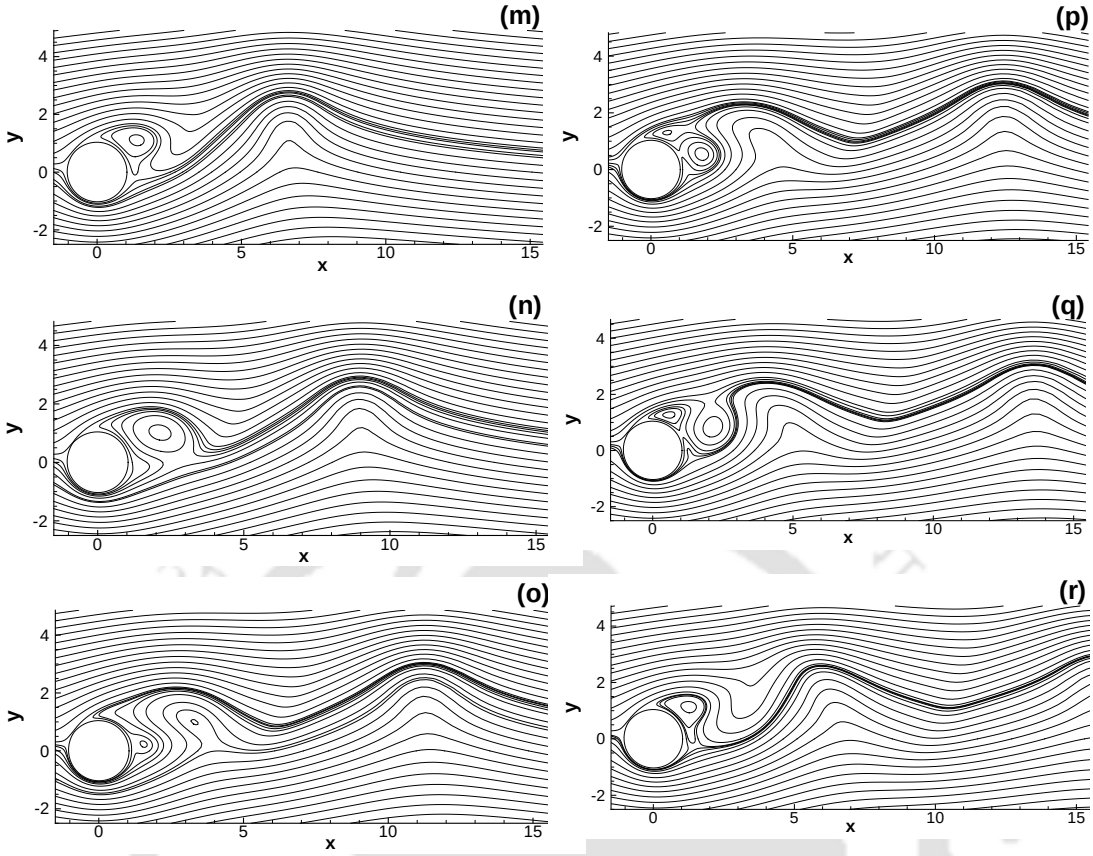

Figure 5.9: *Instantaneous streamlines for Re = 200, α = 1.0 at various times. (m) t=11.0, (n) t=13.0, (o) t=16.0, (p) t=17.0, (q) t=19.0, (r) t=22.0.*

this, more grid points are required in the radial direction in the vicinity of the cylinder surface for accurate resolution of the flow. To tackle this problem, some studies (as in [29]) had to resort to using finer grids and smaller time steps. However, the use of clustered grids on the surface of the cylinder coupled with the implicitness of our formulation allows us to handle this issue very efficiently even without increasing the grid size and reducing the time step. This will be clear from our simulations for this Re-α combination that follows.

Time evolution of streamline contours for $\alpha = 2.07$ have been shown in figures 5.13 to 5.15. Here, the primary vortex forms above the axis of flow at around $t = 1$ (figure 5.13(a)). Gradually, this vortex grows in size, detaches from the cylinder surface and and moves into the downstream (figures 5.13(b) to 5.13(e)). Our numerical result shown at $t = 5$ is very close to the experimental result of Coutanceau and Menard ([36]) at the same instant (figure 5.13(f)). Till $t = 6.5$, no development of secondary vortex is seen (figures 5.14(g) and 5.14(h)). At around $t = 7$, a small secondary vortex appears on the cylinder surface much above the positive x-axis (figure 5.14(i)). This secondary vortex then grows in size but does not move (figure 5.14(k)). Exactly same flow patterns can be

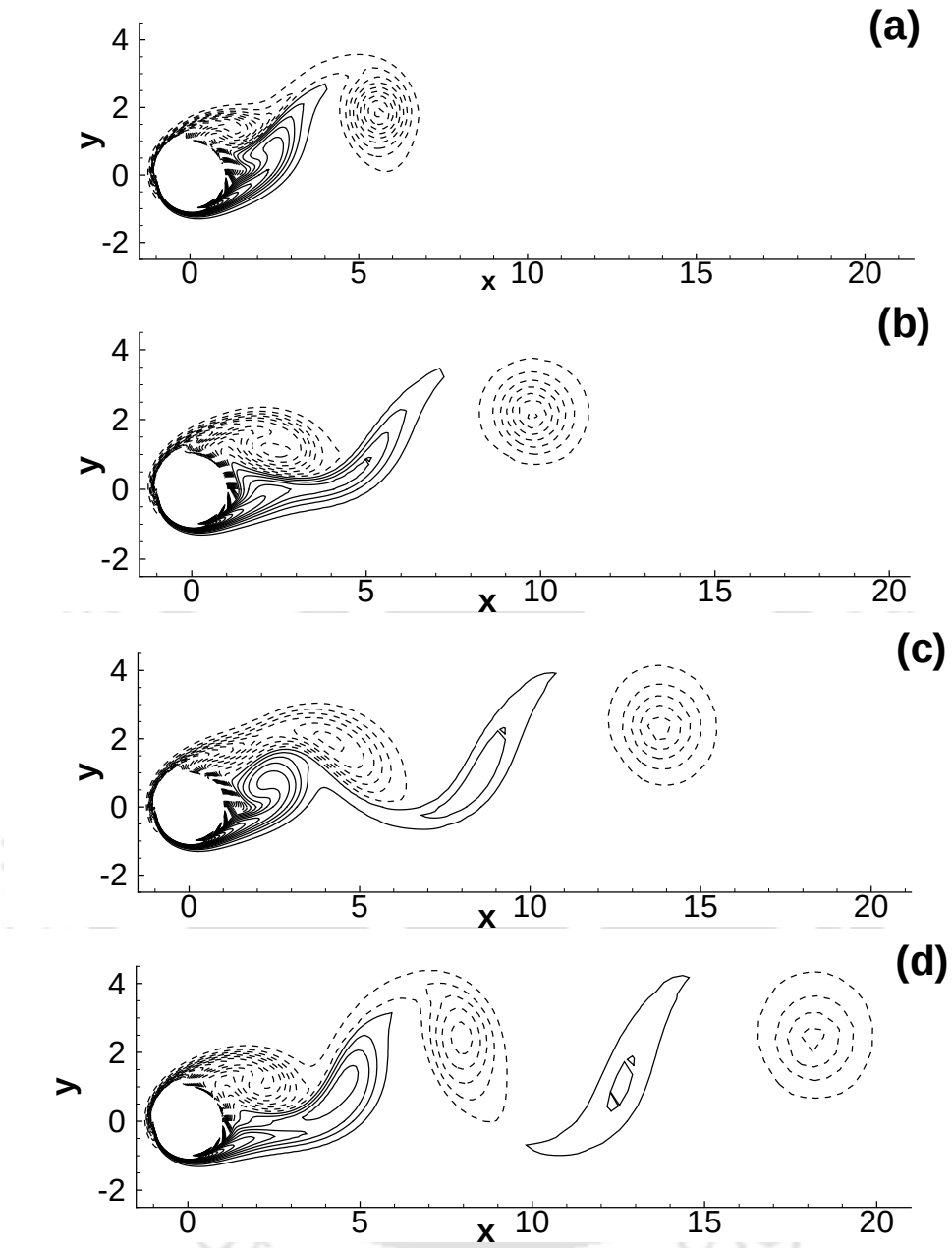

Figure 5.10: *Vorticity contours for* $Re = 200$ *and* $\alpha = 1.0$ *at (a) t=8.0, (b) 10.0, (c) 14.0, (d) 20.0.*

seen from the experimental results of [36] at time $t = 7$ and $t = 9$ (figure 5.14(j), 5.14(l)). As time progresses, the first vortex moves into the far downstream and sheds slowly, but the second vortex stays at the same location for some time and then disappears without shedding into the downstream (figure 5.15(m) to 5.15(r)). All our computed results show excellent agreements with the experimental results of [36] as well as the numerical results of [19] and [98].

In figure 5.16, we show the time development of the vorticity contours for this α

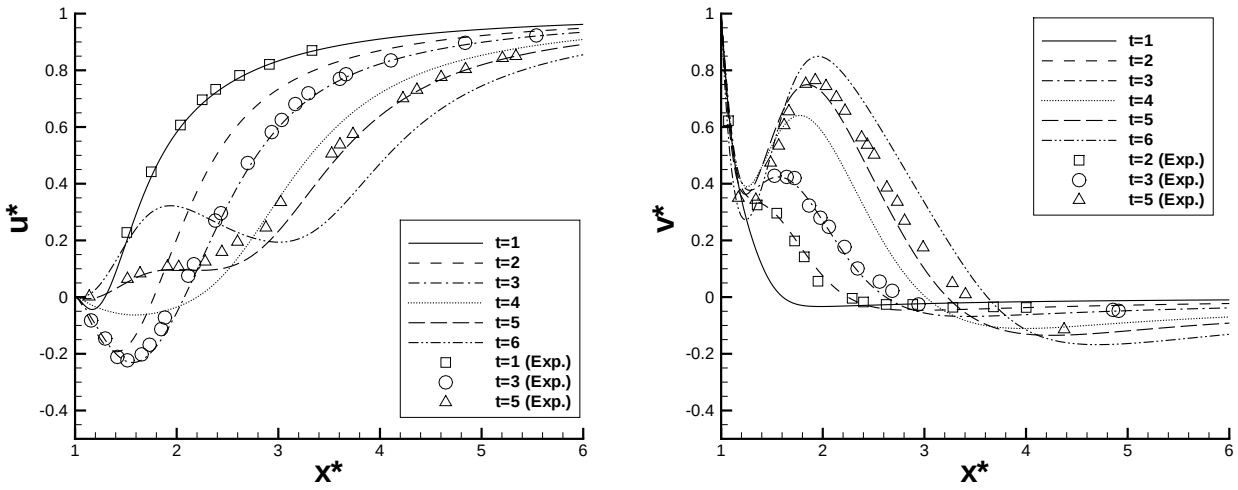

(a) (b)

Figure 5.11: *For $Re = 200$, $\alpha = 1.0$, along $\theta = 0$, comparison with the experimental results of [36], evolution of (a) u-velocity and (b) v-velocity.*

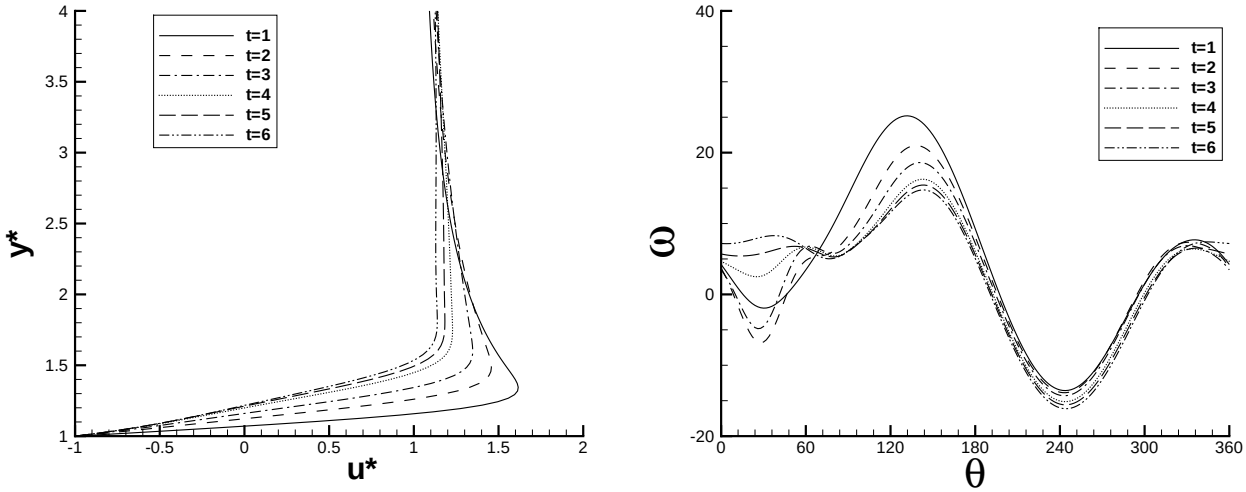

(a) (b)

Figure 5.12: *For $Re = 200$, $\alpha = 1.0$, evolution of (a) u-velocity on $\theta = 90^0$ and (b) solid surface vorticity.*

value. No vortex street is observed here, which means that the periodic nature of the flow no longer exists. Our observations are consistent with Coutanceau and Menard [36] and Badr and Dennis [19].

Figure 5.17(a) shows the evolution of u-velocity profiles on $\theta = 0$, which shows that unlike $\alpha = 0.5$ and 1, the u values are almost positive for all the time levels considered

here. Figure 5.17(b) depicts the vorticity values on the cylinder surface at different time levels, which significantly differ from the ones obtained for the previous α values (figures 5.5(b) and 5.11(b)).

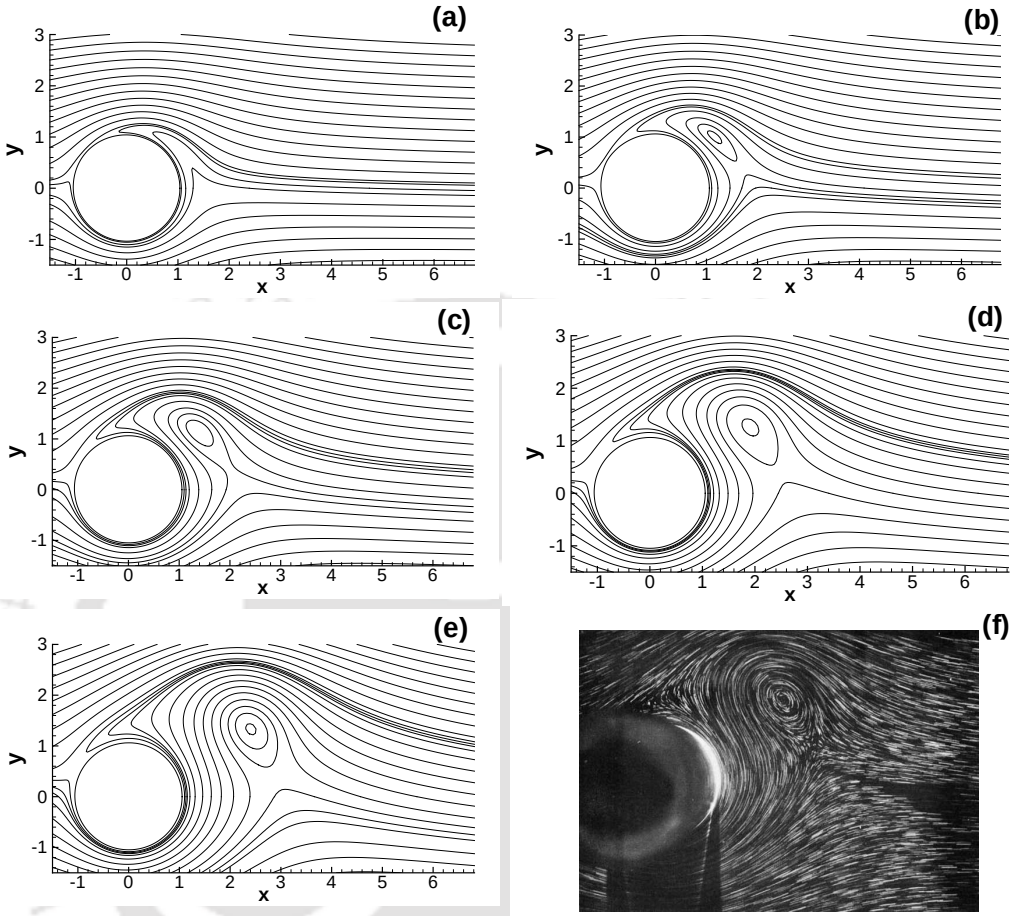

Figure 5.13: *Instantaneous streamlines for* $Re = 200$, $\alpha = 2.07$ *at various times. (a) t=1.0, (b) t=2.0, (c) t=3.0, (d) t=4.0, (e) t=5.0, (f) t=5.0 ([36]).*

5.4.1.4 $Re = 200$ and $\alpha = 3.25$

Finally we consider the case for $\alpha = 3.25$. This large rotational parameter value at larger time invokes the three-dimensional as well as sidewall boundary effects in the flow [36]. Chen *et al.* [29] reported errors in the numerical solutions for this large α value at greater t values. However, our computation on a time range $0 \leq t \leq 20$ was free of such errors.

For $\alpha = 3.25$, much more different flow patterns are observed than the previous three α values. In this case the first vortex appears much above the positive x-axis at time $t = 1$ (figure 5.18(a)). During next few instants, the vortex grows in size and starts to detach from the cylinder surface (figures 5.18(b) to 5.18(e)). Our computed results at

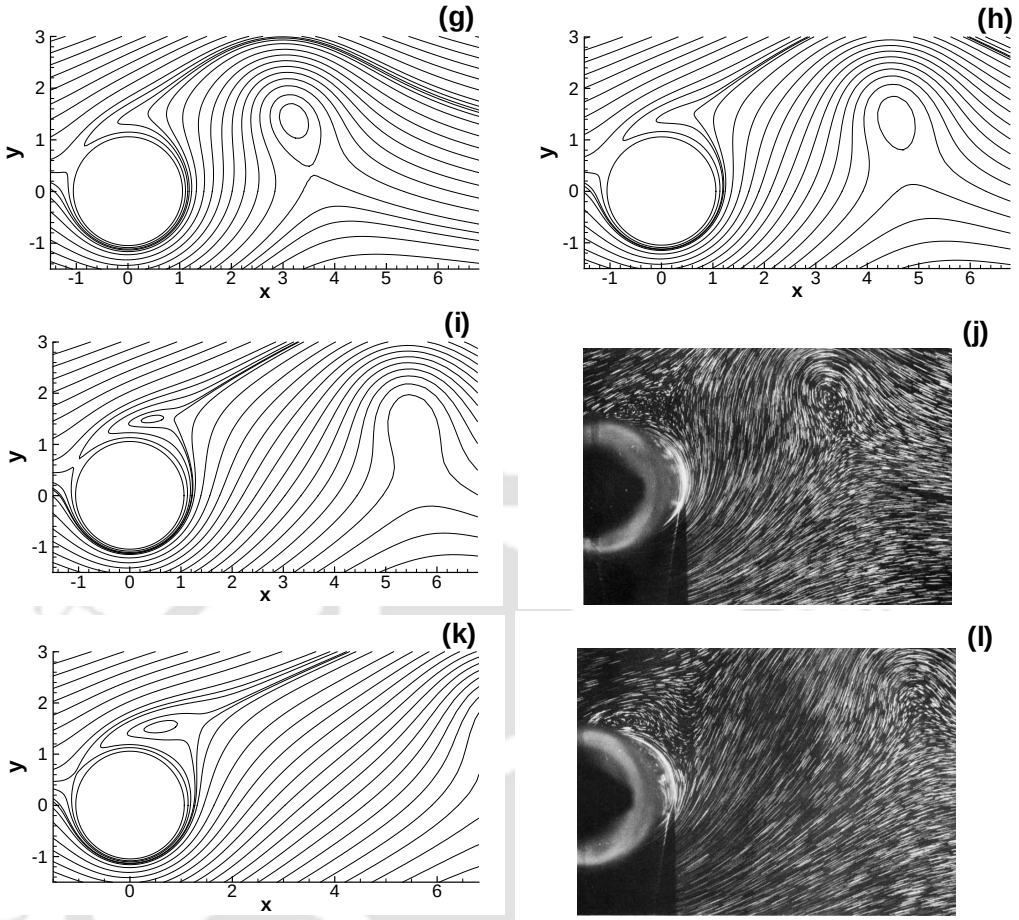

Figure 5.14: *Instantaneous streamlines for Re = 200, α = 2.07 at various times. (g) t=6.0, (h) t=6.5, (i) t=7.0, (j) t=7.0 ([36]), (k) t=9.0, (l) t=9.0 ([36]).*

$t = 9.0$ shown in figure 5.18(e) is in excellent agreement with the experimental result of [36] (figure 5.18(f)) at the same instant. This vortex slowly moves and sheds into the downstream till it reaches the end of our computational time range at $t = 20.0$. Throughout our computation, no other vortex was seen to develop (figures 5.19(g) to 5.19(i)), which had also been observed by other studies ([36, 98]). Our computed results show excellent agreements with those of experimental results of Coutanceau and Menard [36] in the range $0 \leq \alpha \leq 13$ and the numerical results of Sanyasiraju and Manjula [98] for $0 \leq \alpha \leq 25$, but differ from the results of Chen *et. al.* [29] from $t = 13$ onwards. We show the evolution of the vorticity contours in figure 5.20 for $5 \leq t \leq 20$ which are in conformity with the formation of the single vortex depicted in the streamlines of the preceding figures.

In figure 5.21(a) we show the u-velocity profiles along $\theta = 0$ line for the same time levels that had been considered for the previous α values. Here, the u-velocity profiles for the initial time stations are totally different from the corresponding lower α-values.

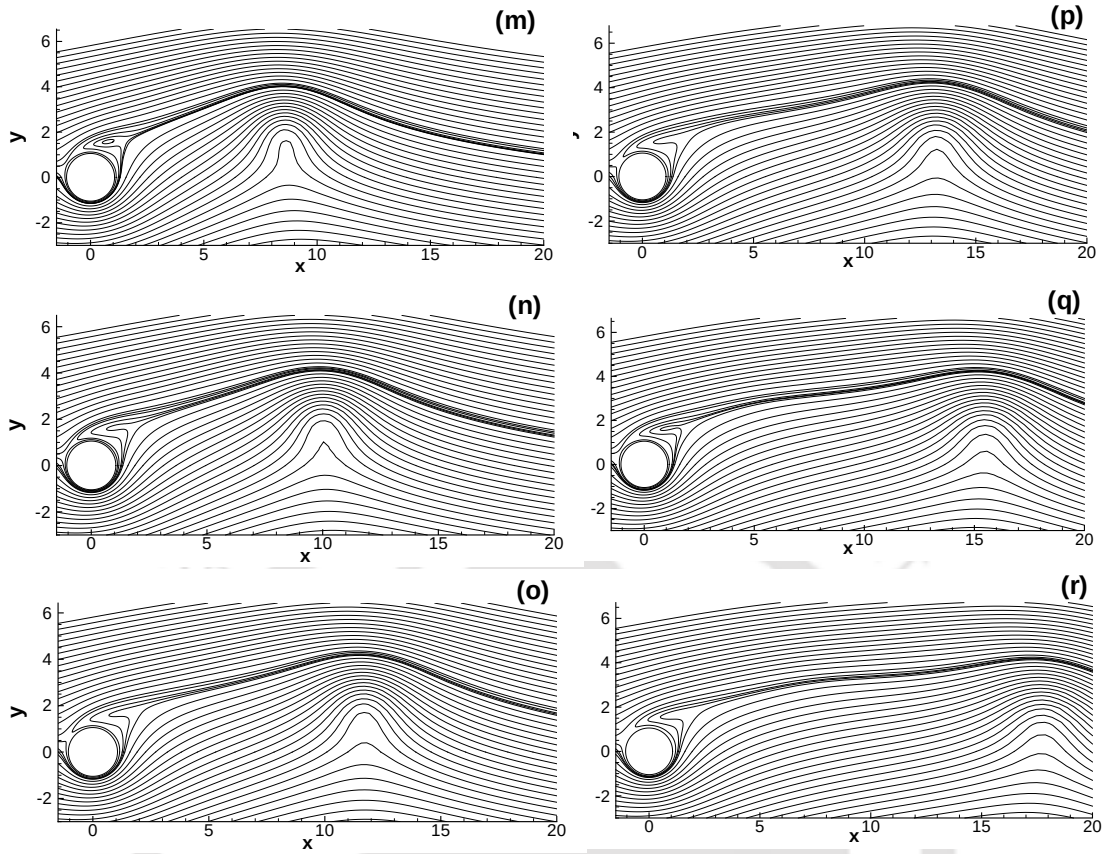

Figure 5.15: *Instantaneous streamlines for* $Re = 200$, $\alpha = 2.07$ *at various times. (m) t=10.0, (n) t=12.0, (o) t=15.0, (p) t=18.0, (q) t=22.0, (r) t=24.0.*

Figure 5.21(b) shows the vorticity values on the cylinder surface. Though the difference in variation is apparent from the upstream ($0 < \theta < 40^o$) to the downstream direction ($320^o < \theta < 360^o$), it is on a lesser scale compared to the ones observed for lower values of α.

5.4.1.5 Influence of α

From the above discussions, it is clear that rotation strongly influences the near-wake formation. This influence of rotation strongly effects the formation of the secondary and other vortices at the next level (tertiary, quaternary etc.). When $\alpha \leq 1$, i.e. when the wall speed is less than or equal to the free stream, the flow shows periodic nature but for $\alpha > 1$, i.e. when the wall speed becomes greater than the free stream velocity, the flow loses its periodic nature slowly.

For $Re = 200$, four different α values, i.e. $\alpha = 0.5,\ 1.0,\ 2.07,\ 3.25$ are considered. From the flow visualization, it can be seen that with the increase in α value, there is a decrease in the number of eddies behind the cylinder (see figure 5.22), i.e., rotation of the cylinder controls the vortex formation. For $\alpha = 2.07$, only two vortices form, out

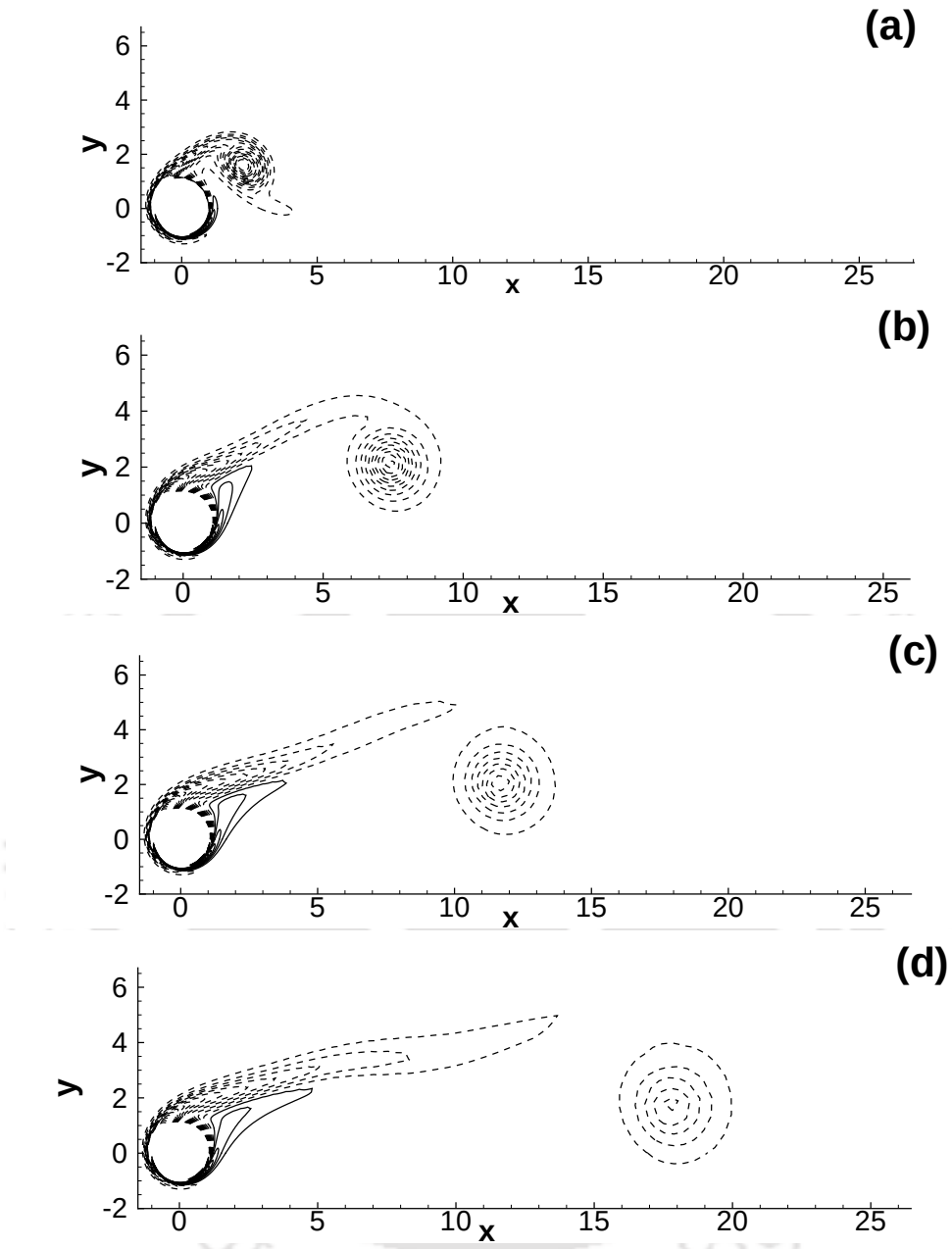

Figure 5.16: *Vorticity contours for* $Re = 200$ *and* $\alpha = 2.07$ *at (a) t=5.0, (b) t=9.0, (c) 13.0, (d) 19.0.*

of which only the primary vortex sheds into the downstream. For $\alpha = 3.25$, only one vortex forms and sheds into the downstream. No secondary vortex is seen to appear till t=20, the upper limit of the present computational time range. It is also noticed that the movement of primary vortex into the downstream is much slower for higher α values.

To observe the influence of α, comparisons between the vorticity contours (vortex street) have been shown in figure 5.22 for $Re = 200$ and α-values varying from 0 to 2.07. In this figure, the vorticity contours for $\alpha = 0$ is equivalent to the flow past an

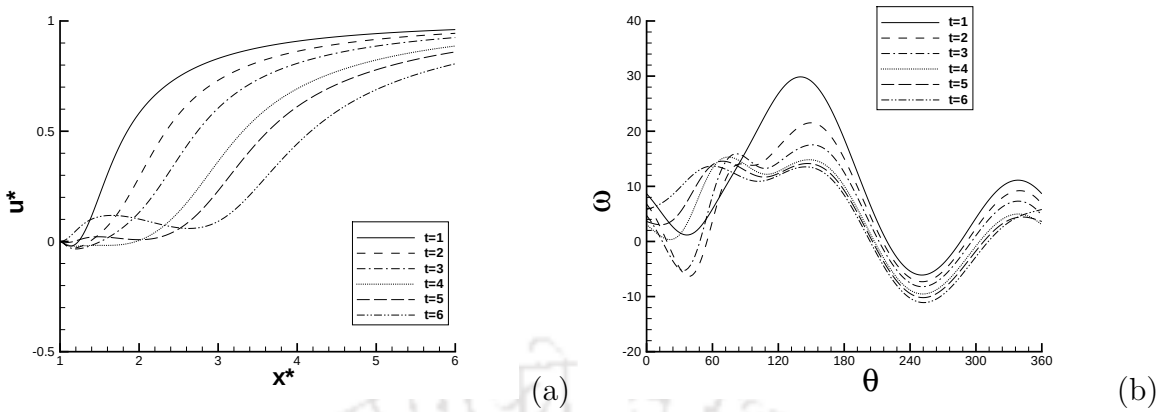

Figure 5.17: *(a) u-velocity profile on $\theta = 0$ and (b) solid surface vorticity at different time levels for $Re = 200$, $\alpha = 2.07$.*

impulsively started circular cylinder. It is obvious from the figure that, increase in α value displaces the midline of the street upward from $\theta = 0$ line (the line of symmetry or the positive x-axis); for $\alpha \geq 1.0$, the flow gradually loses its periodic nature with corresponding decline in the frequency of vortex shedding.

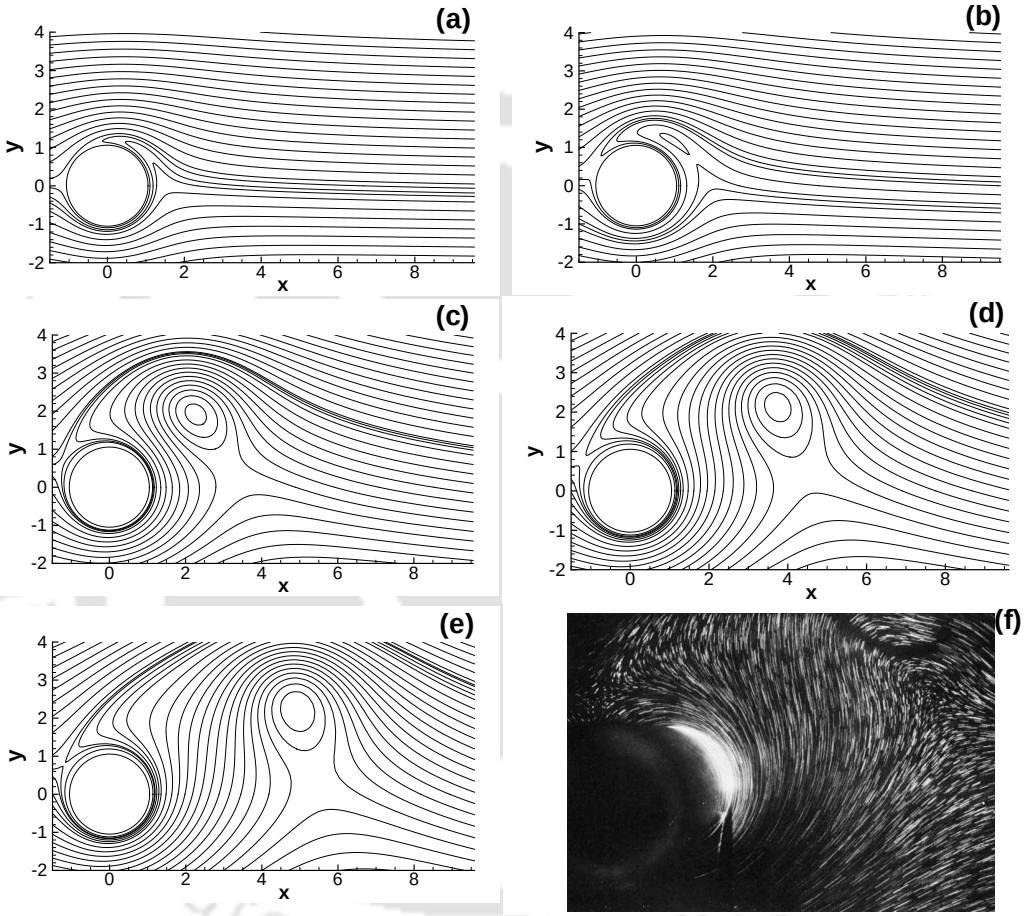

Figure 5.18: *Instantaneous streamlines for* $Re = 200$, $\alpha = 3.25$ *at various times. (a) t=1.0, (b) t=2.0, (c) t=4.0, (d) t=6.0, (e) t=9.0, (f) t=9.0 ([36]).*

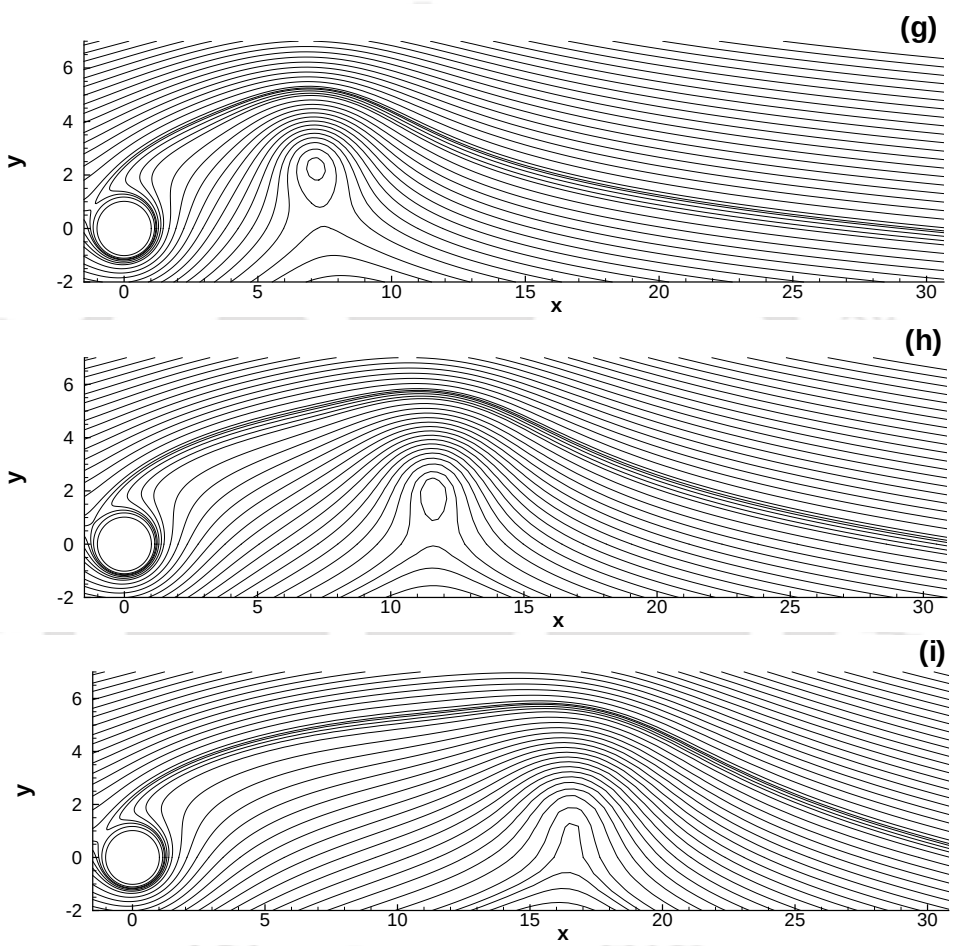

Figure 5.19: *Instantaneous streamlines for* $Re = 200$, $\alpha = 3.25$ *at various times. (g) t=10.0, (h) t=15.0, (i) t=20.0.*

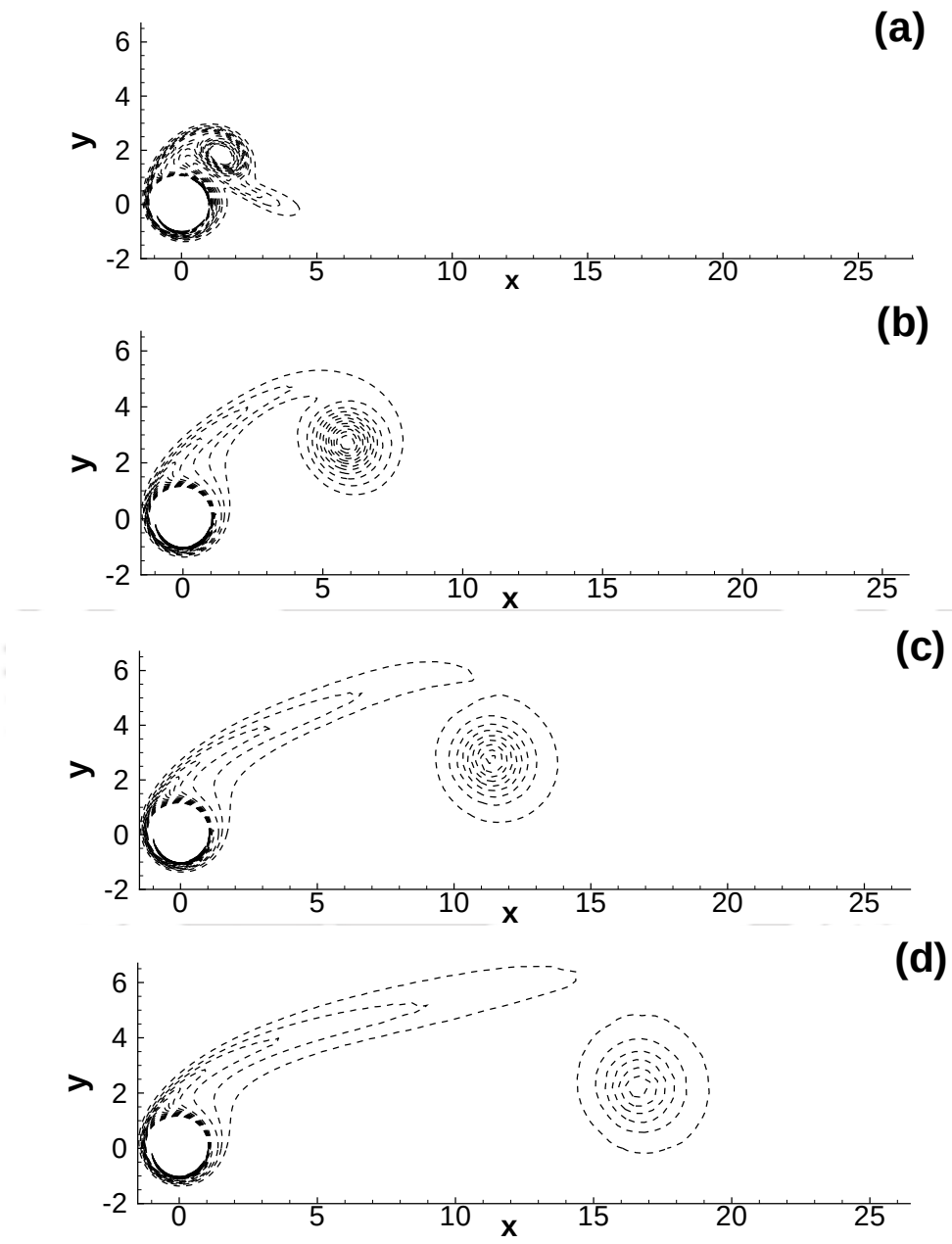

Figure 5.20: *Vorticity contours for* $Re = 200$ *and* $\alpha = 3.25$ *at (a) t=5.0, (b) t=9.0, (c) t=15.0, (d) t=20.0.*

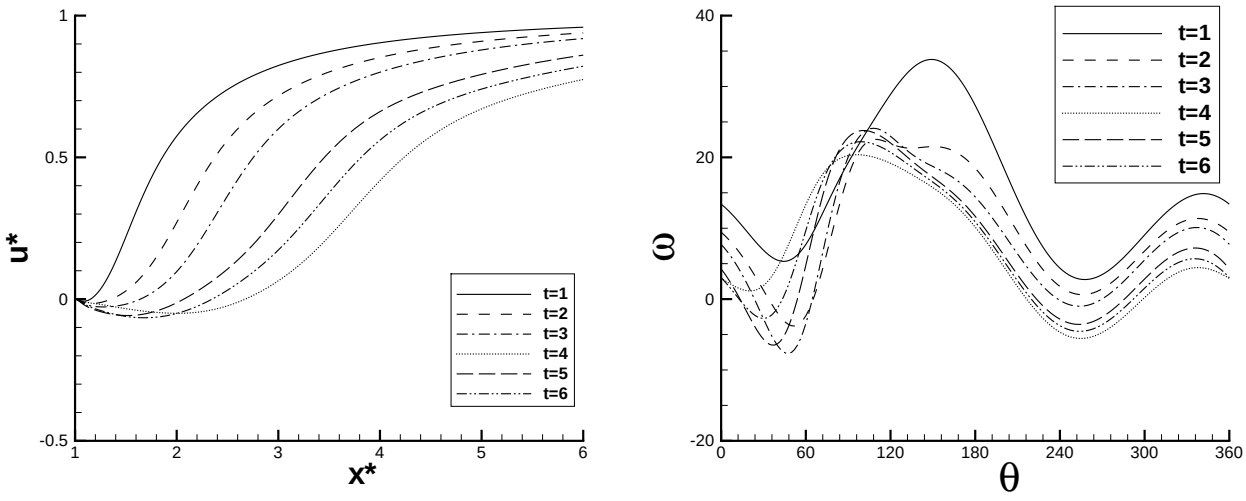

(a) (b)

Figure 5.21: *(a) u-velocity profile on $\theta = 0$ and (b) solid surface vorticity at different time levels for $Re = 200$, $\alpha = 3.25$.*

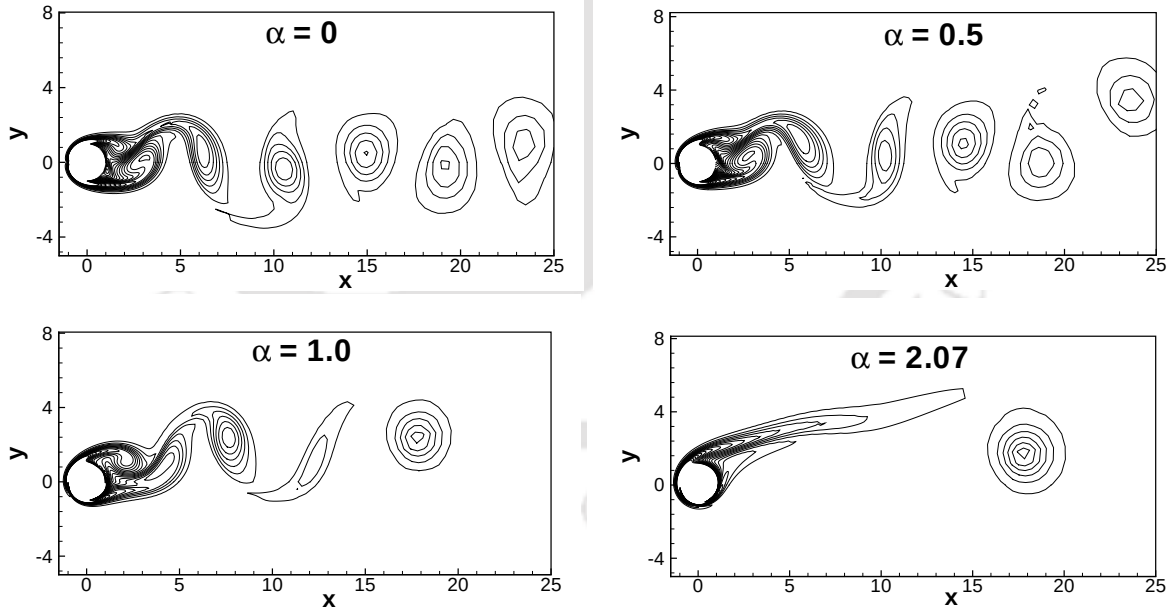

(a)

Figure 5.22: *Influence of α on the vortex street for $Re = 200$.*

5.4.2 Results for $Re = 500$ and $\alpha = 0.5$, 1 and 3

In this section, we present our numerical results for $Re = 500$ for three different non-dimensional rotation parameters $\alpha = 0.5$, 1 and 3.

We start with the case $\alpha = 0.5$; soon after the impulsive start of the motion, at time $t = 1$ (figure 5.23(a)), the first vortex starts to grow behind the cylinder above the axis of flow (the positive x-axis). After a while, a secondary vortex forms and starts to grow below the x-axis along with the first vortex at around $t = 2$ (figures 5.23(b) and 5.23(c)). During the next few instants of time, the first vortex grows in size and begins to detach from the cylinder surface and moves downstream and the secondary vortex slowly moves up and grows in size (figures 5.23(d) and 5.23(e)). At the same time a small tertiary vortex appears between the secondary vortex and the cylinder surface below the x-axis and continues till $t = 6$ (figures 5.23(e)) approximately. At around $t = 8$ (figure 5.23(f)), a new vortex starts to form above the x-axis. Simultaneously, the secondary vortex gets detached from the surface of the cylinder and moves downstream. In the next few instants, the tertiary vortex and the newly formed vortex above the x-axis starts growing and moves towards each other. They come closer and closer and coalesce with each other at around $t = 11$ (figure 5.23(g) and 5.23(h)). This common vortex then starts to grow with time and starts to move into the downstream (figure 5.24(i)). At around $t = 14$, a new vortex forms on the cylinder wall below the x-axis and it starts moving upwards growing in size at the same time and slowly gets detached from the cylinder wall as time progresses (figures 5.24(j) and 5.24(k)). At around $t = 18$, another pair of vortices begins to form, one above the x-axis and the other below it (see figure 5.24(l)) like the one observed at time $t = 9$. The same flow pattern seen between $t = 9$ and $t = 12$ gets repeated for a while and the two vortices club into a single vortex and grows bigger and bigger with time and shed into the downstream (figures 5.24(m) and 5.24(n)).

Figure 5.25 shows the evolution of vorticity contours for the same Re-α combination. As in the case $Re = 200,\ \alpha = 0.5$, the difference in flow patterns between the rotating and non-rotating ($\alpha = 0.0$) cases is apparent. The vortex shedding follows the same pattern as in the case of $Re = 200$ and $\alpha = 0.5$. In figures 5.26 and 5.27, we compare the streamlines at different instants of time side by side with the simulations of Badr and Dennis ([19]) and excellent comparison can be seen from these figures as well.

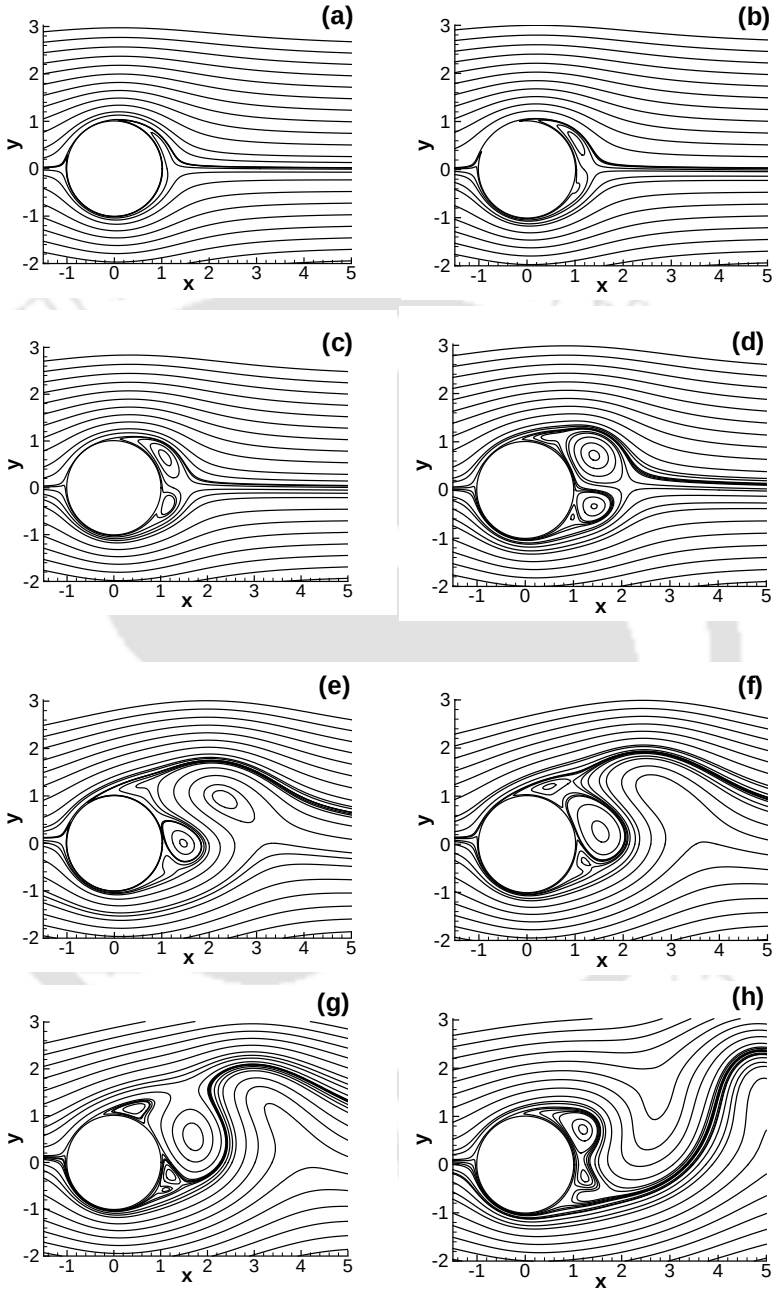

Figure 5.23: *Instantaneous streamlines for* $Re = 500$, $\alpha = 0.5$ *at various times. (a) t=1.0, (b) t=1.5, (c) t=2.0, (d) t=5.0, (e) t=6.0, (f) t=8.0, (g) t=9.0, (h) t=11.0.*

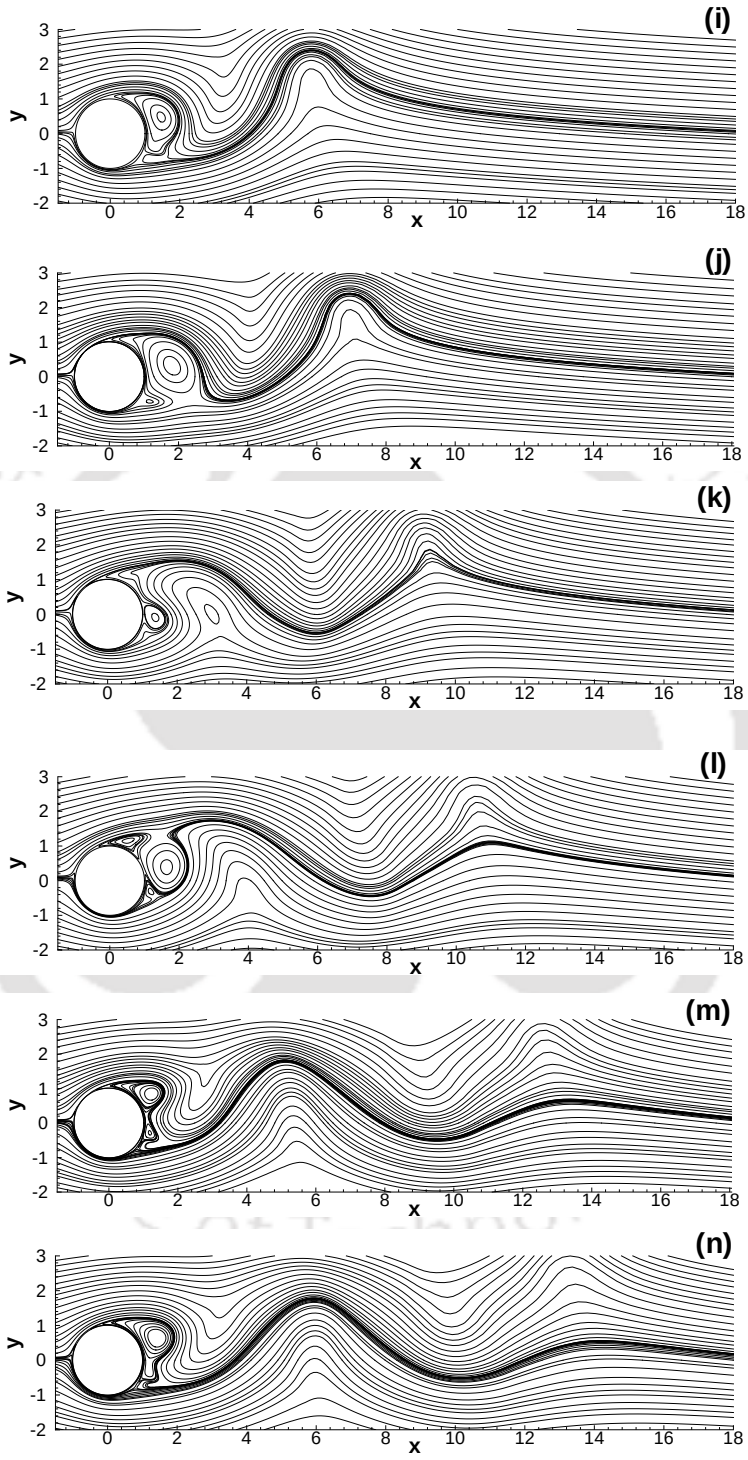

Figure 5.24: *Instantaneous streamlines for* $Re = 500$, $\alpha = 0.5$ *at various times. (i) t=12.0, (j) t=14.0, (k) t=16.0, (l) t=18.0, (m) t=20.0, (n) t=22.0.*

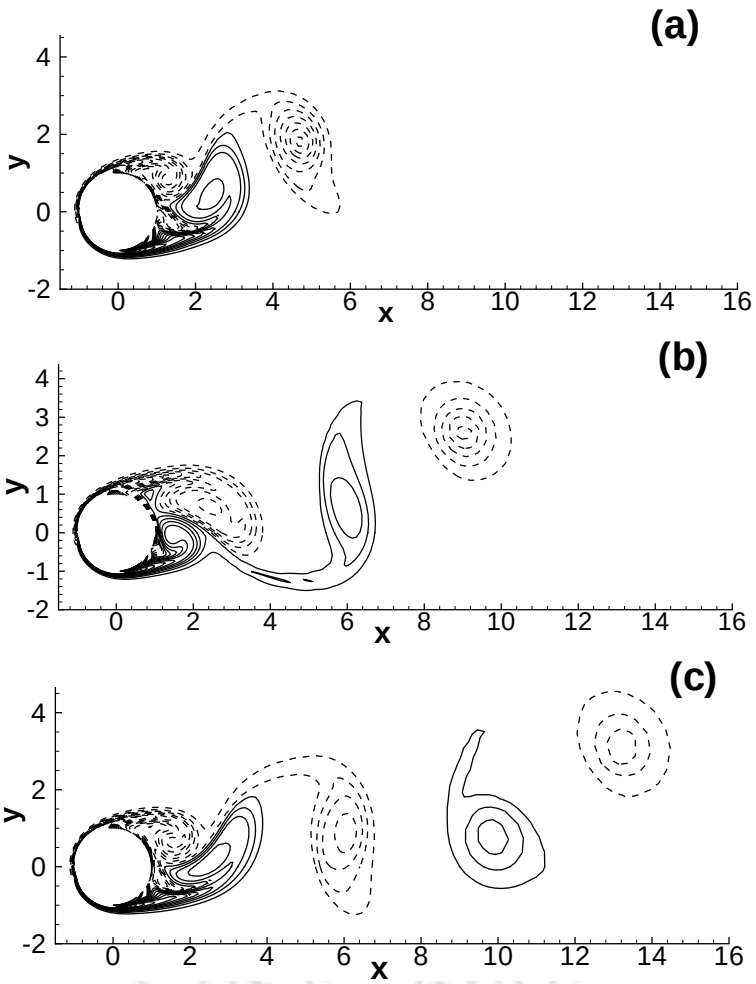

Figure 5.25: *Evolution of vorticity contours for* $Re = 500$, $\alpha = 0.5$ *at (a) t=12.0, (b) t=17.0, (c) t=22.0.*

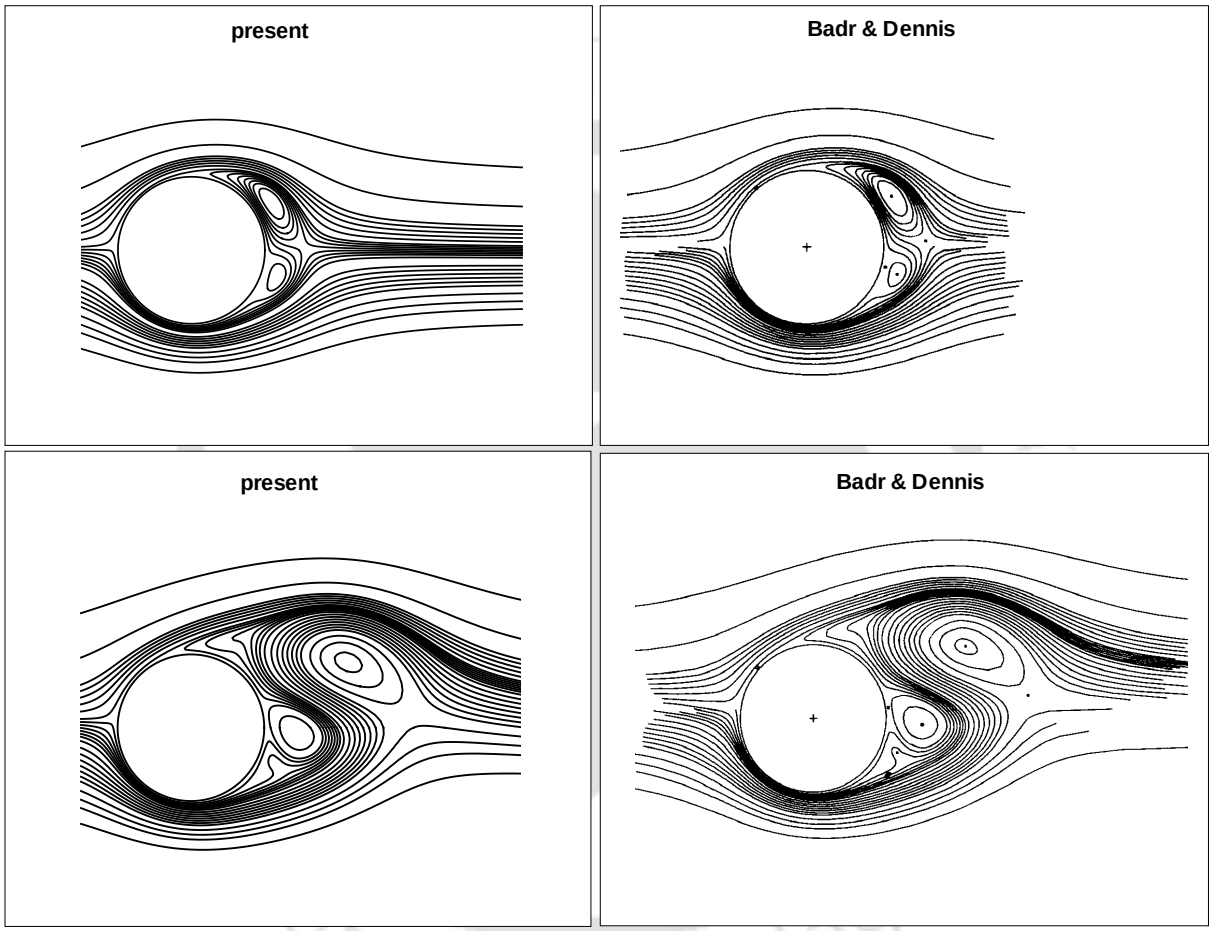

Figure 5.26: *Comparison of streamline contours between present results and computed results of Badr and Dennis [19] for* $Re = 500$ *and* $\alpha = 0.5$ *at t=2.0 (top), and t=6.0 (bottom).*

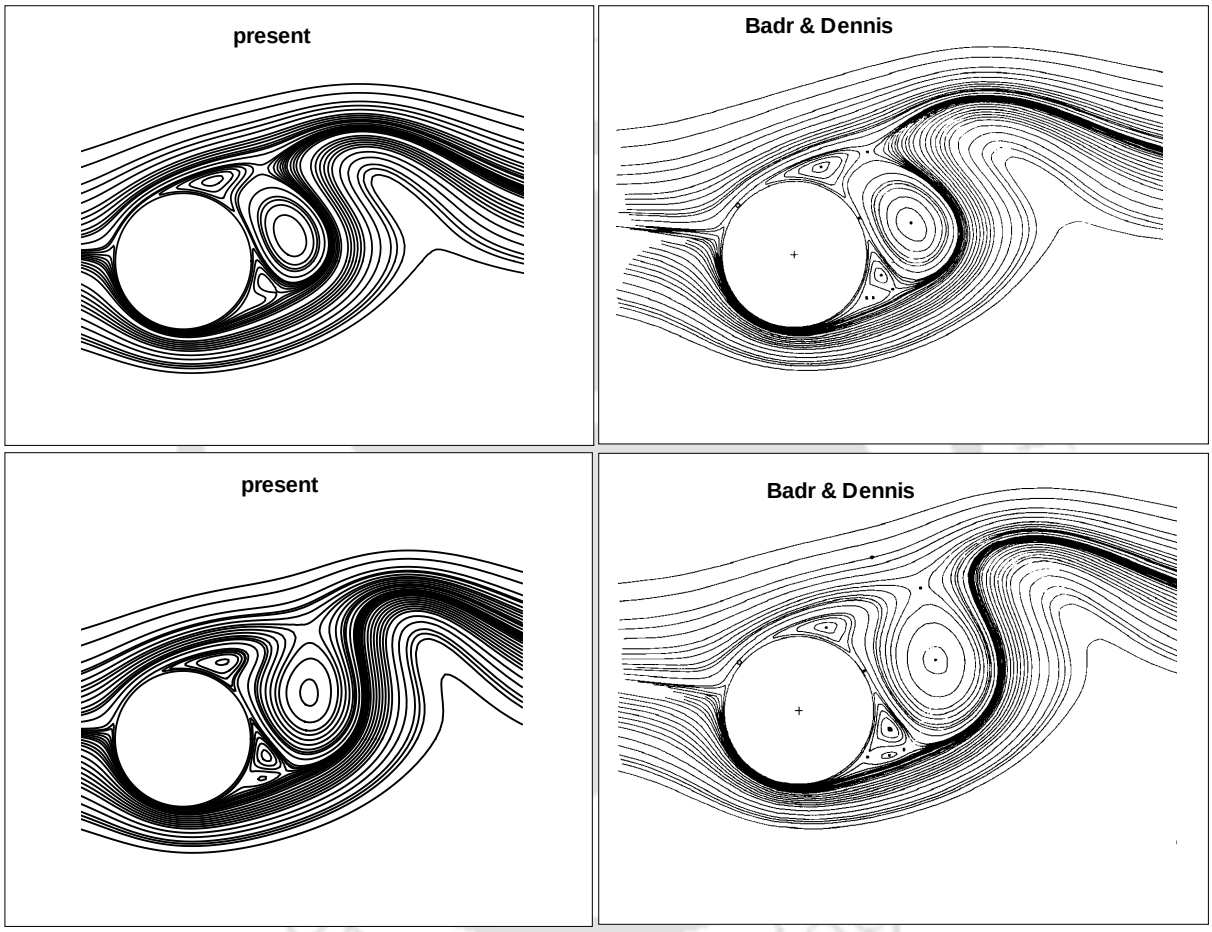

Figure 5.27: *Comparison of streamline contours between present results and computed results of Badr and Dennis [19] for* $Re = 500$ *and* $\alpha = 0.5$ *at t=8.0 (top), and t=9.0 (bottom).*

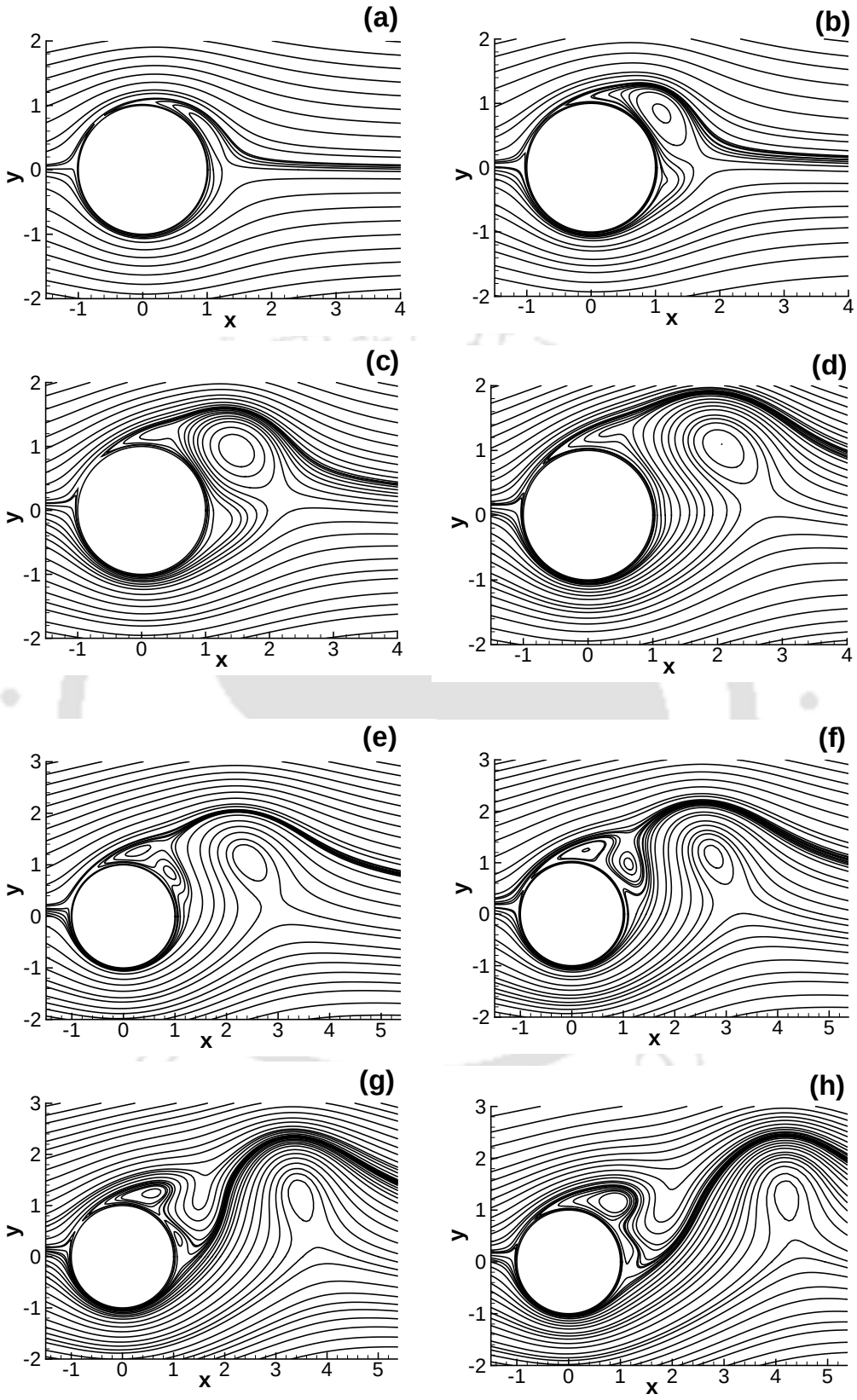

Figure 5.28: *Instantaneous streamlines for $Re = 500$, $\alpha = 1.0$ at various times. (a) t=1.0, (b) t=2.0, (c) t=3.0, (d) t=5.0, (e) t=6.0, (f) t=7.0, (g) t=8.0, (h) t=10.0.*

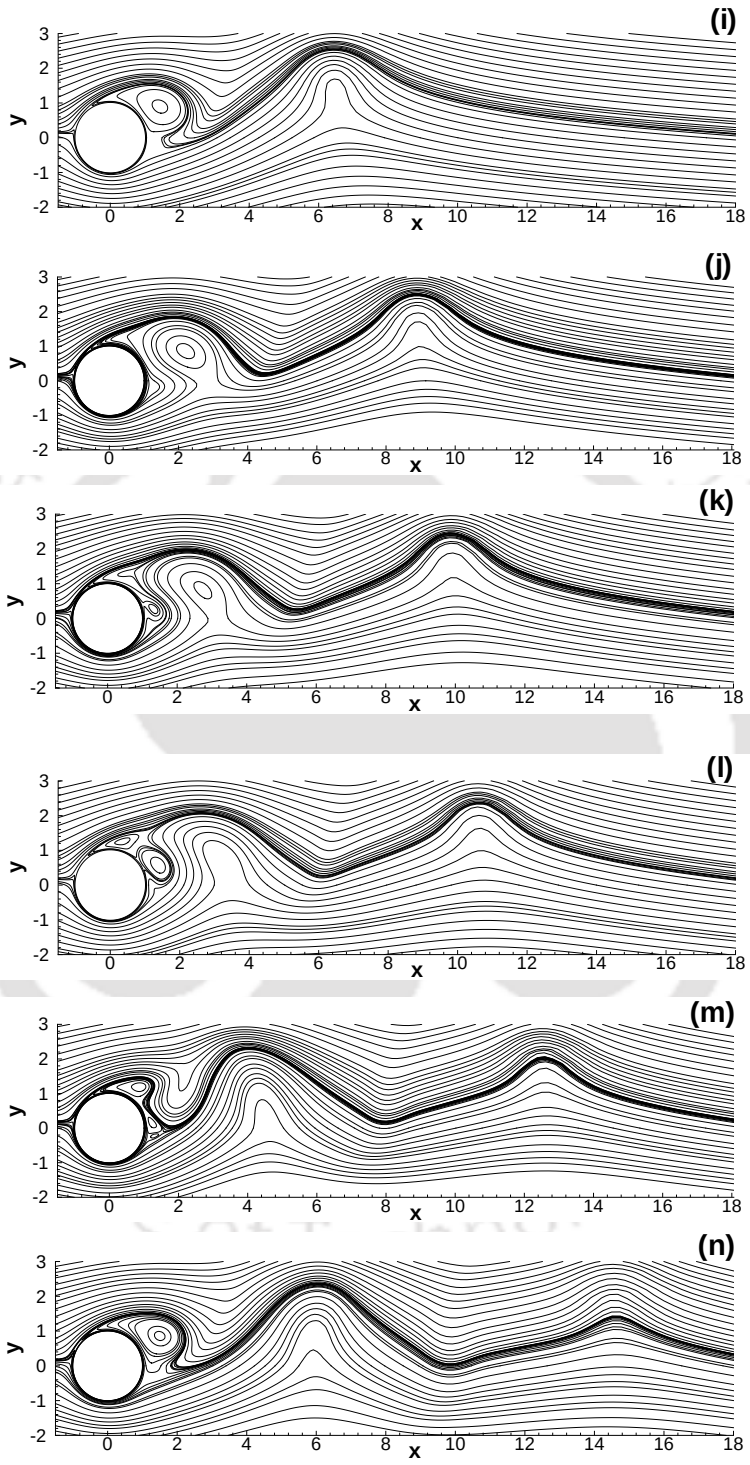

Figure 5.29: *Instantaneous streamlines for* $Re = 500$, $\alpha = 1.0$ *at various times. (i) t=11.0, (j) t=13.0, (k) t=15.0, (l) t=16.0, (m) t=18.0, (n) t=20.0.*

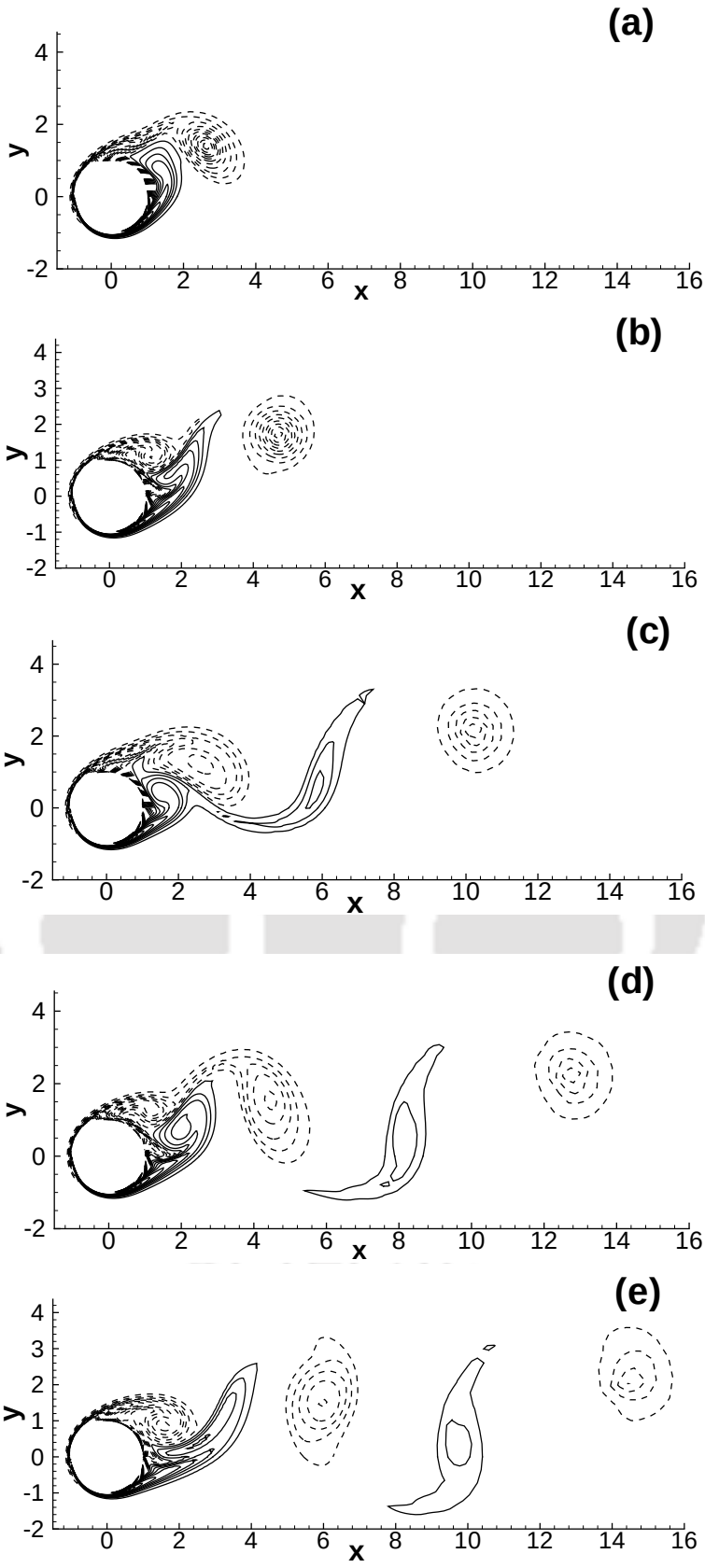

Figure 5.30: *Evolution of vorticity contours for* $Re = 500$, $\alpha = 1.0$. *(a) t=8.0, (b) t=10.0, (c) 14.0, (d) t=20.0, (e) 24.0.*

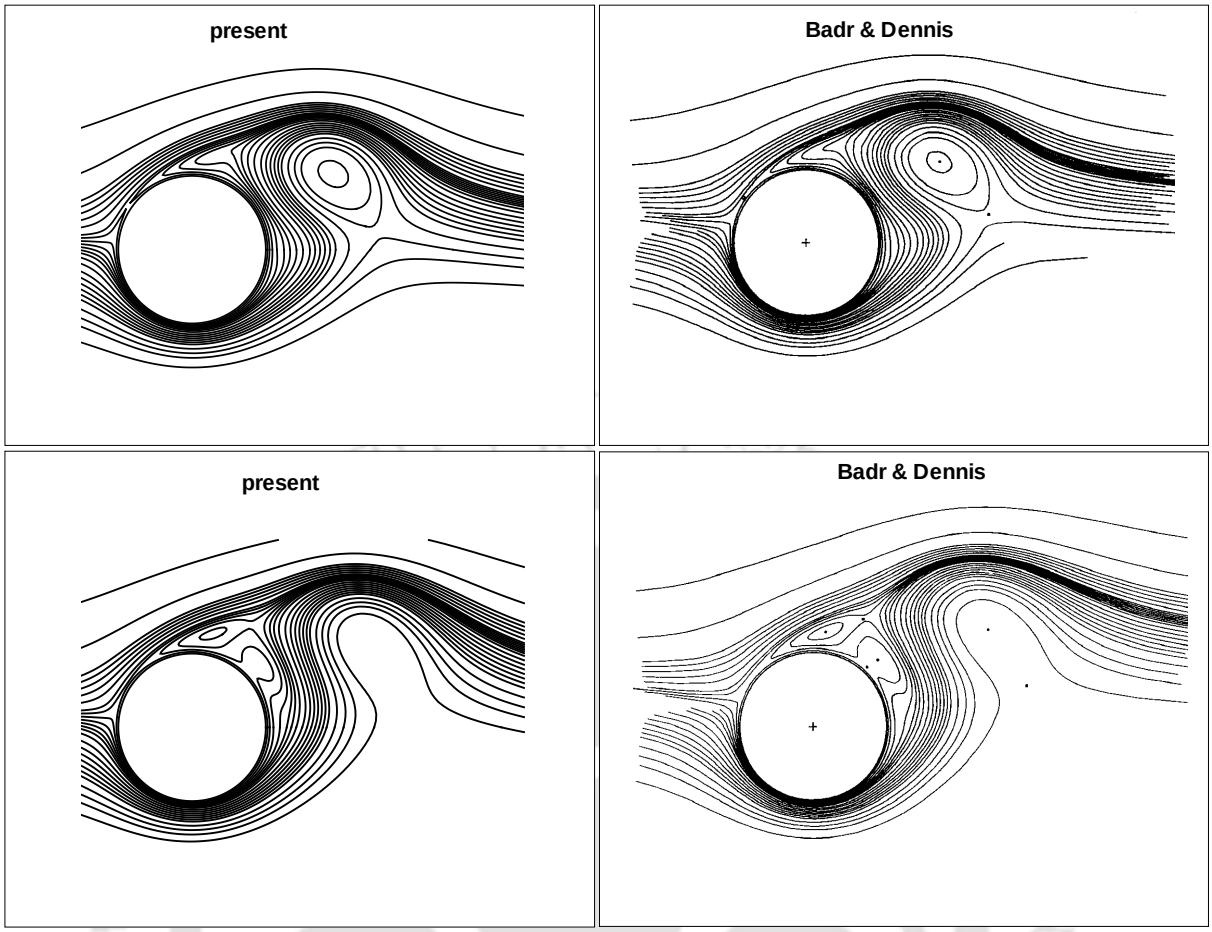

Figure 5.31: *Comparison of streamline contours between present results and computed results of Badr and Dennis [19] for Re = 500 and α = 1.0 at t=5.0 (top), and t=6.2 (bottom).*

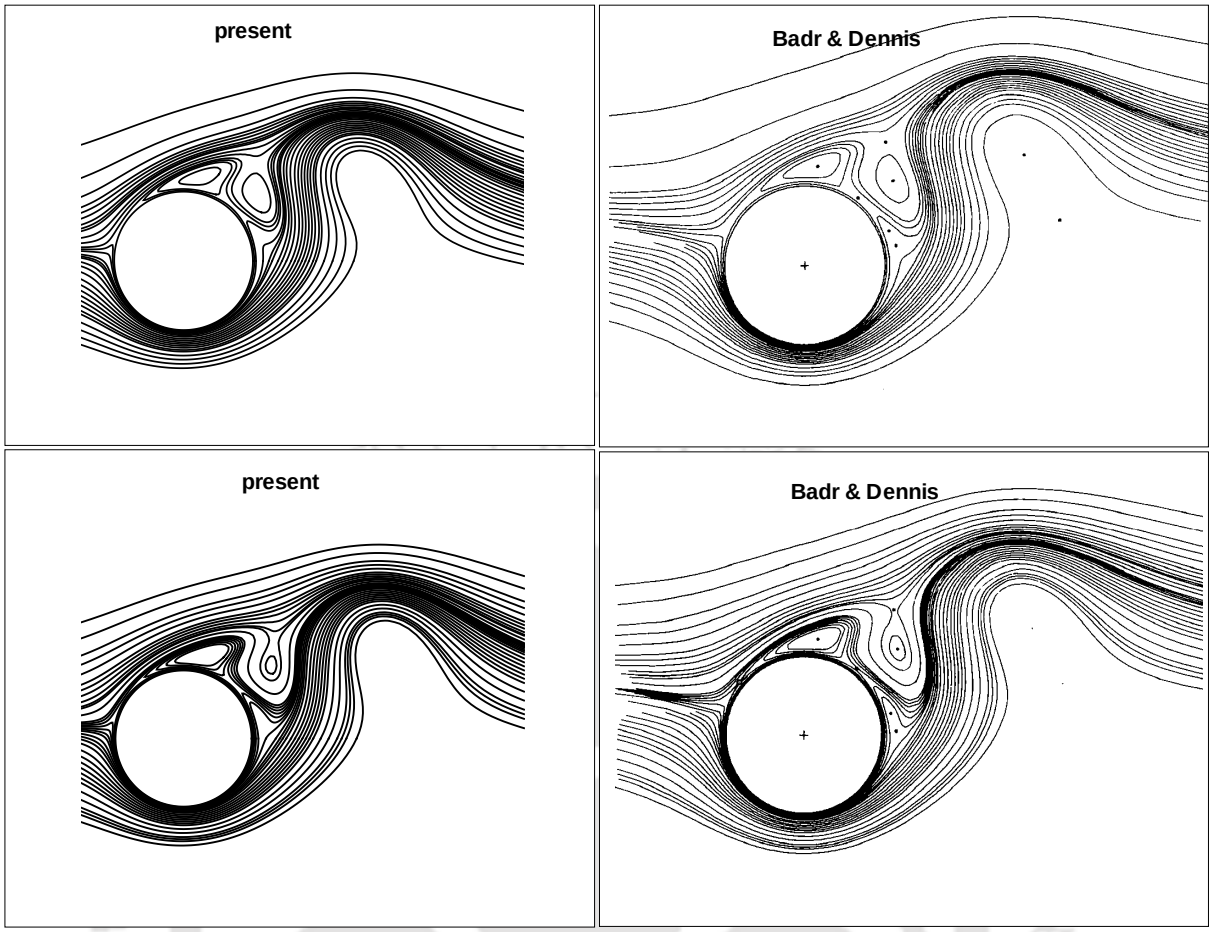

Figure 5.32: *Comparison of streamline contours between present results and computed results of Badr and Dennis [19] for Re = 500 and $\alpha = 1.0$ at t=6.7 (top), and t=7.0 (bottom).*

Now we move to $\alpha = 1$ where a noticeable change in the vortex formation below the x-axis can be seen. While the first appearance of the vortex below the x-axis for $\alpha = 0.5$ was observed at time $t = 1.5$, here it makes its appearance only at around $t = 8.0$ (figure 5.28(g)). Before that, the first vortex starts to form much above the x-axis, grows in size and simultaneously moves towards the downstream till $t = 5$ (figures 5.28(a) to 5.28(d)). At around $t = 6$, two small secondary vortices form very close to each other at angles 40^0 and 80^0 approximately to the cylinder surface (figure 5.28(e)). At time $t = 7$, the vortex between and below the two secondary vertices grows in size and gets detached from the cylinder (figure 5.28(f)). Then at around $t = 8$, a small tertiary vortex appears just below the x-axis. During next few instants, the upper one of the two secondary vortices and the tertiary vortex get closer to each other and ultimately get coalesced at around $t = 10$ (figures 5.28(h)). Then it starts to grow in size and slowly detaches from the cylinder (figures 5.29(i) and 5.29(j)). At around $t = 14$, a new vortex starts to grow just below the x-axis and starts to moves upwards (figure 5.29(k)); meanwhile, another

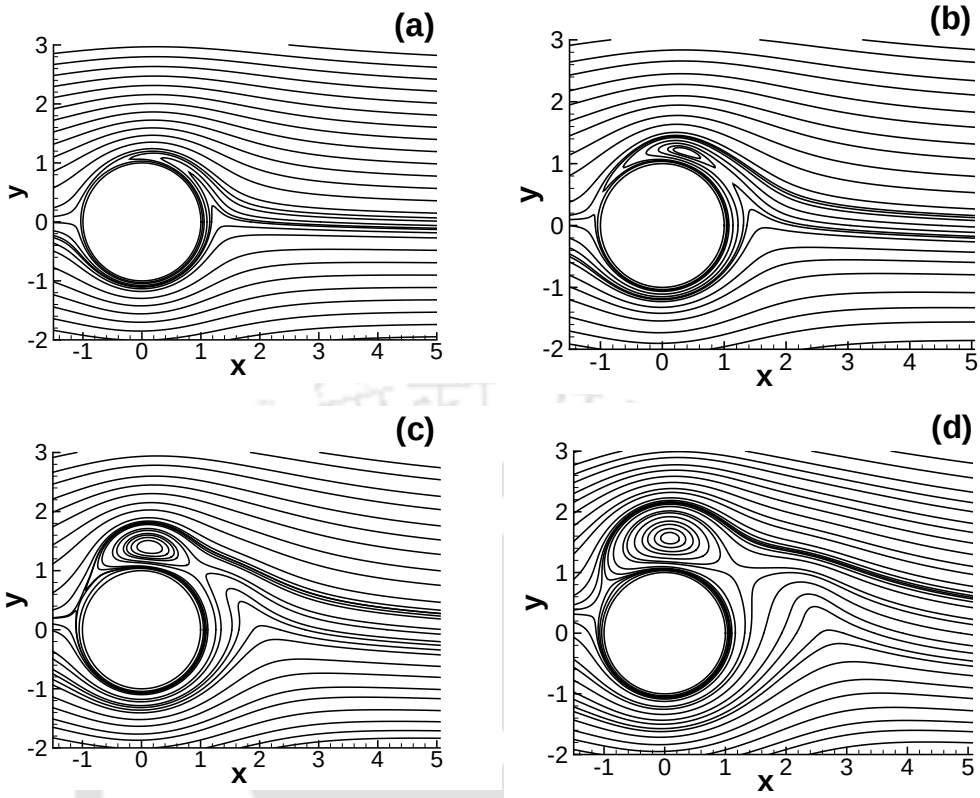

Figure 5.33: *Instantaneous streamlines for Re = 500, α = 3.0 at various times. (a) t=1.0, (b) t=2.0, (c) t=4.0, (d) t=6.0.*

vortex appears at the top of the cylinder (figure 5.29(l)). This new vortex grows in size and the former vortex slowly detaches from the cylinder surface and gets diffused at around $t = 18$. Afterwards the flow patterns observed between $t = 8.0$ and $t = 11$ get repeated (figure 5.29(m), 5.29(n)).

We present the vorticity contours for the same duration of time in figures 5.30(a) to 5.30(e). The trajectories of the shed vortices are similar to that of $\alpha = 0.5$ with the exception that the vortices due to the downstream moving part of the cylinder remains above the $\theta = 0$ line. This continues in subsequent times (see the dotted vorticity contours of figures 5.30(d) and 5.30(e)) on account of the anticlockwise fluid motion generated by rotation in the vicinity of the cylinder surface. In figures 5.31 and 5.32, we compare the streamlines at different instants of time side by side with the simulation of Badr and Dennis ([19]) and again, excellent comparison is obtained.

For $\alpha = 3.0$, the flow patterns observed are much more different than the previous two α values. Here the first vortex appears much above the x-axis at time $t = 1$ (see figure 5.33(a)). While growing in size, it also moves backwards till $t = 6$ (figures 5.33(b) to 5.33(d)). At time $t = 6$, the vortex reaches the top of the cylinder surface and then it starts to move away from the cylinder in the forward direction. In subsequent times,

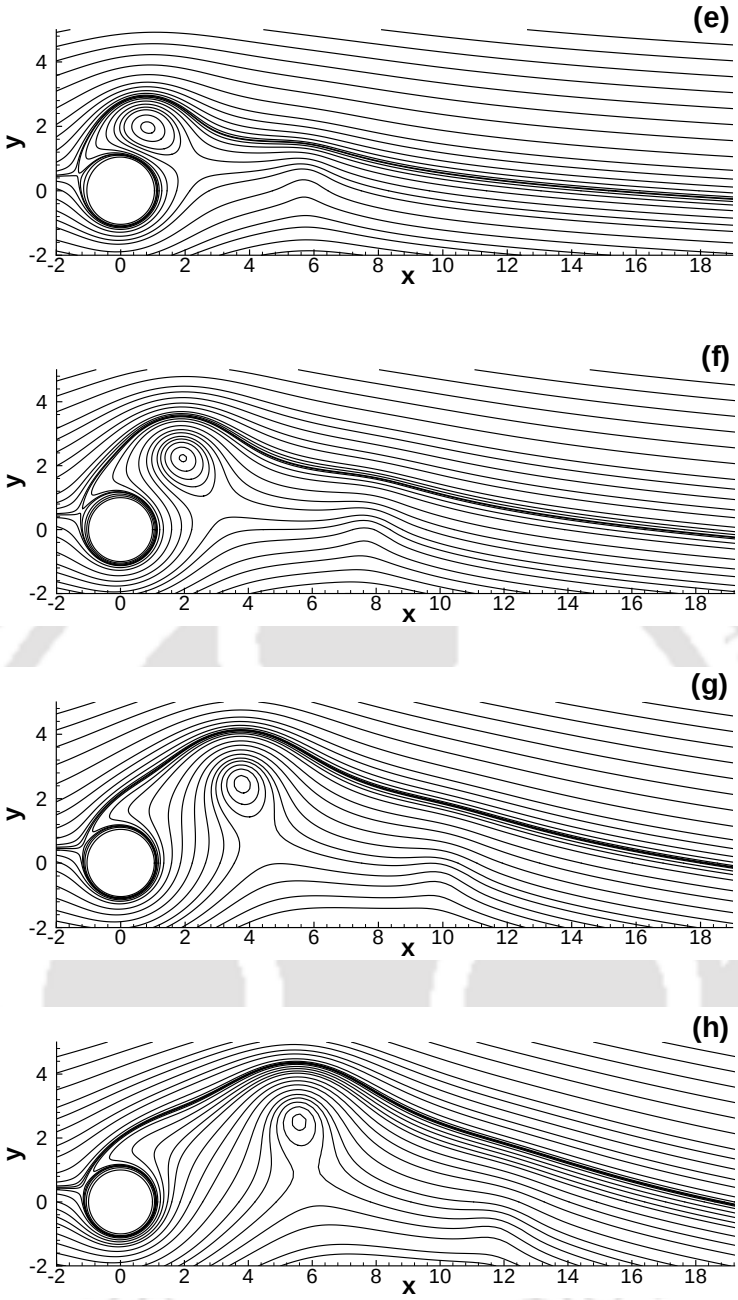

Figure 5.34: *Instantaneous streamlines for* $Re = 500$, $\alpha = 3.0$ *at various times. (e) t=8.0, (f) t=12.0, (g) t=16.0, (h) t=20.0.*

this vortex moves towards downstream (figures 5.34(e) to 5.34(h)). It is worthwhile mentioning that at this particular α value, even till $t = 20$, no secondary vortex is seen. This is also corroborated by the vorticity contours presented in figure 5.35 where no vortex shedding of opposite rotational direction is seen. The vorticity contours shown in the region near the cylinder and further downstream all bear negative values. This also indicates that increasing the value of α suppresses vortex shedding.

In figures 5.36(a) and 5.36(b) we present the evolution of the drag coefficients and the paths of the centers of the first vortex for different α values. While a periodic pattern is observed for $\alpha = 0.5$ and $\alpha = 1.0$, it is not so for $\alpha = 3.0$ (figure 5.36(a)). Figure 5.36(b) clearly indicates that with the increase in α value, the centers move to higher positions. It can also be seen from the trajectory for $\alpha = 3$ in figure 5.36(b) that the center of the first vortex for this α moves in the backward direction first and then moves in the forward direction, which is consistent with our earlier discussion on streamline patterns for this Re-α combination. Figures 5.37 and 5.38 compares our computed vorticity distributions along the surface of the cylinder at different time stations side by side with the numerical results of Badr and dennis ([19]) for $\alpha = 0.5$ and 1 respectively. These comparisons exhibit excellent agreements between the two results. It is obvious from these figures that the variation in the separated region where the cylinder is moving upstream ($0 < \theta < 40^o$) is different from where it is moving in the downstream direction ($320^o < \theta < 360^o$).

In figures 5.39(a) and 5.39(b), we show the u-velocity distribution along the axis of the flow for $\alpha = 0.5$ and 1 respectively. However, the pattern is different for $\alpha = 3.0$ for larger t-values as can be seen from figure 5.40(a) and 5.40(b), where we have shown the u-velocity distribution along the axis and the solid surface vorticity distribution of the flow for $\alpha = 3$. These figures are in conformity with the sense of rotation and formation of the vortices in the early stages of the flow depicted in figures 5.23(a) to 5.23(e), 5.28(a) to 5.28(d) and 5.33(a) to 5.33(d) respectively for $\alpha = 0.5$, 1.0 and 3.0.

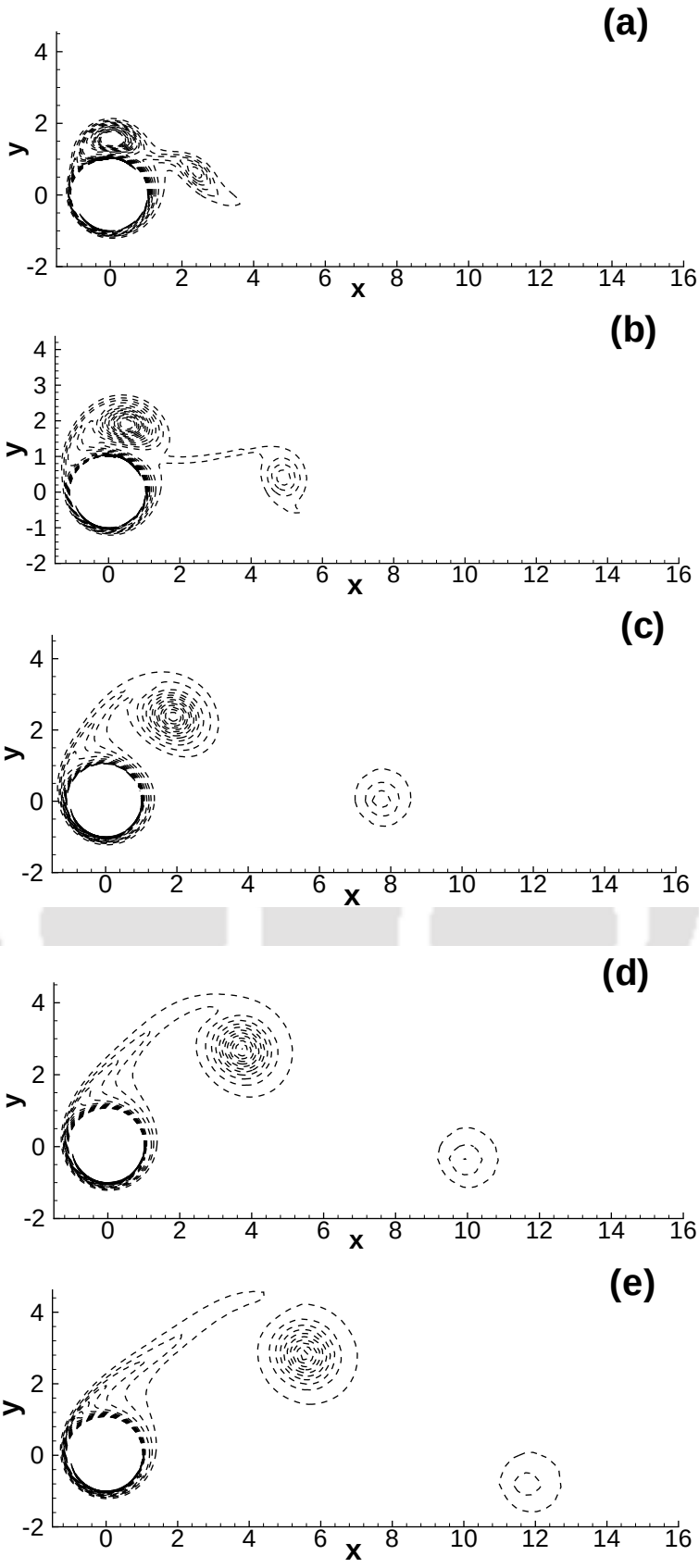

Figure 5.35: *Evolution of vorticity contours for* $Re = 500$, $\alpha = 3.0$. *(a) t=5.0, (b) t=8.0, (c) t=12.0, (d) t=16.0, (e) t=20.0.*

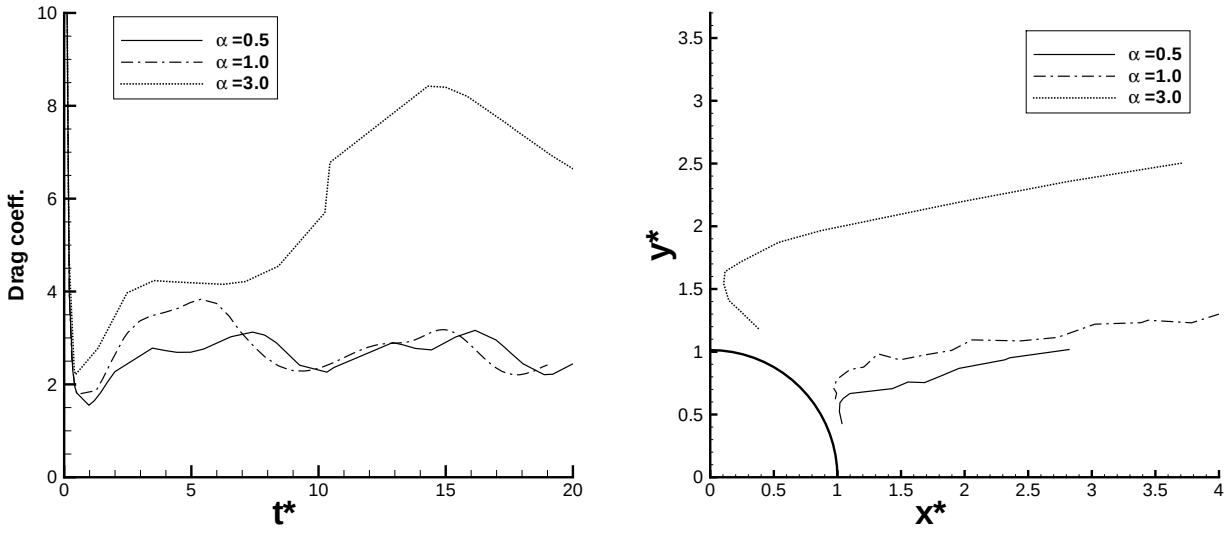

(a) (b)

Figure 5.36: *Time evolution of (a) drag coefficient and (b) path of the center of first vortex for* $Re = 500$ *and different* α *values.*

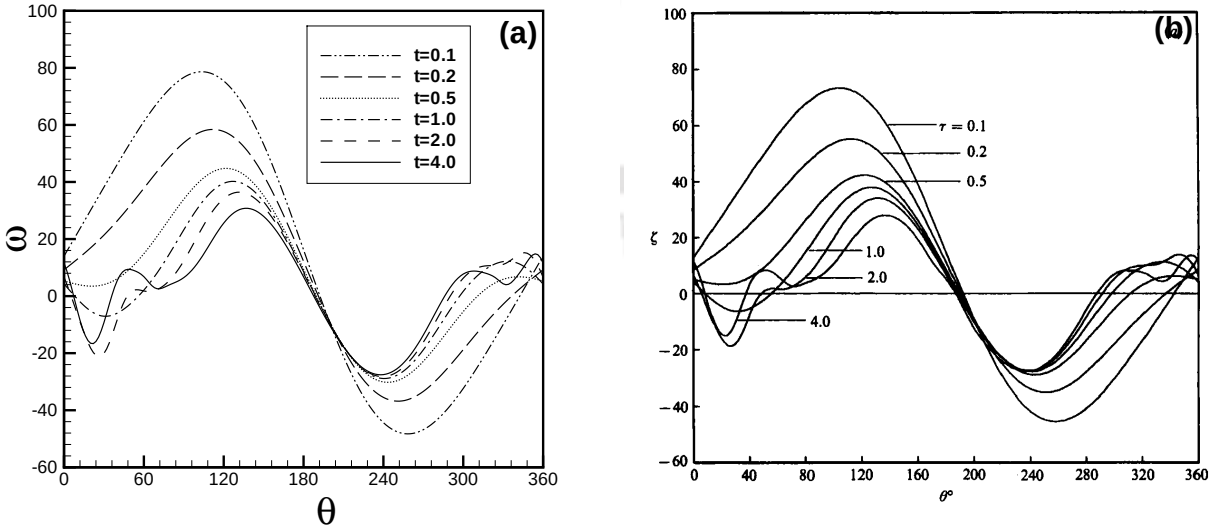

Figure 5.37: *Comparison of vorticity on the cylinder for* $Re = 500$ *and* $\alpha = 0.5$*, (a) present, (b) Badr et.al. ([36]).*

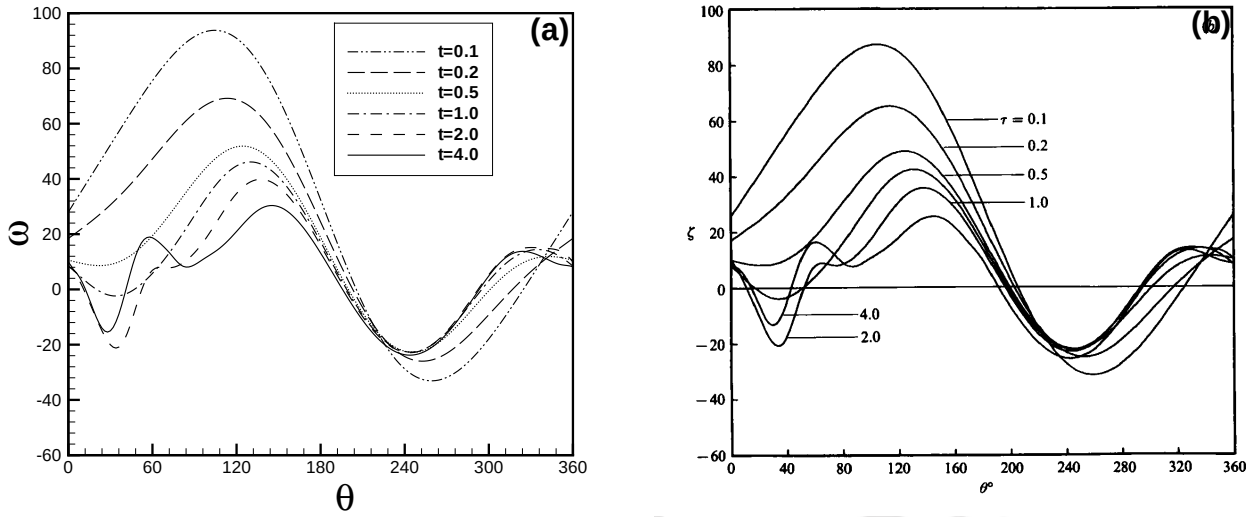

Figure 5.38: *Comparison of vorticity on the cylinder for* $Re = 500$ *and* $\alpha = 1.0$, *(a) present, (b) Badr et.al. ([36]).*

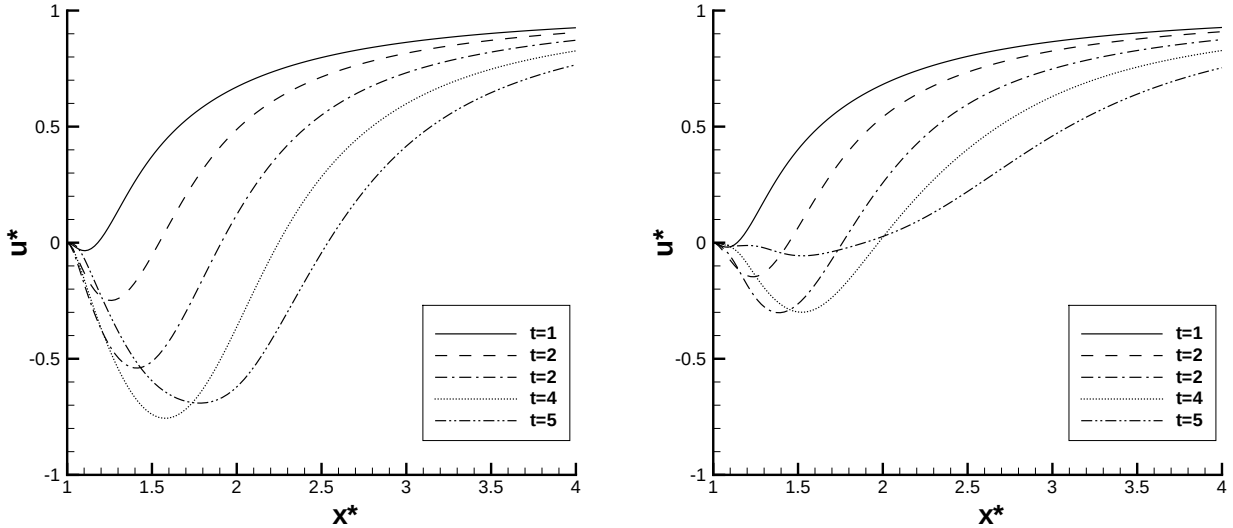

(a) (b)

Figure 5.39: *u-velocity profiles on* $\theta = 0$ *for* $Re = 500$ *and (a)* $\alpha = 0.5$, *(b)* $\alpha = 1.0$ *at different time levels.*

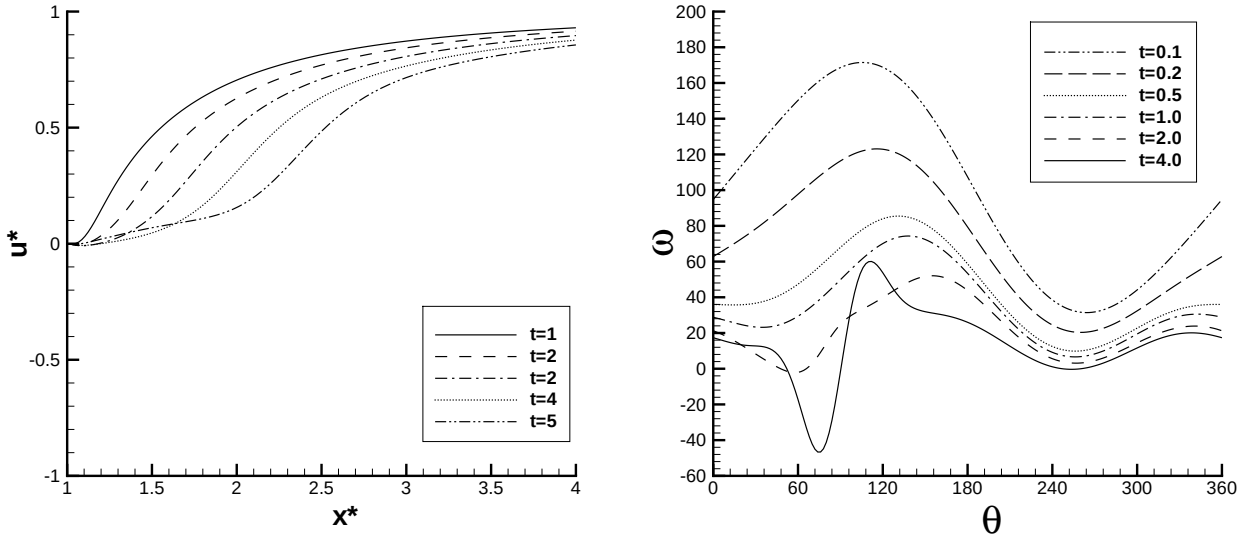

(a) (b)

Figure 5.40: *(a) u-velocity profile on* $\theta = 0$ *and (b) solid surface vorticity for* $Re = 500$, $\alpha = 3.0$ *at different time levels.*

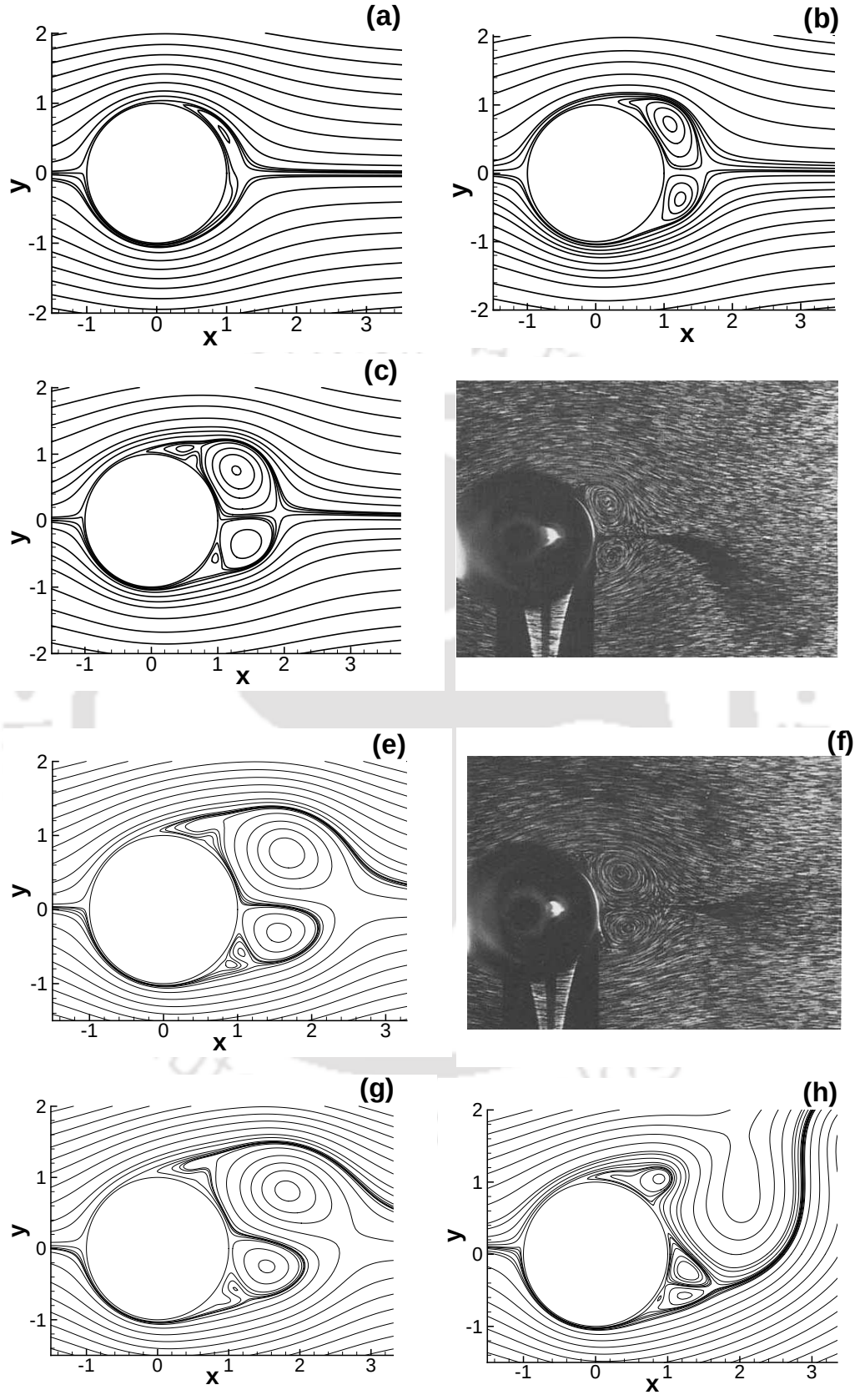

Figure 5.41: *Instantaneous streamlines for $Re = 1000$, $\alpha = 0.5$ at various times. (a) t=1.0, (b) t=2.0, (c) t=3.0, (d) t=3.0 ([36]), (e) t=4.0, (f) t=4.0 ([36]), (g) t=6.0, (h) t=11.0.*

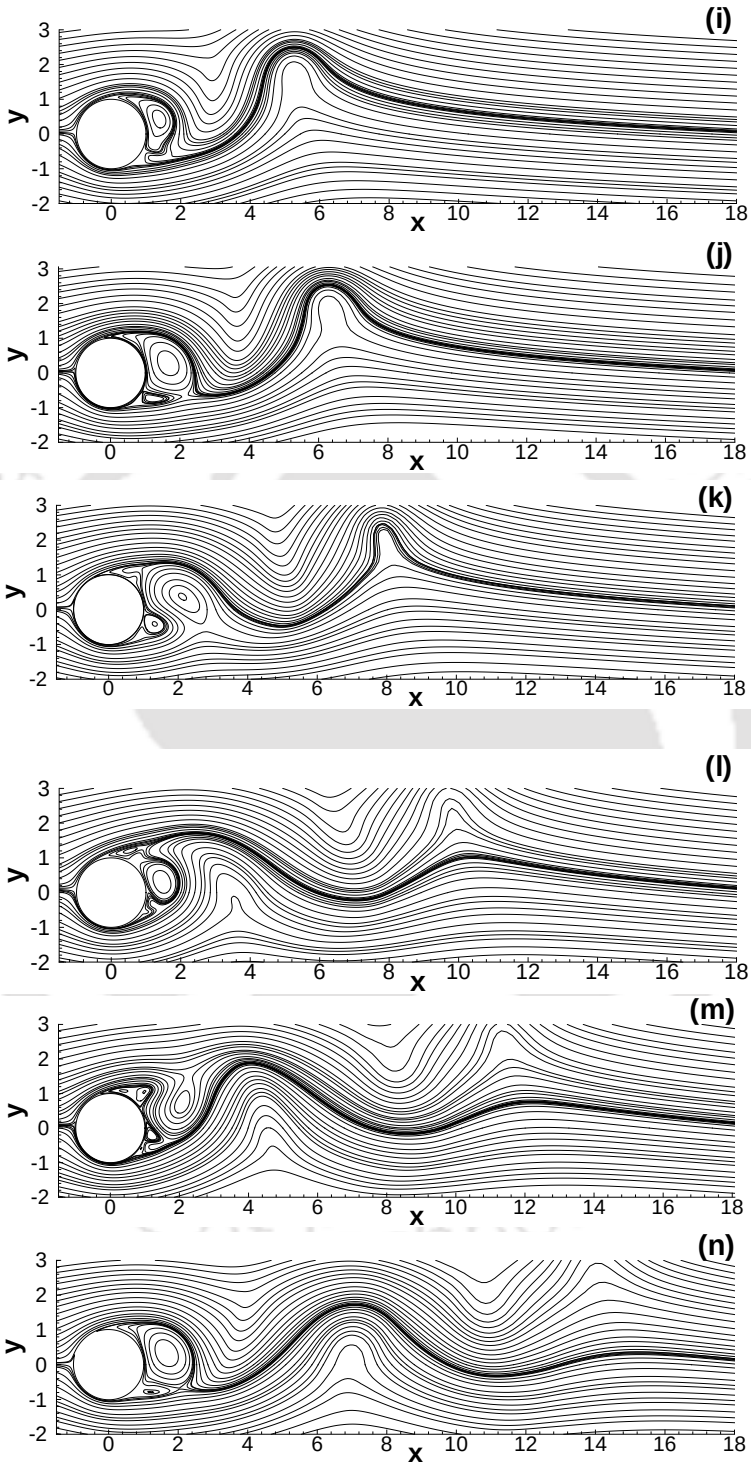

Figure 5.42: *Instantaneous streamlines for* $Re = 1000$, $\alpha = 0.5$ *at various times. (i) t=12.0, (j) t=13.0, (k) t=15.0, (l) t=17.0, (m) t=18.0, (n) t=20.0.*

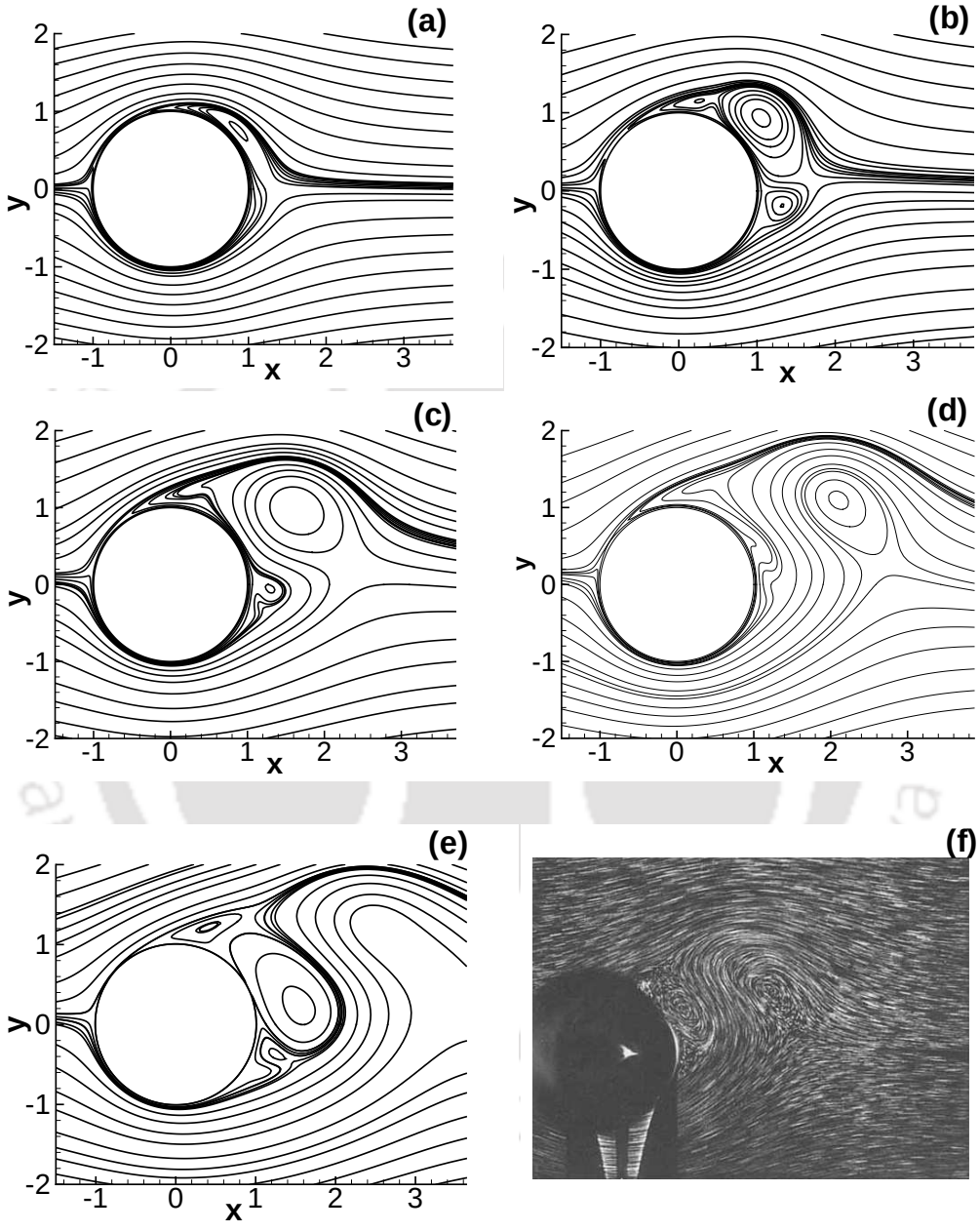

Figure 5.43: *Instantaneous streamlines for Re = 1000, α = 1.0 at various times. (a) t=1.0, (b) t=2.0, (c) t=4.0, (d) t=5.0, (e) t=7.0, (f) t=7.0 ([36]).*

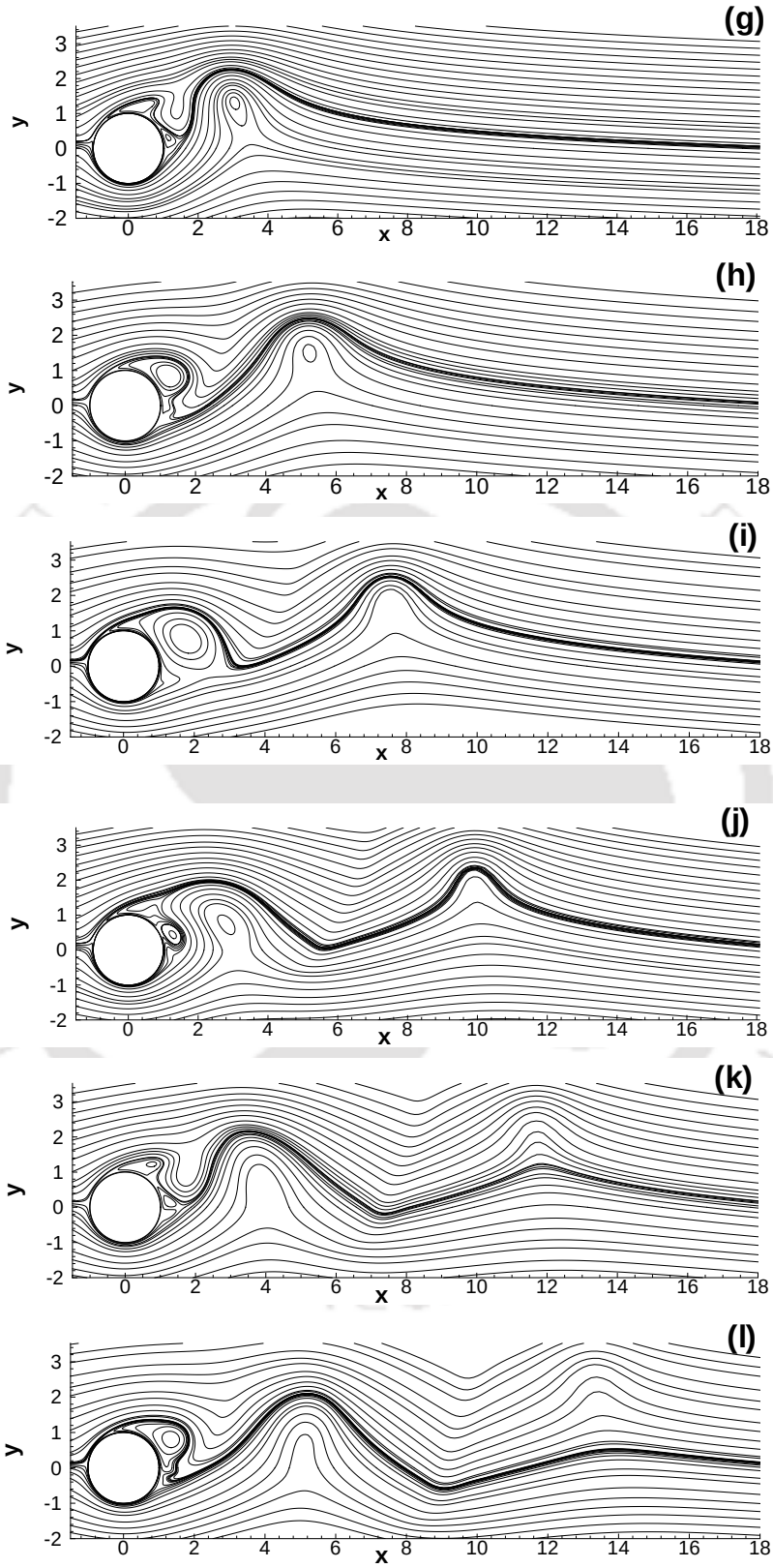

Figure 5.44: *Instantaneous streamlines for* $Re = 1000$, $\alpha = 1.0$ *at various times. (g) t=9.0, (h) t=11.0 (i) t=13.0, (j) t=15.0, (k) t=18.0, (l) t=20.0.*

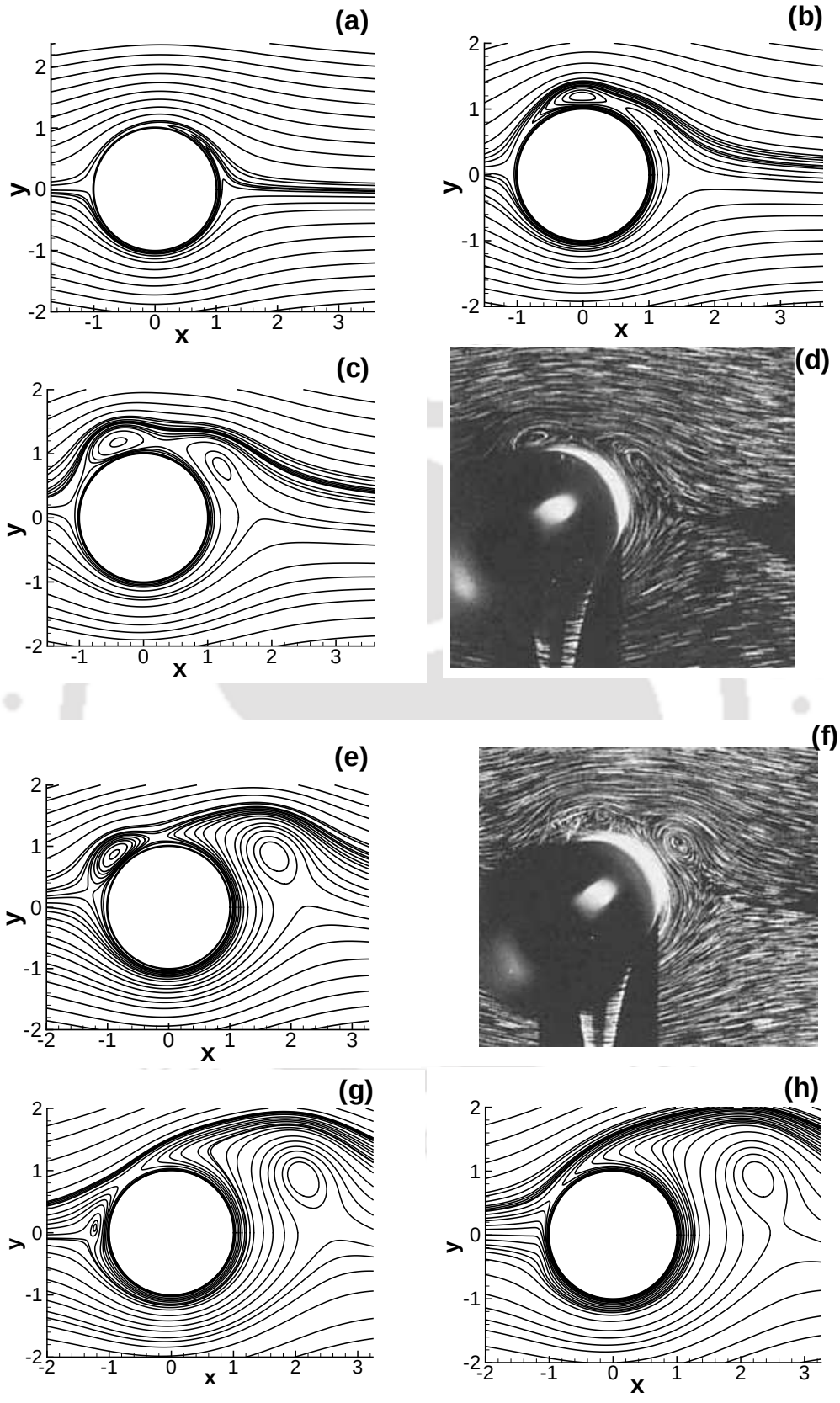

Figure 5.45: *Instantaneous streamlines for* $Re = 1000$, $\alpha = 3.0$ *at various times. (a) t=1.0, (b) t=2.0, (c) t=3.0, (d) t=3.0 ([36]), (e) t=4.0, (f) t=4.0 ([36]), (g) t=4.2, (h) t=4.4.*

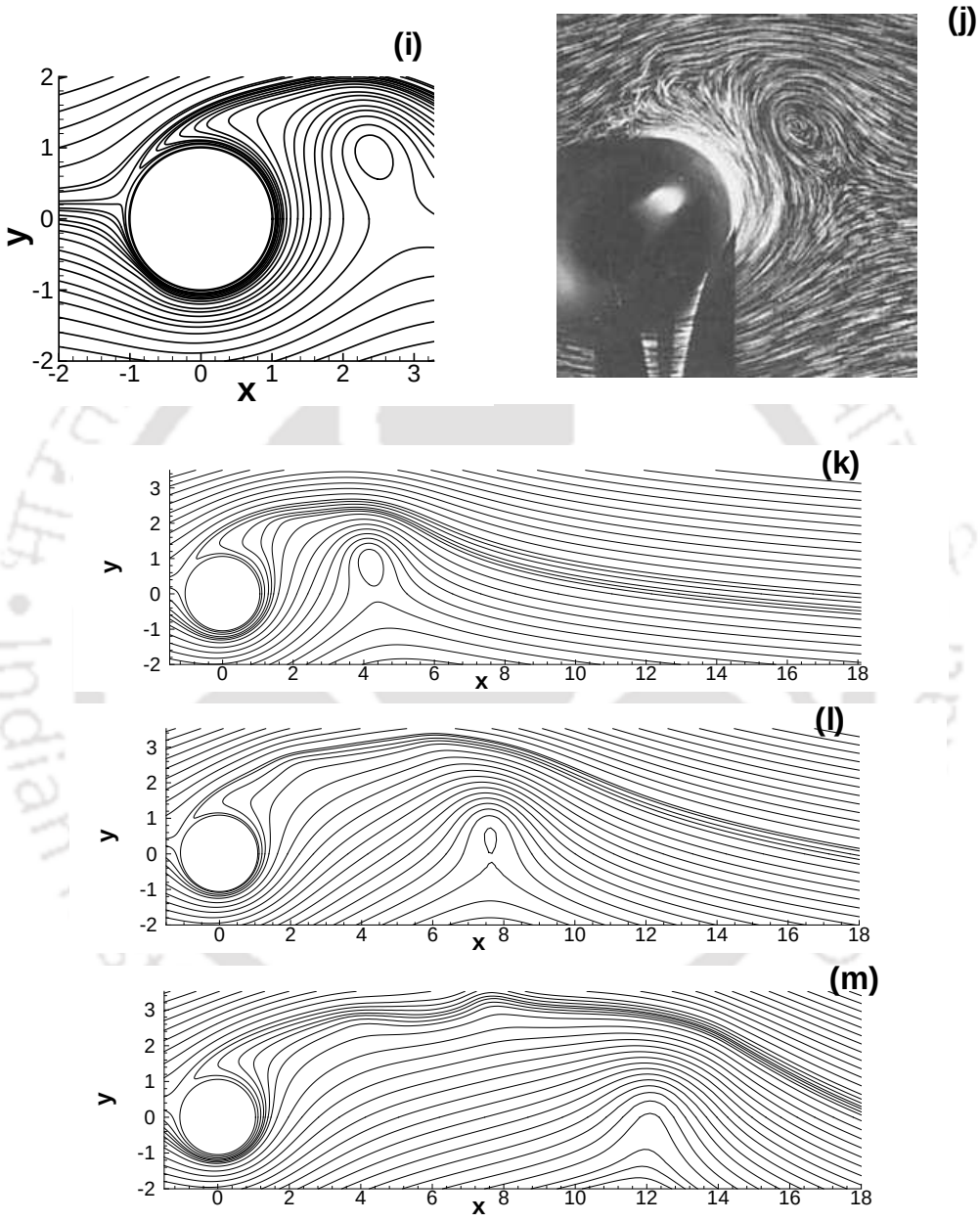

Figure 5.46: *Instantaneous streamlines for* $Re = 1000$, $\alpha = 3.0$ *at various times. (i) t=6.0, (j) t=6.0 ([36]), (k) t=10.0, (l) t=15.0, (m) t=20.0.*

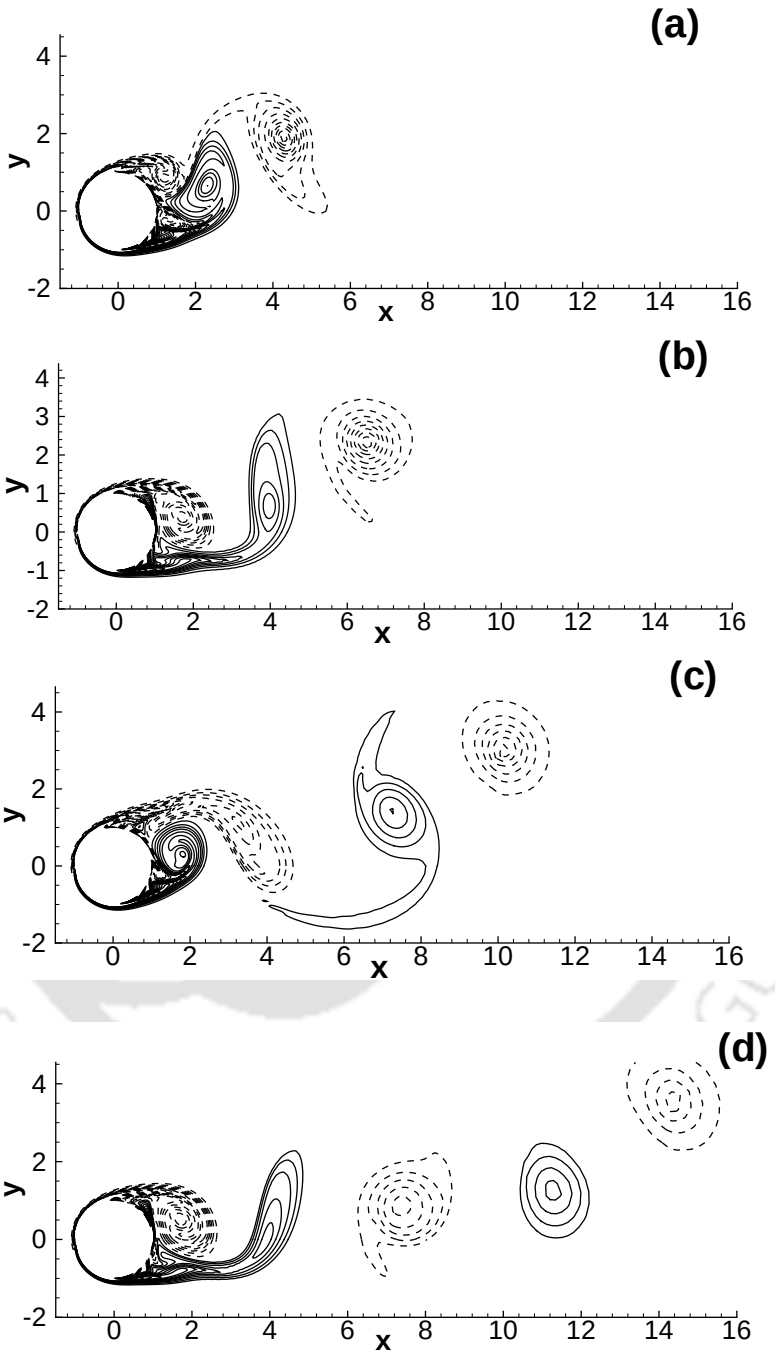

Figure 5.47: *Evolution of vorticity contours for* $Re = 1000$ *and* $\alpha = 0.5$. *(a) t=8.0, (b) t=12.0, (c) t=18.0, (d) t=24.0.*

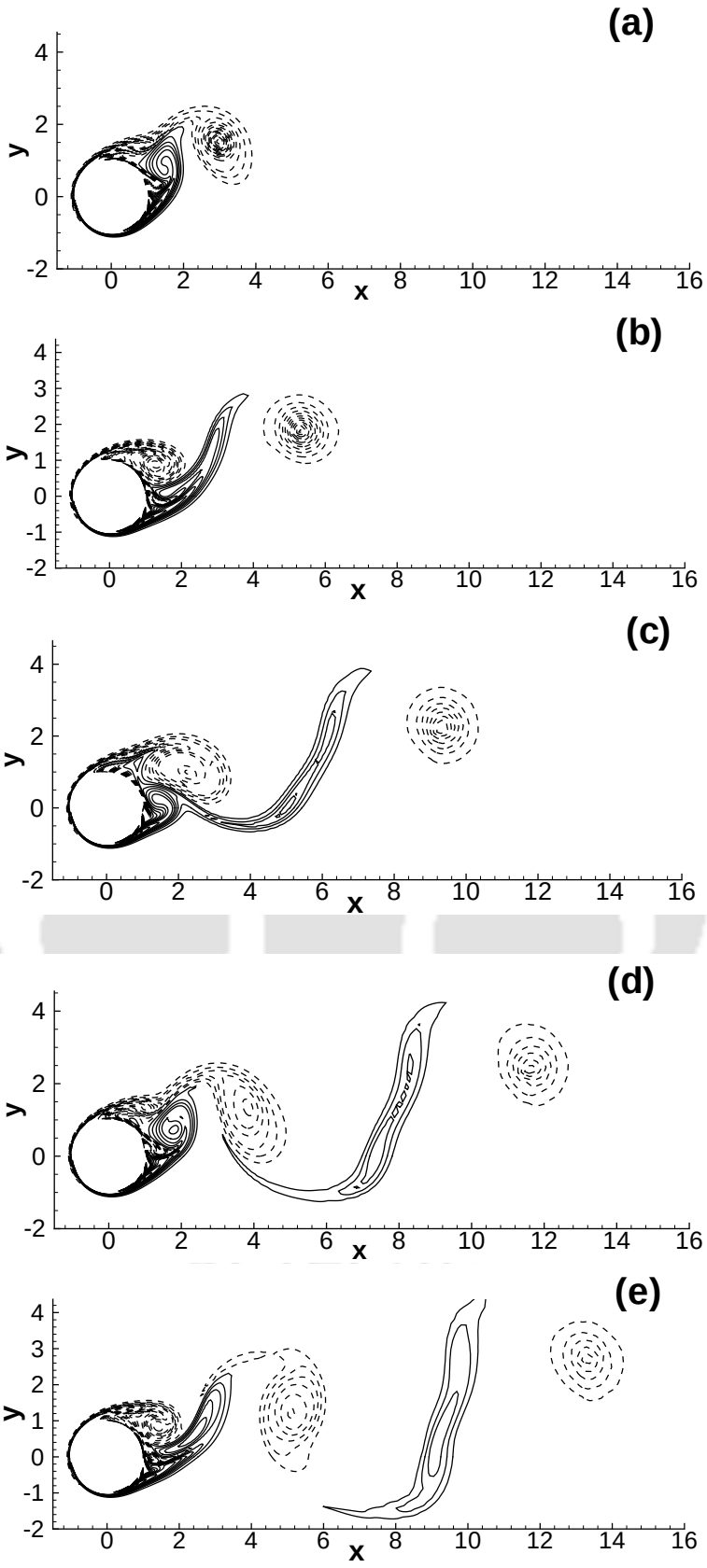

Figure 5.48: *Evolution of vorticity contours for* $Re = 1000$ *and* $\alpha = 1.0$. *(a) t=5.0, (b) t=9.0, (c) t=12.0, (d) t=16.0, (e) t=20.0.*

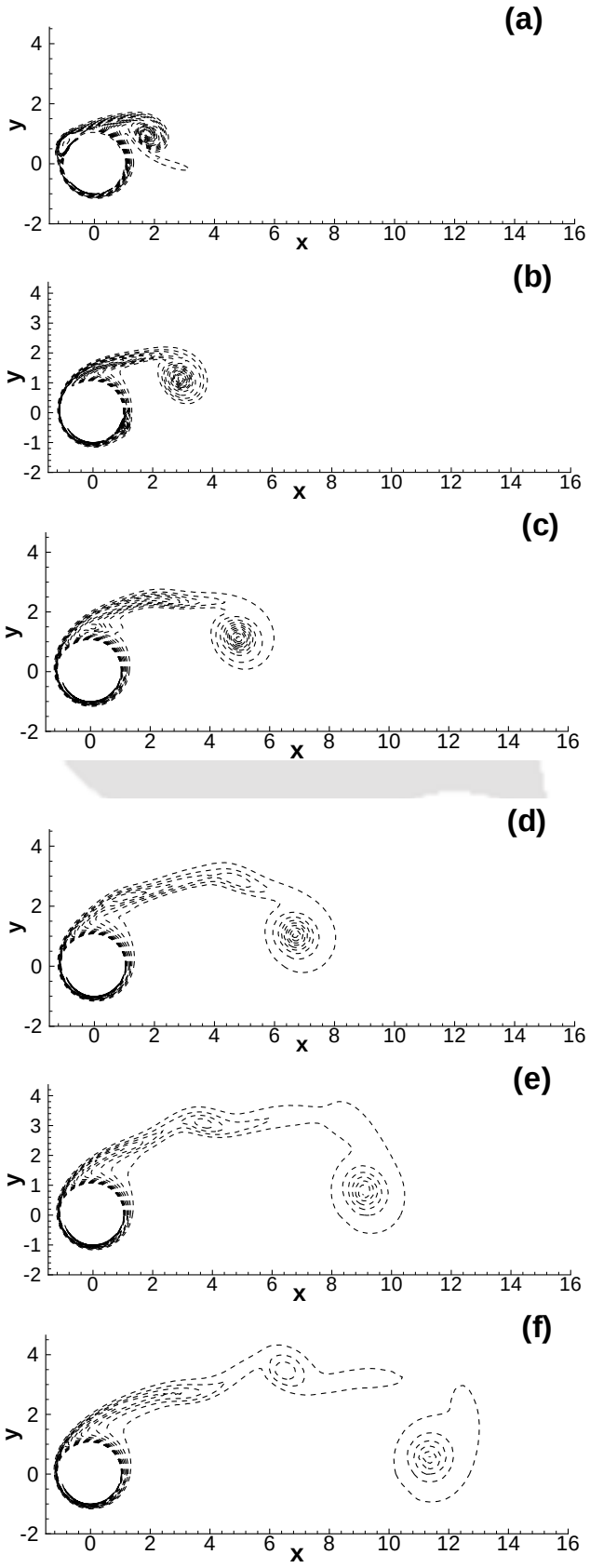

Figure 5.49: *Evolution of vorticity contours for* $Re = 1000$ *and* $\alpha = 3.0$. *(a) t=5.0, (b) t=9.0, (c) t=12.0, (d) t=16.0, (e) t=18.0, (f) t=20.0.*

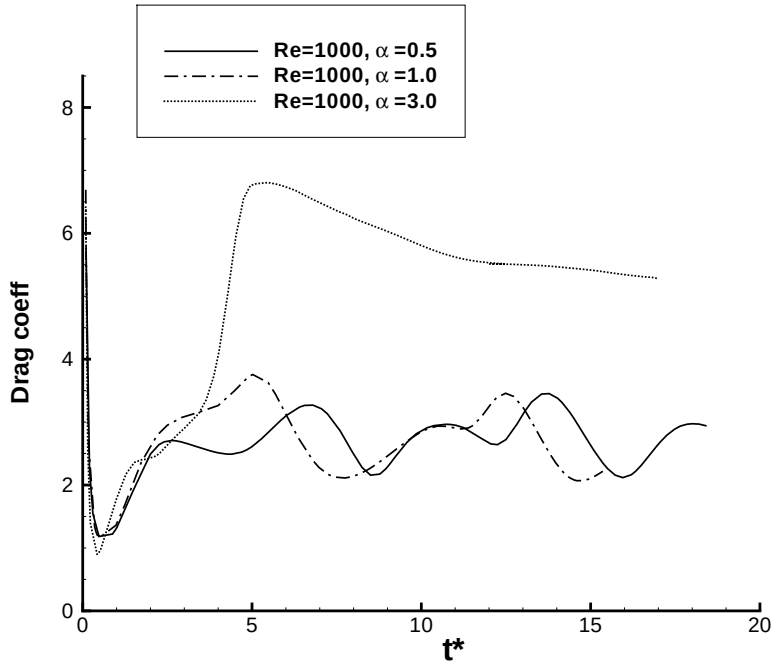

Figure 5.50: *Evolution of drag coefficients for* $Re = 1000$ *for different* α *values.*

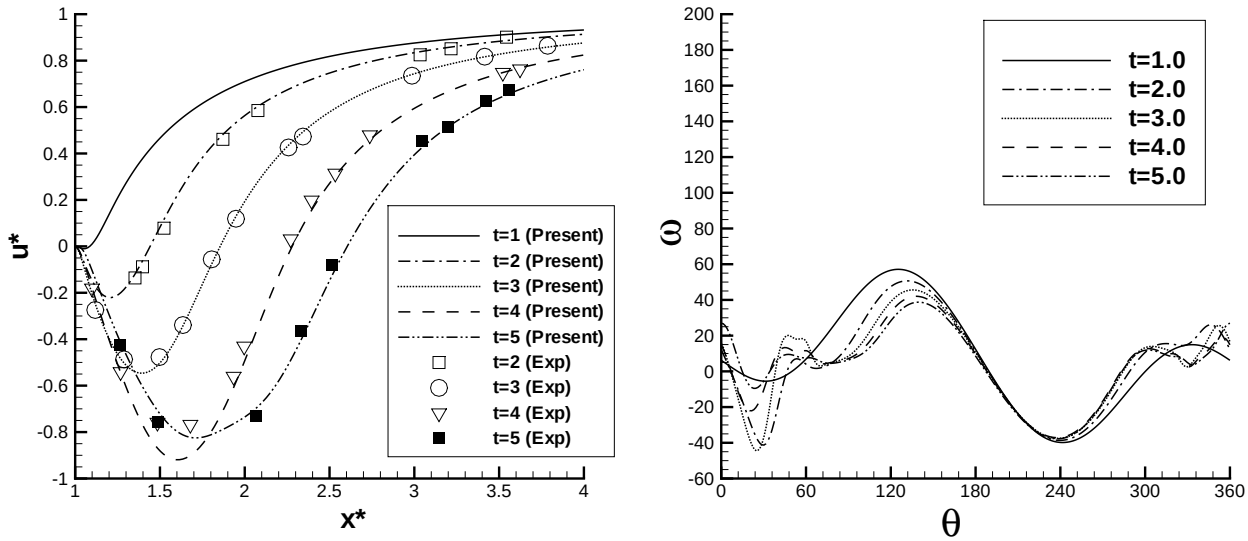

(a) (b)

Figure 5.51: *(a) u-velocity profile on* $\theta = 0$ *and (b) solid surface vorticity for* $Re = 1000$, $\alpha = 0.5$ *at different time levels.*

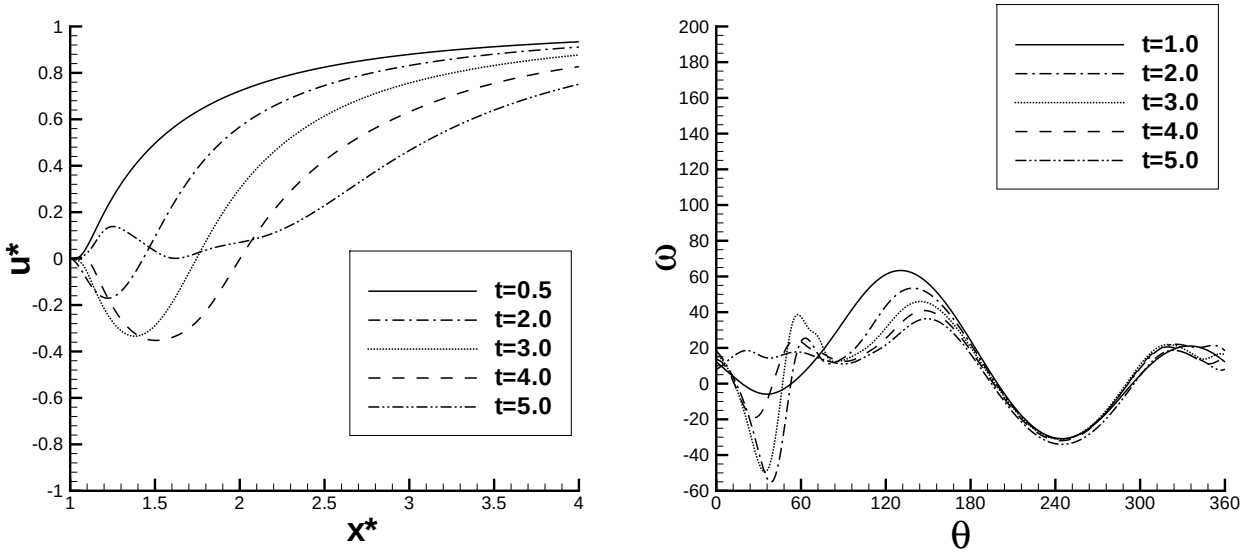

(a) (b)

Figure 5.52: *(a) Comparison of u-velocity profile on $\theta = 0$ and (b) solid surface vorticity for $Re = 1000$, $\alpha = 1.0$ at different time levels.*

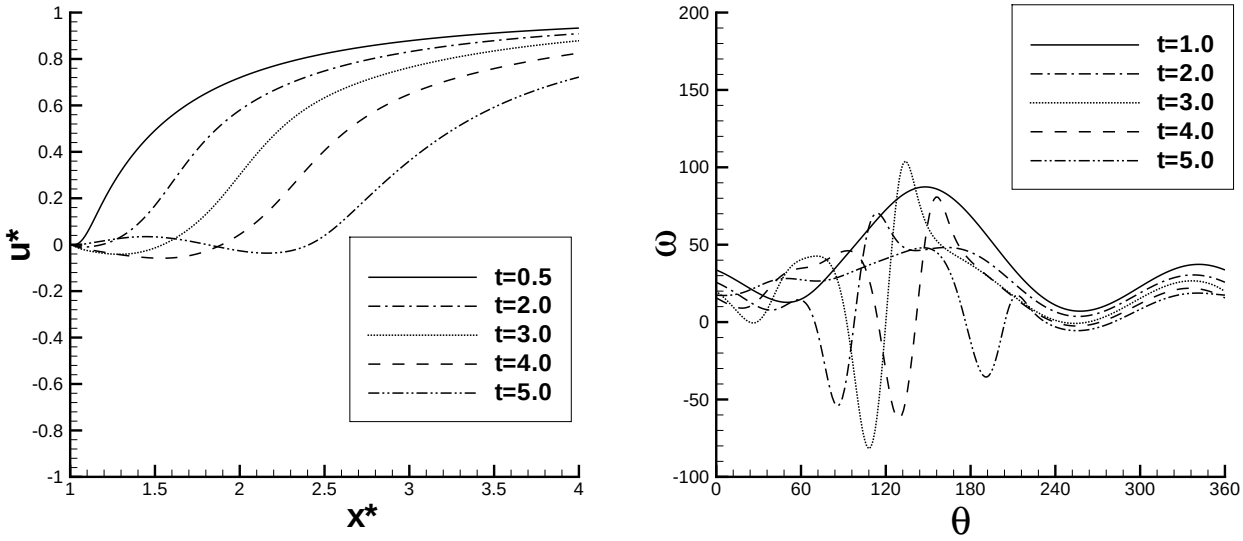

(a) (b)

Figure 5.53: *(a) u-velocity profile on $\theta = 0$ and (b) solid surface vorticity for $Re = 1000$, $\alpha = 3.0$ at different time levels.*

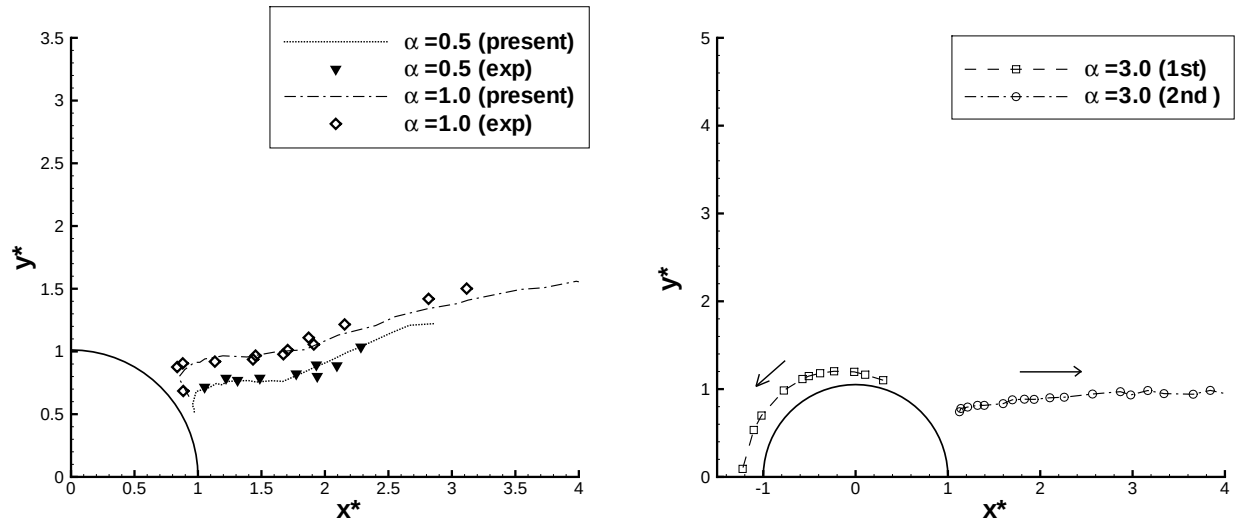

(a) (b)

Figure 5.54: *Trajectories of (a) the first vortex for $\alpha = 0.5$ and 1.0 and (b) both first and second vortices for $\alpha = 3.0$ for $Re = 1000$.*

5.4.3 Results for $Re = 1000$ and $\alpha = 0.5$, 1 and 3

In this section, we discuss the effect of the rotating parameter over a slightly high Reynolds number $Re = 1000$. As in the case for $Re = 500$, we take three different rotating parameter values $\alpha = 0.5$, 1 and 3.

For $\alpha = 0.5$, soon after the impulsive start, the first vortex starts to form above the x-axis, growing in size. At the same time, a secondary vortex develops just below the x-axis (see fig 5.41(a) and 5.41(b)). At around $t = 3$, two small tertiary vortices start to form almost at the same time, one just behind the first vortex and other one between the second vortex and the cylinder surface. Figure 5.41(c) is our computed result at $t = 3$, which is almost same as the corresponding experimental result of Badr *et al.* [21] (figure 5.41(d)). Till this moment, the flow patterns are almost same as that of the experimental results of Bouard and Coutanceau [26]. At around $t = 4$, the first vortex reaches its maximum size; the second vortex moves upwards and grows in size, and the lower tertiary vortex starts to change its shape. Figures 5.41(e) and 5.41(f) are the corresponding numerical and experimental ([21]) results at $t = 4$. Both the figures 5.41(c) and 5.41(e) are very close to the corresponding experimental results (figures 5.41(d) and 5.41(f)). At around $t = 6$, the first vortex starts to move downstream and the second vortex increases in size and moves upwards (see figure 5.41(g)). During subsequent times, the secondary vortex grows in size and detaches from the cylinder surface and sheds in the downstream. In the mean time the two tertiary vortices get close to each other to form a single vortex and a small quaternary vortex develops below the lower tertiary vortex (figure 5.41(h)). The single tertiary vortex then starts to grow in size with time (figure 5.42(i)). At around $t = 13$, that single vortex starts detaching from the cylinder surface and the small quaternary vortex starts growing (figure 5.42(j)). As time progresses, the single vortex opens up and shed to the downstream and the small vortex grows in size and starts to move upwards through the solid surface (figures 5.42(k) and 5.42(l)). After some time, this vortex also detaches from the cylinder wall and shed in the downstream. At the same time, a pair of vortices start to form above and below the positive x-axis and next to the cylinder wall. Afterwards the flow patterns observed between $t = 11$ and $t = 13$ get repeated (figures 5.42(m) and 5.42(n)).

For $\alpha = 1$, we get almost similar patterns for first few time steps. After the impulsive start, the first vortex starts to grow above the x-axis. In a few moments, the secondary vortex starts to develop below the x-axis and simultaneously another small vortex forms in front of the first vortex (figures 5.43(a) and 5.43(b)). At around $t = 4$, this small vortex disappears and the first vortex starts to open up and move towards the downstream (figure 5.43(c)). During this time, the secondary vortex starts to sink and at around $t = 5$, this vortex disappears (figure 5.43(d)). At around $t = 7$, two new vortices come into the picture. One is much above the x-axis and other one is below the x-axis.

Meanwhile, the secondary vortex starts to move up and grows in size. We compare the numerical and the corresponding experimental ([21]) results of the flow pattern at $t = 7$ in figures 5.43(e) and 5.43(f); as can be seen from the figures, a very good agreement is obtained. After a very short time, the secondary vortex open up and shed into the downstream (figure 5.44(g)). During next few instants of time, the twin vortices approach each other and coalesce (figure 5.44(h)). At around $t = 13$, this new vortex starts to shed into the downstream and another vortex develops at the middle of the cylinder surface (figure 5.44(i)). During subsequent times, flow patterns which was seen after $t = 7$ onwards (figures 5.44(e), 5.44(g), 5.44(h)), get repeated (figures 5.44(j) to 5.44(l)). This indicates that periodic pattern is carried over for $\alpha = 1$ as well.

Finally, we consider the case for $\alpha = 3$; as was the case for $Re = 500$, a noticeable change is observed in the flow patterns. Unlike the previous α values, no vortex is seen till $t = 1$ (fig 5.45(a)). At around $t = 2$, the first vortex starts to grow from the top of the cylinder (figure 5.45(b)). Soon after that, at around $t = 3$, another vortex starts to grow above the x-axis (see fig 5.45(c)). The patterns shown in the experimental result of [21] in figure 5.45(d) are almost identical with our computed result. These two vortices then start to move in opposite directions. The first vortex starts to move along the rotational direction and the second vortex starts to move along the main flow direction (figure 5.45(e)) at $t = 4.0$. The experimental result of [21] shown in figure 5.45(f) is very close to the numerical result in figure 5.45(e). The first and second vortices then move further in the same direction; the first vortex starts to sink while second vortex grows in size. At around $t = 6$, the first vortex totally vanishes and the second vortex starts to open up (figures 5.45(g), 5.45(h) and 5.46(i)). As time progresses, the secondary vortex sheds into the downstream but no further vortex develops (see fig 5.46(k) to 5.46(m)). Figures 5.45(d) and 5.45(f) and 5.46(j) show the corresponding experimental results at time $t = 3.0$, $t = 4.0$ and $t = 6.0$. In all the cases our numerical results are pretty close to the experimental ones; however, at $t = 6.0$, the closeness is less apparent. This is due to the fact that around this time, the effects of three-dimensional instability become pronounced, specially in the wake. Our observations are consistent with the ones given by Badr *et al.* [21].

In figures 5.47, 5.48, and 5.49, we present the evolution of the vorticity contours for $\alpha = 0.5$, 1.0 and 3.0 respectively for the same time intervals as the streamline patterns shown in figures 5.41 to 5.46. One can see a similar pattern for the contours corresponding to their counterparts for $Re = 500$. The only difference is that the contours are more stretched out and the midlines dividing the von Kármán streets lie slightly above the $\theta = 0$ line compared to the ones for $Re = 500$.

Figure 5.50 shows the variation of drag coefficients for the three rotational parameters discussed above. As in the case for $Re = 500$, the periodic nature of the flows is evident

for the first two α values, which no longer persists for $\alpha = 3$. Figures 5.51((a),(b)), 5.52((a),(b)) and 5.53((a),(b)) depict the distribution of u-velocity along $\theta = 0$ and the vorticity along the cylinder wall side by side for $\alpha = 0.5$, 1.0 and 3.0 respectively for different times. These figures again show the difference in the variations in regions where the cylinder is moving in upstream and downstream directions. In figure 5.51(a), we also compare our computed u-velocity distribution at different times with the experimental ones of Badr *et al.* [21] for $\alpha = 0.5$. Again our computed results are excellent match with the experimental ones. In figure 5.54(a), we show the time variation of the computed centers of the first vortex with that of the experimental results of Badr et al. [21] for $\alpha = 0.5$ and 1; our results are much closer to the experimental results than their numerical results. Finally, in figure 5.54(b), we show the time variation of the computed centers of first and second vortex for $\alpha = 3$. This figure clearly shows the opposite movements of these two vortices which is consistent with our earlier discussion on streamline patterns for this Re-α combination.

5.5 Conclusion:

In this chapter, we carry out a numerical investigation of the unsteady flow past an impulsively started rotating and translating circular cylinder for Reynolds numbers $Re = 200,\ 500$ and 1000 in the range of the rotational parameter $0.5 \leq \alpha \leq 3.25$ using the transient HOC scheme developed in Chapter 3. We present a detailed discussion on the effect of the rotational parameters on the flow patterns. We observe that for all the Reynolds numbers, a periodic pattern is seen for moderate values of α, namely, 0.5 and 1.0, while it no longer exists for $\alpha \geq 2.0$. We notice that higher the values of Re and α, more complicated is the flow. For example, for $Re = 1000$, $\alpha = 3.0$, after the emergence of the first and second vortices, they begin to move in different directions; the first one along the rotational and the second one along the translating flow directions. In all the cases, increase in the rotation speed was seen to suppress the vortex shedding. We compare our computed results with the existing experimental and numerical results and excellent comparison is obtained in all the cases.

भारतीय प्रौद्योगिकी संस्थान गुवाहाटी
Indian Institute of Technology Guwahati

Chapter 6

An efficient HOC scheme for Parabolic Equations with Discontinuities

In this chapter we propose a novel approach of clubbing an existing HOC idea with specifically devised approximation of the derivatives at certain points of the problem domain to tackle problems represented by elliptic and parabolic equations having discontinuities of different types [1]. This approach for 1D equations will later be extended to 2D elliptic equations with circular interfaces in Chapter 7.

6.1 Introduction

The 1D elliptic equation in the variable ϕ can be written as

$$(\beta(x)\phi'(x))' + \kappa(x)\phi(x) = f(x) \tag{6.1}$$

in a simple region Ω. We are interested in the situation where there is an irregular point α in Ω across which β, κ, and f may be discontinuous or there may exist a point source term thereat. As a result, the solution or its derivatives will be discontinuous across α. For example, if β is discontinuous across the interface, while κ, and f are continuous, then ϕ and $\beta\dfrac{\partial\phi}{\partial n}$ will be discontinuous if the normal derivative $\dfrac{\partial\phi}{\partial n}$ is discontinuous. A dipole source may also occur, in which f contains the derivative of the delta function, and as a result the solution ϕ itself becomes discontinuous across the interface. Equation (6.1) with the above assumptions describes many situations that arise quite frequently in science and engineering [1, 4, 18]. They include biochemical processing, solid mechanics, porous media flow, heat transfer, multiphase flow, mining and many others. For example, in problems involving dissimilar materials, at the interfaces, the material properties (elastic moduli, permeability, conductivity, etc) are discontinuous.

[1] Review of this work is in progress in *Journal of Applied Mathematics and Computation.*

The last few decades have seen several approaches for numerically solving the interface equations [3, 23, 43, 79, 73]. Most of them were on uniform space grids and their global order of accuracy was at most second. For example, Leveque and Li's Immersed interface Method [73] considered the interface which was typically not aligned to the grid but rather cut between grid points. They used central difference approximation for the points far from the point of discontinuity (termed regular points) and to tackle the the discontinuity, special treatment was made for the approximation at the points just next to the discontinuity (termed irregular points). This method is second order accurate for the regular points and first order accurate for the irregular points. In their work [56], Huang and Li have shown second order convergence of the immersed interface method for a one-dimensional model problem. In [23], Beyer and Leveque discuss the one-dimensional model for the Immersed Boundary Method. They use the idea of Peskin's Immersed Boundary Method [92] for incompressible fluid dynamics which applies to the two or three dimensional version of (6.1). The idea was to solve the Navier-Stokes equations on a uniform grid in a rectangular region containing the complicated time-varying geometry like that of the heart wall. The one-dimensional analogue of this numerical method is based on the notion of solving the difference equations only on the uniform grid, obtaining the solution value at the point α via some form of interpolation. Typically the point α will not lie exactly at a grid point, and therefore the delta function must be replaced by inhomogeneous terms in the difference equations on the uniform grid. One way to accomplish this is to replace the delta function $\delta(x)$ by a discrete approximation $d_h(x)$. They introduced a new discrete delta function d_h^4, which yielded a second-order accurate approximation for any singular source function f. They further provided a brief analysis of the one-dimensional Immersed Interface Method for both steady and time-dependent problems. They had also shown that good accuracy (second order) can be obtained through this method if certain amount of care is exercised in designing this method.

As outlined in the introduction chapter, one way of obtaining higher order compactness is the use of the original partial differential equation. Using this approach, MacKinnon and Carey [79] developed an analysis of the material discontinuities in the one-dimensional elliptic problem and a class of high order accurate formula to compute derivatives for both 1D and 2D cases. But as uniform grids could not capture the material properties (e.g., heat flux) properly at the interface on coarser grids, to reach higher accuracy, they used some local correction terms. Their method mainly dealt with the situation when there is a discontinuity in the coefficients of the partial derivatives but they did not include the case where there could be a discontinuity in the source term or there is a point source or both.

In the present study, we use a similar approach to discretize the most general form

of (6.1) and its time-dependent variant which includes discontinuities of the dependent variable, the flux, the convection coefficient and the source term. Our scheme is at least third order accurate at the regular points and exactly third order accurate at the irregular points. In our method we use nonuniform space grids in such a way that grid points cluster around the point of discontinuity and the point of discontinuity or the interface itself is not a node. We use different approaches to discretize the given differential equation at the regular and irregular points. For the steady case, at regular points, it is based on a recently developed HOC scheme [62] on nonuniform space grids for two-dimensional convection-diffusion equations with variable, smooth and continuous coefficients and for the time-dependent case it is based on the transient HOC scheme [64] on nonuniform space grids for two-dimensional transient Navier-Stokes equations. At the points just next to the discontinuity, the grids points are so clustered that the interval formed by the two points on either side of it behaves almost like one single point. We derive special schemes at those two points for both steady and transient cases, which in conjunction with the scheme at the regular points produces excellent results for all the cases which have been considered here. We also perform some convergence and related analysis for the approximation of the steady-state case.

This chapter is organized in the following way: Section 6.2 deals with the mathematical formulations and discretization procedures, Section 6.3 with convergence related analysis for the steady state formulation, Section 6.4 with numerical examples, and finally Section 6.5, the conclusions.

6.2 Mathematical Formulations and Discretization Procedures

6.2.1 Steady state case

The one dimensional elliptic equation (6.1) in conservation form may be put in the form

$$-(\beta\phi')' + \kappa\phi = f + C_2\delta(x-\alpha) \tag{6.2}$$

where Ω is the interval $[0,1]$, δ is the Dirac Delta function and C_2 is the value of the point source at $x=\alpha$. The boundary conditions for ϕ are given at $x=0$ and $x=1$. Here, the function $\beta(x)$ is allowed to be discontinuous at $x=\alpha$. For simplicity, we assume that they are smooth functions, although discontinuities in the functions $b(x)$, $\kappa(x)$ and $f(x)$ could be handled with minor modifications ([73]). We also allow an additional constraint to be imposed on the solution: that the function ϕ should have a jump discontinuity at $x=\alpha$ of specified strength C_1. That is

$$[\phi] = \phi^+ - \phi^- = C_1 \tag{6.3}$$

with [.] denoting the jump and $\phi^+ = \lim_{x\to\alpha+} \phi(x)$, $\phi^- = \lim_{x\to\alpha-} \phi(x)$. From equation (6.2) we can get another jump relation of flux at x=α of the form

$$[\beta\phi_x] = \beta^+\phi_x^+ - \beta^-\phi_x^- = C_2. \tag{6.4}$$

We now divide $[0, 1]$ with the nonuniform grid points $0 = x_0$, x_1, x_2,.....,x_{n-1}, $x_n = 1$. We assume that α is not a grid point, that is $x_j < \alpha < x_{j+1}$ with $0 < j < n$ for some subinterval $[x_j, x_{j+1}]$ of $[0, 1]$. The grid points are clustered about the point α in such a manner that the subinterval $[x_j, x_{j+1}]$ is extremely small. In other words the jump at α will be the difference between the corresponding values at x_{j+1} and x_j. So we can easily express the jumps $[\phi]$ and $[\beta\phi_x]$ at $x = \alpha$ as follows

$$[\phi] = \phi_{j+1} - \phi_j = C_1 \tag{6.5}$$

and

$$[\beta\phi_x] = \beta_{j+1}(\phi_x)_{j+1} - \beta_j(\phi_x)_j = C_2 \tag{6.6}$$

Here we have used the following transformation to generate a nonuniform grid with clustering near $x = \alpha$ [13]

$$x_i = \alpha\left\{1 + \frac{\sinh(r(i - B))}{\sinh(rB)}\right\}$$

where r is a parameter determining the intensity of clustering and

$$B = \frac{1}{2r} ln\left[\frac{1 + \alpha(e^r - 1)}{1 + \alpha(e^{-r} - 1)}\right]$$

with $0 \le i \le n$. The grids generated with different values of r and n can be seen in figures 6.1(a) and 6.1(b).

Let us first consider the points away from $x = \alpha$ (regular points [73]). For this, firstly, we divide the interval $[0, 1]$ into two subintervals $[0, \alpha)$ and $(\alpha, 1]$ together with the two interface boundary conditions (6.3) and (6.4) at $x = \alpha$. For $i \neq j$, $j + 1$ the solution ϕ is smooth in the interval (x_i, x_{i+1}). The equation (6.2) will be jump free in each of the subintervals $[0, \alpha)$ and $(\alpha, 1]$ and in each subintervals (6.2) can be written in a more general form as

$$-\beta(x)\frac{d^2\phi}{dx^2} + b(x)\frac{d\phi}{dx} + \kappa(x)\phi = f \tag{6.7}$$

where, $b(x) = -\dfrac{d\beta(x)}{dx}$. To discretize equation (6.7) at the i^{th} point, we use the 1D version of the scheme proposed in reference [62]:

$$(-A_i\delta_x^2 + B_i\delta_x + \tilde{C}_i)\phi_i = F_i \tag{6.8}$$

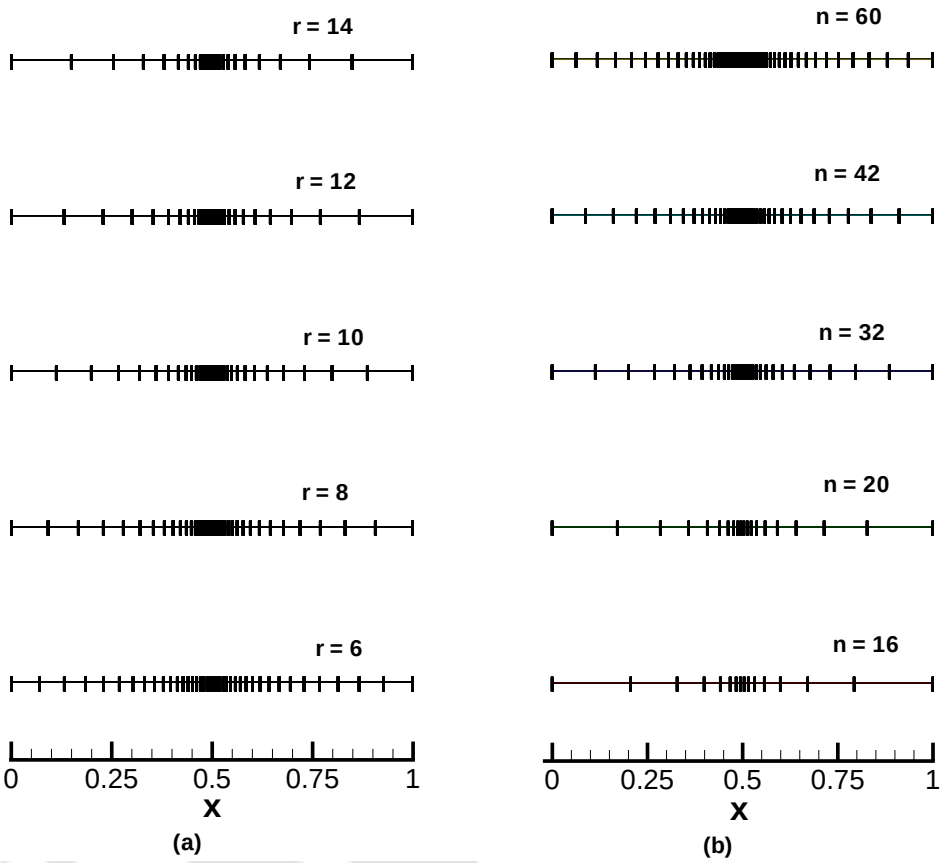

Figure 6.1: *Grids with (a) r-variation ($n = 40$) and (b) n-variation ($r = 8$) with clustering about the point* $x = \dfrac{1}{2}$.

for all $i \neq j, j+1$, where,

$$\tilde{C}_i = \frac{1}{\beta}((H_1 - \gamma H_2)\{\delta_x - 0.5(x_f - x_b)\delta_x^2\} + H_2\delta_x^2)\kappa$$

$$B_i = \left(1 + \frac{1}{\beta}(H_1 - \gamma H_2)\delta_x + \frac{1}{\beta}\left\{H_2 - 0.5(x_f - x_b)(H_1 - \gamma H_2)\right\}\delta_x^2\right) b$$
$$+\frac{1}{\beta}\left((H_1 - \gamma H_2) + 2H_2\left\{\delta_x - 0.5(x_f - x_b)\delta_x^2\right\}\right)\kappa$$

$$A_i = \beta + \frac{1}{\beta}\left((H_1 - \gamma H_2)\{\delta_x\beta - 0.5(x_f - x_b)\delta_x^2\beta - b\} + H_2\delta_x^2\beta + \kappa\right) + 0.5(x_f - x_b)B_i$$

$$F_i = \left(1 + \frac{1}{\beta}(H_1 - \gamma H_2)\delta_x + \frac{1}{\beta}\{H_2 - 0.5(x_f - x_b)(H_1 - \gamma H_2)\}\delta_x^2\right) f_i$$

$$H_1 = \frac{1}{6}\left\{2\beta(x_f - x_b) - bx_f x_b\right\}$$

$$H_2 = \frac{1}{24}\left\{2\beta(x_f^2 + x_b^2 - x_f x_b) - bx_f x_b(x_f - x_b)\right\}$$

$$\gamma = \frac{1}{\beta}\left\{2(\delta_x\beta - 0.5(x_f - x_b)\delta_x^2\beta) - b\right\}$$

Here at the i^{th} point $x_f = x_{i+1} - x_i$ and $x_b = x_i - x_{i-1}$, δ_x and δ_x^2 are the first and second order central difference operators (see the appendix) and the local truncation error is of order $O\left(\frac{x_f^5 + x_b^5}{x_f + x_b}\right)$ thereat.

For the points in the immediate neighborhood of $x = \alpha$, namely, the points x_j and x_{j+1} (which we call irregular points), we may take $x_{j+1} - \alpha = d_2 \to 0$ and $\alpha - x_j = d_1 \to 0$ as these points are extremely close to α.

For the points x_1, x_2, ..., x_{j-1}, x_{j+2}, x_{j+3}, ..., x_{n-1} equation (6.8) will give $(n-3)$ equations in $(n-1)$ unknowns. To find the solution of the linear algebraic system having $(n-1)$ unknowns, we need further two relations that will enable us to determine the solution vector uniquely. They can be easily found from the jump conditions (6.5) and (6.6) at $x = \alpha$.

Differentiating (6.7) with respect to x (assuming ϕ and the coefficients to be smooth enough) we get

$$\phi_{xxx} = \left(\frac{\beta_x + b}{\beta}\right)\phi_{xx} + \left(\frac{b_x + \kappa}{\beta}\right)\phi_x + \frac{\kappa_x}{\beta}\phi - \frac{f_x}{\beta} \tag{6.9}$$

Using onesided difference at the point x_{j+1} we have

$$\begin{aligned}
(\phi_x)_{j+1} &= \delta_x^+\phi_{j+1} - \frac{x_f}{2}(\phi_{xx})_{j+1} - \frac{x_f^2}{6}(\phi_{xxx})_{j+1} + O\left(x_f^3\right) \\
&= \delta_x^+\phi_{j+1} - \frac{x_f}{2}(\phi_{xx})_{j+1} - \frac{x_f^2}{6}\left\{\left(\frac{\beta_x + b}{\beta}\right)_{j+1}\phi_{xx}|_{j+1}\right. \\
&\left. + \left(\frac{b_x + \kappa}{\beta}\right)_{j+1}(\phi_x)_{j+1} + \left(\frac{\kappa_x}{\beta}\right)_{j+1}\phi_{j+1} - \left(\frac{f_x}{\beta}\right)_{j+1}\right\} + O\left(x_f^3\right) \\
&= \delta_x^+\phi_{j+1} - \left(\frac{x_f}{2} + \frac{x_f^2}{6}\frac{(\beta_x)_{j+1} + b_{j+1}}{\beta_{j+1}}\right)\left\{\frac{b_{j+1}}{\beta_{j+1}}(\phi_x)_{j+1} + \frac{\kappa_{j+1}}{\beta_{j+1}}\phi_{j+1} - \frac{f_i}{\beta_{j+1}}\right\} \\
&- \frac{x_f^2}{6}\frac{(b_x)_{j+1} + \kappa_{j+1}}{\beta_{j+1}}(\phi_x)_{j+1} - \frac{x_f^2}{6}\frac{(\kappa_x)_{j+1}}{\beta_{j+1}}\phi_{j+1} - \frac{x_f^2}{6}\frac{(f_x)_{j+1}}{\beta_{j+1}} + O(x_f^3)
\end{aligned}$$

$$\begin{aligned}
&\Rightarrow \left\{1 + \left(\frac{x_f}{2} + \frac{x_f^2}{6}\frac{(\beta_x)_{j+1} + b_{j+1}}{\beta_{j+1}}\right)\frac{b_{j+1}}{\beta_{j+1}} + \frac{x_f^2}{6}\frac{(b_x)_{j+1} + \kappa_{j+1}}{\beta_{j+1}}\right\}(\phi_x)_{j+1} \\
&= \frac{\phi_{j+2}}{x_f} - \left\{\frac{1}{x_f} + \left(\frac{x_f}{2} + \frac{x_f^2}{6}\frac{(\beta_x)_{j+1} + b_{j+1}}{\beta_{j+1}}\right) \times \frac{\kappa_{j+1}}{\beta_{j+1}} + \frac{x_f^2}{6}\frac{(\kappa_x)_{j+1}}{\beta_{j+1}}\right\}\phi_{j+1} \\
&+ \frac{x_f^2}{6}\frac{(f_x)_{j+1}}{\beta_{j+1}} + \left(\frac{x_f}{2} + \frac{x_f^2}{6}\frac{(\beta_x)_{j+1} + b_{j+1}}{\beta_{j+1}}\right)\frac{f_{j+1}}{\beta_{j+1}} + O(x_f^3)
\end{aligned}$$

Hence,

$$(\phi_x)_{j+1} = \frac{1}{P_{j+1}}\left\{\frac{\phi_{j+2}}{x_f} - l_{j+1}\phi_{j+1} + \frac{x_f^2}{6}\frac{(f_x)_{j+1}}{\beta_{j+1}} + m_{j+1}f_{j+1}\right\} + O(x_f^3) \quad (6.10)$$

where

$$P_{j+1} = 1 + \left(\frac{x_f}{2} + \frac{x_f^2}{6}\frac{(\beta_x)_{j+1} + b_{j+1}}{\beta_{j+1}}\right)\frac{b_{j+1}}{\beta_{j+1}} + \frac{x_f^2}{6}\frac{(b_x)_{j+1} + \kappa_{j+1}}{\beta_{j+1}} \quad (6.11)$$

$$l_{j+1} = \frac{1}{h_{j+1}} + \left(\frac{x_f}{2} + \frac{x_f^2}{6}\frac{(\beta_x)_{j+1} + b_{j+1}}{\beta_{j+1}}\right)\frac{\kappa_{j+1}}{\beta_{j+1}} + \frac{x_f^2}{6}\frac{(\kappa_x)_{j+1}}{\beta_{j+1}} \quad (6.12)$$

$$m_{j+1} = \frac{1}{\beta_{j+1}}\left(\frac{x_f}{2} + \frac{x_f^2}{6}\frac{(\beta_x)_{j+1} + b_{j+1}}{\beta_{j+1}}\right) \quad (6.13)$$

On a similar line

$$\begin{aligned}
(\phi_x)_j &= \delta_x^-\phi_j + \frac{x_b}{2}(\phi_{xx})_j - \frac{x_f^2}{6}(\phi_{xxx})_j + O\left(x_b^3\right) \\
&= \delta_x^-\phi_j + \frac{x_b}{2}\phi_{xx}|_j - \frac{x_b^2}{6}\left\{\left(\frac{\beta_x + b}{\beta}\right)_j(\phi_{xx})_j + \left(\frac{b_x + \kappa}{\beta}\right)_j\phi_x|_j + \left(\frac{\kappa_x}{\beta}\right)_j\phi_j\right. \\
&- \left.\left(\frac{f_x}{\beta}\right)_j\right\} + O\left(x_b^3\right) \\
&= \delta_x^-\phi_j + \left(\frac{x_b}{2} - \frac{x_b^2}{6}\frac{(\beta_x)_j + b_j}{\beta_j}\right)\left\{\frac{b_j}{\beta_j}(\phi_x)_j + \frac{\kappa_j}{\beta_j}\phi_j - \frac{f_i}{\beta_j}\right\} \\
&- \frac{x_b^2}{6}\frac{(b_x)_j + \kappa_j}{\beta_j}\phi_x|_j - \frac{x_b^2}{6}\frac{(\kappa_x)_j}{\beta_j}\phi_j + \frac{x_b^2}{6}\frac{(f_x)_j}{\beta_j} + O(x_b^3)
\end{aligned}$$

$$\begin{aligned}
\Rightarrow \left\{1 - \left(\frac{x_b}{2} - \frac{x_b^2}{6}\frac{(\beta_x)_j + b_j}{\beta_j}\right)\frac{b_j}{\beta_j} + \frac{x_b^2}{6}\frac{(b_x)_j + \kappa_j}{\beta_j}\right\}(\phi_x)_j &= \left\{\frac{1}{x_b} + \left(\frac{x_b}{2} - \frac{x_b^2}{6}\frac{(\beta_x)_j + b_j}{\beta_j}\right)\right. \\
\left.\frac{\kappa_j}{\beta_j} - \frac{x_b^2}{6}\frac{(\kappa_x)_j}{\beta_j}\right\}\phi_j - \frac{\phi_{j-1}}{x_b} + \frac{x_b^2}{6}\frac{(f_x)_j}{\beta_j} - \left(\frac{x_b}{2} - \frac{x_b^2}{6}\frac{(\beta_x)_j + b_j}{\beta_j}\right)\frac{f_j}{\beta_j} + O\left(x_b^3\right)
\end{aligned}$$

$$\Rightarrow (\phi_x)_j = \frac{1}{Q_j}\left\{r_j\phi_j - \frac{\phi_{j-1}}{x_b} + \frac{x_b^2}{6}\frac{(f_x)_j}{\beta_j} - t_j f_j\right\} + O(x_b^3) \quad (6.14)$$

where

$$Q_j = 1 - \left(\frac{x_b}{2} - \frac{x_b^2}{6}\frac{(\beta_x)_j + b_j}{\beta_j}\right)\frac{b_j}{\beta_j} + \frac{x_b^2}{6}\frac{(b_x)_j + \kappa_j}{\beta_j}, \quad (6.15)$$

$$r_j = \frac{1}{x_b} + \left(\frac{x_b}{2} - \frac{x_b^2}{6}\frac{(\beta_x)_j + b_j}{\beta_j}\right)\frac{\kappa_j}{\beta_j} - \frac{x_b^2}{6}\frac{(\kappa_x)_j}{\beta_j}, \quad (6.16)$$

$$\tau_j = \frac{1}{\beta_j}\left(\frac{x_f}{2} - \frac{x_f^2}{6}\frac{(\beta_x)_j + b_j}{\beta_j}\right). \quad (6.17)$$

Using equations(6.6), equations (6.10) and (6.14) yield

$$C_2 = \frac{\beta_{j+1}}{P_{j+1}}\left(\frac{\phi_{j+2}}{x_f} - l_{j+1}\phi_{j+1} + \frac{h_{j+1}^2}{6}\frac{(f_x)_{j+1}}{\beta_{j+1}} + m_{j+1}f_{j+1}\right) - \frac{\beta_j}{Q_j}\left(r_j\phi_j - \frac{1}{x_b}\phi_{j-1} + \frac{x_b^2}{6}\frac{(f_x)_j}{\beta_j} - \tau_j f_j\right) + O(x_f^3, x_b^3) \tag{6.18}$$

where P_{j+1}, l_{j+1}, m_{j+1}, Q_j, r_j, τ_j are as defined in (6.11)-(6.13) and (6.15)-(6.17).

Thus equations (6.5) and (6.18) are the two extra relations for grid points j and $j+1$. With this, we have exactly $(n-1)$ equations in the same number of unknowns and ϕ_i's can be computed at all the specified points.

6.2.2 Unsteady case

For the unsteady case our 1D equation (6.2) in conservation form can be written as

$$\eta\frac{\partial\phi}{\partial t} - (\beta\phi')' + \kappa\phi = f + C_3\delta(x-\alpha) \tag{6.19}$$

where Ω is the interval $[0,1]$, δ is the Dirac Delta function and C_3 is the value of the point source at $x = \alpha$. For the regular grids, we can express (6.19) in a more general form like (6.7) as

$$\eta\frac{\partial\phi(x,t)}{\partial t} - \beta(x,t)\frac{\partial^2\phi(x,t)}{\partial x^2} + b(x,t)\frac{\partial\phi(x,t)}{\partial x} + \kappa(x,t)\phi(x,t) = f(x,t) \tag{6.20}$$

where, $b(x,t) = -\dfrac{\partial b(x,t)}{\partial x}$. We use the recently developed transient HOC method on nonuniform grids (Kalita et al [64]) and for the irregular grids points we adopt the same strategy as in the steady-state case. Now, for the regular points, HOC discretization of (6.20) yields

$$\big(-A_i\delta_x^2 + B_i\delta_x + \tilde{C}_i\big)\phi_i^n = G_i, \qquad \forall\ i \neq j, j+1 \tag{6.21}$$

where the expressions for the terms A_i, B_i, $\tilde{C}_i$, H_1, H_2 and ν are same as the corresponding terms described in the steady-state case in section 6.2.1 with the exception of β, b, κ and f being functions of both x and t now. Also

$$G_i = \left(1 + \frac{1}{\beta}\big(H_1 - \nu H_2\big)\delta_x + \frac{1}{\beta}\{H_2 - 0.5(x_f - x_b)(H_1 - \nu H_2)\}\delta_x^2\right)\big(f_i - \eta\frac{\partial\phi}{\partial t}\big).$$

Applying forward differencing for the time derivative, (6.21) can be written as

$$E_i\delta_t^+\phi_i^n + \big(-A_i\delta_x^2 + B_i\delta_x + \tilde{C}_i\big)\phi_i^n = F_i \tag{6.22}$$

Where,

$$E_i = \eta\left(1 + \frac{1}{\beta}(H_1 - \gamma H_2)\delta_x + \frac{1}{\beta}\{H_2 - 0.5(x_f - x_b)(H_1 - \gamma H_2)\}\delta_x^2\right),$$

and F_i as defined in section 6.2.1. Here δ_t^+ denotes the forward difference operator for time with uniform time step Δt and n represents the time level; the coefficients A_i, B_i, $\tilde{C}_i$ and F_i are to be evaluated at the n^{th} time level. Now we introduce a weighted average parameter μ through the approximation of the time derivative $\dfrac{\partial \phi}{\partial t}$ such that $t_\mu = (1-\mu)t^{(n)} + \mu t^{(n+1)}$ where $0 \leq \mu \leq 1$; varying μ yields different time integrators. Thus equation (6.22) reduces to

$$E_i\delta_t^+\phi_i^n + \big(-A_i\delta_x^2 + B_i\delta_x + \tilde{C}_i\big)\big(\mu\phi_i^n + (1-\mu)\phi_i^{n+1}\big) = \mu F_i^n + (1-\mu)F_i^{n+1}. \quad (6.23)$$

Letting $\mu = \frac{1}{2}$ in (6.23) we get a scheme of the Crank-Nicolson type:

$$E_i\big(\frac{\phi_i^{n+1}-\phi_i^n}{\Delta t}\big) + 0.5\big(-A_i\delta_x^2 + B_i\delta_x + \tilde{C}_i\big)\phi_i^{n+1} = 0.5\big(A_i\delta_x^2 - B_i\delta_x - \tilde{C}_i\big)\phi_i^n + 0.5F_i^n + 0.5F_i^{n+1}.$$

After some simplifications and making use of the spatial operators we get

$$\begin{aligned} 0.5\Delta t\left(\frac{B_i}{2h} - \frac{A_i}{hx_f}\right)\phi_{i+1}^{n+1} &+ \{0.5\Delta t\left(\frac{A_i}{h}(\frac{1}{x_f}+\frac{1}{x_b}) + \tilde{C}_i\right) + E_i\}\phi_i^{n+1} \\ - 0.5\Delta t\left(\frac{A_i}{hx_b} + \frac{B_i}{2h}\right)\phi_{i-1}^{n+1} &= 0.5\Delta t\left(\frac{A_i}{hx_f} - \frac{B_i}{2h}\right)\phi_{i+1}^n \\ + \{E_i - 0.5\Delta t\left(\frac{A_i}{h}(\frac{1}{x_f}+\frac{1}{f_b}) + \tilde{C}_i\right)\}\phi_i^n & \\ + 0.5\Delta t\left(\frac{A_i}{hx_b} + \frac{B_i}{2h}\right)\phi_{i-1}^n &+ 0.5\left(F_i^n + F_i^{n+1}\right)\Delta t \end{aligned} \quad (6.24)$$

In short, (6.24) can be written as

$$\sum_{k_1=-1}^{1} W_{i+k_1}\phi_{i+k_1}^{n+1} = \sum_{k_1=-1}^{1} \tilde{W}_{i+k_1}\phi_{i+k_1}^n + 0.5\left(F_i^{n+1} + F_i^n\right)\Delta t \quad (6.25)$$

Where,

$$W_{i+k_1} = -0.5\Delta t p_{i+k_1} + q_{i+k_1},$$

$$\tilde{W}_{i+k_1} = 0.5\Delta t p_{i+k_1} + q_{i+k_1},$$

with

$$p_{i+1} = \frac{A_i}{hx_f} - \frac{B_i}{2h}; \qquad p_i = -\frac{A_i}{h}\left(\frac{1}{x_f}+\frac{1}{x_b}\right) - \tilde{C}_i;$$

$$p_{i-1} = \frac{A_i}{hx_f} - \frac{B_i}{2h}; \qquad q_{i+1} = \frac{\eta}{2\beta h}\left(H_1 - \gamma H_2\right) + \frac{\eta}{\beta h x_f}\{H_2 - 0.5(x_f - x_b)(H_1 - \gamma H_2)\};$$

$$q_i = \eta + \frac{\eta}{\beta h}\left(\frac{1}{x_f}+\frac{1}{x_b}\right)\{H_2 - 0.5(x_f - x_b)(H_1 - \gamma H_2)\};$$

$$q_{i-1} = -\frac{\eta}{2\beta h}(H_1 - \gamma H_2) + \frac{\eta}{\beta h x_b}\{H_2 - 0.5(x_f - x_b)(H_1 - \gamma H_2)\};$$

We may write the jump conditions at $x = \alpha$ as

$$\phi^n_{j+1} - \phi^n_j = C^n_3 \tag{6.26}$$

$$\phi_x|^n_{j+1} - \phi_x|^n_j = C^n_4 \tag{6.27}$$

for all $n > 0$. As in the steady-state case, using onesided difference at the points x_j and x_{j+1}, equation (6.27) takes the form

$$\left(\frac{\phi^n_{j+2} - \phi^n_{j+1}}{x_f} - \frac{x_f}{2}\phi_{xx}|^n_{j+1}\right) - \left(\frac{\phi^n_j - \phi^n_{j-1}}{x_b} - \frac{x_b}{2}\phi_{xx}|^n_j\right) = C^n_4 + O(x^2_f, x^2_b) \tag{6.28}$$

Now using the original differential equation (6.20) in (6.28) for the second derivative terms we get

$$\begin{aligned} - & \frac{\eta x_f}{2\beta\Delta t}\phi^{n+1}_{j+1} - \frac{\eta x_b}{2\beta\Delta t}\phi^{n+1}_j = -\left(\frac{1}{x_f} - \frac{b}{2\beta}\right)\phi^n_{j+2} + \left(\frac{1}{x_f} - \frac{\eta x_f}{2\beta\Delta t} - \frac{b}{2\beta} + \frac{\kappa x_f}{2\beta}\right)\phi^n_{j+1} \\ + & \left(\frac{1}{x_b} - \frac{\eta x_f}{2\beta\Delta t} + \frac{b}{2\beta} + \frac{\kappa x_b}{2\beta}\right)\phi^n_j - \left(\frac{1}{x_b} - \frac{b}{2\beta}\right)\phi^n_{j-1} - \frac{x_f}{2}f^n_{j+1} - \frac{x_b}{2}f^n_j + C^n_4 \end{aligned} \tag{6.29}$$

Now from (6.26), the relation between ϕ_{j+1} and ϕ_j at the $(n+1)^{th}$ time level will be

$$\phi^{n+1}_{j+1} - \phi^{n+1}_j = C^{n+1}_3 \tag{6.30}$$

Using this relation in (6.29) we get

$$\begin{aligned} - & \left(\frac{\eta x_f}{2\beta\Delta t} + \frac{\eta x_b}{2\beta\Delta t}\right)\phi^{n+1}_j = -\left(\frac{1}{x_f} - \frac{b}{2\beta}\right)\phi^n_{j+2} + \left(\frac{1}{x_f} - \frac{\eta x_f}{2\beta\Delta t} - \frac{b}{2\beta} + \frac{\kappa x_f}{2\beta}\right)\phi^n_{j+1} \\ + & \left(\frac{1}{x_b} - \frac{\eta x_b}{2\beta\Delta t} + \frac{b}{2\beta} + \frac{\kappa x_b}{2\beta}\right)\phi^n_j - \left(\frac{1}{x_b} - \frac{b}{2\beta}\right)\phi^n_{j-1} - \frac{x_f}{2}f^n_{j+1} - \frac{x_b}{2}f^n_j \\ + & C^n_4 + \frac{\eta x_f}{2\beta\Delta t}C^{n+1}_3 \end{aligned} \tag{6.31}$$

Equations (6.30) and (6.31) yield the finite difference approximations of ϕ at the irregular points. We calculate the flux at $x = \alpha$ using the formula

$$F(\alpha) = ((x_{j+1} - \alpha)F1 + (\alpha - x_j)F2)/(x_{j+1} - x_j) \tag{6.32}$$

with

$$F1 = \beta_j\frac{\phi_j - \phi_{j-1}}{(x_j - x_{j-1})} + \frac{\beta_j(x_j - x_{j-1})}{2}(\phi_{xx})_j$$

$$F2 = \beta_{j+1}\frac{\phi_{j+2} - \phi_{j+1}}{(x_{j+2} - x_{j+1})} - \frac{\beta_{j+1}(x_{j+2} - x_{j+1})}{2}(\phi_{xx})_{j+1}$$

It may be noted that the term ϕ_{xx} appearing in F_1 and F_2 is calculated by replacing it with lower order terms appearing in the original differential equation.

6.3 Convergence and Related Analysis

Consider the one dimensional elliptic problem

$$(\beta(x)\phi^{'}(x))^{'} + \kappa(x)\phi(x) = f(x) + C_2\delta(x-\alpha) \tag{6.33}$$

on the domain $\Omega = [0,1]$ with specific boundary conditions on ϕ at $x = 0$ and $x = 1$. The function $\beta(x)$ is allowed to be discontinuous at $x = \alpha$. We also consider that $\kappa(x)$ and $f(x)$ are smooth functions. Let us assume that $u \in \mathrm{C}^{l+1}[0,\alpha)\bigcup \mathrm{C}^{l+1}(\alpha,1]$ and $0 = x_0 < x_1 < x_2 < ... < x_j < x_{j+1} < ... < x_{n-1} < x_n = 1$ be a set of nonuniform grid points on the domain Ω with grid spacing $h_i = (x_{i+1} - x_i), \quad i = 0, 1, 2...n-1$. Also we assume that $\alpha \in (x_j, x_{j+1})$. Then we construct a clustered grid around the point of discontinuity α in such a way that the interval formed by the two adjacent points on the either side of α behaves almost like a single point. In other words

$$\phi^{+} = \lim_{x\to\alpha^{+}} \phi(x) = \phi(x_{j+1}) \quad \text{and} \quad \phi^{-} = \lim_{x\to\alpha^{-}} \phi(x) = \phi(x_j)$$

and $d_1 = (\alpha - x_j)$, $d_2 = (x_{j+1} - \alpha)$ are such that $d_1 \to 0$ and $d_2 \to 0$, where $h_j = d_1 + d_2$ and $h_j << 1$. We also assume that ϕ is $(l+1)^{\text{th}}$ order differentiable except at the point $x = \alpha$. There may exist a jump discontinuity of the solution ϕ and it's derivatives. Now, using Taylor series expansion of ϕ^{+} (i.e. $\lim_{x\to\alpha^{+}} \phi(x)$, which is differentiable up to $(l+1)^{\text{th}}$order) around the point x_{j+1} we get

$$\phi^{+} = \phi(x_{j+1}) - d_2\phi^{(1)}(x_{j+1}) + \frac{d_2^2}{2!}\phi^{(2)}(x_{j+1}) - \frac{d_2^3}{3!}\phi^{(3)}(x_{j+1}) + ... \tag{6.34}$$

where, $\phi^{(i)}(x)$ denotes the i^{th} order derivative of ϕ with respect to x. Similarly using Taylor series expansion of ϕ^{-} (i.e. $\lim_{x\to\alpha^{-}} \phi(x)$, which is also differentiable up to $(l+1)^{\text{th}}$order) around the point x_j we get

$$\phi^{-} = \phi(x_j) + d_1\phi^{(1)}(x_j) + \frac{d_1^2}{2!}\phi^{(2)}(x_j) + \frac{d_1^3}{3!}\phi^{(3)}(x_j) + ... \tag{6.35}$$

Now,

$$\begin{aligned}
[\phi(x)]_\alpha &= \lim_{x\to\alpha^{+}} \phi(x) - \lim_{x\to\alpha^{-}} \phi(x) \\
&= \phi^{+} - \phi^{-} \\
&= \big(\phi(x_{j+1}) - \phi(x_j)\big) - \big(d_2\phi^{(1)}(x_{j+1}) + d_1\phi^{(1)}(x_j)\big) + \big(d_2\phi^{(1)}(x_{j+1}) \\
&+ d_1\phi^{(1)}(x_j)\big) - ...
\end{aligned}$$

Our mesh structure allows us to let $d_1, d_2 \to 0$ (see figure 6.1) which leads to

$$[\phi(x)]_\alpha = \phi(x_{j+1}) - \phi(x_j). \tag{6.36}$$

In a similar way one can prove that when $d_1, d_2 \to 0$

$$[\phi^{(1)}(x)]_\alpha = \phi^{(1)}(x_{j+1}) - \phi^{(1)}(x_j) \tag{6.37}$$

$$[\phi^{(2)}(x)]_\alpha = \phi^{(2)}(x_{j+1}) - \phi^{(2)}(x_j) \tag{6.38}$$

and so on. Note that on uniform coarser grids or when the intensity of clustering is not enough about $x = \alpha$ on nonuniform grids, we cannot take $d_1, d_2 \to 0$. In such cases

$$[\phi(x)]_\alpha = \big(\phi(x_{j+1}) - \phi(x_j)\big) + O\big(d_1, d_2\big) \tag{6.39}$$

Similarly,

$$[\phi^{(1)}(x)]_\alpha = \phi^{(1)}(x_{j+1}) - \phi^{(1)}(x_j) + O\big(d_1, d_2\big) \tag{6.40}$$

Or

$$[\phi(x)]_\alpha = \big(\phi(x_{j+1}) - \phi(x_j)\big) - \big(d_2\phi^{(1)}(x_{j+1}) + d_1\phi^{(1)}(x_j)\big) + O\big(d_1^2, d_2^2\big) \tag{6.41}$$

Similarly,

$$[\phi^{(1)}(x)]_\alpha = \big(\phi^{(1)}(x_{j+1}) - \phi^{(1)}(x_j)\big) - \big(d_2\phi^{(2)}(x_{j+1}) + d_1\phi^{(2)}(x_j)\big) + O\big(d_1^2, d_2^2\big) \tag{6.42}$$

Lemma-1: Considering the above assumptions, the following inequality holds

$$\left|\phi(x_{j+1}) - \sum_{r=0}^{l} \frac{(h_j)^r}{r!}\phi^{(r)}(x_j) - \sum_{r=0}^{l} \frac{(d_2)^r}{r!}[\phi^{(r)}(x)]_\alpha\right| \le \frac{K}{(l+1)!}h_j^{l+1} \tag{6.43}$$

Where,

$$K = \max\left(\max_{x\in[0,\alpha)}\left|(\phi)^{(l+1)}(x)\right|, \max_{x\in(\alpha,1]}\left|(\phi)^{(l+1)}(x)\right|\right) \tag{6.44}$$

Proof: Using Taylor series expansion of $\phi(x_{j+1})$ around ϕ^+ yields

$$\phi(x_{j+1}) = \sum_{r=0}^{l} \frac{(d_2)^r}{r!}(\phi^+)^{(r)} + \frac{(d_2)^{l+1}}{(l+1)!}(\phi)^{(l+1)}(\zeta_1)$$

for some $\zeta_1 \in (\alpha, x_{j+1})$. Also

$$(\phi^+)^{(r)} = (\phi^-)^{(r)} + [\phi^{(r)}(x)]_\alpha.$$

Therefore,

$$\phi(x_{j+1}) = \sum_{r=0}^{l} \frac{(d_2)^r}{r!}\left\{(\phi^-)^{(r)} + [\phi^{(r)}(x)]_\alpha\right\} + \frac{(d_2^{(l+1)})}{(l+1)!}\phi^{(l+1)}(\zeta_1). \tag{6.45}$$

Using Taylor expansion for $(\phi^-)^{(r)}$ around $\phi(x_j)$,

$$(\phi^-)^{(r)} = \sum_{p=r}^{l} \frac{(d_1)^{p-r}}{(p-r)!}\phi^{(p)}(x_j) + \frac{(d_1)^{(l-r+1)}}{(l-r+1)!}\phi^{(l+1)}(\zeta_r),$$

for some $\zeta_r \in (x_j, \alpha)$, where $r = 0, 1, 2, \ldots, l$. Making use of these relations in (6.45), we have

$$\begin{aligned}\phi(x_{j+1}) = &\sum_{r=0}^{l} \frac{(d_2)^r}{r!} \sum_{p=r}^{l} \frac{(d_1)^{p-r}}{(p-r)!}\phi^{(p)}(x_j) + \sum_{r=0}^{l} \frac{(d_2)^r}{r!}[\phi^{(r)}(x)]_\alpha \\ &+ \sum_{r=0}^{l} \frac{(d_2)^r}{r!} \frac{(d_1)^{l-r+1}}{(l-r+1)!}(\phi)^{(l+1)}(\zeta_r) + \frac{(d_2)^{l+1}}{(l+1)!}(\phi)^{(l+1)}(\zeta_1)\end{aligned} \tag{6.46}$$

Now,

$$\begin{aligned}\textstyle\sum_{r=0}^{l} \quad &\frac{(d_2)^r}{r!} \sum_{p=r}^{l} \frac{(d_1)^{p-r}}{(p-r)!}\phi^{(p)}(x_j) = \phi^{(0)}(x_j) + (\frac{d_1}{1!} + \frac{d_2}{1!})\phi^{(1)}(x_j) + (\frac{d_1^2}{2!} + \frac{d_1 d_2}{1!1!} \\ + \quad &\frac{d_2^2}{2!})\phi^{(2)}(x_j) + \ldots + (\frac{d_1^l}{l!} + \frac{d_1^{l-1} d_2}{(l-1)!1!} + \frac{d_1^{l-2} d_2^2}{(l-2)!2!} + \ldots + \frac{d_1 d_2^{l-1}}{1!(l-1)!} + \frac{d_2^l}{l!}) \\ \times \quad &\phi^{(l)}(x_j) = \phi^{(0)}(x_j) + \frac{h_j}{1!}\phi(1)(x_j) + \frac{h_j^2}{2!}\phi^{(2)}(x_j) + \ldots + \frac{h_j^l}{l!}\phi^{(l)}(x_j)\end{aligned} \tag{6.47}$$

Hence,

$$\sum_{r=0}^{l} \frac{(d_2)^r}{r!} \sum_{p=r}^{l} \frac{(d_1)^{p-r}}{(p-r)!}\phi^{(p)}(x_j) = \sum_{q=0}^{l} \frac{h_j^q}{q!}\phi^{(q)}(x_j) \tag{6.48}$$

Using this relation in (6.46),

$$\begin{aligned}\phi(x_{j+1}) \quad = \quad &\sum_{r=0}^{l} \frac{h_j^r}{r!}\phi^{(r)}(x_j) + \sum_{r=0}^{l} \frac{(d_2)^r}{r!}[\phi^{(r)}(x)]_\alpha \\ + \quad &\sum_{r=0}^{l} \frac{(d_2)^r}{r!} \frac{(d_1)^{l-r+1}}{(l-r+1)!}(\phi)^{(l+1)}(\zeta_r) + \frac{(d_2)^{l+1}}{(l+1)!}(\phi)^{(l+1)}(\zeta_1)\end{aligned} \tag{6.49}$$

Let,

$$K = \max\left(\max_{x\in[0,\alpha)} \mid \phi^{(l+1)}(x) \mid, \max_{x\in(\alpha,1]} \mid \phi^{(l+1)}(x) \mid\right)$$

With this, (6.49) reduces to

$$\begin{aligned}\left|\phi(x_{j+1}) - \sum_{r=0}^{l} \frac{h_j^r}{r!}\phi^{(r)}(x_j) - \sum_{r=0}^{l} \frac{(d_2)^r}{r!}[\phi^{(r)}(x)]_\alpha\right| \leq \quad &K \quad \sum_{r=0}^{l+1} \frac{(d_2)^r}{r!} \frac{(d_1)^{l-r+1}}{(l-r+1)!} \\ = \quad &K\frac{(d_1+d_2)^{l+1}}{(l+1)!} \\ = \quad &K\frac{h_j^{l+1}}{(l+1)!}\end{aligned} \tag{6.50}$$

Hence we get the required relation

$$\left|\phi(x_{j+1}) - \sum_{r=0}^{l} \frac{h_j^r}{r!}\phi^{(r)}(x_j) - \sum_{r=0}^{l} \frac{(d_2)^r}{r!}[\phi^{(r)}(x)]_\alpha\right| \leq \frac{K}{(l+1)!}h_j^{l+1} \tag{6.51}$$

Corollary: Putting $l = 0$ in the above relation (6.51) we get,

$$\left|\phi(x_{j+1}) - \phi(x_j) - [\phi(x)]_\alpha\right| \leq Kh_j \tag{6.52}$$

This indicates that in this case the jump condition in ϕ at α is first order accurate.

Consider the problem (6.33) with $\beta = -a < 0$ is constant, $\kappa(x) \geq k > 0$, $C_2 = 0$ and $f(x)$ has a discontinuity at $x = \alpha$. Then the equation (6.33) can be written as a self-adjoint two point boundary value problem

$$-a\phi''(x) + \kappa(x)\phi(x) = f(x). \tag{6.53}$$

Here $\kappa(x)$, $f(x)$ are sufficiently smooth on $\Omega\backslash\{\alpha\}$. As $f(x)$ is discontinuous at α, the solution ϕ does not necessarily have a continuous second order derivative at the point α. Thus, $\phi \notin C^2$ but the first derivative of ϕ exists and is continuous.

Theorem-1: The problem (6.53), has a solution $\phi \in C^1(\Omega)\bigcap C^2(\Omega^- \bigcup \Omega^+)$.

Proof: The proof is by construction method [42]. Let y_1 and y_2 be two particular solutions of the differential equation

$$-ay_1''(x) + \kappa(x)y_1 = f(x), \quad x \in \Omega^-$$

and

$$-ay_2''(x) + \kappa(x)y_2 = f(x), \quad x \in \Omega^+$$

Let us consider two functions $\phi_1(x)$ and $\phi_2(x)$ which respectively satisfy the boundary value problems

$$-a\phi_1''(x) + \kappa(x)\phi_1(x) = 0, \quad x \in \Omega, \quad \phi_1(0) = 1, \quad \phi_1(1) = 0$$

$$-a\phi_2''(x) + \kappa(x)\phi_2(x) = 0, \quad x \in \Omega, \quad \phi_2(0) = 0, \quad \phi_2(1) = 1$$

Now we construct a function

$$y(x) = \begin{cases} y_1(x) + \big(\phi(0) - y_1(0)\big)\phi_1(x) + A\phi_2(x), & x \in \Omega^- \\ y_1(x) + B\phi_1(x) + \big(\phi(1) - y_2(1)\big)\phi_2(x), & x \in \Omega^+ \end{cases}$$

where A and B are constants to be chosen so that $y(x) \in C^1(\Omega)$. Now on the open interval $(0, 1)$, $0 < \phi_i < 1$; $i = 1, 2$. Thus ϕ_1, ϕ_2 cannot have an internal maximum, or

minimum. Hence $\phi_1^{'} < 0$ and $\phi_2^{'} > 0$, for all $x \in (0,1)$. Now we have to show that we can find A, B for which $y(x) \in C^1(\Omega)$. Now if $y(x) \in C^1(\Omega)$, it will satisfy

$$y(\alpha^-) = y(\alpha^+) \quad \text{and} \quad y^{'}(\alpha^-) = y^{'}(\alpha^+).$$

These lead to

$$A\phi_2(\alpha) - B\phi_1(\alpha) = F_1 \tag{6.54}$$

where

$$F_1 = (\phi(1) - y_2(1)\phi_2(\alpha)) - (\phi(0) - y_1(0))\phi_1(\alpha).$$

and

$$A\phi_2^{'}(\alpha) - B\phi_1^{'}(\alpha) = F_2 \tag{6.55}$$

where

$$F_2 = \big(\phi(1) - y_2(1)\big)\phi_2^{'}(\alpha) - \big(\phi(0) - y_1(0)\big)\phi_1^{'}(\alpha).$$

Now A and B will have unique solutions if the determinant of the coefficient matrix

$$\begin{vmatrix} \phi_2(\alpha) & -\phi_1(\alpha) \\ \phi_2^{'}(\alpha) & -\phi_1^{'}(\alpha) \end{vmatrix} = \phi_1(\alpha)\phi_2^{'}(\alpha) - \phi_1^{'}(\alpha)\phi_2(\alpha)$$

is not equal to zero.
From the above relations we know that $\phi_1^{'}(\alpha) < 0$, $\phi_1(\alpha), \phi_2(\alpha), \phi_2^{'}(\alpha) > 0$. Therefore

$$\phi_1(\alpha)\phi_2^{'}(\alpha) - \phi_1^{'}(\alpha)\phi_2(\alpha) > 0$$

Hence, $y(x) \in C^1(\Omega) \bigcap C^2(\Omega^- \bigcup \Omega^+)$ is a solution of (6.53).

Lemma-2: Suppose that a function $w \in C^{(0)}(\bar{\Omega}) \bigcap C^2(\Omega^- \bigcup \Omega^+)$ satisfies

$$w(0) \geq 0, \quad w(1) \geq 0$$

$$lw(x) \equiv -aw^{''}(x) + \kappa(x)w(x) \geq 0, \quad \forall \quad x \in \Omega^- \bigcup \Omega^+;$$

$$[w(x)]_\alpha = 0, \quad [w^{'}(x)]_\alpha \leq 0$$

Then $w(x) \geq 0$ for all $x \in \bar{\Omega}$.

Proof: Let p be any point in $\bar{\Omega}$, at which w attains its minimum value. If $w(p) \geq 0$, there is nothing to prove. Suppose therefore that $w(p) < 0$, then the proof is completed by showing that this leads to a contradiction. Now there are two possibilities, either $p \in \Omega^- \bigcup \Omega^+$ or $p = \alpha$. If $p \in \Omega^- \bigcup \Omega^+$, then $w(p)$ is the minimum value implying that

$$w^{'} = 0 \quad \text{and} \quad w^{''}(p) \geq 0.$$

Also, $a > 0$ and $\kappa(x) \geq k > 0, \forall x$. Therefore,

$$lw(p) \equiv -aw^{''}(p) + \kappa(p)w(p) < 0.$$

Hence a contradiction.

If $p = \alpha$, then there again will be two cases; either $w(x)$ is differentiable at p, or $w(x)$ is not differentiable at p. Let $w(x)$ is differentiable at p. Since $w(x)$ attains its minimum value at p, $w^{'}(\alpha) = 0$ and $w \in C^1(\Omega)$. As $w(\alpha) < 0$, it follows that there exits a neighborhood $N_\epsilon = (\alpha - \epsilon, \alpha)$ such that $w(x) < 0$ for all points $x \in N_\epsilon$. Now choose a point $x_1 \neq \alpha$ and $x_1 \in N_\epsilon$ such that $w(x_1) > w(\alpha)$. It follows from the mean value theorem that, for some $x_2 \in N_\epsilon$

$$w^{'}(x_2) = \frac{w(\alpha) - w(x_1)}{\alpha - x_1} < 0$$

and also that for some $x_3 \in N_\epsilon$

$$w^{''}(x_3) = \frac{w^{'}(\alpha) - w^{'}(x_2)}{\alpha - x_2} = \frac{-w^{'}(x_2)}{\alpha - x_2} > 0.$$

Again $w(x_3) < 0$; since $x_3 \in N_\epsilon$. Therefore,

$$lw(x_3) \equiv -aw^{''}(x_3) + \kappa(x_3)w(x_3) < 0$$

which is a contradiction.

If w is not differentiable at p, then $[w^{'}(x)]_\alpha \neq 0$. Now since, $w^{'}(\alpha^-) \leq 0$ and $w^{'}(\alpha^+) \geq 0$,

$$[w^{'}]_\alpha = w^{'}(\alpha^+) - w^{'}(\alpha^-) > 0$$

which is again a contradiction. Hence $w(p) \geq 0$ and if the minimum value of $w(x)$ on $\bar{\Omega}$ is non-negative, it immediately follows that $w(x) \geq 0$ for all $x \in \bar{\Omega}$.

An immediate consequence of the minimum principle is the following stability result.

Theorem-2: Let ϕ be a solution of (6.53), then

$$\left|\phi\right|_{\bar{\Omega}} \leq \max\left(|\phi_0|, |\phi_1|, \frac{1}{k} \parallel f \parallel_{\Omega^- \cup \Omega^+} \right), \tag{6.56}$$

Proof: Let $\psi_\pm(x) = M \pm \phi(x)$, where $M = \max\left(|\phi_0|, |\phi_1|, \frac{1}{k} \parallel f \parallel_{\Omega^- \cup \Omega^+} \right)$. Then clearly $\psi_\pm(0) \geq 0$, $\psi_\pm(1) \geq 0$ and for each $x \in \Omega^- \bigcup \Omega^+$,

$$\begin{aligned} L\psi_\pm(x) &= \kappa(x)M \pm L\phi(x) \\ &\geq kM \pm f(x) \\ &\geq 0 \end{aligned} \tag{6.57}$$

Also, since $\phi \in C^1(\Omega)$

$$[\psi_\pm]_\alpha = \pm[\phi]_\alpha = 0$$

and,

$$[\psi_{\pm}^{'}]_{\alpha} = \pm[\phi^{'}]_{\alpha} = 0.$$

Hence, it follows from the minimum principle that $\psi_{\pm} \geq 0 \quad \forall x \in \bar{\Omega}$.
Hence, $\parallel \phi \parallel \leq M$ That is,

$$|\phi|_{\bar{\Omega}} \leq \max\left(|\phi_0|, |\phi_1|, \frac{1}{k} \parallel f \parallel_{\Omega^- \cup \Omega^+}\right) \tag{6.58}$$

Lemma-3: Let $x_j \leq \alpha < x_{j+1}, \quad d_1 = \alpha - x_j, \quad d_2 = x_{j+1} - \alpha$. Suppose $\phi \in C^3[x_{j-1}, \alpha) \cap C^3(\alpha, x_{j+2}]$, with derivatives extending continuously up to the boundary α. Then the following approximations hold to $O(h^3)$ using the given differential equation

$$-\beta\phi_{xx} + b\phi_x + \kappa\phi = C_2\delta(x - \alpha),$$

where coefficients are constants

$$\phi_x(x_j) \approx \left(1/B_{j-1}\right)\left\{\left(\frac{1}{h_{j-1}} + \frac{h_{j-1}\kappa}{2\beta} - \frac{h_{j-1}^2 b\kappa}{6\beta^2}\right)\phi_j - \frac{\phi_{j-1}}{h_{j-1}} - \frac{h_{j-1}C_2}{2\beta}\right\} + O\left(h_{j-1}^3\right) \tag{6.59}$$

$$\phi_x(x_{j+1}) \approx \left(1/A_{j-1}\right)\left\{\frac{\phi_{j+2}}{h_{j+1}} - \left(\frac{1}{h_{j+1}} + \frac{h_{j+1}\kappa}{2\beta} + \frac{h_{j+1}^2 b\kappa}{6\beta^2}\right)\phi_{j+1} + \frac{h_{j+1}C_2}{2\beta}\right\} + O\left(h_{j+1}^3\right) \tag{6.60}$$

where,

$$B_{j-1} = 1 - \frac{h_{j-1}b}{2\beta} + \frac{h_{j-1}^2\kappa}{6\beta} - \frac{h_{j-1}^2 b^2}{6\beta^2}$$

$$A_{j+1} = 1 + \frac{h_{j+1}b}{2\beta} + \frac{h_{j+1}^2\kappa}{6\beta} + \frac{h_{j+1}^2 b^2}{6\beta^2}$$

Proof: It follows from the formulations involving equations (6.10) and (6.14) subject to the conditions that $d_1, d_2 \to 0$.

Lemma-4: If coefficients of the given differential equation are variables of x and smooth (up to minimum second order) Lemma-3 can be written as the following with the same order

$$\phi_x(x_j) \approx \left(1/Q_j\right)\left\{r_j\phi_j - \frac{1}{h_{j-1}}\phi_{j-1} - t_j C_2\right\} + O\left(h_{j-1}^3\right) \tag{6.61}$$

$$\phi_x(x_{j+1}) \approx \left(1/P_{j+1}\right)\left\{\frac{\phi_{j+2}}{h_{j+1}} - l_{j+1}\phi_{j+1} + m_{j+1}C_2\right\} + O\left(h_{j+1}^3\right) \tag{6.62}$$

where

$$P_{j+1} = 1 + \left\{ \left(\frac{h_{j+1}}{2} + \frac{h_{j+1}^2}{6} \frac{(\beta_x)_{j+1} b_{j+1}}{\beta_{j+1}} \right) \frac{b_{j+1}}{\beta_{j+1}} + \frac{h_{j+1}^2}{6} \frac{(b_x)_{j+1} + \kappa_{j+1}}{\beta_{j+1}} \right\}$$

$$l_{j+1} = \frac{1}{h_{j+1}} + \left\{ \left(\frac{h_{j+1}}{2} + \frac{h_{j+1}^2}{6} \frac{(\beta_x)_{j+1} b_{j+1}}{\beta_{j+1}} \right) \frac{\kappa_{j+1}}{\beta_{j+1}} + \frac{h_{j+1}^2}{6} \frac{(\kappa_x)_{j+1}}{\beta_{j+1}} \right\}$$

$$m_{j+1} = \frac{1}{\beta_{j+1}} \left(\frac{h_{j+1}}{2} + \frac{h_{j+1}^2}{6} \frac{(\beta_x)_{j+1} b_{j+1}}{\beta_{j+1}} \right)$$

$$Q_j = 1 - \left\{ \left(\frac{h_{j-1}}{2} - \frac{h_{j-1}^2}{6} \frac{(\beta_x)_j b_j}{\beta_j} \right) \frac{b_j}{\beta_j} + \frac{h_{j-1}^2}{6} \frac{(b_x)_j + \kappa_j}{\beta_j} \right\}$$

$$r_j = \frac{1}{h_{j-1}} + \left(\frac{h_{j-1}}{2} - \frac{h_{j-1}^2}{6} \frac{(\beta_x)_j b_j}{\beta_j} \right) \frac{\kappa_j}{\beta_j} - \frac{h_{j-1}^2}{6} \frac{(\kappa_x)_j}{\beta_j}$$

$$t_j = \frac{1}{\beta_j} \left(\frac{h_{j-1}}{2} - \frac{h_{j-1}^2}{6} \frac{(\beta_x)_j b_j}{\beta_j} \right)$$

Proof: The proof is similar to that for Lemma 3 except that it is for variable coefficients now.

Lemma-5: Using Lemma-4, the jump on ϕ_x at α can be approximated up to $O(h^3)$, where

$$h = \max\left\{ h_{j-1}, h_{j+1} \right\}$$

.

$$[\phi_x]_\alpha \approx \frac{1}{A_{j-1}} \left\{ \frac{\phi_{j+2}}{h_{j+1}} - \left(\frac{1}{h_{j+1}} + \frac{h_{j+1}\kappa}{2\beta} + \frac{h_{j+1}^2 b\kappa}{6\beta^2} \right) \phi_{j+1} + \frac{h_{j+1} C_2}{2\beta} \right\} - \frac{1}{B_{j-1}} \left\{ \left(\frac{1}{h_{j-1}} + \frac{h_{j-1}\kappa}{2\beta} - \frac{h_{j-1}^2 b\kappa}{6\beta^2} \right) \phi_j - \frac{\phi_{j-1}}{h_{j-1}} - \frac{h_{j-1} C_2}{2\beta} \right\} \tag{6.63}$$

where A_{j+1}, B_{j-1} are as in Lemma 3.

Proof: This immediately follows on using onesided Taylor series expansion of ϕ at x_{j+1} and using the jump on the flux at $x = \alpha$.

Lemma-6: Using Lemma-5, jump on (ϕ_x) at α can be approximated up to $O(h^3)$, where $h = \max\left\{ h_{j-1}, h_{j+1} \right\}$

$$[\phi_x]_\alpha \approx \frac{1}{P_{j+1}} \left(\frac{\phi_{j+2}}{h_{j+1}} - l_{j+1}\phi_{j+1} + m_{j+1} C_2 \right) - \frac{1}{Q_j} \left(r_j \phi_j - \frac{1}{h_{j-1}} \phi_{j-1} - t_j C_2 \right) \tag{6.64}$$

where P_{j+1}, Q_j, l_{j+1}, m_{j+1}, r_j, t_j are as in Lemma 4.

Proof: The proof is similar to that of Lemma 5.

Theorem-3: Suppose $\hat{\Phi}_i$ satisfies the third order accurate difference equation

$$\text{Œ}(\hat{\Phi}_i) \equiv \gamma_{i+1}\hat{\Phi}_{i+1} + \gamma_i\hat{\Phi}_i + \gamma_{i-1}\hat{\Phi}_{i-1} = -C_{i-(j-1)}(\delta_{i,j} + \delta_{i,j+1}) \tag{6.65}$$

where Œ is a linear operator, $[x_j, x_{j+1}]$ is the interval of infinitesimal length containing the point α as described in section 6.2.1, C_1 and C_2 are same as in equations (6.5) and (6.6), $\delta_{i,j}$ the Kronecker delta and $\hat{\Phi}_0 = \hat{\Phi}_N = 0$; assume further that (6.65) is third order accurate discrete equation of

$$\phi_{xx} = -C_2\delta(x - \alpha). \tag{6.66}$$

Let $\hat{\phi}(x)$ be the true solution of given differential equation i.e

$$\hat{\phi}(x) = \begin{cases} C_2x(1-\alpha)\,, & x \le \alpha \\ C_2\alpha(1-x)\,, & x \ge \alpha. \end{cases}$$

then

$$\hat{\Phi}_i = \hat{\phi}(x) + O(h^3).$$

Proof: Let $G(x;\alpha_1)$ be the Green's function for the given problem with a unit strength source at α_1,

$$G(x;\alpha_1) = \begin{cases} x(1-\alpha_1)\,, & x \le \alpha_1 \\ \alpha_1(1-x)\,, & x \ge \alpha_1. \end{cases}$$

Then the function G satisfies

$$G_{xx} = -\delta(x - \alpha_1).$$

Setting a nonuniform grid over the interval $[0, 1]$ with clustering around the point α such that $d_1 = (\alpha - x_j) \to 0$ and $d_1 = (x_{j+1} - \alpha) \to 0$, then it is easy to check that G also satisfies

$$\text{Œ}(G(x_i, x_j)) = -(\delta_{i,j} + \delta_{i,j+1}).$$

Now taking $\alpha_1 = \alpha$, the right hand side of (6.65) can be written as

$$-C_{i-(j-1)}(\delta_{i,j} + \delta_{i,j+1}) = C_{i-(j-1)}\text{Œ}(G(x_i, x_j)).$$

By linearity, the solution $\hat{\Phi}_i$ of the the given difference equation (6.65) can be expressed as

$$\hat{\Phi}_i = C_{i-(j-1)}\text{Œ}(G(x_i, x_j))$$

at each grid point x_i, This can be considered as the exact solution of the given difference equation (6.65) at the grid points. But this difference equation is third order accurate approximation of the actual differential equation (6.66) at every grid point from which it immediately follows that

$$\hat{\Phi}_i = \hat{\phi}(x) + O(h^3). \tag{6.67}$$

6.4 Numerical Examples

We now apply the scheme proposed in section 6.2 to four problems: three steady and one unsteady, all having analytical solutions which allows us to compute the numerical errors. In all the cases the problem domain is taken as $0 \leq x \leq 1$.

6.4.1 Problem 1

Consider a differential equation with discontinuous coefficient. Here the equation [79] is

$$-\left(\beta\phi_x\right)_x = 1 \tag{6.68}$$

with homogeneous Dirichlet boundary data $\phi(0) = 0$ and $\phi(1) = 1$. The analytical solution of the problem is

$$\phi(x) = \begin{cases} a_1\frac{x^2}{2} + b_1 x, & 0 \leq x \leq \frac{1}{2} \\ a_2\frac{x^2}{2} + b_2 x + c_2, & \frac{1}{2} \leq x \leq 1 \end{cases}$$

where $a_i = -\dfrac{1}{\beta_i}$, $b_1 = -\dfrac{1}{4}\left(3a_2 + a_1\right)\left(\dfrac{\beta_2}{\beta_1 + \beta_2}\right)$, $b_2 = \dfrac{\beta_1}{\beta_2}b_1$ and $c_2 = -\left(b_2 + \dfrac{a_2}{2}\right)$. The equation has a discontinuity in β and it take values $\beta = \beta_1 = 0.1$ for $0 \leq x < \dfrac{1}{2}$ and $\beta = \beta_2 = 1.0$ for $\dfrac{1}{2} < x \leq 1$.

Since all derivatives of the analytical solution higher than ϕ_{xx} are zero, it can easily be concluded that the finite difference equations resulting from (6.5), (6.8) and (6.18) will yield the same solutions as its analytical representations. Therefore the finite difference solution to (6.68) using our scheme will be exactly same as the analytical ones at the nodes.

Table 6.1: *Problem 1: the computed values, analytical values of ϕ and corresponding absolute errors at the grid points for n= 8, r=36 and interface at $x = 0.5$*

grid points	*computed*	*analytical*	*abs.err*
0.000000e+00	0.000000	0.000000	0.000000e+00
4.970795e-01	0.233204	0.233204	2.909573e-07
4.999829e-01	0.227307	0.227308	2.926567e-07
4.999999e-01	0.227273	0.227273	2.926667e-07
5.000001e-01	0.227273	0.227273	6.978987e-08
5.000171e-01	0.227269	0.227269	6.978750e-08
5.029205e-01	0.226671	0.226671	6.938224e-08
1.000000e+00	0.000000	0.000000	0.000000e+00

In table 6.1 we show the computed values and corresponding analytical results at the grids when number of grid points are 8 and the clustering parameter $r = 36$. It is

Table 6.2: *Problem 1: Flux σ^* (for r=27) and σ_h Evaluated at x= 0.5; $\sigma_{analytical}$ = 0.204545*

h	σ^*	σ_h	$\lvert\sigma_h - \sigma_{analytical}\rvert$	$\lvert\sigma^* - \sigma_{analytical}\rvert$
1/3	0.204520	0.181818	0.022727	2.523980e-05
1/7	0.204544	0.200372	0.004173	1.890747e-06
1/11	0.204545	0.202854	0.001691	8.945325e-07
1/15	0.204545	0.203971	0.000911	6.328821e-07

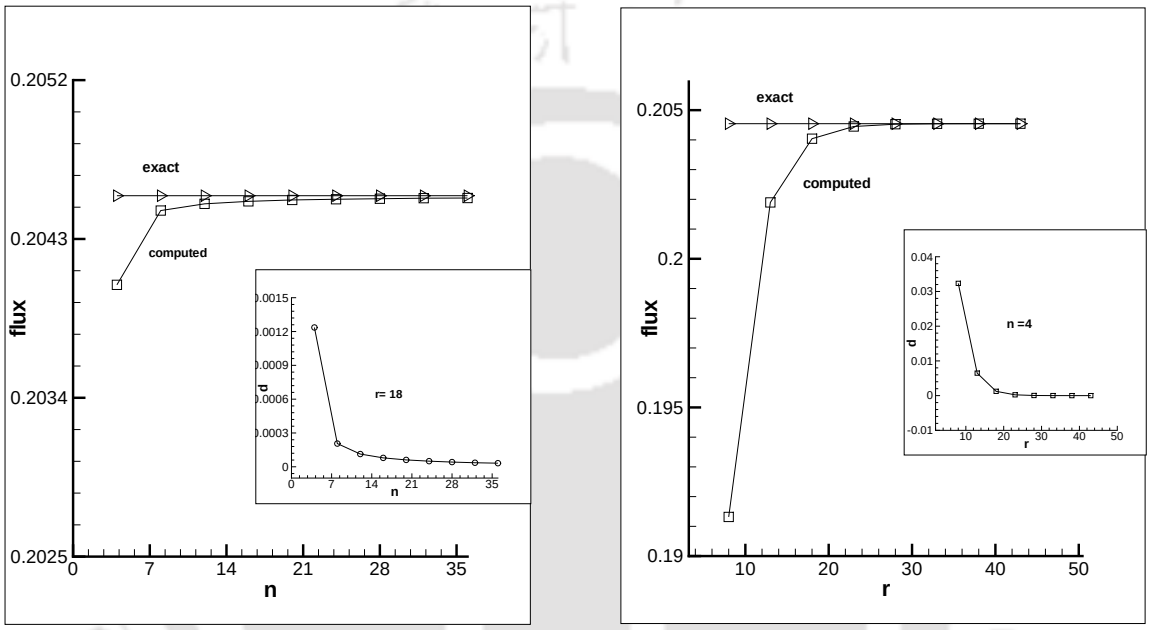

(a) (b)

Figure 6.2: *Problem 1: computed flux and corresponding analytical solution at $x = \frac{1}{2}$ for (a) different n when $r = 18$ and (b) different r when $n = 4$.*

heartening to note that with only 8 nodal points our scheme produces a maximum error that is as low as 2.9×10^{-7}. Table 6.2 exhibits the comparison of the flux values at $x = \frac{1}{2}$ for different values of n with a fixed $r = 36$ using our scheme with those obtained by MacKinnon & Carey [79]. Here σ^* and σ_h respectively denote the computed flux values using our scheme and those of reference [79]. To compute the flux, we have used the formula given in (6.32). In all the cases, our scheme produces significantly better results as can be seen from the last two columns of Table 6.2.

We also compute the flux values at $x = \frac{1}{2}$ for a fixed value of r with n-variation and vice versa. The computed values of the flux with the analytical ones are plotted in figures 6.2(a) and 6.2(b) along with the variations of d_1 and d_2 with respect to n and r. Figure 6.3 shows the absolute errors in the flux at $x = \frac{1}{2}$ using our scheme for varying n and r variations. From the figures, it is clear that with increasing r and n,

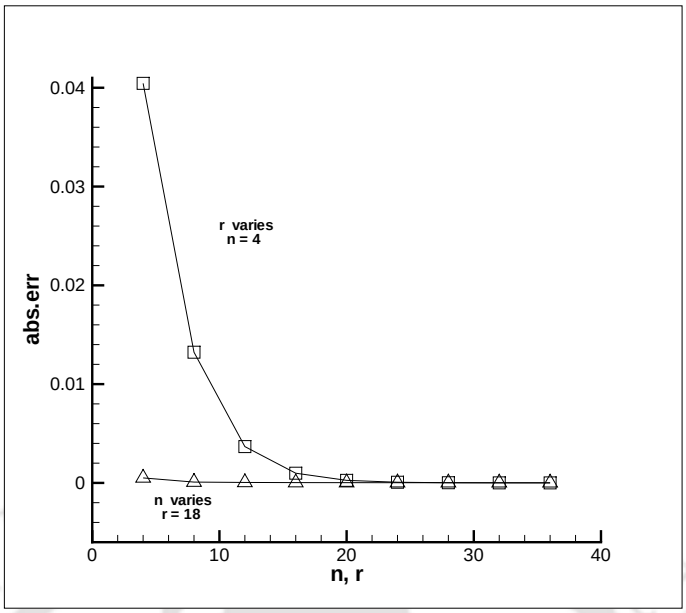

Figure 6.3: *Problem 1: absolute errors in flux at* $x = \frac{1}{2}$ *using our scheme for different values of n fixing r at 18 and for different values of r fixing n at 4*

the solution becomes more accurate as expected. Interesting, however is the role played by r; with a higher value of r, one can obtain much more accurate results on a coarser grid with better computational economy than on a finer grid with a lower value of r. This is due to the fact that the values of d_1, d_2 do not decrease proportionately with increasing grid size while d_1, d_2 decrease at a much faster rate with slight increase in the value of r. These observations are in conformity with the development of the scheme where the condition $d_1, d_2 \to 0$ is a prerequisite for accurate solutions by our scheme. This is also reflected in the errors presented in Table 6.2; on a uniform grid with 4 grid points $d_1 = d_2 = 0.166667$ whereas on the same grid with a moderate value of $r = 22$ yields $d_1 = d_2 = 0.000326$ and as such in all the cases, the flux calculated by our scheme on a 4-point grid produces much less error than the flux computed in reference [79] on a 16-point grid.

6.4.2 Problem 2.

Now we consider a problem where the differential equation has a singular source term. Here we take the equation

$$\phi_{xx} = -c\delta(x - \alpha), \qquad 0 < x < 1 \tag{6.69}$$

with Dirichlet boundary conditions $\phi(0) = \phi(1) = 0$ and a discontinuous source term at $x = \alpha$. The analytical solution of (6.69) is

$$\phi(x) = \begin{cases} cx(1-\alpha)\,, & 0 \le x \le \alpha \\ c\alpha(1-x)\,, & \alpha < x \le 1 \end{cases}$$

where α and c are constants. We have computed our solutions with $\alpha = \frac{1}{2}$ and $c = 1$. Table 6.3 shows the computed values of ϕ at different points along with the analytical ones and the corresponding absolute errors for $n = 14$, and $r = 8$. As in Problem 1, since $\frac{d^k\phi}{dx^k} = 0 \ \ \forall\, k \geq 3$, the finite difference solution of (6.69) should be exactly same with the analytical solution at the nodes. This is also observed in table 6.3 where it is seen that our computed solutions at all the grid points are almost exact. In figure 6.4, we plot the infinity norm $||e||_\infty$ of the error for varying n and r and their effect on the solution is similar to that Problem 1.

Table 6.3: *Problem 2: the computed values, analytical values of ϕ and corresponding absolute errors at the grid points for n= 14, r= 8; interface point is $x = 0.5$*

grid points	*computed*	*analytical*	*abs.err*
0.000000	0.000000	0.000000	0.00000e+00
0.230003	0.115002	0.115002	3.787585e-08
0.354492	0.177246	0.177246	5.759830e-08
0.422115	0.211057	0.211057	6.740169e-08
0.459301	0.229650	0.229650	7.182279e-08
0.480581	0.240291	0.240291	7.336235e-08
0.494273	0.247137	0.247137	7.336235e-08
0.505727	0.247137	0.247137	7.336235e-08
0.519419	0.240291	0.240291	7.238501e-08
0.540699	0.229650	0.229650	6.992188e-08
0.577885	0.211057	0.211057	6.474363e-08
0.645508	0.177246	0.177246	5.458977e-08
0.769997	0.115002	0.115002	3.541925e-08
1.000000	0.000000	0.000000	0.00000e+00

Problem 3. Now we consider the problem in which the differential equation contains both discontinuous coefficient as well as singular source term. Consider the equation

$$(\beta\phi_x)_x = \delta(x - \alpha) \tag{6.70}$$

where, $\alpha = \frac{1}{3}$, $\beta = \beta^- = 1$ in $0 \leq x < \alpha$ and $\beta = \beta^+ = 100$ in $\alpha < x \leq 1$. The boundary conditions are taken from the analytical solution

$$\phi(x) = \begin{cases} Bx(1-\alpha), & 0 \leq x \leq \alpha \\ B\alpha(1-x), & \alpha < x \leq 1 \end{cases}$$

where $B = -1/\big(\beta^+\alpha + \beta^-(1-\alpha)\big)$.

Table 6.4 shows the computed results, analytical solutions and corresponding absolute errors using our scheme for $n = 10$ and $r = 28$. From the table 6.4, it is clear that our numerical results are almost exact. The graphical results are shown in figure 6.5

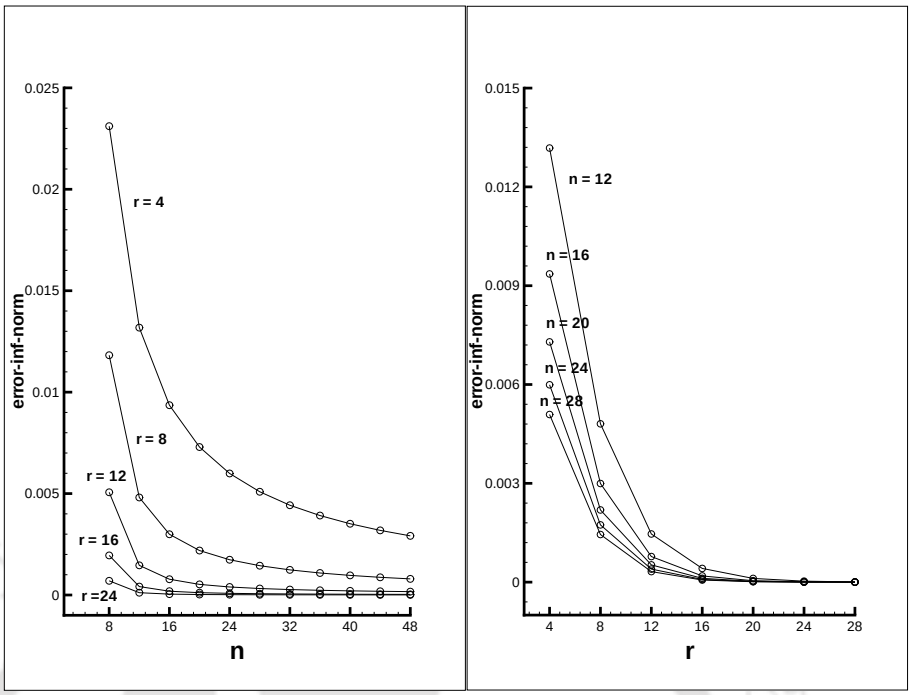

Figure 6.4: *Problem 2: absolute errors in flux at* $x = \frac{1}{2}$ *using our scheme for different values of* n *with* $r = 20$ *and for different values of* r *with* $n = 4$.

Table 6.4: *Problem 3: the computed values and analytical values of* ϕ *and corresponding absolute errors at the grid points for n= 10, r= 28; interface point is* $x = \frac{1}{3}$

grid points	*computed*	*analytical*	*abs.err*
0.000000	0.000000	0.000000	0.000000e+00
0.318483	-0.006245	-0.006245	2.606880e-07
0.332672	-0.006523	-0.006523	2.723020e-07
0.333304	-0.006536	-0.006535	2.728256e-07
0.333332	-0.006536	-0.006536	2.728670e-07
0.333336	-0.006536	-0.006536	2.745877e-07
0.333392	-0.006536	-0.006535	2.745647e-07
0.334657	-0.006523	-0.006523	2.740441e-07
0.363034	-0.006245	-0.006245	2.623557e-07
1.000000	0.000000	0.000000	0.000000e+00

with fixed $n = 10$, but with a different $r = 12$ so that the grid points are not clustered as in the table. It is clear from the figure that our computed results are much better than those produced by the smoothing method [7] and qualitatively as good as the computed results of Li and Ito [7]. It is also heartening to note that both those schemes in reference [7] used 41 grid points while our scheme produced almost exact result using 10 points only.

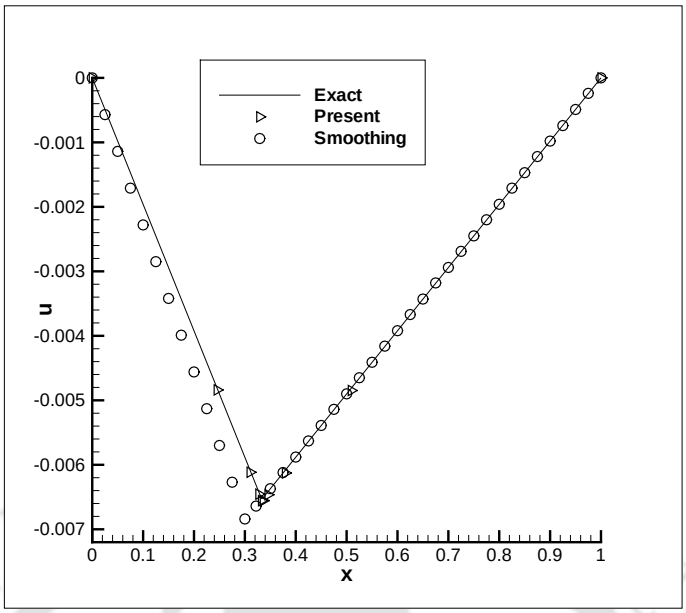

Figure 6.5: *Problem 3: The computed values, analytical values with* $n = 10$ *and* $r = 12$.

Problem 4. Consider the time dependent problem

$$\phi_t = \phi_{xx} + c(t)\delta(x - \alpha) \tag{6.71}$$

where

$$c(t) = -[\phi_x]_\alpha = -\frac{3}{2}\pi \exp(-\frac{9}{4}\pi^2 t) - 3\pi \exp(-9\pi^2 t).$$

We have taken $\alpha = \frac{1}{3}$ and the boundary conditions are taken from the analytical solution

$$\phi(x,t) = \begin{cases} \sin(3\pi x)\exp(-9\pi^2 t), & 0 \le x \le \frac{1}{3} \\ \sin(\frac{3}{2}\pi(1-x))\exp(-\frac{9}{4}\pi^2 t), & \frac{1}{3} \le x \le 1 \end{cases}$$

Note that $\phi(\alpha, t) = 0$ for all t.

Table 6.5 shows the computed solution, analytical solution and corresponding absolute errors using our scheme for $n = 10$ and $r = 18$ at $t = 1$. Table 6.6 shows the comparison between the infinity norm of error for the same number of grid points using our scheme and the scheme used by Beyer and Leveque ([23]). Here $||E||_\infty$ is the error-infinity-norm using our scheme and $||\hat{E}||_\infty$ is the same based on the best results of [23]. Here we have used the best possible combination of n and r to minimize the error. In all the cases our results are much better than those reported in [23].

It may be noted that although our computed results show huge improvements over the results obtained by earlier schemes for all the problems considered here, the errors tabulated in tables 6.2 and 6.6 do not reflect the true rate of convergence outlined in section 6.3. This is because of the fact that in reality the two step lengths around the point of discontinuity (d_1 and d_2) can never actually become zero and therefore

Table 6.5: *Problem 4: the computed values and analytical values of ϕ and corresponding absolute errors at the grid points for n= 10, r= 18; interface point is $x = \frac{1}{3}$*

grid points	*computed*	*analytical*	*abs.err*
0.000000	0.000000	0.000000	0.00000e+00
0.276996	0.505395	0.505416	2.135778e-05
0.323814	0.088354	0.088365	1.053413e-05
0.331740	0.013784	0.013761	2.269228e-06
0.333153	0.000785	0.000433	3.522289e-04
0.333831	0.000785	0.001083	2.979453e-04
0.336544	0.013865	0.013872	6.243955e-06
0.353276	0.088386	0.088389	2.654588e-06
0.446009	0.505447	0.505452	5.339823e-06
1.000000	0.000000	0.000000	0.00000e+00

Table 6.6: *Problem 4: The comparison between the infinity norm of errors $||E||_\infty$ with best fit r values and $||\hat{E}||_\infty$; interface point is $x = \frac{1}{3}$*

n	$\|\|E\|\|_\infty$	$\|\|\hat{E}\|\|_\infty$
10	0.246e-03	0.219e-01
20	0.112e-03	0.637e-02
40	0.955e-04	0.155e-02
80	0.490e-04	0.393e-03
160	0.110e-04	0.978e-04

the truncation errors in expressions (6.39), (6.40) and (6.52) would not tend to zero. Similar observations were also made in reference [104] where due to the possible lack of regularity of the solution, the expected higher rate of convergence could not be achieved on nonuniform grids.

6.5 Conclusion

In this chapter, we propose an HOC scheme for the 1D elliptic and parabolic equations with discontinuous coefficients and singular source terms on nonuniform space grids. As against earlier schemes which were at most second order accurate, this scheme is at least third order accurate at regular points. Moreover, use of nonuniform grids and clustering in the neighbourhood of the point of discontinuity enables the scheme to capture the flux thereat more accurately. We also perform some convergence and related analysis to substantiate our claims. To bring out the different aspects of the scheme it is applied to four problems (i) a steady state problem with discontinuous coefficient,

(ii) a steady state problem with singular source term, (iii) a steady state problem with discontinuous coefficient as well as singular source term and (iv) an unsteady problem with discontinuous source term. In all the cases our numerical results are in excellent agreement with the analytical ones. Particularly, in capturing the flux at the point of discontinuity, our approach is seen to be more efficient than the existing ones ([23], [79]). In the next chapter, extension of the formulation to two-dimensional cases will be discussed.

भारतीय प्रौद्योगिकी संस्थान गुवाहाटी
Indian Institute of Technology Guwahati

Chapter 7

An efficient HOC scheme for 2D Elliptic Equations with Discontinuous Coefficients and Singular Source Terms

7.1 Introduction

In this chapter, we borrow some of the ideas developed in Chapter 6 to propose a new approach for numerically solving 2D elliptic equations with discontinuous coefficients and singular source terms on uniform space grids.

Consider a 2D elliptic equation

$$(\beta\phi_x)_x + (\beta\phi_y)_y + \kappa(x,y)\phi = f(x,y)\ , \qquad (x,y) \in \Omega\ , \quad (x^*,y^*) \in \Gamma \tag{7.1}$$

with some specified boundary conditions, where β, κ and f are piecewise continuous, but may have a finite jump discontinuity across some interface (a curve in 2D case) Γ within the domain Ω; along with it f may have a delta function singularity.

Two physical jump conditions involving the unknown variables and its first derivatives (i.e. flux here) are required to solve this problem numerically. These jump conditions across the interface can be defined as

$$[\phi] = u^+ - u^- = \hat{C} \tag{7.2}$$

$$[\beta\phi_n] = \beta^+\frac{\partial\phi^+}{\partial n} - \beta^-\frac{\partial\phi^-}{\partial n} = \sigma, \tag{7.3}$$

where the jump discontinuities in ϕ and the flux (along the outward normal direction to the interface) across the interface with specific strengths are given as $\hat{C}$ and σ respectively.

Problems governed by equations of type (7.1) arises frequently in multiphase flow, composite materials, potential theory and many fields. With some minor adjustments,

complex flow problems like flow past bluff bodies can easily be accommodated into this type. For example, many researchers have tackled the flow past circular cylinder problem as an immersed interface problem ([15, 27, 75, 119]) by assuming the surface of the cylinder to be a circular interface enclosed in a closed domain. Here also, our interest will be mainly focussed on developing an HOC scheme in rectangular domains having circular interfaces in the same vein as in chapters 2 and 3. We rope in some aspects of the Alternating Direction Implicit (ADI) method [1, 4, 13] along with some of the 1D ideas developed in Chapter 6 to formulate this 2D extension; here we use the same assumptions considered in the 1D case but on uniform grids. This HOC formulation is fourth order accurate at regular grid points and second order accurate at irregular grid points. We then apply the formulation to two problems and compare our results with those obtained with immersed interface and other well known methods. In all the cases our formulation is found to produce reasonably accurate results on relatively coarser grids.

This chapter is organized in the following way: Section 7.2 deals with the mathematical formulations and discretization procedures, Section 7.3 with numerical examples, and finally Section 7.4, the conclusions.

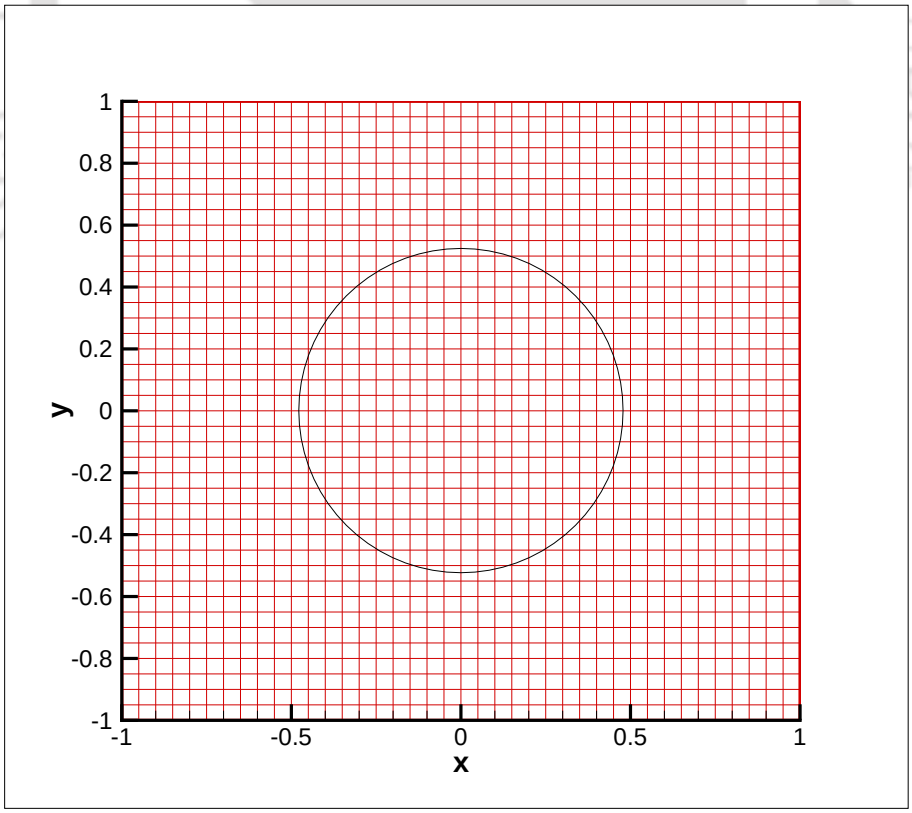

Figure 7.1: *two dimensional* 41×41 *mesh in uniform grid with circular interface.*

7.2 Mathematical Formulation and Discretization Procedure

Without loss of generality, we consider the solution domain to be the square $[-1,1] \times [-1,1]$ with a circular interface (see figure 7.1). A uniform Cartesian grid is generated by drawing vertical and horizontal lines through the points

$$x_i = -1 + ih_1, \quad y_j = -1 + jh_2, \quad i = 0,1,2,...,n-1 \quad and \quad j = 0,1,2,...,m-1,$$

such that the origin of the coordinate system is located at the center of the circular interface. The uniform grid spacings along x- and y-directions are denoted as $h_1 = \dfrac{2}{(n-1)}$ and $h_2 = \dfrac{2}{(m-1)}$ respectively. A typical uniform mesh along with the circular interface is shown in figure 7.1.

As in 1D case, the grid points are categorized into two types: regular and irregular grid points. Any point which is within one step length of the interface (either in x or y-direction) is termed as irregular point (see figure 7.2). All other points are termed as regular points. The treatment of the points on the interface that are grid points will be discussed at appropriate juncture.

For the regular grid points, the equation 7.1 is smooth enough and it can be written as

$$\beta\frac{\partial^2\phi}{\partial x^2} + \beta\frac{\partial^2\phi}{\partial y^2} + c(x,y)\frac{\partial\phi}{\partial x} + d(x,y)\frac{\partial\phi}{\partial y} + \kappa(x,y)\phi = f(x,y) \tag{7.4}$$

where all the variables are smooth enough and $c(x,y) = \dfrac{\partial\beta(x,y)}{\partial x}$ and $d(x,y) = \dfrac{\partial\beta(x,y)}{\partial y}$. We use the HOC formulation on uniform grids by Kalita *et al.* ([61]) to discretize equation (7.4), which at the (i,j)-th point is given by

$$[-A_{ij}\delta_x^2 - B_{ij}\delta_y^2 + C_{ij}\delta_x + D_{ij}\delta_y + G_{ij}\delta_x\delta_y - H_{ij}\delta_x\delta_x^2 - K_{ij}\delta_x^2\delta_y - L_{ij}\delta_x^2\delta_x^2 + M_{ij}]\phi_{ij} = F_{i,j} \tag{7.5}$$

with,

$$A_{ij} = \beta + \frac{c^2h_1^2}{12\beta} - \frac{h_1^2}{12}\kappa, \quad B_{ij} = \beta + \frac{d^2h_2^2}{12\beta} - \frac{h_2^2}{12}\kappa,$$

$$C_{ij} = c - \frac{ch_1^2}{12\beta}\kappa + \frac{h_1^2}{6}\kappa_x, \quad D_{ij} = d - \frac{dh_2^2}{12\beta}\kappa + \frac{h_2^2}{6}\kappa_y,$$

$$G_{ij} = -\left(\frac{cdh_1^2}{12\beta} + \frac{h_2^2dc}{12\beta}\right), \quad H_{ij} = -\left(\frac{ch_1^2}{12} + \frac{h_2^2c}{12}\right),$$

$$K_{ij} = -\left(\frac{dh_1^2}{12} + \frac{h_2^2d}{12}\right), \quad L_{ij} = -\left(\frac{\beta h_1^2}{12} + \frac{h_2^2\beta}{12}\right),$$

$$M_{ij} = -\frac{ch_1^2}{12\beta}\kappa_x - \frac{dh_2^2}{12\beta}\kappa_y + \frac{h_1^2}{12}\kappa_{xx} + \frac{h_2^2}{12}\kappa_{yy},$$

$$F_{ij} = \frac{h_1^2}{12} f_{xx} + \frac{h_2^2}{12} f_{yy} - \frac{h_1^2 c}{12\beta} f_x - \frac{h_2^2 d}{12\beta} f_y + f_{ij}.$$

where δ_x, δ_y and δ_x^2, δ_y^2 are the first and second order central difference operators along the x and y directions respectively.

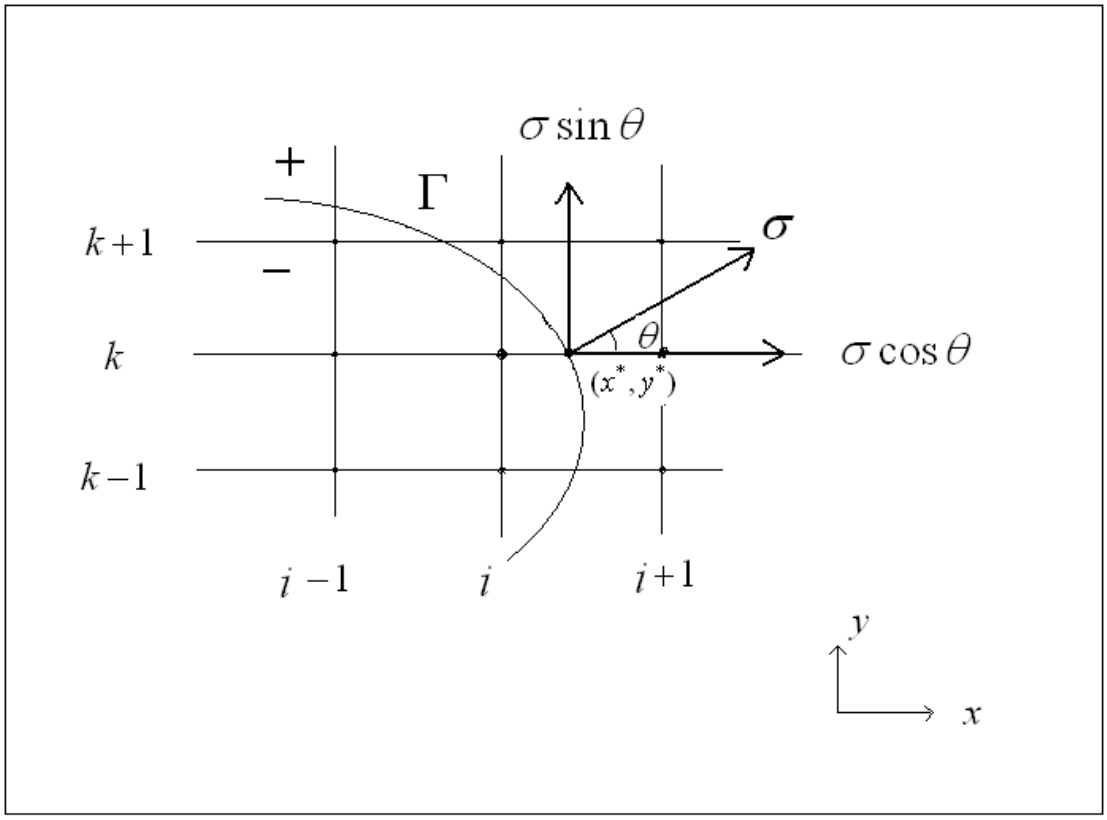

Figure 7.2: *The geometry at an irregular point (i, k) along x-direction. (x^*, y^*) is the interface point.*

At irregular grid points, we cannot use central difference oriented HOC approximation (7.5) directly because of possible discontinuity of ϕ, f and their first derivatives on the interface. Using the jump conditions (7.2) and (7.3) along with the original differential equation (7.1), one can get higher order accurate approximation of the differential equation at the irregular points. In figures 7.2 and 7.3, we show the geometry at an irregular grid point (i, k) or (l, j), where the jump on the flux, σ acts along the normal to the interface. In order to rope in the 1D approach described in Chapter 6, we need to find jumps in ϕ and its flux $(\beta\phi_n)$ along x and y directions separately. This can be accomplished by splitting the jumps along along x and y directions. From the figure 7.2,

jump condition (7.3) can be resolved along x and y directions respectively as

$$[\beta\phi_x] = \beta^+\frac{\partial\phi^+}{\partial x} - \beta^-\frac{\partial\phi^-}{\partial x} = \sigma\ cos\theta, \tag{7.6}$$

$$[\beta\phi_y] = \beta^+\frac{\partial\phi^+}{\partial y} - \beta^-\frac{\partial\phi^-}{\partial y} = \sigma\ sin\theta, \tag{7.7}$$

where θ is the angle made by this normal with the x-axis.

Now, we are ready to club an ADI type of approach with the 1D concept developed in Chapter 6 for the irregular points. Note that, despite the problem under consideration being a 2D problem, we do not use the regular nine point HOC stencil to discretize equation (7.1) at the irregular points. Instead, an algorithm is developed in such a way that it identifies the irregular points making a sweep first along the horizontal lines (call it x-sweep) through the grid points and once done with the horizontal lines, sweeps will be performed along the vertical lines (y-sweep). In an x-sweep, at an irregular point, for equation (7.1), firstly, partial derivatives with respect to y will be approximated using the ϕ values from previous y-sweep iterations or from the regular points whatever may be case and then (7.1) will be solved as an 1D equation. Similar procedure will be repeated for the y-sweep. This will result in two finite difference relations at the same point, once in x-direction at a particular y-level and the other one in y-direction at a particular x-level. However, at the regular points, formulation (7.5) will be used at each x- or y-sweep. Once all the sweeps in both x- and y-directions are over, the process is subjected to more iterations till desired accuracy is achieved.

In what follows, we discuss the development of these two finite difference relations.

7.2.1 Irregular points along x-direction (at a fixed y-level)

In this case, the irregular points on a particular y-line (i.e., for a fixed y-value) are those points which are directly adjacent to the interface (lying either to the left or right) and the points of intersection between the interface and that y-line will be the interface points for that particular y-line. In figure 7.2, (i, k) and $(i+1, k)$ are the irregular points on $y = k$ line and (x^*, y^*) is an interface point. Unlike the 1D case, an interface point here may be a grid point. However, an interface point in that case will not be considered as a regular point and the two grid points on either side in the horizontal direction will be considered as irregular points. The value on that particular grid point exactly lying on the interface will then be calculated by interpolation.

7.2.1.1 (a) Interface point is not a grid point:

To rope in the 1D approach of Chapter 6, we assume that the irregular points (i, k) and $(i + 1, k)$ (see figure 7.2) are very close to the interface point (x^*, y^*), so that we can

write the jump conditions as

$$\phi_{i+1,k} - \phi_{i,k} = \hat{C}\ cos\theta \tag{7.8}$$

$$(\beta\phi_x)_{(i+1,k)} - (\beta\phi_x)_{(i,k)} = \sigma\ cos\theta \tag{7.9}$$

Now using the one-sided Taylor expansion along with equation (7.1) we get

$$\left(1+\frac{h_1 c_{i+1,k}}{2\beta_{i+1,k}}\right)\left(\phi_x\right)_{(i+1,k)} = \frac{\phi_{(i+2,k)} - \phi_{(i+1,k)}}{h_1} - \frac{h_1}{2}\left(-\phi_{yy}+\frac{d}{\beta}\phi_y+\frac{\kappa}{\beta}\phi-\frac{1}{\beta}f\right)_{(i+1,k)} + O(h_1^2) \tag{7.10}$$

Similarly,

$$\left(1-\frac{h_1 c_{i,k}}{2\beta_{i,k}}\right)\left(\phi_x\right)_{(i,k)} = \frac{\phi_{(i,k)} - \phi_{(i-1,k)}}{h_1} + \frac{h_1}{2}\left(-\phi_{yy}+\frac{d}{\beta}\phi_y+\frac{\kappa}{\beta}\phi-\frac{1}{\beta}f\right)_{(i,k)} + O(h_1^2) \tag{7.11}$$

Using (7.10) and (7.11) in (7.9) we get the second order accurate finite difference jump-flux relation along x-axis as

$$\begin{aligned} a1_{i,k}a2_{i,k}\sigma\ cos\theta &= a1_{i,k}\beta_{i+1,k}\left(\frac{\phi_{i+2,k}}{h_1} - L1_{i,k}\phi_{i+1,k} + L2_{i,k}\phi_{i+1,k+1} + \frac{h_1}{2h_2^2}\phi_{i+1,k-1}\right. \\ &+ \left.\frac{h_1}{2\beta_{i+1,k}}f_{i+1,k}\right) - a2_{i,k}\beta_{i,k}\left(-\frac{h_1}{2h_2^2}\phi_{i,k+1} + l1_{i,k}\phi_{i,k} - l2_{i,k}\phi_{i,k-1}\right. \\ &- \left.\frac{1}{h_1}\phi_{i-1,k} - \frac{h_1}{2\beta_{i,k}}f_{i,k}\right) + O(h_1^2) \end{aligned} \tag{7.12}$$

where,

$$a1_{i,k} = \left(1-\frac{h_1 c_{i,k}}{2\beta_{i,k}}\right), \qquad a2_{i,k} = \left(1+\frac{h_1 c_{i+1,k}}{2\beta_{i+1,k}}\right), \tag{7.13}$$

$$L1_{i,k} = \left(\frac{1}{h_1}+\frac{h_1}{h_2^2}-\frac{h_1}{2}\frac{d_{i+1,k}}{\beta_{i+1,k}h_2}+\frac{h_1}{2}\frac{\kappa_{i+1,k}}{\beta_{i+1,k}}\right), \tag{7.14}$$

$$L2_{i,k} = \left(\frac{h_1}{2h_2^2}-\frac{h_1}{2h_2}\frac{d_{i+1,k}}{\beta_{i+1,k}}\right), \tag{7.15}$$

$$l1_{i,k} = \left(\frac{1}{h_1}+\frac{h_1}{h_2^2}+\frac{h_1}{2h_2}\frac{d_{i,k}}{\beta_{i,k}}+\frac{h_1}{2}\frac{\kappa_{i,k}}{\beta_{i,k}}\right), \tag{7.16}$$

$$l2_{i,k} = \left(\frac{h_1}{2h_2^2}+\frac{h_1}{2h_2}\frac{d_{i,k}}{\beta_{i,k}}\right). \tag{7.17}$$

Relations (7.8) and (7.12) yield the required relations for $\phi_{i,k}$ and $\phi_{i+1,k}$.

7.2.1.2 (b) Interface point is a grid point:

Let, (i,k) be the grid point which lies exactly on the interface. Then, $(i-1,k)$ and $(i+1,k)$ will be the two irregular points. Therefore, the jump relations in this case will be

$$\phi_{i+1,k} - \phi_{i-1,k} = \hat{C}\ cos\theta \tag{7.18}$$

$$(\beta\phi_x)_{(i+1,k)} - (\beta\phi_x)_{(i-1,k)} = \sigma\ cos\theta \tag{7.19}$$

and the equation (7.12) will reduce to

$$\begin{aligned} a1_{i-1,k}a2_{i-1,k}\sigma\ cos\theta &= a1_{i-1,k}\beta_{i+1,k}\left(\frac{\phi_{i+2,k}}{h_1} - L1_{i-1,k}\phi_{i+1,k} + L2_{i-1,k}\phi_{i+1,k+1} + \frac{h_1}{2h_2^2}\phi_{i+1,k-1}\right. \\ &+ \left.\frac{h_1}{2\beta_{i+1,k}}f_{i+1,k}\right) - a2_{i-1,k}\beta_{i-1,k}\left(-\frac{h_1}{2h_2^2}\phi_{i-1,k+1} + l1_{i-1,k}\phi_{i-1,k}\right. \\ &- \left. l2_{i-1,k}\phi_{i-1,k-1} - \frac{1}{h_1}\phi_{j-2,k} - \frac{h_1}{2\beta_{i-1,k}}f_{i-1,k}\right) + O(h_1^2) \end{aligned} \tag{7.20}$$

where,

$$a1_{i-1,k} = \left(1 - \frac{h_1 c_{i-1,k}}{2\beta_{i-1,k}}\right), \qquad a2_{i-1,k} = \left(1 + \frac{h_1 c_{i+1,k}}{2\beta_{i+1,k}}\right), \tag{7.21}$$

$$L1_{i-1,k} = \left(\frac{1}{h_1} + \frac{h_1}{h_2^2} - \frac{h_1}{2}\frac{d_{i+1,k}}{\beta_{i+1,k}h_2} + \frac{h_1}{2}\frac{\kappa_{i+1,k}}{\beta_{i+1,k}}\right), \tag{7.22}$$

$$L2_{i-1,k} = \left(\frac{h_1}{2h_2^2} - \frac{h_1}{2h_2}\frac{d_{i+1,k}}{\beta_{i+1,k}}\right), \tag{7.23}$$

$$l1_{i-1,k} = \left(\frac{1}{h_1} + \frac{h_1}{h_2^2} + \frac{h_1}{2h_2}\frac{d_{i-1,k}}{\beta_{i-1,k}} + \frac{h_1}{2}\frac{\kappa_{i-1,k}}{\beta_{i-1,k}}\right), \tag{7.24}$$

$$l2_{i-1,k} = \left(\frac{h_1}{2h_2^2} + \frac{h_1}{2h_2}\frac{d_{i-1,k}}{\beta_{i-1,k}}\right). \tag{7.25}$$

Relation (7.18) and (7.20) yield the required relations for $\phi_{i+1,k}$ and $\phi_{i-1,k}$.

Now, in order to calculate the value at $(i,k)^{th}$ point we use a second order accurate interpolation formula. We use three points each from the left and right of (i,k), i.e., $(i+1,k)$, $(i+2,k)$, $(i+3,k)$ and $(i-1,k)$, $(i-2,k)$, $(i-3,k)$ to get two one-sided interpolated values, $\tilde{F}_1$ and $\tilde{F}_2$ of (i,k), where

$$\tilde{F}_1 = 2.5\phi_{i+1,k} - 2\phi_{i+2,k} + 0.5\phi_{i+3,k} + O(h_1^2)$$

$$\tilde{F}_2 = 2.5\phi_{i-1,k} - 2\phi_{i-2,k} + 0.5\phi_{i-3,k} + O(h_1^2).$$

Finally, we take the average of these two to get

$$\phi_{i,k} = \left(\frac{\tilde{F}_1 + \tilde{F}_2}{2}\right).$$

7.2.2 Irregular points along y-direction (at a fixed x-level)

Here, the procedure is analogous to the treatment of irregular points along x-direction.

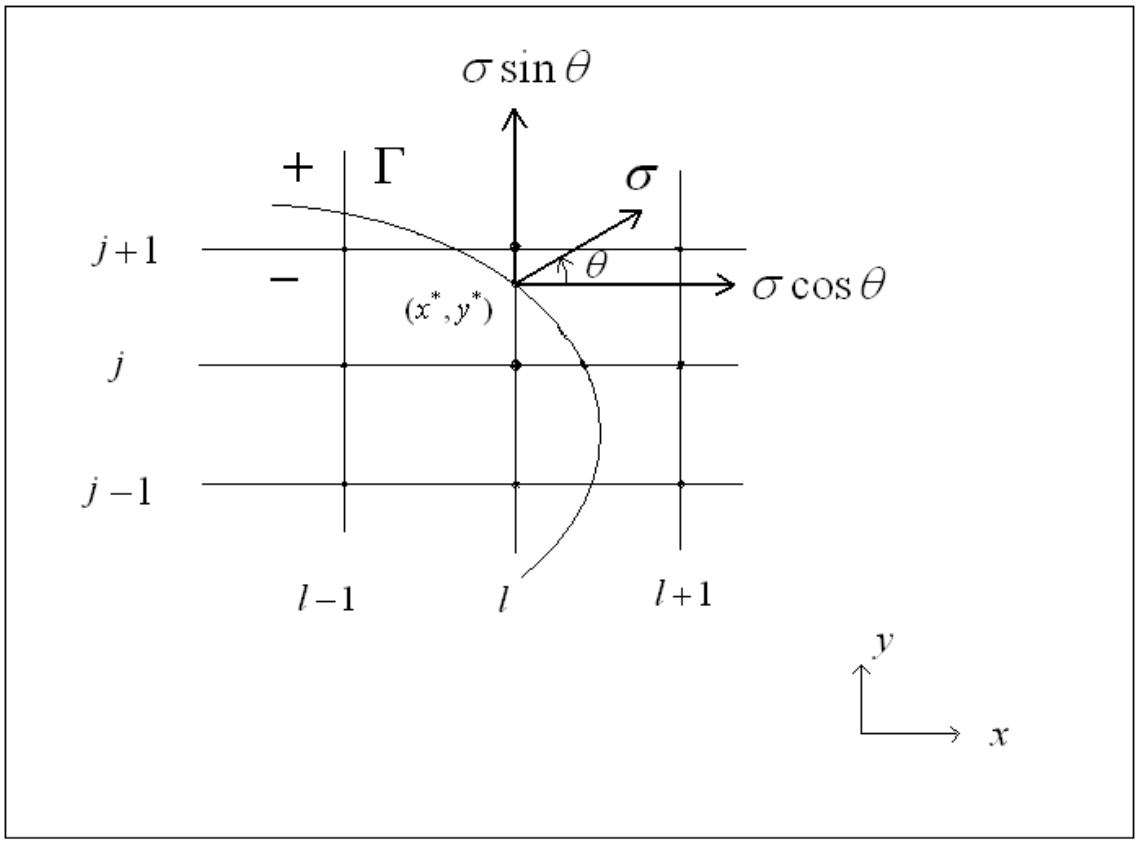

Figure 7.3: *The geometry at an irregular point (l, j) along y-direction. (x^*, y^*) is the interface point.*

7.2.2.1 (a) Interface point is not a grid point:

In figure 7.3, (l, j) and $(l, j+1)$ are the irregular points on $x = l$ line and (x^*, y^*) is an interface point. Here, the jump relations are

$$\phi_{l,j+1} - \phi_{l,j} = \hat{C}\ sin\theta \tag{7.26}$$

$$(\beta\phi_y)_{(l,j+1)} - (\beta\phi_y)_{(l,j)} = \sigma\ sin\theta \tag{7.27}$$

Using one-sided Taylor expansion along with equation (7.1) and proceeding as in the

x-direction case, the final difference relation will be

$$\begin{aligned} b1_{l,j}b2_{l,j}\sigma\ sin\theta &= b1_{l,j}\beta_{l,j+1}\Bigg(\frac{\phi_{l,j+2}}{h_2} - M1_{l,j}\phi_{l,j+1} + M2_{l,j}\phi_{l+1,j+1} + \frac{h_2}{2h_1^2}\phi_{l-1,j+1} \\ &+ \frac{h_2}{2\beta_{l,j+1}}f_{l,j+1}\Bigg) - b2_{l,j}\beta_{l,j}\Bigg(- \frac{h_2}{2h_1^2}\phi_{l+1,j} + m1_{l,j}\phi_{l,j} - m2_{l,j}\phi_{l-1,j} \\ &- \frac{1}{h_2}\phi_{l,j-1} - \frac{h_2}{2\beta_{l,j}}f_{l,j}\Bigg) + O(h_2^2) \end{aligned} \tag{7.28}$$

where,

$$b1_{l,j} = \left(1 - \frac{h_2 d_{l,j}}{2\beta_{l,j}}\right), \qquad b2_{l,j} = \left(1 + \frac{h_2 d_{l,j+1}}{2\beta_{l,j+1}}\right), \tag{7.29}$$

$$M1_{l,j} = \left(\frac{1}{h_2} + \frac{h_2}{h_1^2} - \frac{h_2}{2h_1}\frac{c_{l,j+1}}{\beta_{l,j+1}} + \frac{h_2}{2}\frac{\kappa_{l,j+1}}{\beta_{l,j+1}}\right), \tag{7.30}$$

$$M2_{l,j} = \left(\frac{h_2}{2h_1^2} - \frac{h_2}{2h_1}\frac{c_{l,j+1}}{\beta_{l,j+1}}\right), \tag{7.31}$$

$$m1_{l,j} = \left(\frac{1}{h_2} + \frac{h_2}{h_1^2} + \frac{h_2}{2h_1}\frac{c_{l,j}}{\beta_{l,j}} + \frac{h_2}{2}\frac{\kappa_{l,j}}{\beta_{l,j}}\right), \tag{7.32}$$

$$m2_{l,j} = \left(\frac{h_2}{2h_1^2} + \frac{h_2 c_{l,j}}{2\beta_{l,j}}\right), \tag{7.33}$$

(7.26) and (7.28) are the required relations for ϕ at the grid points (l, j) and $(l, j+1)$ respectively.

7.2.2.2 (b) Interface point is a grid point:

Let, (l, j) be a grid point which is on the interface. Then, $(l, j-1)$ and $(l, j+1)$ will be the two irregular points. Therefore, the jump relations will be

$$\phi_{l,j+1} - \phi_{l,j-1} = \hat{C}\ sin\theta \tag{7.34}$$

$$(\beta\phi_y)_{(l,j+1)} - (\beta\phi_y)_{(l,j-1)} = \sigma\ sin\theta \tag{7.35}$$

As before, equation (7.28) will get modified as

$$\begin{aligned} b1_{l,j-1}b2_{l,j-1}\sigma\ sin\theta &= b1_{l,j-1}\beta_{l,j+1}\Bigg(\frac{\phi_{l,j+2}}{h_2} - M1_{l,j-1}\phi_{l,j+1} + M2_{l,j-1}\phi_{l+1,j+1} + \frac{h_2}{2h_1^2}\phi_{l-1,j+1} \\ &+ \frac{h_2}{2\beta_{l,j+1}}f_{l,j+1}\Bigg) - b2_{l,j-1}\beta_{l,j-1}\Bigg(- \frac{h_2}{2h_1^2}\phi_{l+1,j-1} + m1_{l,j-1}\phi_{l,j-1} \\ &- m2_{l,j-1}\phi_{l-1,j-1} - \frac{1}{h_2}\phi_{l,j-2} - \frac{h_2}{2\beta_{l,j}}f_{l,j-1}\Bigg) + O(h_2^2) \end{aligned} \tag{7.36}$$

where,

$$b1_{l,j} = \left(1 - \frac{h_2 d_{l,j-1}}{2\beta_{l,j-1}}\right), \qquad b2_{l,j} = \left(1 + \frac{h_2 d_{l,j+1}}{2\beta_{l,j+1}}\right), \tag{7.37}$$

$$M1_{l,j} = \left(\frac{1}{h_2} + \frac{h_2}{h_1^2} - \frac{h_2}{2h_1} \frac{c_{l,j+1}}{\beta_{l,j+1}} + \frac{h_2}{2} \frac{\kappa_{l,j+1}}{\beta_{l,j+1}} \right), \tag{7.38}$$

$$M2_{l,j} = \left(\frac{h_2}{2h_1^2} - \frac{h_2}{2h_1} \frac{c_{l,j+1}}{\beta_{l,j+1}} \right), \tag{7.39}$$

$$m1_{l,j} = \left(\frac{1}{h_2} + \frac{h_2}{h_1^2} + \frac{h_2}{2h_1} \frac{c_{l,j-1}}{\beta_{l,j-1}} + \frac{h_2}{2} \frac{\kappa_{l,j-1}}{\beta_{l,j-1}} \right), \tag{7.40}$$

$$m2_{l,j} = \left(\frac{h_2}{2h_1^2} + \frac{h_2 c_{l,j-1}}{2\beta_{l,j-1}} \right), \tag{7.41}$$

Relation (7.34) together with (7.36) give the required expressions for $\phi_{l,j+1}$ and $\phi_{l,j-1}$.

As before, in order to calculate the value at $(l,j)^{th}$ point we use second order accurate interpolation by making use of three points from both sides of (l,j), i.e., $(l,j+1)$, $(l,j+3)$, $(l,j+3)$ and $(l,j-1)$, $(l,j-2)$, $(l,j-3)$ to get two one-sided interpolated values, $\tilde{F}_3$ and $\tilde{F}_4$ of (l,j), where

$$\tilde{F}_3 = 2.5\phi_{l,j+1} - 2\phi_{l,j+2} + 0.5\phi_{l,j+3} + O(h_2^2)$$

$$\tilde{F}_4 = 2.5\phi_{l,j-1} - 2\phi_{l,j-2} + 0.5\phi_{l,j-3} + O(h_2^2).$$

Finally, taking average of these two yields

$$\phi_{l,j} = \left(\frac{\tilde{F}_3 + \tilde{F}_4}{2} \right).$$

7.3 Numerical Examples

To validate our 2D formulation, we present two examples which were also used by LeVeque and Li [73] to validate their second order IIM method. In both these examples, Γ is the circle $x^2 + y^2 = \frac{1}{4}$ inside the square $-1 \leq x, y \leq 1$.

Example 1: First we consider the problem ([73, 122]), where there is a singular source term along Γ. The differential equation is:

$$\phi_{xx} + \phi_{yy} = \int_\Gamma 2\delta\left(x - X(s)\right)\delta\left(y - Y(s)\right) ds. \tag{7.42}$$

Dirichlet boundary conditions are specified along the boundary by using the analytical solution

$$\phi(x,y) = \begin{cases} 1, & r \leq \frac{1}{2} \\ 1 + log(2r), & r > \frac{1}{2} \end{cases} \tag{7.43}$$

where $r = \sqrt{x^2 + y^2}$. The jumps conditions at all points of Γ can easily be determined from equation (7.42) as

$$[\phi]_\Gamma = 0$$

$$\left[\frac{\partial \phi}{\partial n}\right]_\Gamma = 2$$

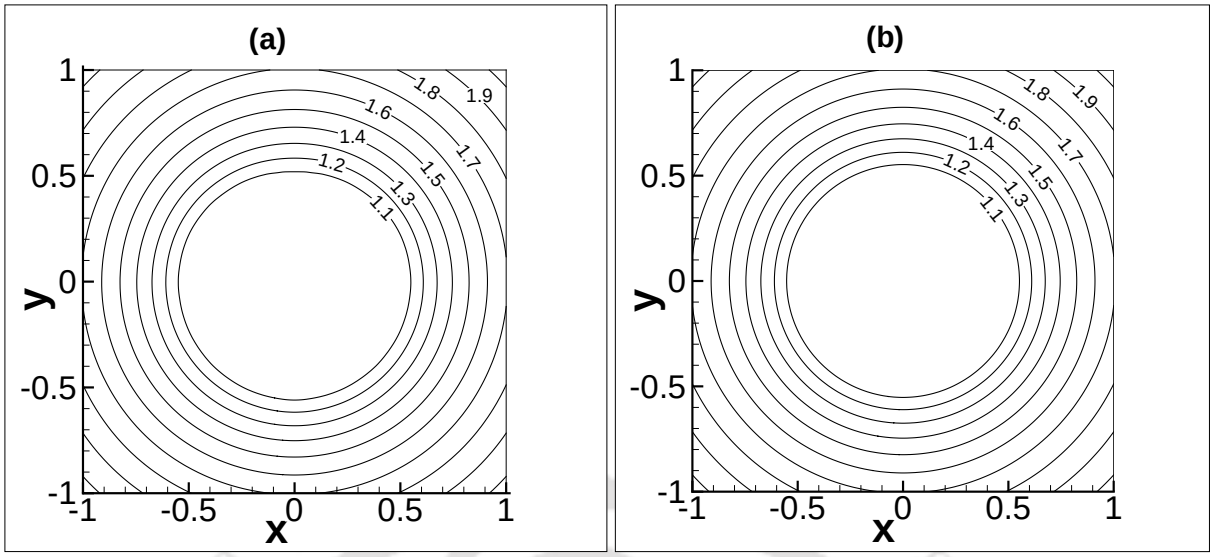

Figure 7.4: *Problem 1: Contour plots of (a) present numerical solution on* 81×81 *grid and (b) analytical solution.*

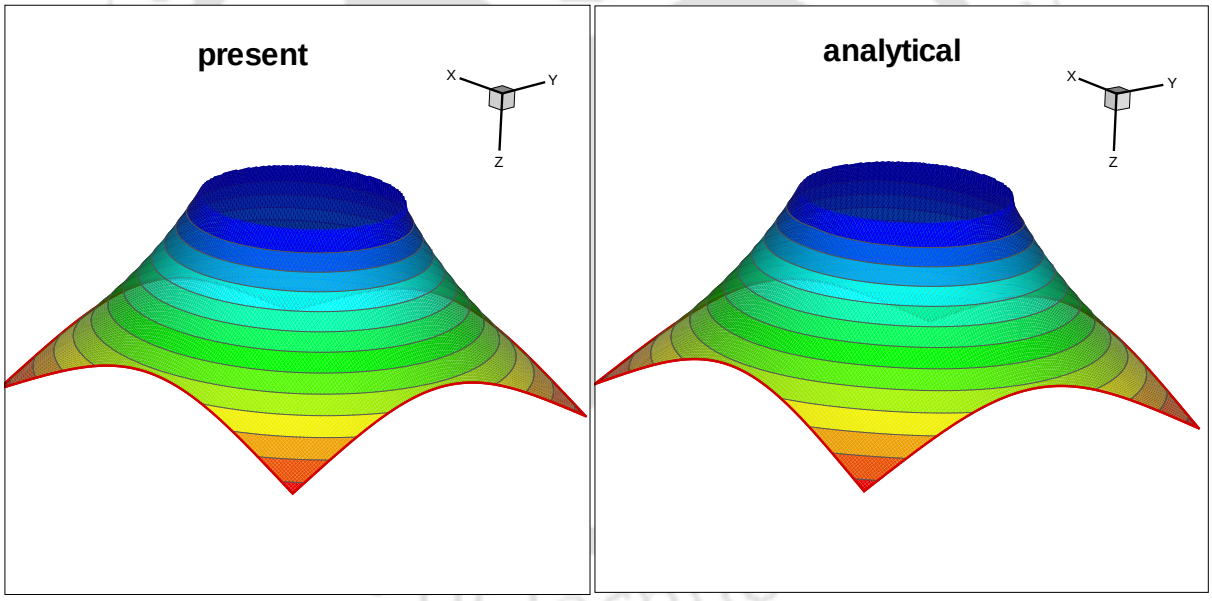

Figure 7.5: *Problem 1: Surface plots of present numerical solution on* 81×81 *grid and analytical solution.*

Figure 7.4 shows the comparison of the two dimensional contour plots between the analytical solution and the numerical solution computed by our scheme on a 81×81 grid. The surface plot of these two solutions are presented in figure 7.5. In both the figures, the numerical and analytical plots are almost indistinguishable. In figure 7.6, we plot the errors on 81×81 and 161×161 grids. The maximum absolute errors on these two grids were 8.7×10^{-4} and 2.1×10^{-4} respectively, thus predicting an $O(h^2)$

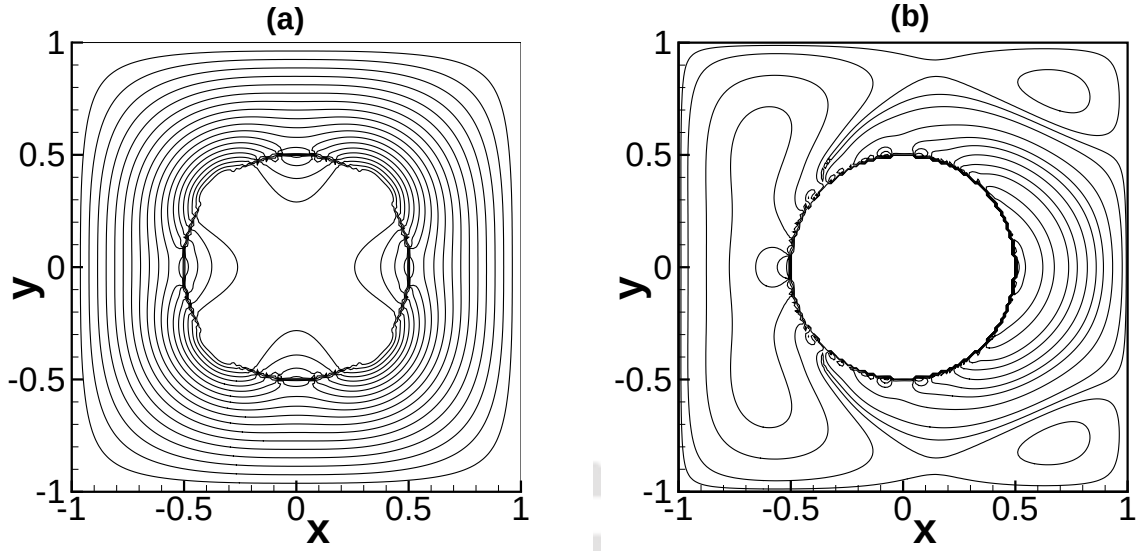

Figure 7.6: *Problem 1: Error contours computed by present scheme on (a) 81×81 and (b) 161×161 grids.*

convergence rate, which is lower than the theoretical convergence rate.

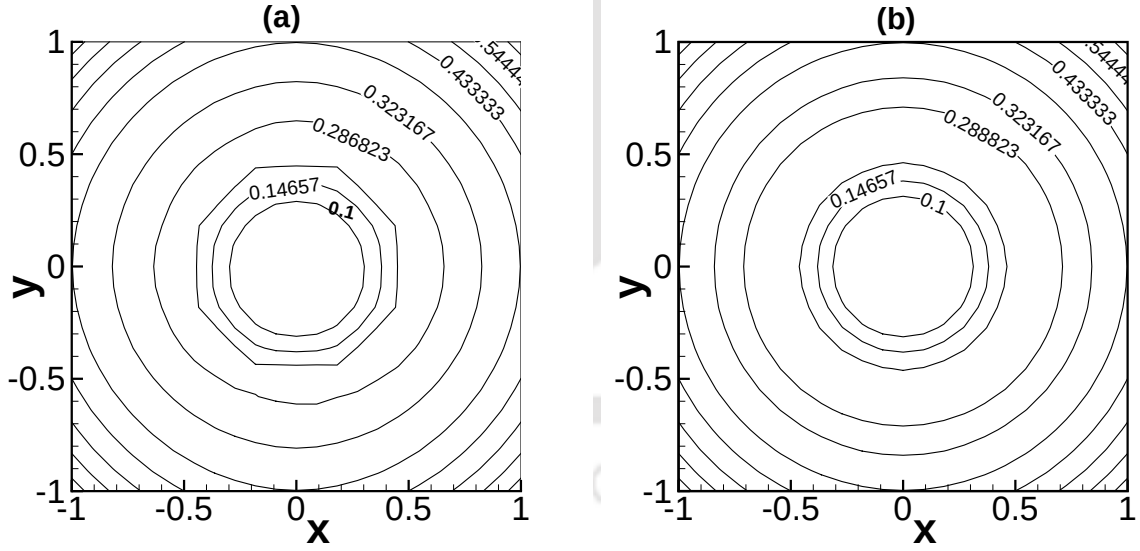

Figure 7.7: *Problem 2: Contour plots of (a) present numerical solution on* 23×23 *grid and (b) analytical solution.*

Example-2: We now consider a problem which has discontinuous coefficients as well as a singular source term ([73, 122]). The equation is

$$(\beta\phi_x)_x + (\beta\phi_y)_y = f(x,y) + C\int_\Gamma \delta\left(\vec{x} - \vec{X}(s)\right) ds \tag{7.44}$$

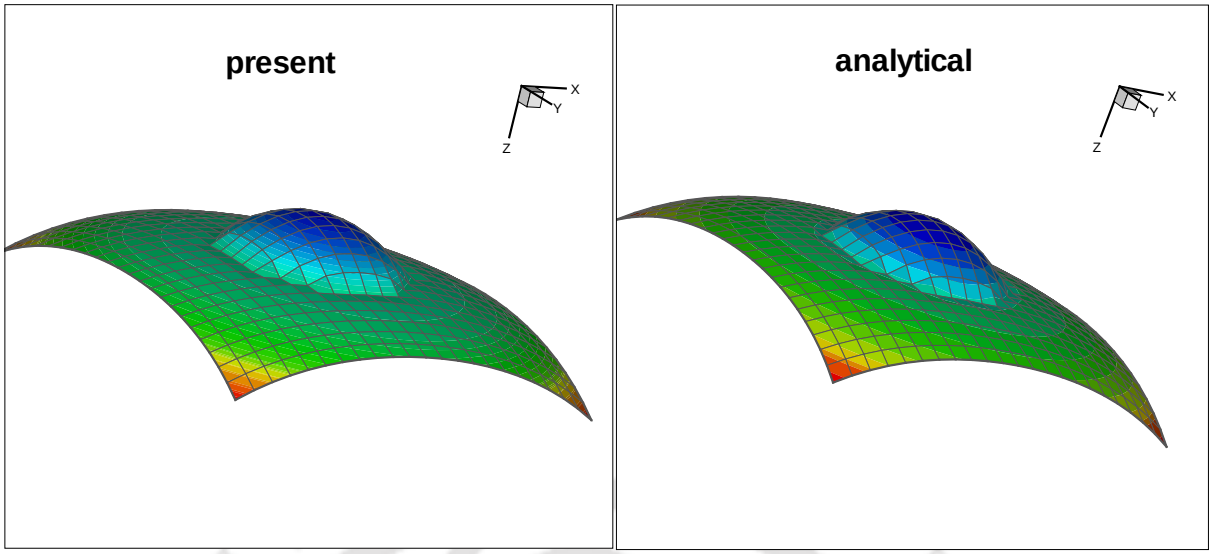

Figure 7.8: *Problem 2: Surface plots of the present numerical solution on* 23×23 *grid and analytical solution.*

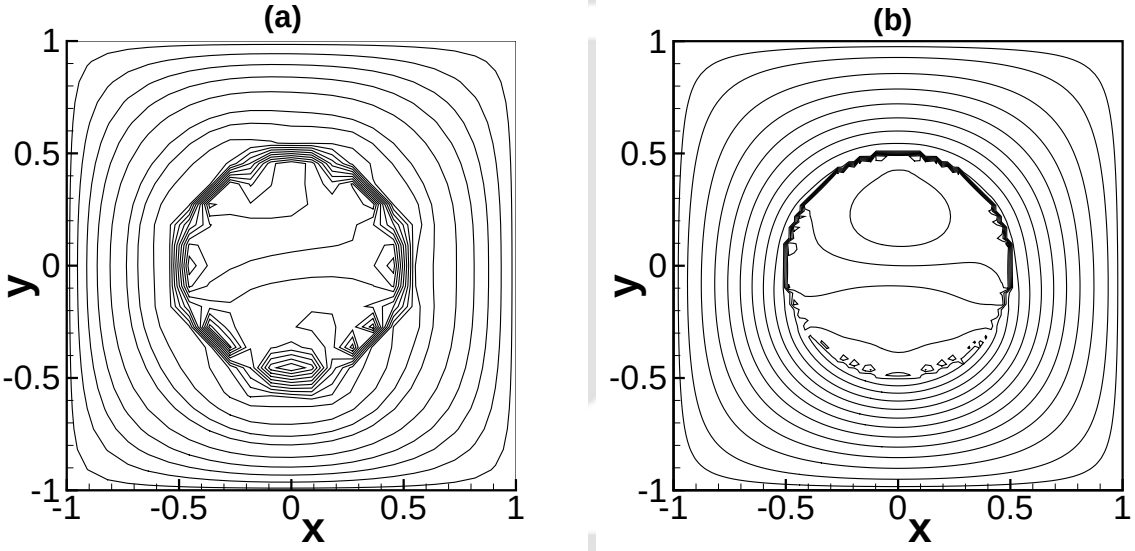

Figure 7.9: *Problem 2: Error contours computed by present scheme using (a)* 23×23 *and (b)* 43×43 *grids.*

with $$f(x,y) = 8(x^2+y^2)+4,$$

$$\beta(x,y) = \begin{cases} x^2+y^2+1, & x^2+y^2 \leq \frac{1}{4} \\ b, & x^2+y^2 > \frac{1}{4} \end{cases}$$

The value of b determines the magnitude of jump in β across the interface. Dirichlet boundary conditions are determined from the analytical solution

$$\phi(x,y) = \begin{cases} r^2, & r \leq \frac{1}{2} \\ (1-\frac{1}{8b}-\frac{1}{b})/4 + (\frac{r^4}{2}+r^2)/b + C\ log(2r/b), & r > \frac{1}{2} \end{cases} \tag{7.45}$$

Figure 7.7 shows the comparison of the two dimensional contour plots between the analytical solution and the numerical solution computed by our scheme on a 23×23 grid for $b = 10.0$ and $C = 0.1$. It is worth mentioning that, with a grid as coarse as 23×23, our computed solutions are reasonably close to the analytical ones. The surface plots shown in figure 7.8 reconfirms this fact. In figure 7.8, we present the contour plot of the errors on 23×23 and 43×43 grids. The maximum absolute errors of the numerical solution on these two grids were 4.1×10^{-3} and 5.6×10^{-4} respectively, which are comparable to the studies of [73, 122].

7.4 Conclusion

In this chapter, we propose an HOC scheme on uniform grids for 2D elliptic equations with discontinuous coefficients and source term by borrowing some ideas from the 1D approach developed in Chapter 6. To validate our numerical scheme, it is applied to (i) a problem having singular source term and (ii) a problem having discontinuous coefficients as well as a singular source term. Though reasonably accurate results are obtained in both the cases, the scheme's theoretical rate of convergence could not be established completely. There is still some room for improvement in the scheme and its application to problems governed by the N-S equations is another area which has not been explored here as it is beyond the scope of this PhD work. However, this novel approach has the potential for extension to 3D problems as the 2D flux splitting strategy can be easily extended to three dimensions.

Chapter 8

Conclusion

8.1 Observations and Remarks

This dissertation is concerned with the development of Higher Order Compact (HOC) schemes for convection-diffusion equations on nonuniform grids in general and incompressible viscous flows for tackling circular geometries in particular. Firstly, a class of new HOC schemes are developed in cylindrical polar coordinates, whose extension to curvilinear coordinate system is straightforward. In contrast to the earlier HOC schemes which were able to handle only unit diffusion coefficients in Cartesian coordinates, this new class of HOC schemes are able to handle variable coefficients of the second order derivatives appearing in convection-diffusion type of equations: both in cartesian and other orthogonal curviliear coordinate systems. The second part of the PhD work is concerned with clubbing some existing HOC methodology with novel discretization strategies at certain points of the physical domain in order to capture discontinuities and to solve circular interface problems in Cartesian coordinates. All the schemes are then employed to different complex physical flow situations to examine their accuracy, efficiency and robustness. Extensive validation exercise is carried out by comparing the present results with existing analytical, numerical and experimental results. In what follows, we firstly summarize the PhD work and then the achievements in line with the objectives that were set at the outset of the dissertation. Finally, some insightful comments are made on the possible extension of this work in the near future.

- *Scheme 1:* An HOC scheme for the 2D convection-diffusion equations on Cartesian coordinates [62] is extended to cylindrical polar coordinates on nonuniform grids and more specifically to the steady 2D incompressible viscous flows governed by the Navier-Stokes equations. The formulation is first applied to a problem having analytical solution and its fourth order spatial accuracy is demonstrated. It is then applied to the flow past an impulsively started circular cylinder problem and finally to the driven polar cavity problem. Comparison of the numerical results with

established numerical, and, analytical and experimental results produces excellent match in all the cases.

- *Scheme 2:* Next, a Crank-Nicolson type of implicit HOC scheme is developed for the unsteady two-dimensional Navier-Stokes equations on nonuniform polar grids specifically designed for the incompressible viscous flow past circular cylinders. The scheme is second order accurate in time and at least third order accurate in space. The proposed scheme is validated by first applying it to the well-known problem of unsteady flow past an impulsively started circular cylinder for a wide range of Re ranging from 10 to 9500. In the process, a transient HOC approximation for the Neumann boundary condition for vorticity is also developed. For moderate and low Re values, we compute the flow until steady state or till the flow becomes periodic. For the higher range of Re, we compute the solution in the initial stages of the flow. Then, the newly developed transient HOC scheme is applied to capture the more complex phenomena of unsteady flow past a rotating and translating cylinder for $Re = 200, 500$ and 1000 for the range of rotational parameters $0.5 \leq \alpha \leq 3.25$. The flow is computed not only for the early stages, but also for long enough time to investigate the vortex shedding phenomenon as well. For all the Reynolds numbers, detailed discussion on the flow structure and comparison with experimental and numerical results are provided. In each case, the computed solution agrees very well, both qualitatively and quantitatively with established numerical and experimental results, confirming the efficiency of the proposed scheme.

- *Schemes 3 and 4:* Next, an at least third order spatially accurate compact scheme is developed for numerically solving one-dimensional (1D) elliptic equations with discontinuous coefficients, fluxes and singular source terms on nonuniform grids; this is accomplished by the intelligent clubbing of an existing HOC methodology with specific approximation of the derivatives in the neighbourhood of the points of discontinuities. Stability and convergence analysis of this newly developed scheme is carried out in detail. The scheme is then extended to its transient parabolic counterpart with a Crank-Niolson type of temporal discretization yielding a second order temporal accuracy.

- *Scheme 5:*Then, this 1D idea is extended to the 2D elliptic problems in rectangular domains having circular interfaces on uniform cartesian grids. As in the 1D case, the regular points were handled with an existing HOC scheme while a noval stategy was adopted to handle the irregular points in the vicinity of the interface to tackle the discontinuities on the interface. This strategy was seen to handle very effectively the elliptic interface problems that was chosen for the validation of the

proposed scheme. This scheme also has the potential for easy extension to higher dimensional problems as well.

8.2 Achievements:

The work therefore, achieves with great success the major objectives set at the beginning, namely, development of some new HOC algorithms for computation of steady and unsteady viscous flows on curvilinear coordinates, more specifically for the flow past circular cylinders. The development of these new algorithms along with the modification of some existing ones to enhance their strength has clearly broadened the scope of applicability of HOC schemes. In what follows the major achievements of the thesis will be highlighted in the form of observations and comments, further substantiating the claim of objectives having been achieved.

- Most of the earlier HOC schemes could deal only with unit diffusion coefficients in Cartesian coordinates with uniform grids on the computational plane; this constraint restricted the application of the HOC schemes developed on cylindrical polar coordinates to Poisson equation equations only. Scheme 1 removes this debilitating constraint by easy handling of the variable coefficients that appear in the second order derivative terms of convection-diffusion type of equations and thus paves the way for easy extension of the scheme to general orthogonal curvilinear coordinates. Morever, the scheme does not use transformation from the physical plane to the computational plane. In the process, the formulation avoids the complexities invariably associated with transformations. Even the few attempts which were made to develop HOC schemes on geometries beyond recatangular used transformations from the physical to the computational plane at the expense of additional computational cost.

- For the flow past an impulsively started circular cylinder problem, flow is simulated in the range of Reynolds number 10 to 9500. Present computed solutions are in excellent agreement with existing experimental and standard numerical results. To the best of our knowledge, the HOC simulations from our computed solutions for the higher Reynolds numbers are much closer to the experimental visualizations than any numerical results found in literature. The robustness of the scheme however is better realized when it captures the periodic nature of the flow for $Re = 60$ and 200 characterized by vortex shedding represented by the von Kármán street and also by the fact that it very accurately captures the so called α and β-phenomena for higher Re values.

- For the rotating circular cylinder problem also, our computed solutions are in excellent agreement with existing experimental and standard numerical results, where Reynolds numbers in the range of 200 to 1000 are considered. It is worth repeating that for both the impulsively started and rotating cylinder problems, the flow simulations from our computations are much closer to the experimental visualization than any other existing numerical simulation available in the literature.

- HOC schemes on nonuniform grids for the one dimensional elliptic and parabolic problems with different types of discontinuities have been developed in the work. This novel approach is seen to produce better results than the Immersed Interface Method (IIM) and other existing methods. In this way, the present work has contributed significantly towards the enrichment of the existing HOC methodologies.

- The two dimensional extension of the 1D idea is also an important addition to the existing HOC schemes. The idea used to tackle the discontinuities along the interface can be extended easily for higher dimensional problems. Satisfactory comparison is obtained with problems having analytical solutions.

- Another point worth mentioning is that advance iterative solvers like BiCGStab, hybrid BiCGStab are extensively used to solve the discrete algebraic systems throughout the present work. This gives additional strength to the methods to efficiently solve the complex flow problems without much difficulty.

8.3 Scope for Future Works

This dissertation has been an attempt to develop and expand the field of application of HOC schemes, particularly for incompressible viscous flows on circular geometries; but the potential still remains to explore many more areas and the floodgates can open up even further. The followings are the probable areas that could be taken up in future.

- The HOC schemes which are developed here to solve the problems in curvilinear coordinate systems are used on the cylindrical polar coordinate systems only. This opens up the possibility to use these schemes on general curvilinear coordinate system other than those involving circular geometries.

- The present HOC schemes can be used to solve the complex flow problem like the uniform shear flow past a circular cylinder.

- Most of the HOC scheme are developed to solve the two dimensional problems. Only a few attempts have been made to solve real three dimensional (3D) problems.

So, there is a huge possibility to develop and implement HOC schemes to solve 3D problems.

- Extension of the HOC approach for the 2D interface problems have opened up the possibility of using HOC schemes to tackle flows in random geometries governed by the Navier-Stokes equations and moving interface problems.
- 3D extension of the present 2D interface method can be an interesting and important area of research.
- Existing HOC scheme are developed on finite difference setup only, but possible attempt can be made to implement this HOC idea with some modifications, on finite volume setup. This may also be an important area of research.

भारतीय प्रौद्योगिकी संस्थान गुवाहाटी
Indian Institute of Technology Guwahati

Appendix A

Details of the Finite Difference Operators

The expressions for the finite difference operators appearing in the various equations in chapters 2, 3, 4 and 5 are as follows:

$$\delta_r \phi_{i,j} = \frac{\phi_{i+1,j} - \phi_{i-1,j}}{2\Delta r}$$

$$\delta_\theta \phi_{i,j} = \frac{\phi_{i,j+1} - \phi_{i,j-1}}{2\Delta \theta}$$

$$\delta_r^2 \phi_{i,j} = \frac{1}{\Delta r}\left\{ \frac{\phi_{i+1,j}}{r_f} - (\frac{1}{r_f} + \frac{1}{r_b})\phi_{i,j} + \frac{\phi_{i-1,j}}{r_b} \right\}$$

$$\delta_\theta^2 \phi_{i,j} = \frac{1}{\Delta \theta}\left\{ \frac{\phi_{i,j+1}}{\theta_f} - (\frac{1}{\theta_f} + \frac{1}{\theta_b})\phi_{i,j} + \frac{\phi_{i,j-1}}{\theta_b} \right\}$$

$$\begin{aligned} \delta_r^2 \delta_\theta \phi_{i,j} = \frac{1}{2\Delta r \Delta \theta}\Big\{ & \frac{1}{r_f}(\phi_{i+1,j+1} - \phi_{i+1,j-1}) - (\frac{1}{r_f} + \frac{1}{r_b})(\phi_{i,j+1} - \phi_{i,j-1}) \\ & + \frac{1}{r_b}(\phi_{i-1,j+1} - \phi_{i-1,j-1}) \Big\} \end{aligned}$$

$$\begin{aligned} \delta_r \delta_\theta^2 \phi_{i,j} = \frac{1}{2\Delta r \Delta \theta}\Big\{ & \frac{1}{\theta_f}(\phi_{i+1,j+1} - \phi_{i-1,j+1}) - (\frac{1}{\theta_f} + \frac{1}{\theta_b})(\phi_{i+1,j} - \phi_{i-1,j}) \\ & + \frac{1}{\theta_b}(\phi_{i+1,j-1} - \phi_{i-1,j-1}) \Big\} \end{aligned}$$

$$\begin{aligned} \delta_r^2 \delta_\theta^2 \phi_{i,j} = & \frac{1}{\Delta r \Delta \theta}\Big\{ \frac{\phi_{i+1,j+1}}{r_f \theta_f} + \frac{\phi_{i-1,j+1}}{r_b \theta_f} - (\frac{1}{r_f \theta_f} + \frac{1}{r_b \theta_f})\phi_{i,j+1} \\ & - (\frac{1}{r_f \theta_f} + \frac{1}{r_f \theta_b})\phi_{i+1,j} + (\frac{1}{r_f \theta_f} + \frac{1}{r_f \theta_b} + \frac{1}{r_b \theta_f} + \frac{1}{r_b \theta_b})\phi_{i,j} \\ & - (\frac{1}{r_f \theta_b} + \frac{1}{r_b \theta_b})\phi_{i,j-1} - (\frac{1}{r_b \theta_f} + \frac{1}{r_b \theta_b})\phi_{i-1,j} + \frac{\phi_{i+1,j-1}}{r_f \theta_b} + \frac{\phi_{i-1,j-1}}{r_b \theta_b} \Big\} \end{aligned}$$

$$\delta_r \delta_\theta \phi_{i,j} = \frac{1}{4\Delta r \Delta \theta}\Big\{ \phi_{i+1,j+1} - \phi_{i+1,j-1} - \phi_{i-1,j+1} + \phi_{i-1,j-1} \Big\}.$$

Here $r_f = (r_{i+1} - r_i)$, $r_b = (r_i - r_{i-1})$ are the forward and backward step lengths respectively in the r-direction and $\theta_f = (\theta_{j+1} - \theta_j)$, $\theta_b = (\theta_j - \theta_{j-1})$ are the forward and backward step lengths respectively in the θ-direction for $(i,j)^{\text{th}}$ node with $\Delta r = (r_f + r_b)/2$ and $\Delta\theta = (\theta_f + \theta_b)/2$.

Bibliography

[1] Anderson Jr. JD. *Computational Fluid dynamics: The Basics with Applications*, McGraw-Hill, inc: New York, (1995).

[2] Batchelor GK. *An Introduction to Fluid Dynamics*, Cambridge University Press, Cambridge, (2005).

[3] Crank J. *Free and Moving Boundary Problems*, Oxford University Press, New York, (1984).

[4] Hoffman JD. *Numerical Methods for Engineers and Scientists*, McGraw-Hill, inc: New York, First Edition, (1992).

[5] Kelley CT. *Iterative Methods for Linear and Nonlinear Equations*. SIAM Publications, Philadelphia, (1995).

[6] Kopal Z. *Numerical Analysis*. Chapman and Hall, London, UK, second Edition, (1961).

[7] Li Z, Ito K. *The Immersed Interface Method Numerical Solution of PDEs Involving Interfaces and Irregular Domains*, SIAM Publication (2006).

[8] Morton KW, Mayers DF. *Numerical Solution of Partial Differential Equations*, Cambridge University Press, Cambridge, (1995).

[9] Muralidhar K, Sundararajan T (Eds) *Computational Fluid flow and heat transfer: IIT Kanpur series of advanced texts*, Narosa Publishing House: New Delhi, (2003).

[10] Panton RL. *Incompressible Flow*, John Wiley and Sons: New York, (1984).

[11] Prandtl L, Tietjens OG. *Applied Hydro- and Aeromechanics*, Dover, New York, (1934).

[12] Schlichting H, Gersten K. *Boundary Layer Theory*, Springer, 8^{th} Revised and Enlarged Edition, New Delhi, (2004).

[13] Tannehill JC, Anderson DA, Pletcher RH. *Computational Fluid Mechanics and Heat Transfer*, Taylor & Francis, Second Edition (1997).

[14] Zdravkovich MM. *Flow Around Circular Cylinders; Vol 1: Fundamentals*, Oxford University Press inc., New York, (1997).

[15] Le DV. *An Immersed Interface Method for Solving Viscous Incompressible Flows Involving Rigid and Flexible Boundaries*, PhD Thesis, Singapore-MIT Alliance, June 2005.

[16] Abarbanel S and Kumar A. Compact higher-order schemes for the Euler equations. *Journal of Scientific Computing*, 1988; **3**:275–288.

[17] Adam Y. Highly accurate compact implicit methods and boundary conditions. *J. Comput. Phys.*, 1977; **24**:10–22.

[18] Anderson CR and Reider MB. A High Order Explicit Method for the Computation of flow about a Circular Cylinder. *J. Comput. Physics*, 1996; **125**:207–224.

[19] Badr HM and Dennis SCR. Time-dependent viscous flow past an impulsively started rotating and translating circular cylinder. *J. Fluid Mech.*, 1985; **158**:447-488.

[20] Badr HM, Dennis SCR and Young PJS. Steady and unsteady flow past a rotating circular cylinder at low Reynolds numbers. *Comput. Fluids*, 1989; **17**:579–609.

[21] Badr HM, Coutanceau M, Dennis SCR and Menard C. Unsteady flow past a rotating circular cylinder at Reynolds numbers 10^3 and 10^4. *J. Fluid Mech.*, 1990; **220**:459-484.

[22] Berthelsen PA amd Faltinsen OM. A local directional ghost cell approach for incompressible viscous flow problems with irregular boundaries. *J. Comput. Phys.*, 2008; **227**:4354–4397.

[23] Beyer RP and Leveque RJ. Analysis of a One-dimentional model for the Immersed Boundary Method. *SIAM J. Numer. Anal.*, 1992; **29**:332–364.

[24] Blasius H. Grenzschichten in Flussigkeiten mit kleiner Reibung. *Z. Math. Phys.*, 1908; **56**:1–37.

[25] Borges L and Daripa P. A fast parallel algorithm for the Poisson equation on a disk. *J. Comput. Phys.*, 2001; **169**:151–192.

[26] Bouard R and Coutanceau M. The early stage of development of the wake behind an impulsively started cylinder for $40 < Re < 10^4$. *J. Fluid Mech.*, 1980; **101**(3):583–607.

[27] Calhoun D. A Cartesian grid method for solving the two-dimensional streamfunction-vorticity equations in irregular regions. *J. Comput. Phys.*, 2002; **176**:231–275.

[28] Candilarov JD and Vulkov LG. Analysis of immersed interface Difference Schemes for Reaction-diffusion problems with singular own sources. *Comp. Meth. In Appl. Math.*, 2003; **3**:253–273.

[29] Chen YM, Ou YR and Pearlstein AJ. Development of the wake behind a circular cylinder impulsively started into rotatory and rectilinear motion. *J. Fluid Mech.*, 1993; **253**:449-484.

[30] Chew YT, Cheng M, Luo SC. A numerical study of flow past a rotating circular cylinder using a hybrid vortex scheme. *J. Fluid Mech.*, 1995; **299**:35-71.

[31] Chou MH. Numerical study of vortex shedding from a rotating cylinder immersed in a uniform flow field. *Intl J. Numer. Meth. Fluids*, 2000; **32**:545-567.

[32] Collins WM and Dennis SCR. The initial flow past an impulsively started circular cylinder. *Q. J. Mech. Appl. Math*, 1973a; **26**:53–75.

[33] Constantinescu GS and Lele SK. A Highly Accurate Technique for the Treatment of Flow Equations at the Polar Axis in Cylindrical Coordinates Using Series Expansions. *J. Comput. Phys.*, 2002; **183**:165–186.

[34] Coutanceau M and Bouard R. Experimental determination of the main feratures of the viscous flow in the wake of a circular cylinder in uniform translation. Part 1. Steady flow. *J. Fluid Mech.*, 1977; **79**:231–256.

[35] Coutanceau M and Bouard R. Experimental determination of the main feratures of the viscous flow in the wake of a circular cylinder in uniform translation. Part 2. Unsteady flow. *J. Fluid Mech.*, 1977; **79**:257-272.

[36] Coutanceau M and Menard C. Influence of rotation on the near-wake development behind an impulsively started circular cylinder. *J. Fluid Mech.*, 1985; **158**:399-446.

[37] D'Alessio SJD and Dennis SCR. A vorticity model for viocous flow past a cylinder. *Comp. Fluids*, 1994; **23**:279–293.

[38] Dennis SCR and Chang GZ. Numerical solution for study flow past a circular cylinder at Reynolds numbers up to 100. *J. Fluid Mech.*, 1970; **42**:471–489.

[39] Dennis SCR and Hudson JD. Compact h^4 finite difference approximations to operators of Navier-Stokes type. *J. Comput. Phys.*, 1989; **85**:390–416.

[40] Dipankar A, Sengupta TK and Talla SB. Suppression of vortex shedding behind a circular cylinder by another control cylinder at low Reynolds numbers. *J. Fluid Mech.*, 2007; **573**:171-190.

[41] Dukowicz JK and Ramshaw JD. Tensor viscosity method for convection in numerical fluid dynamics. *J. Comput. Phys.*, 1979; **32**:71–79.

[42] Farrell PA, Miller JJH, O'Riordan E and Shishkin GI. Singularly perturbed differential equations with discontinuous source terms, In: Miller JJH, Shishikin GI and Vulkov L. (Eds.). *Proceedings of Analytical and Numerical Methods for Convection-Dominated and Singularly Perturbed Problems, Lozenetz, Bulgaria, 1998*, Nova Science Publishers, New York, USA, 1998: 23-32.

[43] Fauci LJ and Peskin CS. A computational model of aquatic animal locomotion. *J. Comput. Phys.*, 1988; **77**:85–108.

[44] Fornberg B. A numerical study of steady viscous flow past a circular cylinder. *J. Fluid Mech.*, 1980; **98**:819–855.

[45] Fornberg B. Steady viscous flow past a circular cylinder up to Reynolds number 600. *J. Comput. Phys.*, 1985; **61**:297–320.

[46] Franke R, Rodi W and Schonung B. Numerical calculation of laminar vortex-shedding flow past cylinders. *Journal of Wind Engineering and Industrial Aerodynamics,*, 1990; **35**:237–257.

[47] Friehe CA. Vortex shedding from cylinders at low Renolds numbers. *J. Fluid Mech.*, 1980; **100**:237–241.

[48] Fuchs L and Tillmark N. Numerical and Experimental study of Driven Flow in a Polar Cavity. *Int. J. Numer. Meth. Fluids*, 1985; **5**:311–329.

[49] Gartland Jr. EC. Discrete weighted mean approximation of a model convection-diffusion equation. *SIAM J. Sci. Stat. Comp.*, 1982; **3**:460–472.

[50] Goldstein S and Rosenhead L. Boundary layer growth. *Proc. Cam. Phil. Soc.*, 1936; **32**:392–401.

[51] Gupta MM, Manohar RP and Stephenson JW. A single cell high order scheme for the convection-diffusion equation with variable coefficients. *Int. J. Numer. Meth. Fluids*, 1984; **4**:641–651.

[52] Gupta MM. A fourth order Poisson solver. *J. Comput. Phys.*, 1984; **55**:166–172.

[53] Gupta MM. High accuracy solutions of incompressible Navier-Stokes equations. *J. Comput. Phys.*, 1991; **93**:343–359.

[54] He X and Doolen G. Lattice Boltzmann Method on Curvilinear Coordinates system: Flow arround a Circular Cylinder. *J. Comput. Phys.*, 1997; **134**:306–315.

[55] Hirsh RS. Higher-order accurate difference solutions of fluid mechanics problems by a compact differencing technique. *J. Comput. Phys.*, 1975; **19**:90–109.

[56] Huang H and Li Z. Convergence analysis of the immersed interface method. *IMA J. Numer. Anal.*, 1999; **19**:583–608.

[57] Ingham DB. Steady flow past a rotating cylinder. *Comput. Fluids*, 1983; **11**:351-366.

[58] Ingham DB and Tang T. A numerical investigation into the steady flow past a rotating circular cylinder at low and intermediate Reynolds numbers. *J. Comput. Phys.*, 1990; **87**:91–107.

[59] Iyengar SRK and Manohar R. High order difference methods for heat equation in polar cylindrical coordinates. *J. Comput. Phys.*, 1988; **77**:425–438.

[60] Jain MK, Jain RK and Krishna M. A fourth-order difference scheme for quasilinear Poisson equation in polar co-ordinates. *Commun. Numer. Meth. Eng.*, 1994; **10**:791–797.

[61] Kalita JC, Dalal DC and Dass AK. A class of higher order compact schemes for the unsteady two-dimensional convection-diffusion equations with variable convection coefficients. *Int. J. Numer. Meth. Fluids*, 2002; **38**:1111–1131.

[62] Kalita JC, Dass AK and Dalal DC. A transformation-free HOC scheme for steady state convection-diffusion on non-uniform grids. *Int. J. Numer. Meth.Fluids*, 2004; **44**:33–53.

[63] Kalita JC, Chhabra P. An improved (9,5) higher order compact scheme for the transient two-dimensional convection-diffusion equation. *Int. J. Numer. Meth. Fluids*, 2006; **51**:703–717.

[64] Kalita JC, Dass AK and Nidhi N. An efficient transient Navier-Stokes solver on compact nonuniform space grids. *J. Comp. appl. Math.*, 2008; **214**:148–162.

[65] Kalita JC, Ray RK. A transformation-free HOC scheme for incompressible viscous flows past an impulsively started circular cylinder. *J. Comput. Phys.*, 2009; **228**:5207–5236.

[66] Kang S, Choi H and Lee S. Laminar flow past a rotating circular cylinder. *Phys. Fluids*, 1999; **11**:3312-3321.

[67] Koumoutsakos P and Leonard A. High-resolution simulations of the flow around an impulsively started cylinder using vortex methods. *J. Fluid Mech.*, 1995; **296**:1–38.

[68] Lai MC. A simple compact fourth-order Poisson solver on polar geometry. *J. Comput. Phys.*, 2002; **182**:337–345.

[69] Lai MC and Wang WC. Fast direct solvers for Poisson equation on 2D polar and spherical geometries. *Numer. Meth. Partial Diff. Eq.*, 2002; **18**:56–68.

[70] Lax, PD and Wendroff B. Systems of conservation laws. *Comm. Pure Appl. Math.*, 1960; **13**:217–237.

[71] Lee D and Tsuei YM. A Hybrid Adaptive Gridding Procedure for Recirculating Flud Flow Problems. *J. Comput. Phys.*, 1993; **108**:122–141.

[72] Lele SK and Lele SK. Compact finite difference schemes with spectral like resolution. *J. Comput. Phys.*, 1992; **103**:16–42.

[73] Leveque RJ and Li Z. The Immersed Interface Method for Elliptic equations with discontinuous coefficients and singular sources. *SIAM J. Nuner. Anal.*, 1994; **31**:1019-1044.

[74] Li M, Tang T and Fornberg B. A compact fourth-order finite difference scheme for the steady incompressible Navier-Stokes equations. *Int. J. Numer. Meth. Fluids*, 1995; **20**:1137–1151.

[75] Linnick MN and Fasel HF. A high-order immersed interface method for simulating unsteady compressible flows on irregular domains. *J. Comput. Phys.*, 2005; **204**:157-192.

[76] Loc TP. Etude numerique de l ecoulement dun fluide visqueux incompressible autour dun cylindre fixe ou en rotation: Effet Magnus. *J. Mech.*, 1975; **14**:109-134.

[77] Loc TP. Numerical analysis of unsteady secondary vortices generated by an impulsively started circular cylinder. *J. Fluid Mech.*, 1980; **100**:111–128.

[78] Loc TP and Bouard R. Numerical solution of the early stage of the unsteady viscous flow arround a circular cylinder: a comparison with experimental visualization and measurements. *J. Fluid Mech.*, 1985; **160**:93–117.

[79] MacKinnon RJ and Carey GF. Analysis of Material Interface Discontinuities and Superconvergent Fluxes in Finite difference theory. *J. Comput. Phys.*, 1988; **75**:151–167.

[80] Mackinnon RJ and Johnson RW. Differential equation based representation of truncation errors for accurate numerical solution. *Int. J. Numer. Meth. Fluids*, 1991; **13**:739–757.

[81] Mittal S and Raghuvanshi A. Control of vortex shedding behind circular cylinder for flows at low Reynolds numbers. *Int. J. Numer. Methods Fluids.*, 2001; **35**:421-447.

[82] Mittal S and Kumar B. Flow past a rotating cylinder. *J. Fluid Mech.*, 2003; **476**:303-334.

[83] Mohseni K and Colonius T. Numerical treatment of polar coordinate singularities. *J. Comput. Phys.*, 2000; **157**:787–795.

[84] Nair MT, Sengupta TK and Chauhan US. Flow past rotating cylinders at high Reynolds numbers using higher order upwind scheme. *Comput. Fluids*, 1998; **27**:47-70.

[85] Niu XD, Chew YT and Shu C. Simulation of flows arround an impulsively started circular cylinder by Taylor series expansion and least squares-based lattice Boltzmann Method. *J. Comput. Phys.*, 2003; **188**:176–193.

[86] Norberg C. An experimental investigation of the flow around a circular cylinder: influence of aspect ratio. *J. Fluid Mech.*, 1994; **258**:287–316.

[87] Noye BJ and Tan HH. A third-order semi-implicit finiti difference method for solving the one-dimensional convection-diffusion equation. *Int. J. Num. Meth. Eng.*, 1988; **26**:1615–1629.

[88] O'Riordan E, Pickett ML and Shishkin GI. Singularly Perturbed Problems Modelling Reaction-Convection-Diffusion Processes. *Comput. Meth. Appl. Math.*, 2003; **3**:424–442.

[89] Padrino JC and Joseph DD. Numerical study of the steady-state uniform flow past a rotating cylinder. *J. Fluid Mech.*, 2006; **557**:191-223.

[90] Pandit SK, Kalita JC and Dalal DC. A fourth-order accurate compact scheme for the solution of steady Navier-Stokes equation on non-uniform grids, *Computers and Fluids*, 2008; **37**(2):121–134.

[91] Pandit SK, Kalita JC and Dalal DC. A transient higher order compact scheme for incompressible viscous flows on geometries beyond rectangular, *J. Comput. Phys.*, 2007; **225**:1100–1124.

[92] Peskin CS. Numerical analysis of blood flow in the heart. *J. Comput.Phys.*, 1977; **25**:220–252.

[93] Prandtl L. The Magnus effect and windpowered ships. *Naturwissenschaften*, 1925; **13**:93–108.

[94] Qian L and Vezza M. A vorticity-based method for incompressible unsteady viscous flows. *J. Comput. Phys.*, 2001; **172**:515–542.

[95] Ray RK and Kalita JC. A transformation-free HOC scheme for incompressible viscous flows on nonuniform polar grids. *Int. J. Numer. Methods Fluids.*, 2009; **DOI**:10.1002/fld.2039.

[96] Ray RK, Kalita JC, Dass AK. An efficient HOC scheme for transient convection-diffusion-reaction equations with discontinuous coefficients and singular source terms. *Proc. Appl. Math. Mech.*, 2007; **7**(1):1025603–1025604.

[97] Sanyasiraju YVSS and Manjula V. Flow past an impulsively started circular cylinder using a higher-order semicompact scheme. *Physical Review E*, 2005; **72**(016709):1–10.

[98] Sanyasiraju YVSS and Manjula V. Fourth-Order Semi-Compact Scheme for Flow Past a Rotating and Translating Cylinder. *J. Sci. Comput.*, 2007; **30**(3):389–407.

[99] Schuh H. Calculation of unsteady boundary layers in two dimensional laminar flow. *Z. Flugwiss.*, 1953; **1**:122–131.

[100] Sengupta TK and Sengupta R. Flow past an impulsively started circular cylinder at high Reynolds number. *Computational Mechanics*, 1994; **14**:298-310.

[101] Sengupta TK, Ganeriwal G and De S. Analysis of central and upwind compact schemes. *J. Comput. Phys.*, 2003; **192**(2):677–694.

[102] Sesterhenn J. A characteristic-type formulation of the Navier-Stokes equations for high order upwind schemes. *Comp. Fluids*, 2001; **30**(1):37–67.

[103] Sherer SE and Scott JN. High order compact finite-difference methods on general overset grids. *J. Comput. Physics*, 2005; **210**:459–496.

[104] Shukla RK, Tatineni M and Zhong X. Very high order compact finite difference schemes on non-uniform grids for incompressible Navier-Stokes equations. *J. Comput. Physics*, 2007; **224**:1064–1094.

[105] Sleijpen GLG, van der Vorst HA. Hybrid bi-conjugate gradient methods for CFD problems: in Hafez M. and Oshima K. (Eds.). *Computational Fluid Dynamics Review, Wiley, Chichester*, 1995; 457–476.

[106] Spotz WF and Carey GF. High-order compact scheme for the steady stream-function vorticity equations. *Int. J. Numer. Meth. Eng.*, 1995; **38**:3497–3512.

[107] Spotz WF and Carey GF. Formulation and experiments with high-order compact schemes for nonuniform grids, *Int. J. Numer. Meth. Heat Fluid Flow*, 1998; **8**(3):288–303.

[108] Strikwerda JC. High-order-accurate schemes for incompressible viscous flow. *Int. J. Numer. Meth. Fluids*, 1997; **24**:715–734.

[109] Takami H and Keller HB. Steady two-dimensional viscous flow of an incompressible fluid past a circular cylinder. *Phys. Fluids*, 1969; **12**(Suppl. II):11–51.

[110] Tang T and Ingham DB. On steady flow past a rotating circular cylinder at Reynolds numbers 60 and 100. *Comput. Fluids*, 1991; **19**:217–230.

[111] Tritton DJ. Experiments on the flow past a circular cylinder at low Reynolds numbers. *J. Fluid Mech.*, 1959; **6**:547–567.

[112] Visbal MR and Gaitonde DV. On the Use of Higher-Order Finite-Difference Schemes on Curvilinear and Deforming Meshes. *J. Comput. Phys.*, 2002; **181**:155–185.

[113] Wang CY. The flow past a circular cylinder which is started impulsively from rest. *J. Math. Phys.*, 1967; **46**:195–202.

[114] Watson EJ. Boundary layer growth. *Proc. R. Soc. Lond.*, 1955; **231**(A):104–116.

[115] Wilkes NS and Thompson CP. An evaluation of higher-order upwind differencing for elliptic flow problems. *Proc. 3rd int. Conf. on Num. Meths. in Lamimar and Turbulent flow*, 1983; :248–257.

[116] Williamson CHK. Oblique and parallel modes of vortex shedding in the wake of a circular cylinder at low Renolds numbers. *J. Fluid Mech.*, 1989; **206**:579–627.

[117] Wong HH and Raithby GD. Improved finite-difference methods based on a critical evaluation of the approximation errors. *Numer. Heat Transfer*, 1979; **2**:139-163.

[118] Wundt H. Wachstum der laminaren Grenzschicht an schrag angestromten Zylindern bei Anfahrt aua der Ruhe. *Ing.-Arch. Berlin*, 1955; **23**:212.

[119] Xu S and Wang ZJ. An immersed interface method for simulating the interaction of a fluid with moving boundaries. *J. Comput. Phys.*, 2006; **216**:454-493.

[120] Yanwen M, Dexun F, Kobayashi T and Taniguchi N. Numerical solution of the incompressible Navier-Stokes equations with an upwind compact difference scheme. *Int. J. Numr. Meth. Fluids*, 1999; **30**:509-521.

[121] Zhang J, Ge L and Gupta MM. Fourth order compact difference scheme for 3D convection-diffusion equation with boundary layers on nonuniform grids. *Nural. Parallel and Sci. Comput.*, 2000; **8**:373–392.

[122] Zhong X. A new high-order immersed interface method for solving elliptic equations with imbedded interface of discontinuity. *J. Comput. Phys.*, 2007; **225**:1066–1099.

[123] Zhuang Y and Sun XH. A High-Order Fast Direct Solver for Singular Poisson Equations. *J. Comput. Phys.*, 2001; **171**:79–94.